NTIS # PB2009-

SSC-456

BUCKLING COLLAPSE TESTING ON FRICTION STIR WELDED ALUMINUM STIFFENED PLATE STRUCTURES

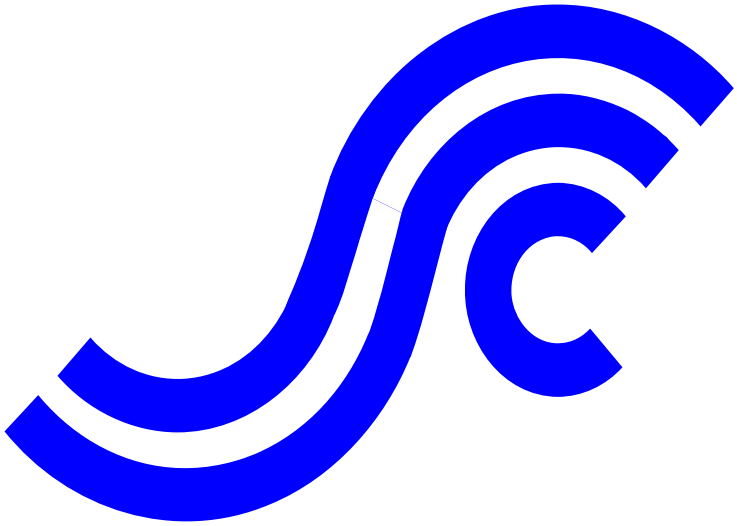

SHIP STRUCTURE COMMITTEE

2009

Ship Structure Committee

RADM Brian M. Salerno
U. S. Coast Guard Assistant Commandant,
Assistant Commandant for Marine Safety, Security and Stewardship
Chairman, Ship Structure Committee

{Name}
{Title}
Naval Sea Systems Command

Dr. Roger Basu
Senior Vice President
American Bureau of Shipping

Mr. Christopher McMahon
Director, Office of Ship Construction
Maritime Administration

Mr. Donald Roussel
Director General, Marine Safety,
Safety & Security
Transport Canada

Mr. Kevin Baetsen
Director of Engineering
Military Sealift Command

Dr. Neil Pegg
Group Leader - Structural Mechanics
Defence Research & Development Canada - Atlantic

UNITED STATES COAST GUARD
Mr. Jeffrey Lantz,
Commercial Regulations and Standards for the
Assistant Commandant for Marine Safety, Security
and Stewardship
Mr. Jeffery Orner
Deputy Assistant Commandant for Engineering and
Logistics

EXECUTIVE DIRECTOR
Lieutenant Commander, Jason Smith
U. S. Coast Guard

ADMINISTRATIVE ASSISTANT
Ms. Jeannette Y. Grant
U. S. Coast Guard

SHIP STRUCTURE SUB-COMMITTEE

AMERICAN BUREAU OF SHIPPING (ABS)

Mr. Glenn Ashe
Mr. Derek Novak
Mr. Phil Rynn
Mr. Balji Menon

DEFENCE RESEARCH & DEVELOPMENT CANADA ATLANTIC
Dr. David Stredulinsky
Mr. John Porter

MARITIME ADMINISTRATION (MARAD)
Mr. Chao Lin
Mr. Carl Setterstrom
Mr. Richard Sonnenschein

MILITARY SEALIFT COMMAND (MSC)
Mr. Michael W. Touma
Mr. Paul Handler

NAVY/ONR / NAVSEA/ NSWCCD
{Name}
{Name}
{Name}
{Name}

TRANSPORT CANADA
Paul Denis Vallee

UNITED STATES COAST GUARD

CDR Charles Rawson
Mr. James Person
CAPT Paul Roden
Mr. Rubin Sheinberg

SOCIETY OF NAVAL ARCHITECTS AND MARINE ENGINEERS (SNAME)
Mr. Jaideep Sirkar
Mr. Al Rowen
Mr. Norman Hammer

Member Agencies:

American Bureau of Shipping
Defence Research and Development Canada
Maritime Administration
Military Sealift Command
Naval Sea Systems Command
Society of Naval Architects & Marine Engineers
Transport Canada
United States Coast Guard

Ship
Structure
Committee

Address Correspondence to:

COMMANDANT (CG-5212/SSC)
ATTN (EXECUTIVE DIRECTOR/SHIP
STRUCTURE COMMITTEE)
US COAST GUARD
2100 2ND ST SW STOP 7126
WASHINGTON DC 20593-7126
Website: http://www.shipstructure.org

SSC – 456
SR – 1454

SEPTEMBER 12, 2009

BUCKLING COLLAPSE TESTING OF FRICTION STIR WELDED ALUMINUM STIFFENED PLATE STRUCTURES

This project examined the structures of friction stir welded (FSW) aluminum plates as an expansion of the work completed in SSC-451 titled *Mechanical Collapse Testing on Aluminum Stiffened Panels for Marine Applications,* where the ultimate limit state of traditional fusion welding was measured. One of the objectives of this study was to measure and collect mechanical tensile fracture and buckling collapse test data of FSW 5000 and 6000 series aluminum stiffened plate structures. Another objective of this study was to compare fabrication induced imperfections plus the ultimate strength performance characteristics of these structures to those welded by fusion welding.

In general, it was found that (1) the tensile strength properties of FSW material were equal to or better than that of fusion welded material; (2) the ultimate compressive strength of FSW structures was about 10 – 20% greater than those of fusion welded structures; and (3) the fabrication induced imperfections in FSW structures were smaller than those made by fusion welding. However, the investigator also encountered problems of delamination at the FSW regions during buckling collapse which indicates that additional research on FSW parameters is necessary.

BRIAN M. SALERNO
Rear Admiral, U.S. Coast Guard
Chairman, Ship Structure Committee

Technical Report Documentation Page

1. Report No. SSC - 456	2. Government Accession No.	3. Recipient's Catalog No.
4. Title and Subtitle Buckling Collapse Testing of Friction Stir Welded Aluminum Stiffened Plate Structures		5. Report Date February 3, 2009 6. Performing Organization Code
7. Author(s) Jeom Kee Paik		8. Performing Organization Report No. SR-1454
9. Performing Organization Name and Address LRET Research Centre of Excellence, Pusan National University 30 Jangjeon-Dong, Geumjeong-Gu, Busan 609-735 Korea		10. Work Unit No. (TRAIS) 11. Contract or Grant No.
12. Sponsoring Agency Name and Address COMMANDANT (CG-5212/SSC) ATTN (ADMIN ASST/SHIP STRUCTURE COMMITTEE) US COAST GUARD 2100 2ND ST SW STOP 7126 WASHINGTON DC 20593-7126		13. Type of Report Final Report 14. Sponsoring Agency Code CG- 5
15. Supplementary Notes Sponsored by the Ship Structure Committee and its member agencies		

16. Abstract

The objectives of this study were to develop a mechanical buckling collapse test database for 5000's and 6000's series aluminum stiffened plate structures fabricated by friction stir welding and to compare these structures with similar aluminum plate panels fabricated by fusion welding in terms of weld-induced initial imperfections and ultimate compressive strength performance. The trends or benefits found to be associated with the fusion welding and friction stir welding procedures are discussed. The following is a summary of these discussions.

• It is found that the yield and ultimate tensile strengths of friction stir butt-welded aluminum alloys are equivalent or even better than that of fusion-welded aluminum alloys.

• The initial imperfections induced by friction stir welding tend to be smaller than those induced by fusion welding. Thus, the benefits of the friction stir welding procedure in this respect are clear.

• The ultimate strength performance is found to be 10-20% greater in the friction stir-welded aluminum structures than it is in the fusion-welded aluminum structures. This implies that the friction stir welding procedure is certainly superior to the fusion welding procedure in terms of ultimate compressive strength performance, as long as delamination is prevented.

• All of the friction stir-welded test structures however showed delamination in the welded region after or even before the ultimate strength had been reached. This indicates that the fusion welding procedure is superior to the friction stir welding procedure in terms of compressive strength performance in the welded region.

• It is reconfirmed that nonlinear finite element method computations depend significantly on the structural modeling techniques applied.

17. Key Words	18. Distribution Statement
Aluminum stiffened plate structures, ultimate strength, friction stir weld, fusion weld, weld induced initial imperfections, buckling collapse tests, nonlinear finite element method computations	Distribution Available From: National Technical Information Service U.S. Department of Commerce Springfield, VA 22151 Ph. (703) 487-4650

19. Security Classif. (of this report)	20. Security Classif. (of this page)	21. No. of Pages	22. Price
Unclassified	Unclassified	206	

CONVERSION FACTORS
(Approximate conversions to metric measures)

To convert from	to	Function	Value
LENGTH			
inches	meters	divide	39.3701
inches	millimeters	multiply by	25.4000
feet	meters	divide by	3.2808
VOLUME			
cubic feet	cubic meters	divide by	35.3149
cubic inches	cubic meters	divide by	61,024
SECTION MODULUS			
$inches^2$ $feet^2$	$centimeters^2$ $meters^2$	multiply by	1.9665
$inches^2$ $feet^2$	$centimeters^3$	multiply by	196.6448
$inches^4$	$centimeters^3$	multiply by	16.3871
MOMENT OF INERTIA			
$inches^2$ $feet^2$	$centimeters^2$ meters	divide by	1.6684
$inches^2$ $feet^2$	$centimeters^4$	multiply by	5993.73
$inches^4$	$centimeters^4$	multiply by	41.623
FORCE OR MASS			
long tons	tonne	multiply by	1.0160
long tons	kilograms	multiply by	1016.047
pounds	tonnes	divide by	2204.62
pounds	kilograms	divide by	2.2046
pounds	Newtons	multiply by	4.4482
PRESSURE OR STRESS			
$pounds/inch^2$	$Newtons/meter^2$ (Pascals)	multiply by	6894.757
kilo $pounds/inch^2$	mega $Newtons/meter^2$ (mega Pascals)	multiply by	6.8947
BENDING OR TORQUE			
foot tons	meter tons	divide by	3.2291
foot pounds	kilogram meters	divide by	7.23285
foot pounds	Newton meters	multiply by	1.35582
ENERGY			
foot pounds	Joules	multiply by	1.355826
STRESS INTENSITY			
kilo $pound/inch^2$ $inch^{½}$($ksi\sqrt{in}$)	mega Newton $MNm^{3/2}$	multiply by	1.0998
J-INTEGRAL			
kilo pound/inch	$Joules/mm^2$	multiply by	0.1753
kilo pound/inch	kilo $Joules/m^2$	multiply by	175.3

Table of Contents

Executive Summary

The objectives of this study were to develop a mechanical buckling collapse test database for 5000's and 6000's series aluminum stiffened plate structures fabricated by friction stir welding and to compare these structures with similar aluminum plate panels fabricated by fusion welding in terms of weld-induced initial imperfections and ultimate compressive strength performance. The trends or benefits found to be associated with the fusion welding and friction welding procedures are discussed. The following is a summary of these discussions.

- It is found that the yield and ultimate tensile strengths of friction-stir welded aluminum alloys are equivalent to or can be better than that of fusion-welded aluminum alloys, for butt welds. Tensile coupon tests of friction stir lap-welded aluminum alloys are recommended for the future study to discuss the similar trends of tensile properties.
- The initial imperfections induced by friction stir welding tend to be smaller than those induced by fusion welding. Thus, the benefits of the friction stir welding procedure in this respect are clear.
- The ultimate compressive strength performance is found to be 10-20% greater in the friction stir-welded aluminum structures than it is in the fusion-welded aluminum structures. This implies that the friction stir welding procedure is superior to the fusion welding procedure in terms of ultimate compressive strength performance.
- However, all of the friction stir-welded test structures showed delamination in the welded region after or even before the ultimate strength had been reached. The pre-collapse delamination in the welded region can significantly reduce the ultimate compressive strength performance of the structure. This indicates that the fusion welding procedure is superior to the friction stir welding procedure in terms of compressive strength performance in the welded region, particularly when involving buckling and crushing. Further study is needed to investigate the delamination characteristics in the friction stir-welded region under compressive actions. For the quality assurance of the friction stir welded region, non-destructive test (NDT) methods can be used to find any defects.
- The friction stir lap-weld between plate sheet and extruded stiffener is considered to be a promising welding method to replace the fusion fillet-weld procedure in construction of aluminum structures. The post-collapse delamination is of no major concern for the friction stir lap-welds because it can still maintain the water tightness of the stiffened plate structure, although the pre- or post-collapse delamination is of great concern for the friction stir butt-welds because it can assure no longer the water tightness of the stiffened panel. However, since the pre-collapse delamination reduces the ultimate strength significantly, further study is needed to verify the mechanical property of the friction stir lap-weld and its parameter which will affect the mechanical property and delamination between base plate and stiffener such as width and depth of molten thin-layer, molten temperature, rotating and forwarding speeds, and possible quick cooling, etc.
- It is reconfirmed that nonlinear finite element method computations depend significantly on the structural modeling techniques applied.

Acknowledgements

The present study was undertaken at the Lloyd's Register Educational Trust (LRET) Research Centre of Excellence, Pusan National University, Korea. Thanks are due to graduate students at the Ship and Offshore Structural Mechanics Laboratory of the Pusan National University for their efforts regarding buckling collapse tests and nonlinear finite element method computations.

In addition, this author would like to thank Ship Structure Committee (SSC) for its financial and technical assistance. SSC is an inter-agency organization chaired by US Coast Guard with the goal of eliminating marine structural failures. Member agencies consist of American Bureau of Shipping (ABS), Defence Research Directorate Canada (DRDC), US Maritime Administration (MARAD), Military Sealift Command (MSC), Naval Sea Systems Command (NAVSEA), Transport Canada, Society of Naval Architects and Marine Engineers (SNAME) and the US Coast Guard (USCG). Without the SSC support, it certainly would not have been able to complete this project. Special thanks are due to the members of SSC Project Technical Committee chaired by Mr. Chao Lin, for their valuable comments and advices.

Notation

a = panel length between transverse frames
A_i = area of the (i)th cross-section in the stiffened panel
b = breadth of the plating between longitudinal stiffeners
b_{HAZ} = half-breadth of the softened zone
b_t = breadth of tensile residual stress block
B = breadth of the entire stiffened panel
E = elastic modulus (Young's modulus)
P_p = fully plastic axial force without consideration of buckling = $\sum_i A_i \sigma_{Yi}$
P_u = ultimate axial compressive force
t = plate thickness
w_{oc} = maximum column-type initial distortion of stiffener
w_{opl} = maximum initial deflection of plating
w_{os} = maximum sideways initial distortion of stiffener
β = plate slenderness ratio
λ = column slenderness ratio for either a single stiffener with attached plating or the entire stiffened panel
σ_{rcx} = compressive residual stress in the x direction
σ_{rtx} = tensile residual stress in the x direction
σ_x = applied compressive stress in the x direction
σ_{xu} = ultimate compressive strength of structure
σ_T = ultimate tensile strength of material
σ_Y = yield strength of material in general
σ_{Yi} = yield strength of material in the (i)th cross-section
σ_{Yeq} = equivalent yield strength of material in general = $\sum_i A_i \sigma_{Yi} / \sum_i A_i$
σ_{YHAZ} = reduced yield strength in the softened zone

Abbreviation

FEA = finite element analysis
FSW = friction stir welding
GMAW = gas metal arc welding, which is also termed metal inert gas (MIG) welding
HAZ = heat-affected zone
SSC = The Ship Structure Committee
TMAZ = thermo-mechanically affected zone
ULS = ultimate limit states

List of Figures

List of Tables

Chapter 1 Introduction

1.1 Objectives

The primary objectives of the present study are as follows.

- To develop a mechanical buckling collapse test database of full-scale prototypes of 5000's and 6000's series aluminum stiffened plate structures fabricated by the friction stir-welding (FSW) procedure.
- To provide a comparison of these structures with similar aluminum plate panels fabricated by the fusion welding procedure and to note any trends or benefits associated with either procedure.

1.2 Background

The use of high-strength aluminum alloys in the shipbuilding industry provides many benefits, but also presents many challenges (Collette 2005, Sielski 2007, 2008). The benefits of using aluminum rather than steel include its lighter weight, which helps increase cargo capacity and/or reduce power requirements, excellent corrosion resistance and low maintenance. The challenges include reduced stiffness, which results in greater sensitivity to deformation, buckling and plastic collapse, and the need for different welding practices.

The aforementioned benefits are now well-recognized, particularly for the design and construction of war ships, littoral surface craft and combat ships, and fast passenger ships, particularly as such ocean-going vessels are becoming increasingly large in size.

The increasing size of these vessels, however, has resulted in a number of design challenges. Aluminum alloys are less stiff than mild steel, and no refined ultimate limit state (ULS) design methods that involve local and overall ULS assessments exist, unlike the case with steel structures for which the necessary information is plentiful. The use of ULS design methods (ISO 2007), in addition to more conventional structural design standards, will help in the design and construction of very large, high-speed, ocean-going aluminum vessel structures (Paik et al. 2005).

The SSC-451 report (Paik et al. 2008b) presented an extensive investigation of the collapse characteristics of the aluminum stiffened plate structures used for marine applications carried out via mechanical testing and nonlinear finite element method computations. The features of the initial imperfections found were examined together with a statistical database of the fabrication-related initial imperfections in fusion-welded aluminum stiffened plate structures, because such imperfections significantly affect ULS behavior. This database and the insights presented in the SSC-451 report are very useful in the design and construction of high-speed, fusion-welded aluminum ocean-going vessel structures.

Various welding methods are used today to fabricate aluminum ship structures, namely, gas metal arc welding (GMAW), laser welding and FSW. The SSC-451 report focuses on the GMAW technique for the construction of its test structures, as it is currently one of the most popular methods of welding in aluminum ship construction.

FSW, however, has also been recognized as a very attractive joining method for aluminum structures because of its many superior features, such as excellent joint

performance, small degree of initial imperfections, low level of energy consumption and lack of harmful emissions (Dawes & Thomas 1995). FSW technology has been applied successfully to various aluminum structures, such as railcars, automobiles and bridges (Thomas & Nicholas 1997, Midling et al. 1998, Sanderson et al. 2000).

However, these applications are mostly suitable for 6000's series aluminum alloys, and more R&D efforts are required to extend them to such structures as fast ships and spherical liquefied natural gas (LNG) cargo tanks made of 5000's series aluminum alloys, which are the major alloys used for marine applications (Kallee 2000, Przydatek 2000).

It was once considered to be too difficult to apply FSW to 5000's series aluminum alloys due to their poor fluidity at welding temperatures. Recently, however, FSW machines have been developed to deal with the fabrication of products made with these alloys, and they are able to produce good-quality welds of up to 25 mm in thickness. Also, it has been confirmed in the literature that the fatigue strength characteristics of 5000's series aluminum structural details fabricated by FSW are good enough when compared to fillet-welded details (Nicholas 1998).

However, there is no mechanical test database in the literature on the buckling collapse strength of 5000's and 6000's series aluminum structures fabricated by FSW. As ultimate buckling strength is today a primary design basis for both aluminum and steel ship structures, the development of a related mechanical buckling collapse test database is a matter of urgency.

Although the SSC-451 report presents a mechanical buckling collapse test database for fusion-welded aluminum plate structures, the results of a comparison of this database with the FSW procedures in terms of the trends and benefits associated with their buckling collapse strength characteristics and fabrication-related initial imperfections would be very useful in the design and construction of large ocean-going aluminum ship structures.

1.3 Requirements

1.3.1 Scope

- Investigate FSW fabrication-related initial imperfections.
- Perform buckling collapse tests on full-scale prototypes of 5000's and 6000's series aluminum plate structures fabricated by FSW.
- Perform non-linear elastic-plastic large deformation finite element method computations on the test structures.
- Perform comparisons between fusion welds and FSW in terms of their fabrication-related initial imperfections and buckling collapse strength characteristics.

1.3.2 Tasks

- Review the state-of-the-art of FSW technologies.
- Design and fabricate aluminum stiffened plate structures for buckling collapse testing.
- Identify the chemical composition and mechanical properties of the materials used for the test structures.
- Measure the fabrication-related initial imperfections of these test structures and compare them with the database of SSC-451 in terms of FSW versus fusion welds.

- Perform buckling collapse testing on the test structures under axial compressive conditions until and after the ultimate strength is reached.
- Perform nonlinear finite element method analyses to compute the ultimate strength behavior of the test structures and compare them with the experimental results.
- Discuss the trends and benefits associated with FSW and fusion welds in terms of their ultimate compressive strength performance.

1.4 Literature Survey

More than 210 articles and papers in the area of FSW technologies published or presented as of January 2009 have been collected, although most are not directly related to the aims and scope of the present project. Only one Ship Structure Committee (SSC) project has previously been undertaken in this area, which produced the SSC-447 report (Kramer 2007), but its focus was on fatigue strength performance.

The following provides a summary of the literature survey, with a focus on the aims and scope of the present project and related findings.

FSW technology was developed in 1991 by the Welding Institute in the U.K. (Thomas et al. 1991, 1995). FSW is a solid-state joining process that is particularly suitable for aluminum alloys that often face problems with fusion welds, such as cracks, porosity, distortion or softening. This technology has been recognized to have many advantages for the construction of aluminum structures, as it is a low-cost welding process. Aluminum alloys tend to show cracks and porosity after fusion welding, but FSW minimizes such problems because of the low input of total heat. The use of protective gases, e.g., for toxic shielding, may be unnecessary.

There have, of course, been useful studies that characterize the mechanical properties of FSW aluminum alloys (e.g., Rhodes et al. 1997, Hagstrom & Sandstrom 1998, Hashimoto et al. 1998, Mahoney et al. 1998, Biallas et al. 1999) and compare the properties of base and welded metals. A large number of studies on the strength performance of FSW aluminum structural details under fatigue conditions have also been undertaken (e.g., Kamioka & Okubo 2005, Kramer 2007).

The applications of FSW technologies for shipbuilding were studied by Thomas (1998) and Thomas et al. (2002, 2005), among others. Colligan (2004) presented FSW applications for ship design and construction, together with a discussion of the use of FSW technology in the United States, and indicated that it is capable of reducing construction costs and welding distortion and improving durability in comparison with fusion welding.

Peel et al. (2003) investigated the mechanical properties and residual stresses of a FSW aluminum 5083 test specimen, and concluded that these properties are governed by the thermal input rather than by the mechanical deformation caused by the FSW tool.

Several studies have also identified the residual stress characteristics in FSW aluminum structures. For example, Bang et al. (2002) predicted the residual stresses of FSW 6061 aluminum alloy using the thermal-elastic-plastic finite element method; Staron et al. (2004) measured the residual stresses in FSW aluminum 2024 sheets; and Fratini & Zuccarello (2006) presented an analysis of the through-thickness residual stresses in aluminum FSW butt joints.

Prime et al. (2006) measured the residual stresses in thick plates (25.4 mm thick)

of dissimilar aluminum alloys, 7050-T7451 and 2024-T351, that had been butt-joined by FSW. The maximum residual stress was found to be only 43 MPa, whereas the residual stress distribution was quite similar to that in fusion welds, thus indicating that the tensile residual stress develops in the heat-affected zone outside of the weld.

Khandkar et al. (2006) studied the residual stress of such FSW metals as aluminum 2024, aluminum 6061 and stainless steel 304L using a sequentially coupled finite element model with the FSW process. Murphy et al. (2007) performed a very similar study to the one presented here in terms of its aims and scope, including weld-induced initial imperfection measurements, buckling collapse testing and nonlinear finite element computations, although the purpose of their study was to examine aerospace structures made of aluminum 2024-T3 sheet with Z-section stiffeners of aluminum 7075-T76511 extrusions. They used the FSW method to construct three stiffened 332.70-mm $\times$ 575-mm panel test structures with 152.4 mm spacing for the three longitudinal stiffeners. The plate (skin) thickness was very thin (1.2 mm thick). Murphy et al. (2007) measured the initial distortions and residual stresses of these structures, as well as the breadth of the heat-affected zone. They carried out buckling collapse tests for the three stiffened panels and compared their experimental results with nonlinear finite element solutions.

Other researchers have investigated the effects of the process parameters on the residual stresses of FSW aluminum alloys (Lombard et al. 2009, Zhang & Zhang 2009a, 2009b), as well as the effects of the welding parameters on the mechanical properties of dissimilar aluminum alloy joints produced by FSW (Cavaliere et al. 2009). The rotating and forwarding speeds were considered as the parameters of influence in these studies.

As we have seen, a large number of studies that deal with micro-structural and fatigue issues in FSW aluminum structures have been undertaken. However, there is a lack of studies on the characterization of FSW-induced initial imperfections and the buckling collapse strength performance of aluminum structures for marine applications. Therefore, research and development are required to identify the characteristics of the ultimate strength performance of FSW aluminum structures.

1.5 Contents of the Report

This report comprises eight chapters and appendix. Chapter 1 addresses the aims and scope of the study together with a literature survey. Chapter 2 presents an outline of the FSW technology in terms of its advantages and limitations. Chapter 3 describes the design and construction of the test structures and documents the chemical composition and mechanical properties of the materials used for these structures, as well as the fabrication methods adopted. Chapter 4 presents the measurements of the weld-induced initial imperfections in the test structures, and a comparison is made between fusion welds and FSW in terms of these imperfections. Chapter 5 summarizes the results of the buckling collapse tests on the test structures, and Chapter 6 presents the nonlinear finite element method computations for these structures by a comparison with the experimental results. Chapter 7 discusses the benefits and trends associated with FSW and fusion welds in terms of their ultimate compressive strength performance, and finally Chapter 8 presents concluding remarks. Appendix presents the mechanical properties of aluminum alloys which experienced

buckling collapse.

It is hoped and believed that the results of the present project will be very useful in the design and construction of aluminum ship structures using FSW technologies in association with ULS-based approaches.

Chapter 2 Fusion Welds versus Friction Stir Welds for Aluminum Structures: An Overview

2.1 Classification of Welding Processes

Although a large number of methods for joining metals are available today, they may be classified into the following five basic categories (Masubuchi 1980).

- Fusion welding, e.g., gas metal arc welding (GMAW), gas tungsten arc welding (GTAW)
- Electrical-resistance welding
- Solid-phase welding, e.g., friction stir welding (FSW)
- Liquid-solid phase joining
- Adhesive bonding

In the fusion-welding process, the parts to be joined are heated until they melt together, and pressure is not a requisite. Examples of fusion welding include gas welding, arc welding, electron-beam welding and laser welding. Fusion welds that use inert gases, such as gas metal arc welding (GMAW) or gas tungsten arc welding (GTAW), are often applied to join aluminum structures.

In the electrical-resistance welding process, heating is first involved via the passage of an electric current through the parts to be welded, followed by the application of pressure. Examples of electrical-resistance welding include spot welding, upset welding and percussion welding.

The solid-phase welding process is similar to that of electrical-resistance welding in terms of the application of pressure, but the metals to be joined are not melted, except for the very thin layers near the surfaces to be joined. Examples of solid-phase welding include friction welding, forge welding and pressure welding. In this regard, FSW can be considered a type of solid-phase welding.

In the liquid-solid phase joining process, the parts to be joined are heated to a temperature lower than their melting points, and a dissimilar molten metal is then added to form a solid joint upon cooling. Examples of liquid-solid phase joining include brazing and soldering.

Finally, the adhesive bonding process makes use of the molecular attraction exerted between the surface to be bonded and the adhesive. Examples of such bonding include animal and vegetable glues, cements, asphaltums and various plastics (e.g., epoxy).

It should be noted that the processes of the first three categories are termed ‘welding’, whereas those of the latter two are often termed ‘joining’.

2.2 Fusion Welds

Although various fusion-weld technologies are used in the fabrication of large-sized metal structures, inert gas-oriented fusion welds are today the most popular in the construction of aluminum structures.

Fusion-weld technology provides a cost-effective tool in terms of speed, accuracy and weld-joint performance in the fabrication of such structures. However, a number

of issues arise from the use of fusion welds in aluminum alloys for marine applications, such as 5000's or 6000's series alloys, including fabrication-related initial imperfections and a subsequent reduction in strength performance. Collette (2007) presented an excellent review of the impact of fusion welds in association with the ultimate strength performance of aluminum structures. Figure 2.1 presents a photo of the GMAW-based fusion-welding process.

Figure 2.1 Photo of GMAW-based fusion-welding process applied for building the present test structures

2.3 Friction Stir Welds

2.3.1 Principles of the Process

FSW is a type of solid-phase welding, as noted in Section 2.1. This technology was developed by the Welding Institute in the U.K. in 1991.

Figure 2.2 illustrates a schematic of the FSW process. The metal plates to be joined are clamped onto a rigid backing body. This set-up is necessary to avoid any movement of the target plates during the welding process, such as movement in the longitudinal, transverse and lateral directions during pressing and plunging. The tip of the FSW tool, with a specially designed and profiled probe called a pin and shoulder, as shown in Figure 2.3, is rotated under sufficient downward force at high speed, and then moves slowly along the joint line.

The FSW process may be classified into the following five steps (see Figure 2.4).

- Step 1: Set-up the target plates to be joined, which are clamped onto a rigid backing body.
- Step 2: Equip the machine with the FSW tool (pin) and place it over the starting point of the joint.
- Step 3: Plunge the rotating FSW tool under sufficient downward force.
- Step 4: After touchdown, heat and plasticize the local material at the starting point of the joint.
- Step 5: Move the FSW tool along the joint line, thus transporting the plasticized material around the rotating pin.

The pin size (e.g., diameter and length), shoulder width, and rotating and forwarding speed of the FSW tool are chosen based on the properties of the target plates to be joined, such as plate thickness, material type and others. Figure 2.5 presents a photo of the FSW process.

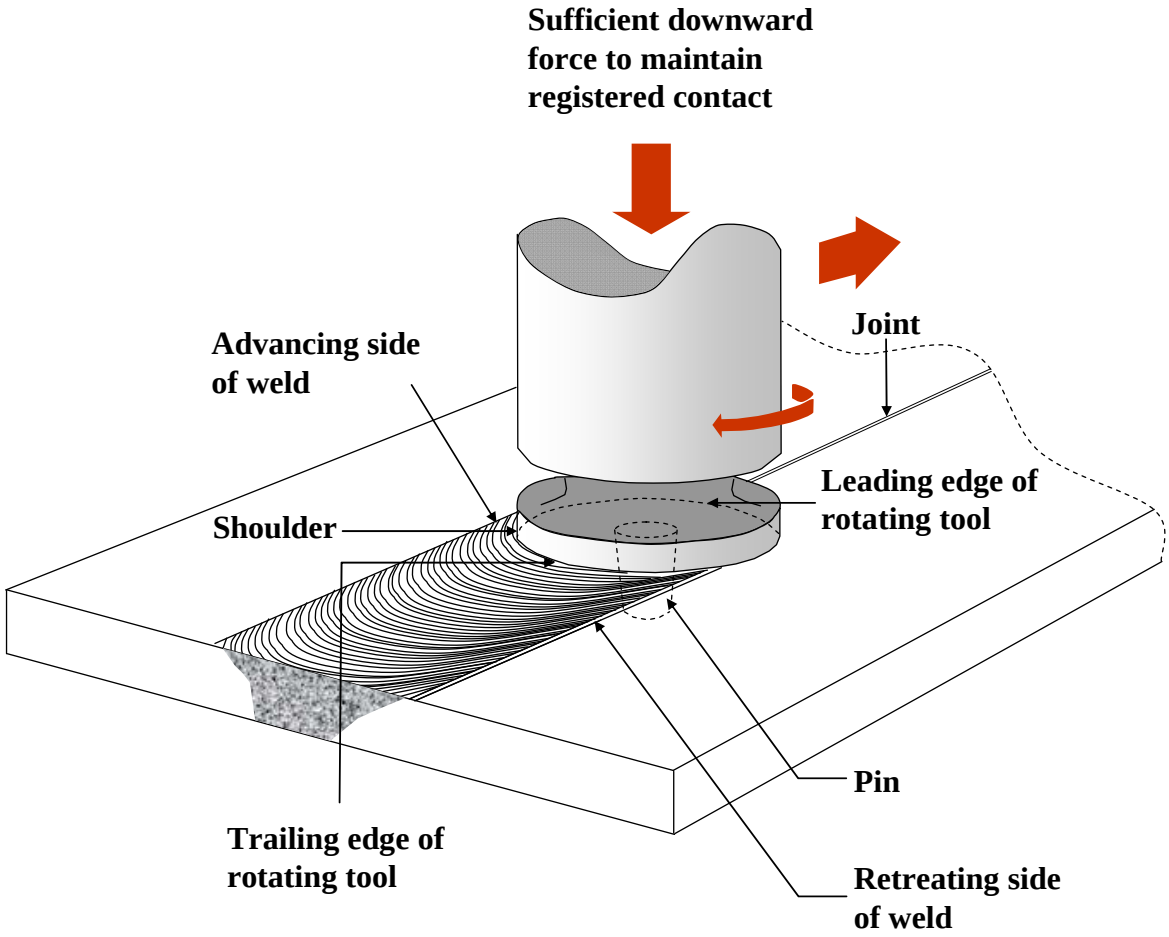

Figure 2.2 Schematic of the FSW process (Thomas et al. 1991)

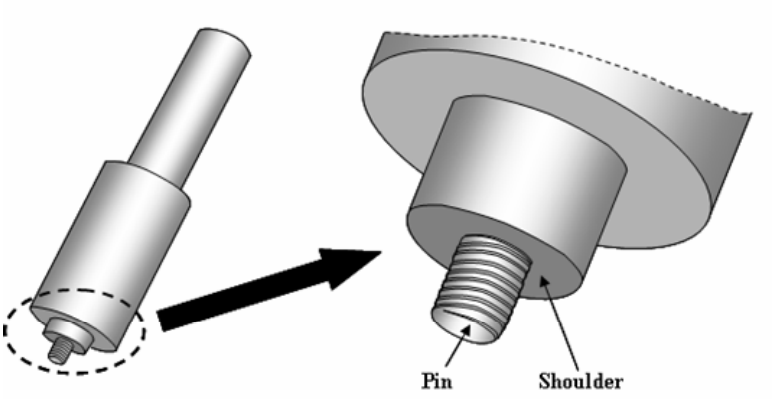

Figure 2.3 Pin and shoulder of the FSW tool (Thomas et al. 1991)

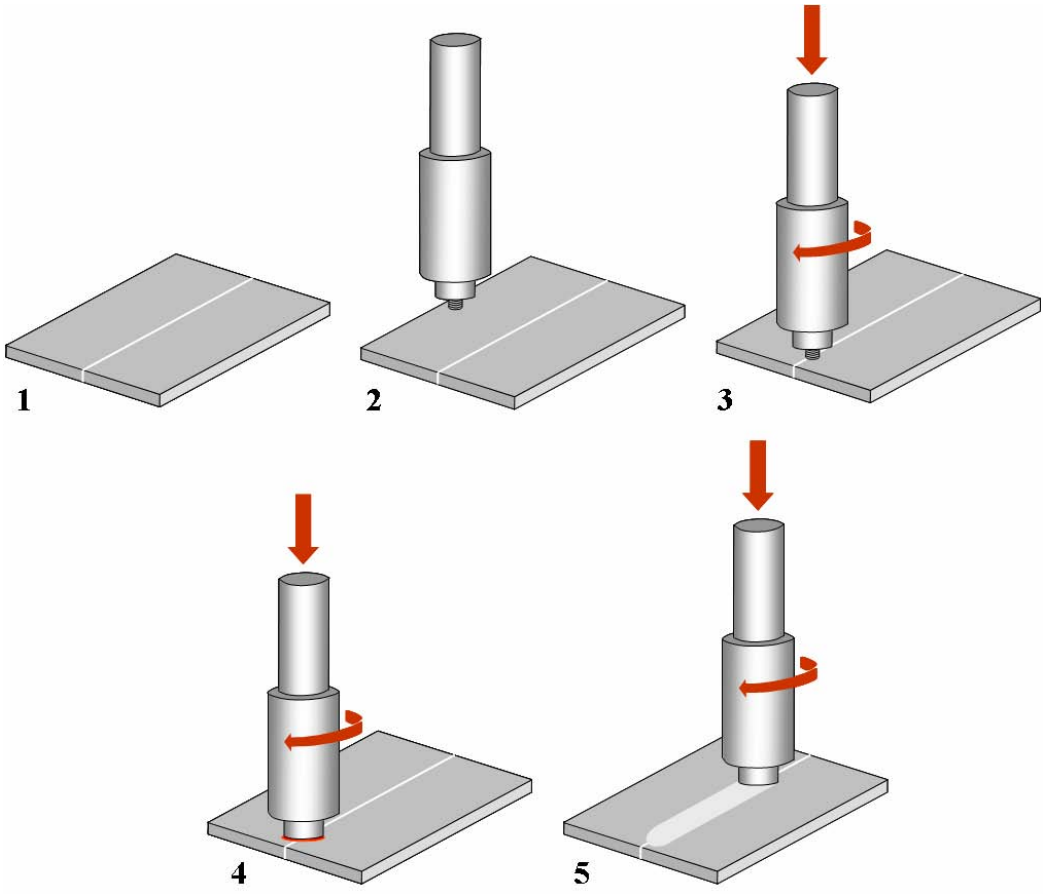

Figure 2.4 Steps of the FSW process (Thomas et al. 1991)

Figure 2.5 Photo of the FSW process applied for building the present test structures

2.3.2 Advantages and Limitations

Compared to the fusion-welding process, that for FSW is considered to be more attractive, although there are some limitations to its application. Kramer (2007) summarized the advantages and limitations of friction stir welds, as discussed below.

The advantages of the FSW process primarily result from the fact that it works in the solid state at a low temperature that is below the melting point of the materials to be joined. This is in contrast to the fusion-welding process. Thus, the level of fabrication related-initial imperfections in structures built by FSW should subsequently be slight and/or less severe than those produced by fusion welds.

The limitations of FSW applications may include the following.

- The pins of the FSW tool are consumable, and their size (diameter and length) differs depending on the properties of the plates to be joined.
- The position of welding is limited due to the orientation of the FSW machine, including the tool. Fillet welding is not relevant because inclining the target plates and/or the FSW machine along the intersections to be joined between the plate and extrusion is not straightforward.
- Butt-joining is relevant, but there must be no obstacles around the FSW machine that can disturb the rotating and forwarding of the tool.
- Lap-joining is relevant, but the pin size must be carefully chosen.
- A keyhole is formed at the end of each weld, as shown in Figure 2.6.

- The speed of FSW is usually slower than that of fusion welding.
- A weld nugget may form at the center of the weld.

Figure 2.6 Keyhole at the end of the friction stir weld

The mechanical property and strength performance in the friction stir welded region is affected by various parameters such as width and depth of molten thin layer, molten temperature, rotating and forwarding speeds, and possible quick cooling, etc. The quality assurance of the friction stir welded region can be performed by non-destructive test (NDT) methods to find any defects.

2.3.3 The Softened Zone

In contrast to fusion welding, in which three distinct regions, i.e., the base (parent or unaffected) material, the weld metal region, and the heat-affected zone (HAZ), typically appear, FSW may produce more complicated micro-structural phenomena, thus exhibiting four regions; A - the unaffected material, B - the heat-affected zone (HAZ), C – the thermo-mechanically affected zone (TMAZ) and D – the weld nugget, as shown in Figure 2.7 (Kramer 2007).

The parent material region is unaffected by heat and/or mechanical deformation. The mechanical properties of this material are supposed to be the same as those of virgin material.

The HAZ of friction stir welds appear to be similar to fusion welds, but have lower peak temperatures. The material in this region undergoes a thermal process cycle during welding, and, subsequently, in the case of aluminum alloys, the mechanical properties of this material are usually softened by micro-structural phenomena in the HAZ, although plasticity may not take place.

The TMAZ typically appears together with plastic deformation in the region in which the FSW tool is plunged and rotated. The TMAZ is often further categorized into two sub-zones, namely, the plastically deformed zone without recrystallization and

the recrystallized (weld-nugget) zone. In the case of aluminum alloys, the mechanical properties of material in the TMAZ may differ from those in the HAZ as well as those of the base material.

For the sake of convenience when evaluating ultimate strength performance, however, both the HAZ and TMAZ are often dealt with as a whole in the form of the softened zone, but with the breadth of this zone being equivalent to approximately two times the width of the FSW tool shoulder.

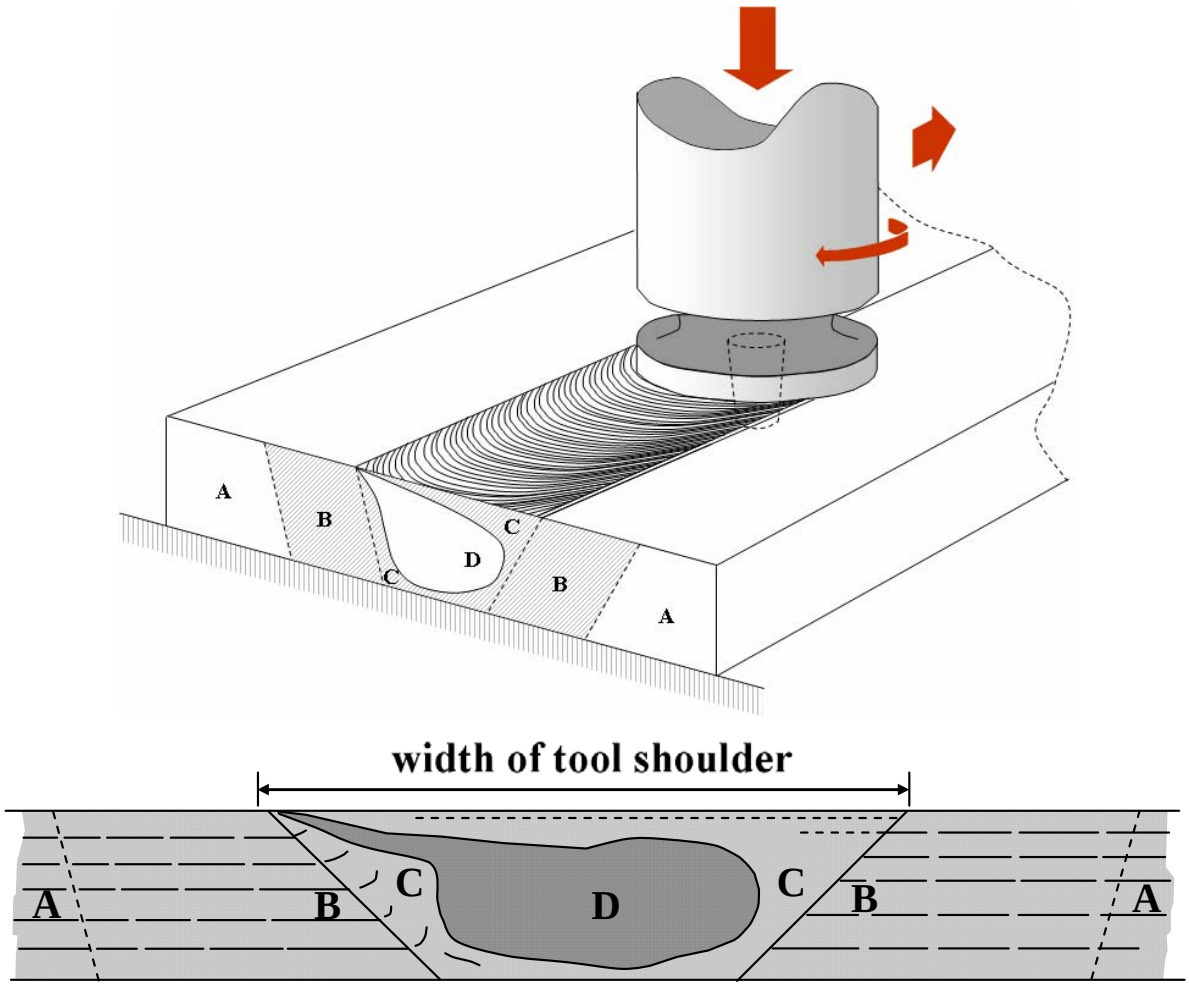

A: Unaffected material
B: Heat-affected zone (HAZ)
C: Thermo-mechanically affected zone (TMAZ)
D: Weld nugget (Part of thermo-mechanically affected zone)

Figure 2.7 Schematic of the TMAZ and HAZ associated with FSW (Kramer 2007)

Chapter 3 Design and Construction of Aluminum Stiffened Plate Structures for Buckling Collapse Testing

3.1 Selection of Materials

3.1.1 Combinations for Plate and Extrusions

Although 5000's and 6000's series aluminum alloys are typically appropriate for marine applications, the plate part is usually fabricated from 5000's series alloys and the extrusions from 5000's or 6000's series alloys.

Considering this trend and the limitations of material procurement, the following combinations of aluminum alloys for the plate and extrusions were chosen for the present study.

- 5083-H112 alloy for the plate and 6082-T6 alloy for the extrusions
- 5083-H112 alloy for the plate and 5083-H112 alloy for the extrusions
- 5383-H116 alloy for the plate and 5083-H112 alloy for the extrusions

The SSC-451 database (Paik et al. 2008b) is used in the comparison stage for fusion welds versus friction stir welds in conjunction with ultimate strength performance. The material combinations for the test structures in SSC-451 are as follows.

- 5083-H116 alloy for the plate and 5383-H112 alloy for the extrusions
- 5083-H116 alloy for the plate and 6082-T6 alloy for the extrusions
- 5383-H116 alloy for the plate and 5383-H112 alloy for the extrusions

The manufacturers (of suppliers) of the aluminum alloys procured for the present study and the year of their production are as follows.

- 5083-H112 alloy for the plate – Alcoa Korea, 2008
- 5083-H112 alloy for the extrusions – Alcoa Korea, 2008
- 5083-H116 alloy for the plate – Alcan France, 2006
- 5383-H112 alloy for the extrusions – Alcan France, 2006
- 5383-H116 alloy for the plate – Alcan France, 2006
- 6082-T6 alloy for the extrusions – Alcoa Korea, 2008

3.1.2 Chemical Composition

Table 3.1 lists the chemical composition of all of the alloys investigated in the present study, which is equivalent to that of the typical aluminum alloys used in marine applications. It should be noted that the chemical composition of rolled plates differs from that of extrusions.

3.1.3 Mechanical Properties

3.1.3(a) Base Material

Tensile coupon tests were carried out to identify the mechanical properties of the base material and the material in the welded parts. Figure 3.1 shows the dimensions

of the tensile coupon test specimen in conjunction with the American Society for Testing and Materials (ASTM) standards.

Three types of specimens with plate thicknesses of 6 mm were cut out of the plate part, namely, in the longitudinal (rolled), transverse and diagonal directions, whereas only one type of specimen with a plate thickness of 4 mm or 6 mm was taken from the extrusions in the length direction.

Table 3.1 Chemical composition (wt. %) of aluminum alloys used in the present study

Alloy & Temper	Si (%)	Fe (%)	Cu (%)	Mn (%)	Mg (%)	Cr (%)	Zn (%)	Ti (%)	Zr (%)
5083-H112 (R)[1)]	0.12	0.29	0.014	0.65	4.55	0.088	0.006	0.031	0.0
5083-H112 (E)[1)]	0.14	0.12	0.010	0.64	4.56	0.080	0.010	0.030	0.0
5083-H116 (R)[2)]	Max. 0.40	Max. 0.40	Max. 0.10	0.4 ~1.0	4.0 ~4.9	0.05 ~0.25	Max. 0.25	Max. 0.15	0.0
5383-H112 (E)[2)]	Max. 0.25	Max. 0.25	Max. 0.20	0.7 ~1.0	4.0 ~5.2	Max. 0.25	Max. 0.40	Max. 0.15	Max. 0.20
5383-H116 (R)[1)]	0.091	0.24	0.077	0.82	4.97	0.088	0.11	0.011	0.002
Al6082-T6 (E)[1)]	1.22	0.22	0.07	0.69	1.05	0.19	0.01	0.03	0.0

Note: [1)]Tested by Alcoa Korea, [2)]Provided by Alcan France, (E) = extruded, (R) = rolled.

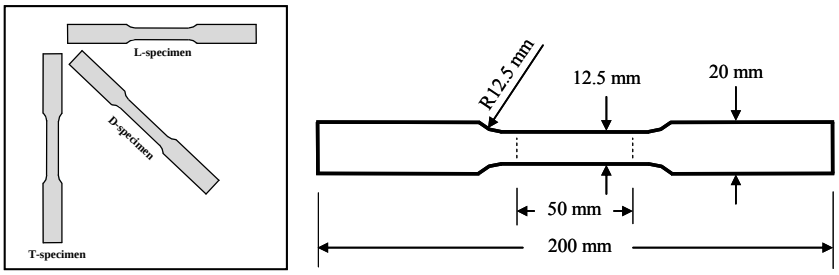

Figure 3.1(a) Specimen of tensile coupon tests for the mechanical property characterization of the base material – rolled plate part

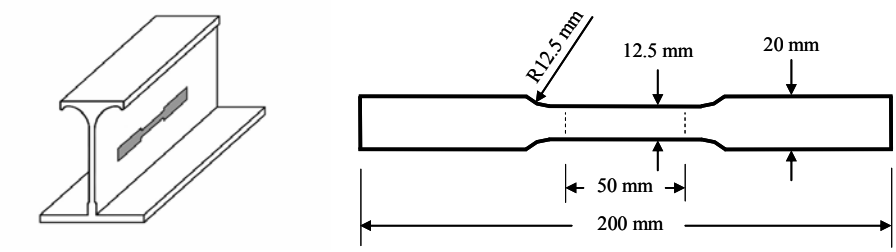

Figure 3.1(b) Specimen of tensile coupon tests for the mechanical property characterization of the base material – extruded web part

Figure 3.1(c) Photos of sample tensile coupon test specimens

It should be noted that the mechanical properties of rolled alloys may differ from those of extruded alloys because their production process is different. Therefore, the specimens corresponding to the plate part and extrusions need to be prepared for testing. For the latter, only the material in the web part was tested in the present study.

Figure 3.2 shows the relationships between the engineering stress and the engineering strain, as obtained from the tensile coupon tests, where some materials were tested with multiple test specimens cut out in the same direction.

Table 3.2 provides a summary of the mechanical properties of the base materials, which were also obtained from these tests. Table 3.3 lists the minimum requirements of the mechanical properties of the base materials, as specified by the classification societies (ABS 2006, LR 2008).

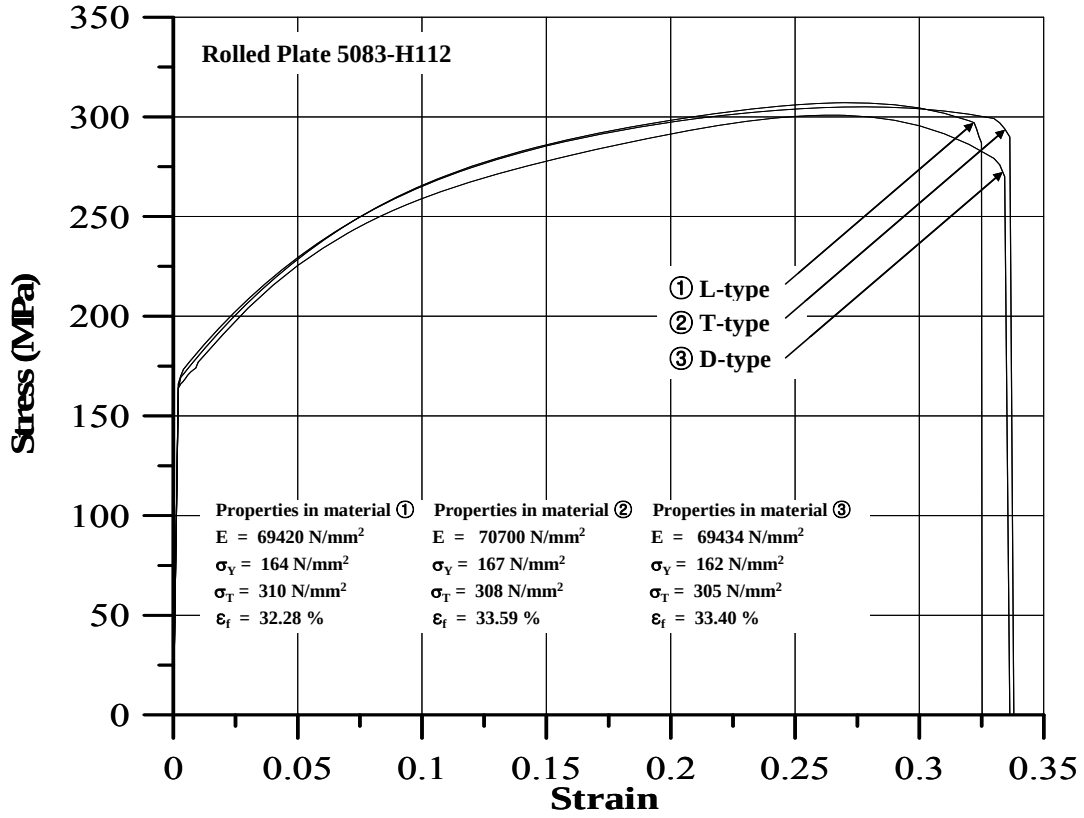

Figure 3.2(a) The stress versus strain curves for the aluminum base material - 5083-H112 (rolled) - obtained from the tensile coupon tests

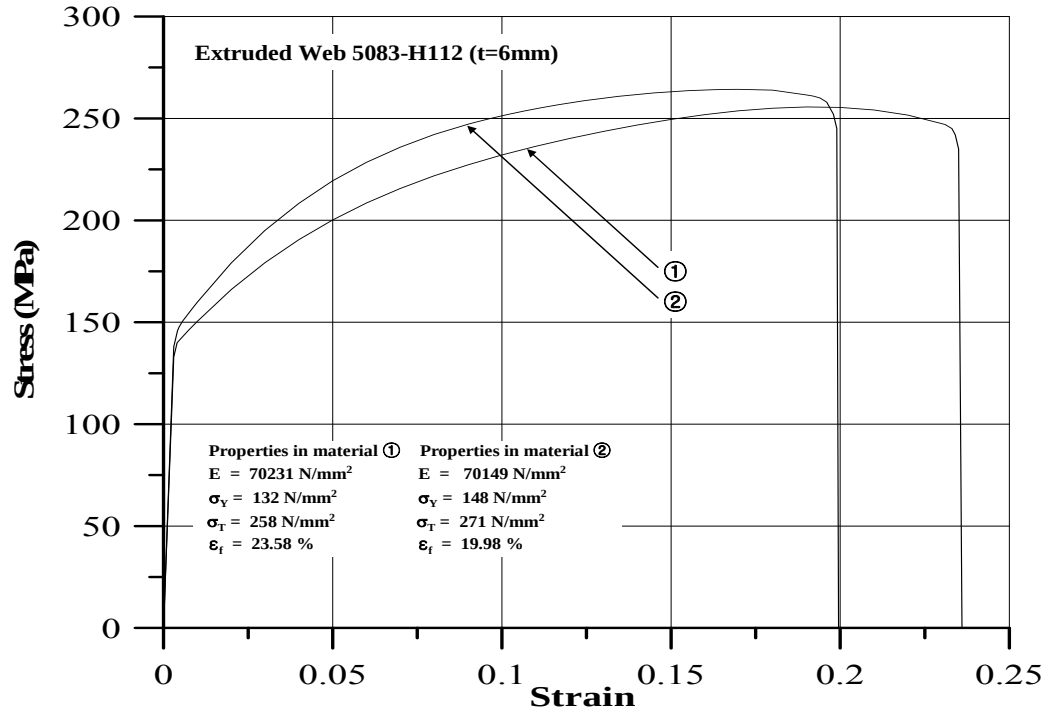

Figure 3.2(b) The stress versus strain curves for the aluminum base material – 5083-H112 (extruded) – obtained from the tensile coupon tests

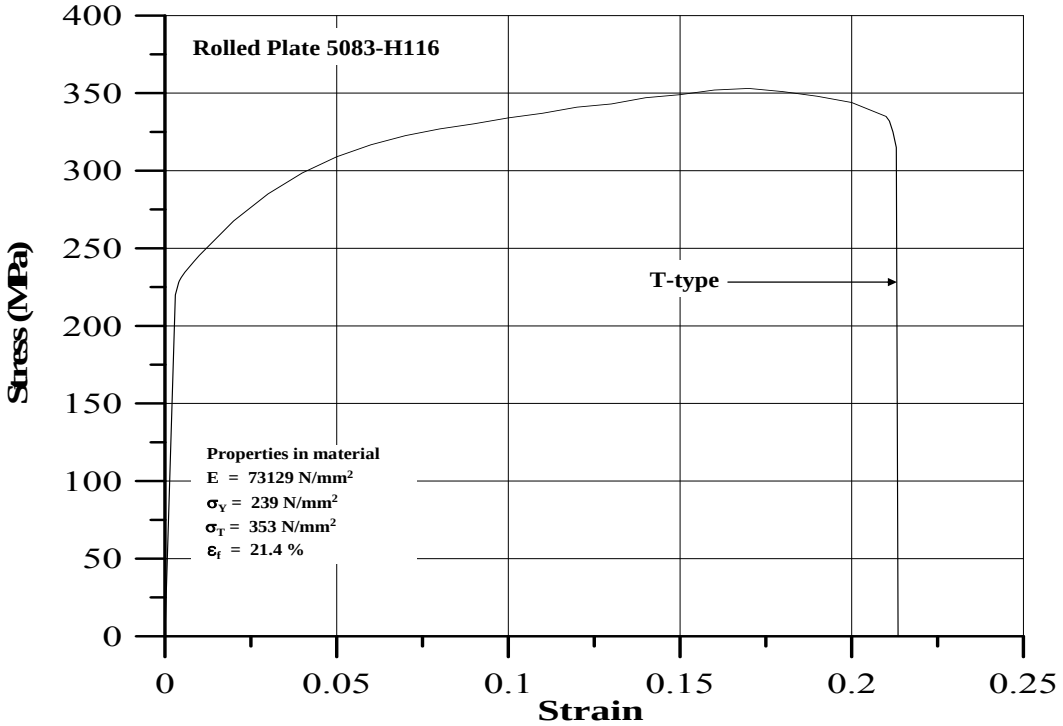

Figure 3.2(c) The stress versus strain curves for the aluminum base material – 5083-H116 (rolled) – obtained from the tensile coupon tests

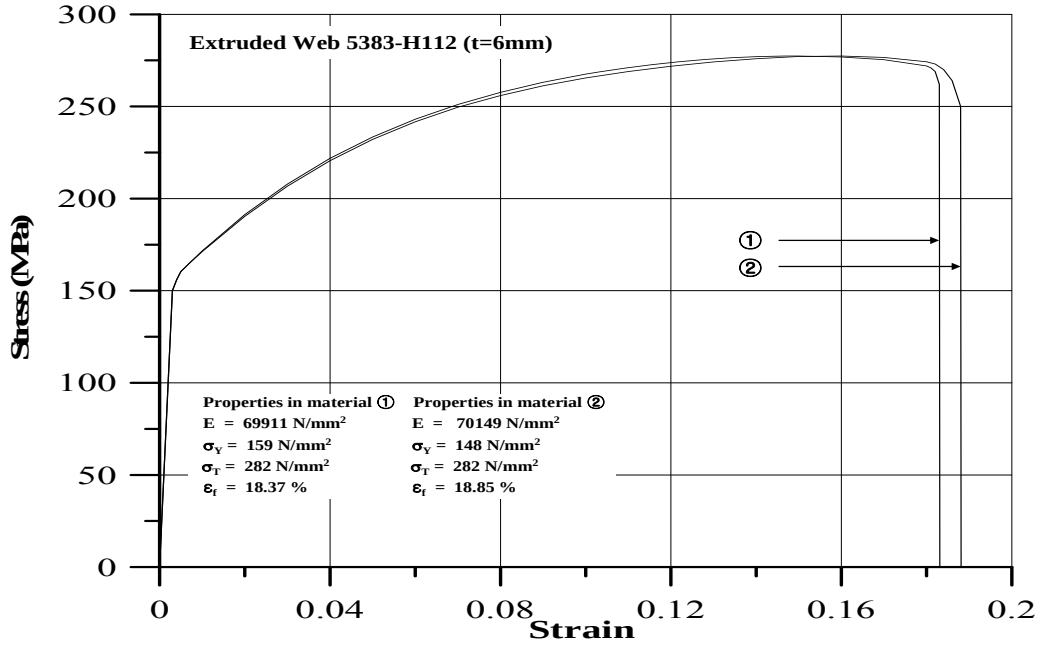

Figure 3.2(d) The stress versus strain curves for the aluminum base material – 5383-H112 (extruded) – obtained from the tensile coupon tests

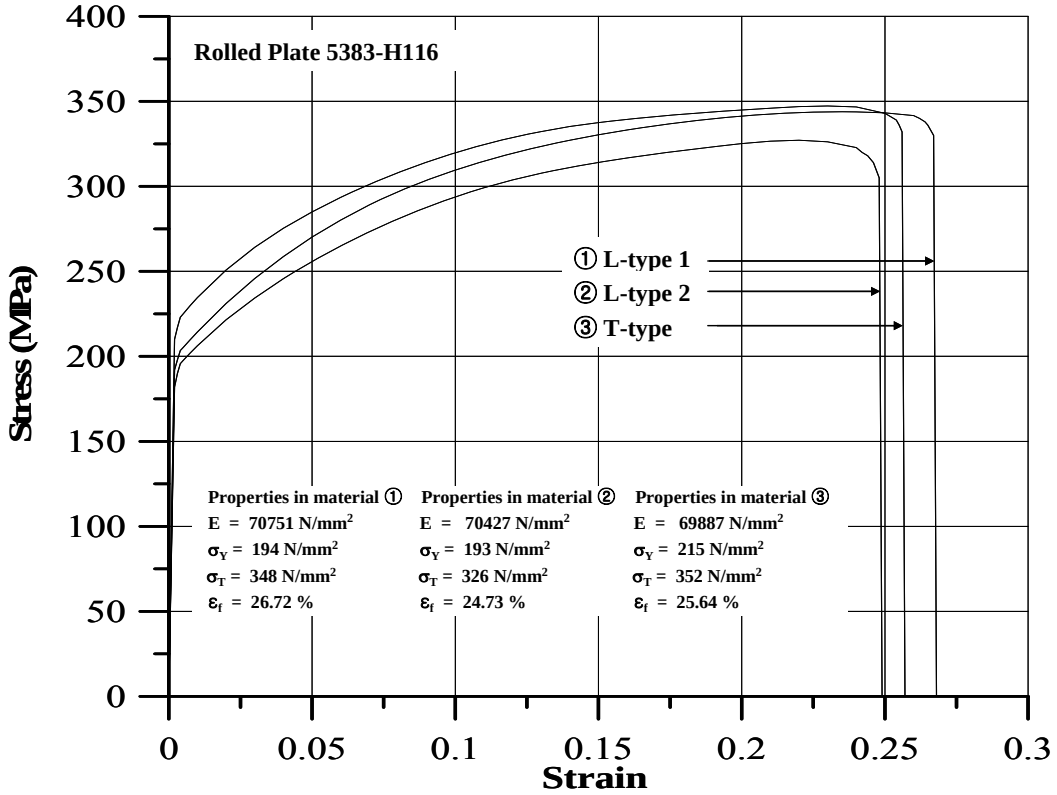

Figure 3.2(e) The stress versus strain curves for the aluminum base material – 5383-H116 (rolled) - obtained from the tensile coupon tests

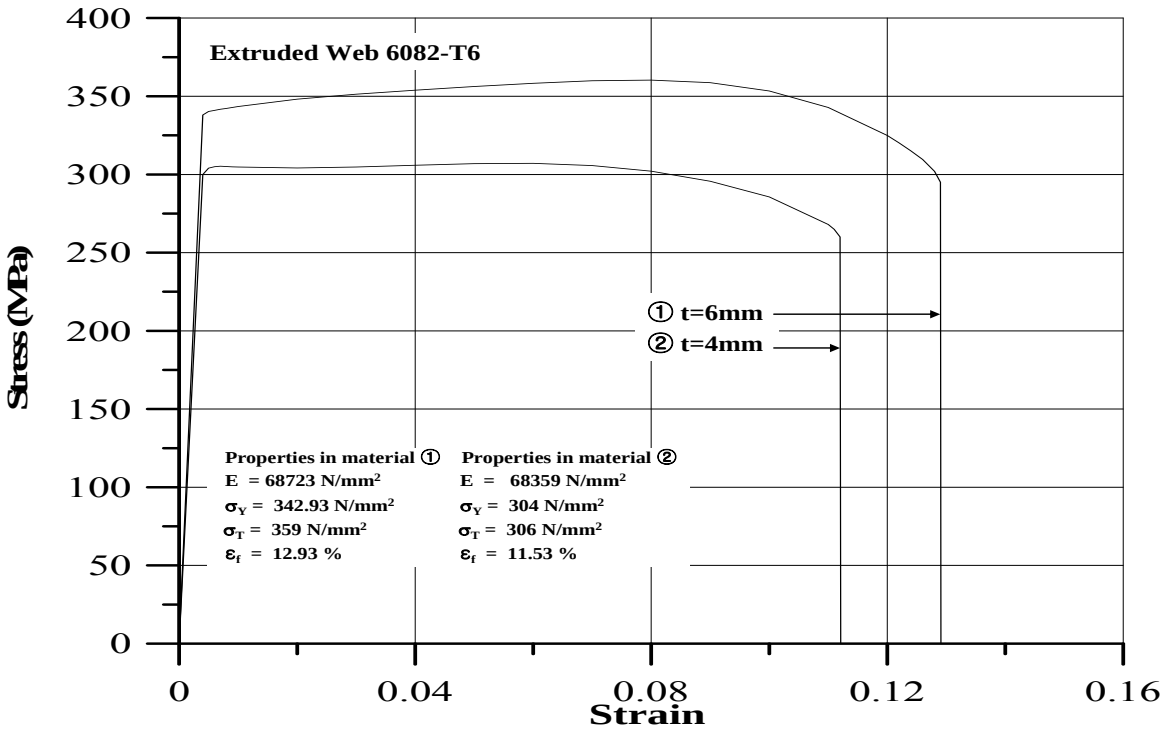

Figure 3.2(f) The stress versus strain curves for the aluminum base material - 6082-T6 (extruded) - obtained from the tensile coupon tests

Table 3.2 Summary of the mechanical properties of the aluminum alloys (base material), obtained from the tensile coupon tests

Material	Specimen	E (N/mm^2)	σ_Y (N/mm^2)	σ_T (N/mm^2)	Elongation (%)
5083-H112 (R) (t = 6mm)	L-type	69420	164	310	32.28
	T-type	70700	167	308	33.59
	D-type	69434	162	305	33.40
Average		69856.8	167.2	307.67	33.09
5083-H112 (E) (t = 6mm)	L-type 1	70231	132	258	23.58
	L-type 2	70149	148	271	19.98
Average		70190	140	264.5	21.78
5083-H116 (R) (t = 6mm)	T-type	73129	239	353	21.4
5383-H112 (E) (t = 6mm)	L-type 1	69911	159	282	18.37
	L-type 2	70149	148	282	18.85
Average		70030	153.5	282	18.61
5383-H116 (R) (t = 6mm)	L-type 1	70751	194	348	26.72
	L-type 2	70427	193	326	24.73
	T-type	69887	215	352	25.64
Average		70355.3	207.9	342	25.85
6082-T6 (E) (t = 4mm)	L-type	68359	304	306	11.53
6082-T6 (E) (t = 6mm)	L-type	68723	343	359	12.93

Note: (R) = rolled; (E) = extruded; E = elastic modulus; σ_Y = yield strength; σ_T = ultimate tensile strength; L-type = Longitudinal; T-Type = Transverse; D-type = Diagonal.

Table 3.3 Minimum requirements for the mechanical properties of aluminum alloys - base material (ABS 2006, LR 2008)

Material	Thickness (mm)	σ_Y (N/mm^2)	σ_T (N/mm^2)	Elongation in 50 mm
5083-H112 (R)	6.5-38.0	124.5	275.4	12
	38.1-76.5	117.6	268.5	12
5083-H112 (E)	-	109.8	268.5	12
5083-H116 (R)	1.6-38.0	213.6	302.8	10
	38.1-76.5	199.9	282.2	10
5083-H321 (R)	1.6-38.0	213.6	302.8	10
	38.1-76.5	199.9	282.8	10
5383-H111 (R)	3.0-5.0	142.1	284.2	17
5383-H111 (E)	-	145.0	290.1	17
5383-H112 (E)	-	190.1	309.7	13
5383-H116 (R)	3.0-5.0	215.6	298.9	10
5383-H321 (R)	3.0-5.0	215.6	298.9	10

Note: (R) = rolled; (E) = extruded; E = elastic modulus; σ_Y = yield strength; σ_T = ultimate tensile strength.

3.1.3(b) Welded Material

To characterize the mechanical properties of the welded aluminum alloys, butt-joined specimens with a plate thickness of 6 mm were prepared via both the fusion-welding and friction stir welding (FSW) processes, as shown in Figure 3.3. The condition of each weld is as follows.

- Fusion weld: Filler metal – 5183 aluminum alloy, diameter of filler wire – 1.2 mm, shield gas – 100% Ar. inert gas, welding speed – 450 mm/min, electricity – 183 A and 21 V, torch angle – 50 degrees, welding progress angle – 80 degrees.
- Friction stir weld: Rotating speed of FSW tool – 1500 RPM, forwarding speed of FSW tool – 4 mm/s, weld temperature – approximately 370ºC, FSW tool size – d_1 = 4mm, d_2 = 5 mm, d_3 = 15 mm, h = 5.4mm, with the nomenclature in Figure 3.4.

The tensile coupon test specimens for the butt-welds were prepared for the combination of dissimilar alloys as well as for the identical alloys as follows.

- 5083-H112 + 5083-H112

- 5383-H116 + 5383-H116
- 5083-H112 + 5383-H116

Figure 3.5 shows the stress versus strain curves of the butt-welded aluminum alloys, as obtained from the tensile coupon tests. Multiple test specimens with the same weld condition were prepared. It is observed that a somewhat significant deviation exists in elongation of friction stir-welded region. A comparison of these curves for welded aluminum alloys fabricated by fusion welding and by FSW is also shown in this figure. It is found that the mechanical properties of aluminum material fabricated by friction stir welding are equivalent to or can be better than those by fusion welding.

Table 3.4 summarizes the mechanical properties of the butt-welded aluminum alloys, as obtained from the tensile coupon tests. Table 3.5 presents the minimum yield strength requirements for fusion-welded aluminum alloys, which are similar to those of the present study.

It is noted that the tensile coupon tests were performed for butt welds only in the present study, and thus further study is needed to verify the tensile properties of the friction stir lap-welded material. A microscopic examination of the friction stir lap-welded material is recommended to find any defects associated with the width and depth of the molten metal thin layer which potentially cause delamination in pre- or post-collapse range of the structure under compressive actions involving buckling or crushing.

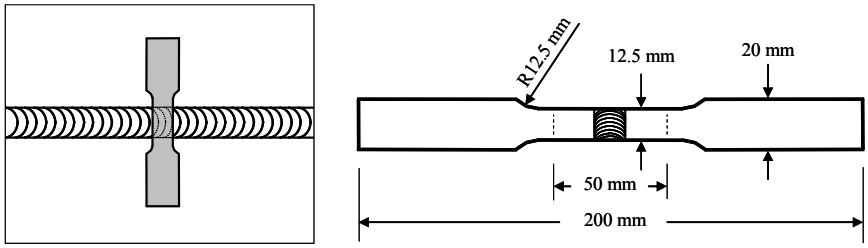

Figure 3.3 Specimen of tensile coupon tests for the mechanical property characterization of the welded material

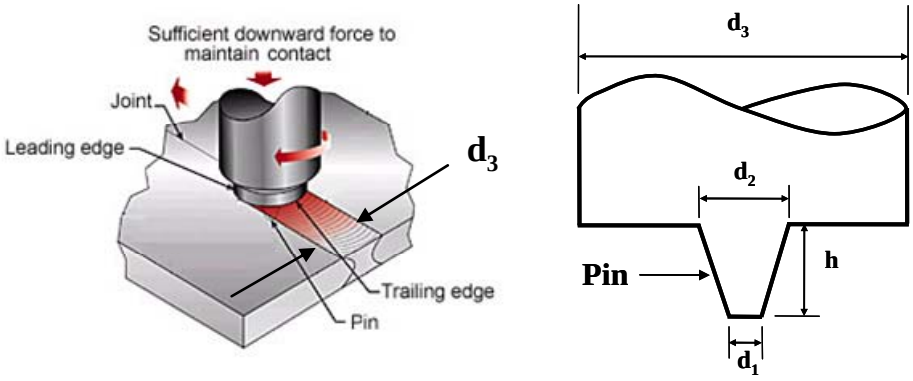

Figure 3.4 Nomenclature for FSW tool size

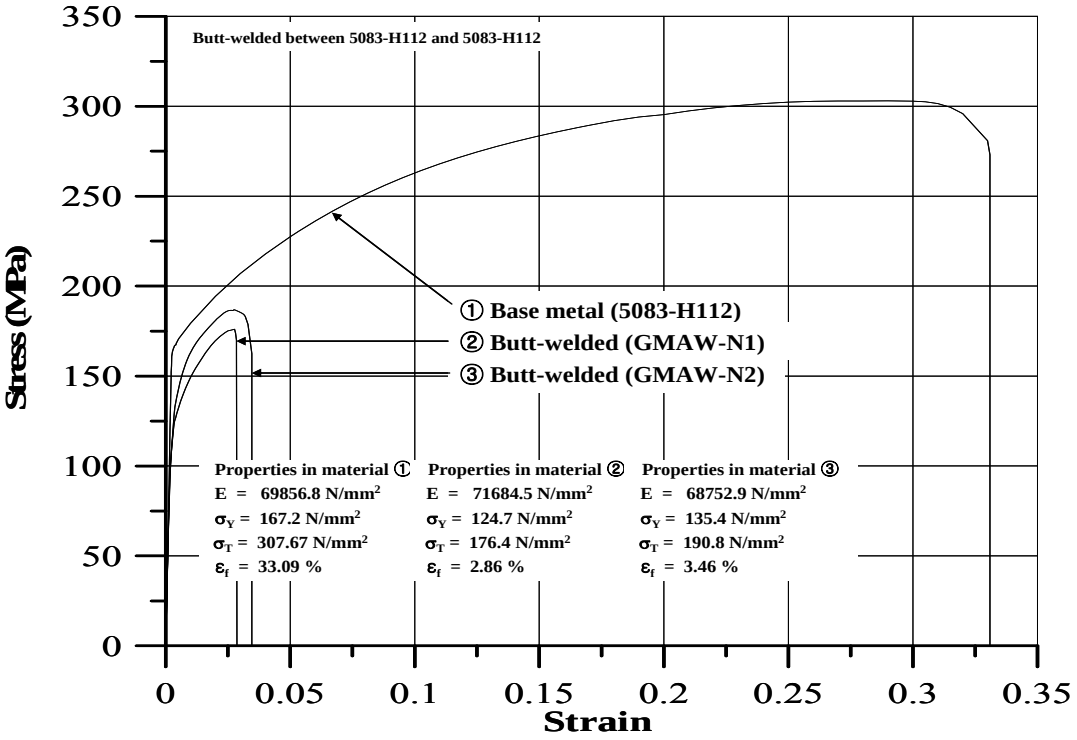

Figure 3.5(a) The stress versus strain curves for fusion-welded aluminum material – 5083-H112 plus 5083-H112 – obtained from the present tensile coupon tests

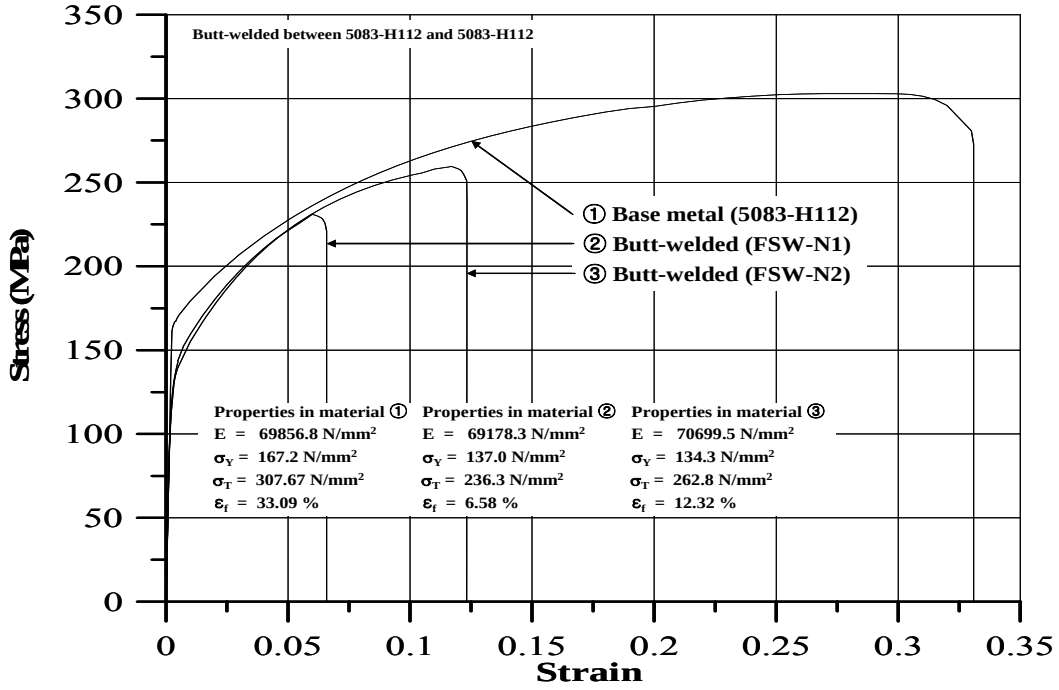

Figure 3.5(b) The stress versus strain curves for FSW aluminum material – 5083-H112 plus 5083-H112 – obtained from the present tensile coupon tests

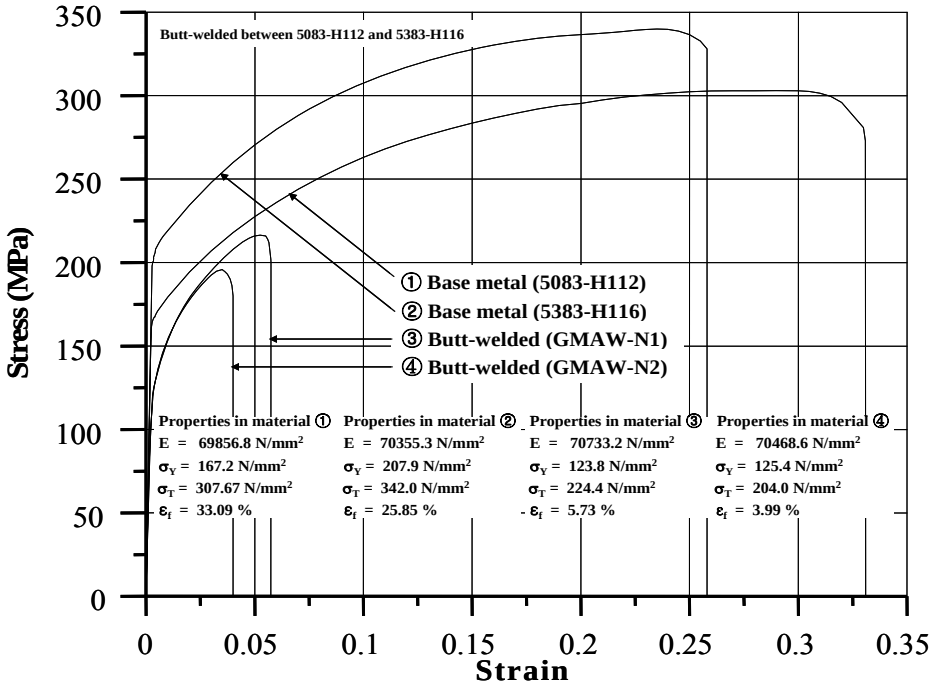

Figure 3.5(c) The stress versus strain curves for fusion welded aluminum material – 5083-H112 plus 5383-H116 – obtained from the tensile coupon tests

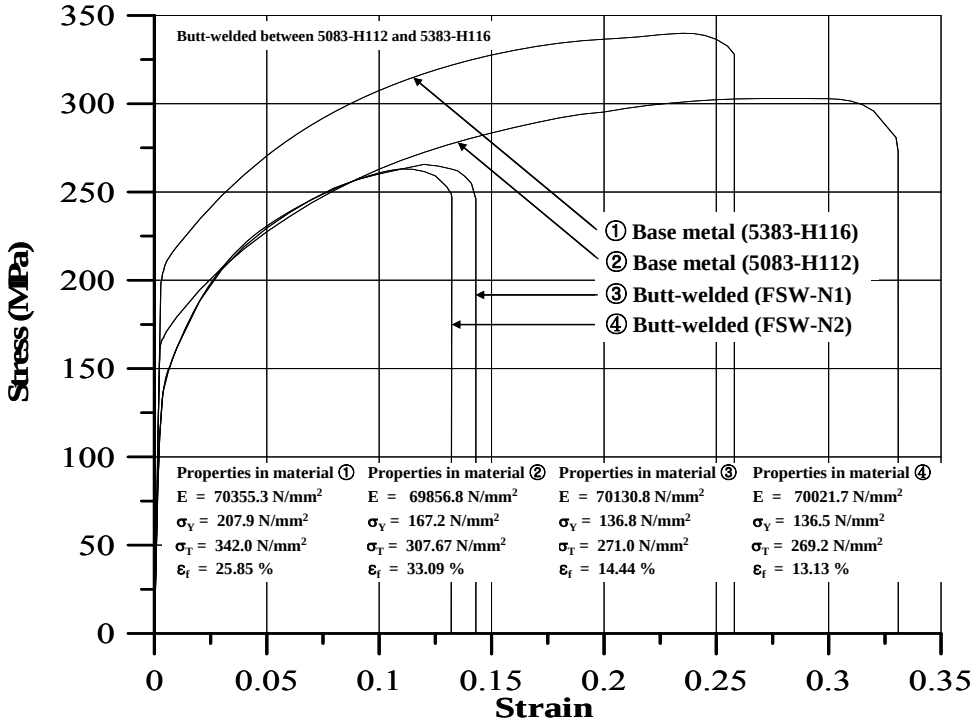

Figure 3.5(d) The stress versus strain curves for FSW aluminum material – 5083-H112 plus 5383-H116 – obtained from the tensile coupon tests

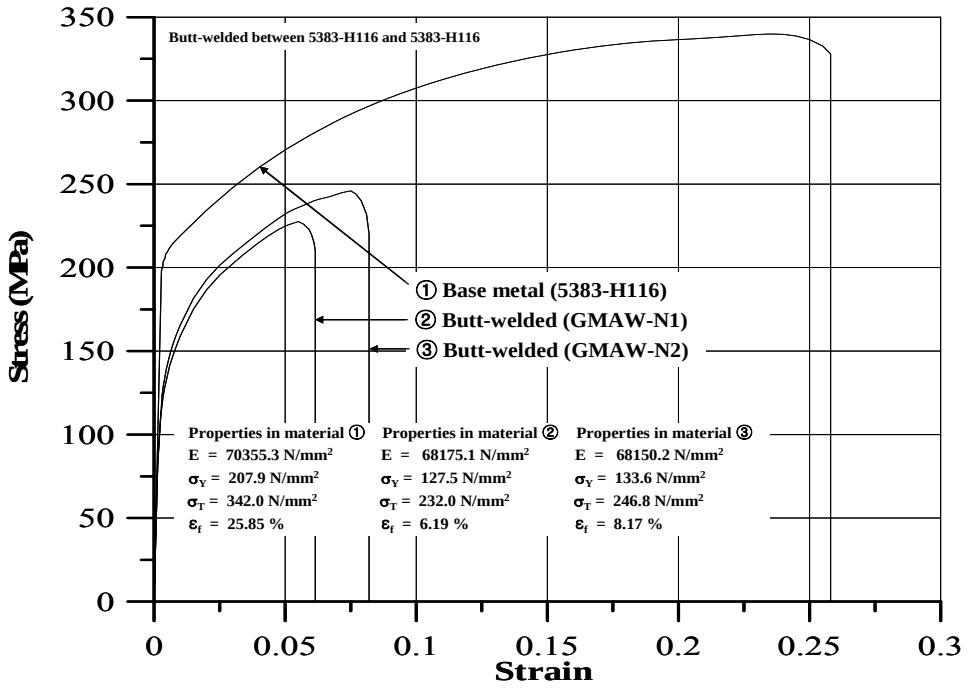

Figure 3.5(e) The stress versus strain curves for fusion-welded aluminum material – 5383-H116 plus 5383-H116 – obtained from the present tensile coupon tests

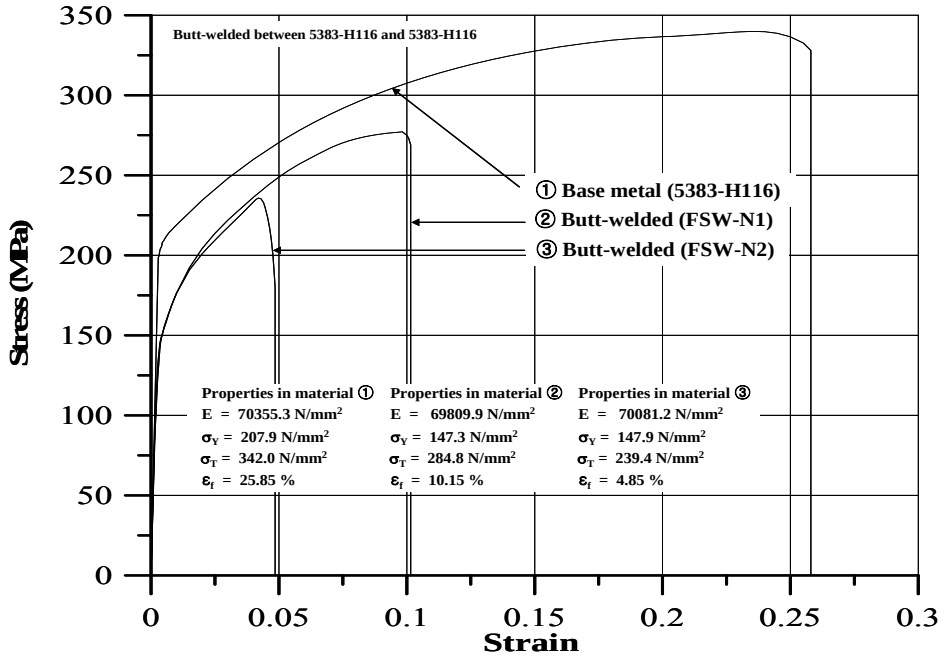

Figure 3.5(f) The stress versus strain curves for FSW aluminum material – 5383-H116 plus 5383-H116 – obtained from the present tensile coupon tests

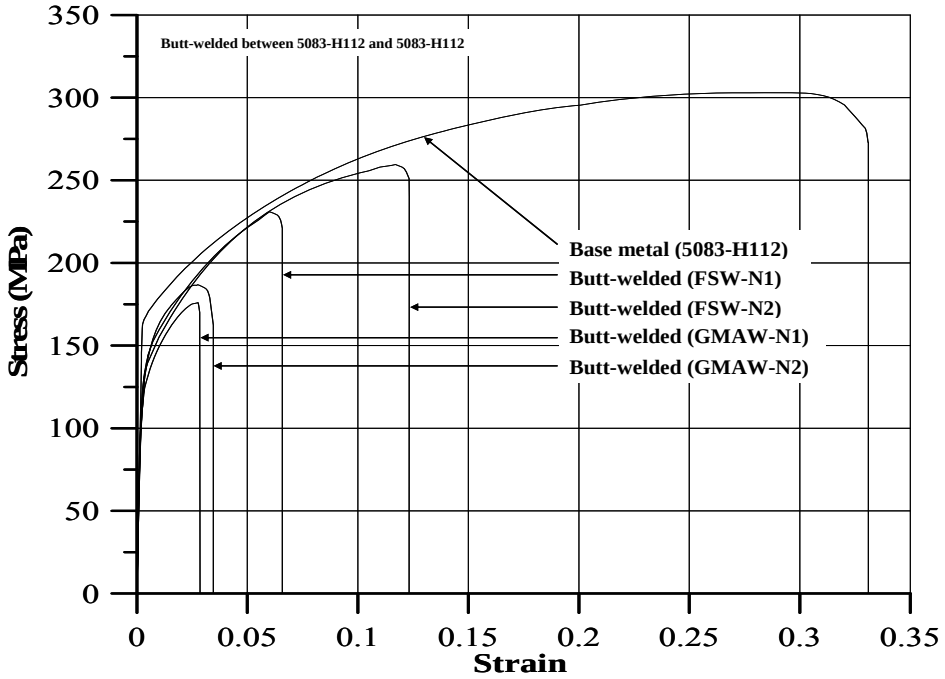

Figure 3.5(g) Comparison of the stress versus strain curves for welded aluminum material fabricated by fusion welding and FSW – 5083-H112 plus 5083-H112 – obtained from the tensile coupon tests

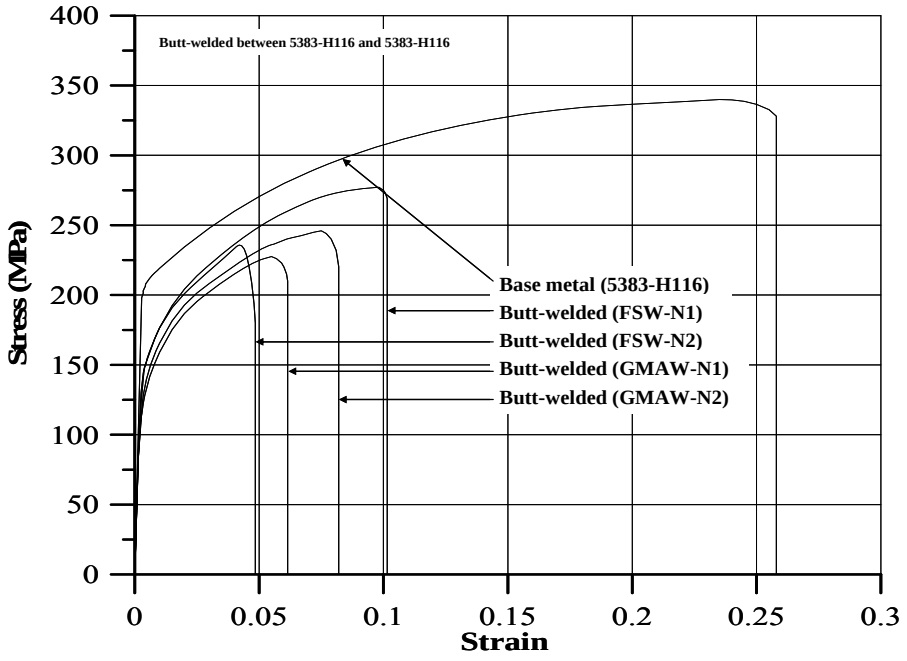

Figure 3.5(h) Comparison of the stress versus strain curves for welded aluminum material fabricated by fusion welding and FSW – 5383-H116 plus 5383-H116 – obtained from the tensile coupon tests

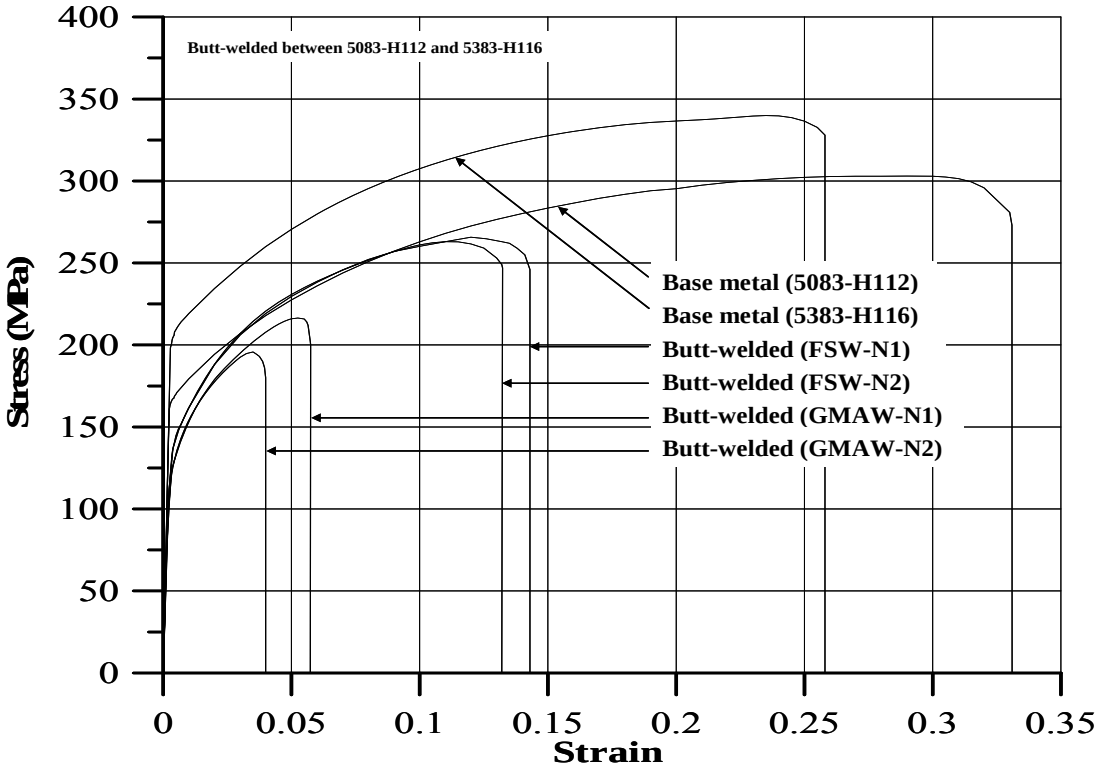

Figure 3.5(i) Comparison of the stress versus strain curves for welded aluminum material fabricated by fusion welding and FSW – 5083-H112 plus 5383-H116 – obtained from the tensile coupon tests

Table 3.4 Summary of the mechanical properties of welded aluminum alloys, obtained from the tensile coupon tests

Material	Weld specimen	E (N/mm^2)	σ_Y (N/mm^2)	σ_T (N/mm^2)	Elongation (%)
5083-H112 + 5083-H112	GMAW 1	71685	125	176	2.86
	GMAW 2	68753	135	191	3.46
Average		70219	130	183.5	3.16
5083-H112 + 5083-H112	FSW 1	69178	137	236	6.58
	FSW 2	70699	134	263	12.32
Average		69938.5	135.5	249.5	9.45
5083-H112 + 5383-H116	GMAW 1	70733	124	224	5.73
	GMAW 2	70469	125	204	3.99
Average		70601	124.5	214	4.86
5083-H112 + 5383-H116	FSW 1	70131	137	271	14.44
	FSW 2	70022	137	269	13.13
Average		70076.5	137	270	13.79
5383-H116 + 5383-H116	GMAW 1	68175	128	232	6.19
	GMAW 2	68150	134	247	8.17
Average		68162.5	131	239.5	7.18
5383-H116 + 5383-H116	FSW 1	69810	147	285	10.15
	FSW 2	70081	148	239	4.85
Average		69945.5	147.5	262	7.5

Note: E = elastic modulus; σ_Y = yield strength; σ_T = ultimate tensile strength.

Table 3.5 Minimum yield strength requirements for fusion-welded aluminum alloys, as specified by various regulations (MPa)

Alloy	ABS (2008)	DNV (2008)	AA (2005)	AWS (2004)	Alcan (2004)
5083-H111(E)	145	-	110	145	-
5083-H116(R)	165	116	115	165	125
5383-H111(E)	145	-	-	-	145
5383-H116(R)	145	140	-	-	145

Note: (E) = extruded; (R) = rolled; ABS = American Bureau of Shipping; DNV = Det Norske Veritas (Yield strength σ_l is determined from the values of f_l published by the equation $\sigma_l = f_l \times 240/1.1$); AA = Aluminum Association; AWS = American Welding Society.

3.2 Structural Dimensions and Profiles

3.2.1 Panel Dimensions

The principal dimensions of the test structures used in the present project were basically the same as those in SSC-451, although some small differences arose because of the different fabrication methods. Figure 3.6 shows a schematic of the dimensions of the test structures with the relevant nomenclature. The panel had a total of four longitudinal stiffeners or extrusions, and the transverse frame was attached at each end of the panel to be used for clamping with the test facility before the buckling collapse testing.

Tables 3.6(a) and 3.6(b) list the details of the principal dimensions of the structures tested in the present study and those in SSC-451, respectively. Twelve models, from a total of 78 test structures, were chosen from SSC-451. These are equivalent to those used in the present study in terms of structural dimensions and material properties, although they were fabricated by fusion welding.

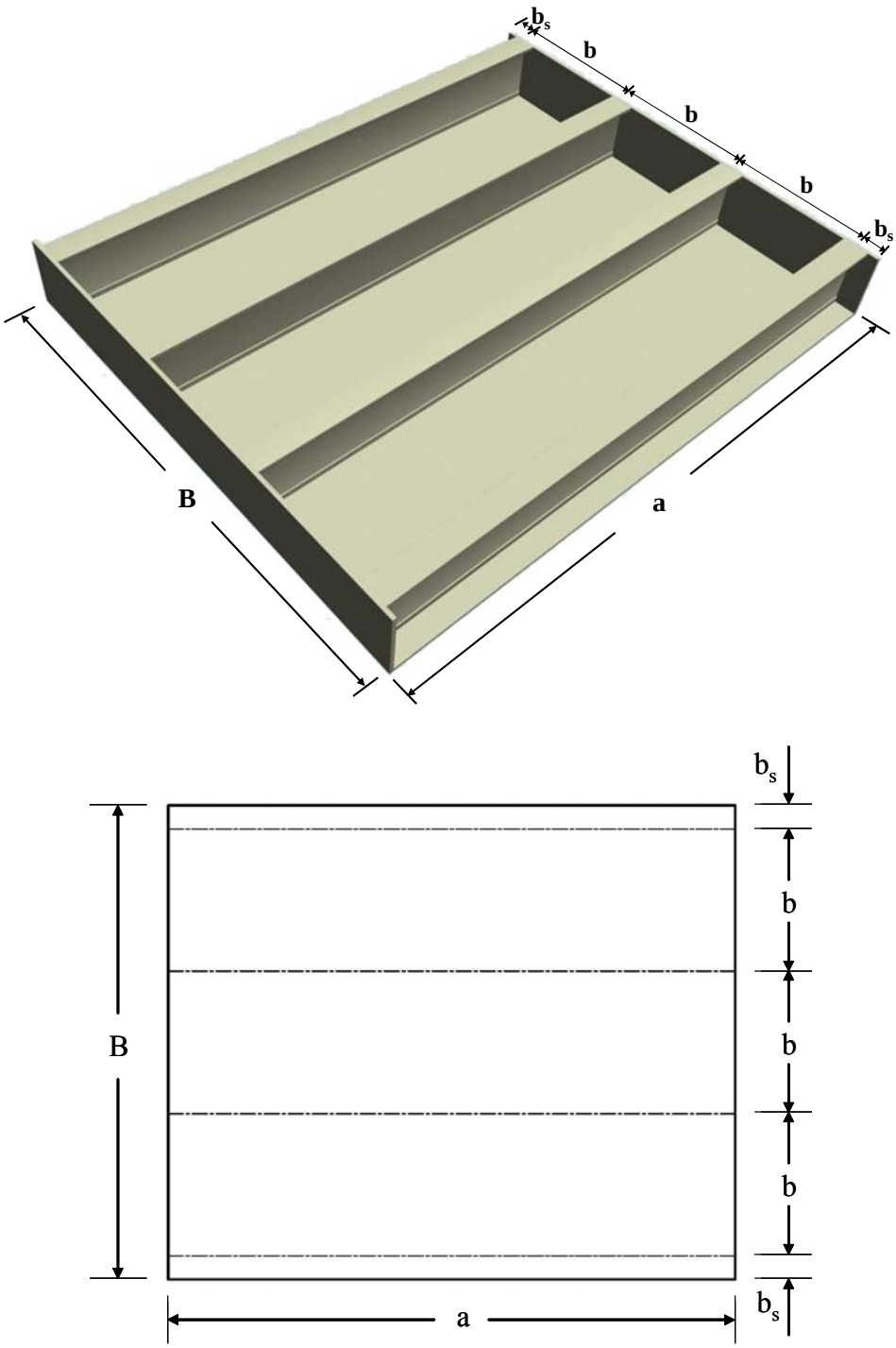

Figure 3.6 Nomenclature of the structural dimensions

Table 3.6(a) Details of the principal dimensions of the test structures used in the present study

Model	Plate					Extrusion	
	a (mm)	b (mm)	b_s (mm)	t (mm)	Material	Stiffener type	Material
19A	1200	300	50	6	5383-H116	ST-3 (35504-Type A)	5083-H112
20A	1200	300	50	6	5383-H116	ST-4 (35579-Type A)	5083-H112
17D	1200	300	50	6	5083-H112	ST-5 (35529-Type D)	6082-T6
18D	1200	300	50	6	5083-H112	ST-6 (35548-Type D)	6082-T6
19D1	1200	300	50	6	5083-H112	ST-7 (35504-Type D)	6082-T6
19D2	1200	300	50	6	5383-H116	ST-7 (35504-Type D)	5083-H112
20D1	1200	300	50	6	5083-H112	ST-8 (35579-Type D)	6082-T6
20D2	1200	300	50	6	5383-H116	ST-8 (35579-Type D)	5083-H112
19C	1200	300	40	6	5083-H112	ST-9 (35504-Type C)	5083-H112
20C	1200	300	30	6	5383-H116	ST-10 (35579-Type C)	5083-H112

Table 3.6(b) Details of the principal dimensions of the test structures in SSC-451

Model	Plate					Extrusion	
	a (mm)	b (mm)	b_s (mm)	t (mm)	Material	Stiffener type	Material
5	1200	300	50	6	5083-H116	ST-1 (35529-Type A)	5383-H112
6	1200	300	50	6	5083-H116	ST-2 (35548-TypeA)	5383-H112
7	1200	300	50	6	5083-H116	ST-3 (35504-Type A)	5383-H112
8	1200	300	50	6	5083-H116	ST-4 (35579-Type A)	5383-H112
17	1200	300	50	6	5083-H116	ST-1 (35529-Type A)	6082-T6
18	1200	300	50	6	5083-H116	ST-2 (35548-TypeA)	6082-T6
19	1200	300	50	6	5083-H116	ST-3 (35504-Type A)	6082-T6
20	1200	300	50	6	5083-H116	ST-4 (35579-Type A)	6082-T6
29	1200	300	50	6	5383-H116	ST-1 (35529-Type A)	5383-H112
30	1200	300	50	6	5383-H116	ST-2 (35548-TypeA)	5383-H112
31	1200	300	50	6	5383-H116	ST-3 (35504-Type A)	5383-H112
32	1200	300	50	6	5383-H116	ST-4 (35579-Type A)	5383-H112

3.2.2 Sectional Profiles and Properties of the Extrusions

The shapes and detailed dimensions of the extrusions in the test stiffened plate structures are indicated in Figure 3.7. A total of 10 different extrusion types were applied for the test structures in the present study and/or in SSC-451. Table 3.6 includes information on the extruded shapes for each of these structures. The cross-sectional properties of the extrusions and the plate panels for the present test structures and the SSC-451 test structures are indicated in Tables 3.7 and 3.8, respectively.

Tables 3.7(a) and 3.8(b) indicate the neutral axis measured from the outer surface of the plate (η) and the moment of inertia (I) calculated for a representative plate-stiffener combination, i.e., a single stiffener with attached plating. These parameters are involved in calculating the column slenderness ratio (λ) which is a primary parameter of the ultimate strength design formula for the entire stiffened plate

structure.

For the purpose of the comparison, Tables 3.7(b) and 3.8(b) give exact solutions of the sectional properties such as the neutral axis (η), the moment of inertia (I), and the column slenderness ratio (λ) calculated for the entire stiffened panel section. It is found that the column slenderness ratio value calculated for the representative plate-stiffener combination model is sufficiently accurate.

In addition, it is noted that the related properties of the extrusions are exact solutions determined for actual cross sections with a non-uniform or varying wall thickness, instead of idealized sections that consist of a uniformly approximated wall thickness. The ratios of the plate and column slenderness for each of the test structures were computed from the following equations.

$$\beta = \frac{b}{t}\sqrt{\frac{\sigma_{Yeq1}}{E}}, \quad \lambda = \frac{a}{r}\sqrt{\frac{\sigma_{Yeq2}}{E}}, \text{ and } \quad r = \sqrt{\frac{I}{A_t}},$$

where σ_{Yeq1} = the equivalent yield strength of the plate part = $\left(\sigma_{Yp}A_p + \sigma_{Ys}A_{ep}\right)/\left(A_p + A_{ep}\right)$; σ_{Yeq2} = the equivalent yield strength of the entire cross section, including the plate and extrusions = $\left(\sigma_{Yp}A_p + \sigma_{Ys}A_s\right)/A_t$; σ_{Yp} = the yield strength of the plate sheet; σ_{Ys} = the yield strength of the extrusions; E = the elastic modulus; b = plate breadth = stiffener spacing; t = plate thickness; a = the plate length between the transverse frames; A_p = the total cross-sectional area of the plate part in the sheet; A_{ep} = the total cross-sectional area of the plate part in the extrusions; A_{es} = the total cross-sectional area of the stiffener part in the extrusions; A_s = the total cross-sectional area of the extrusions = $A_{ep} + A_{es}$; and A_t = the total cross-sectional area of the entire plate panel = $A_p + A_s$.

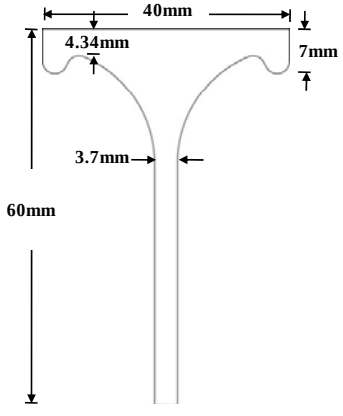

Figure 3.7 Cross-sectional profiles of the extrusions

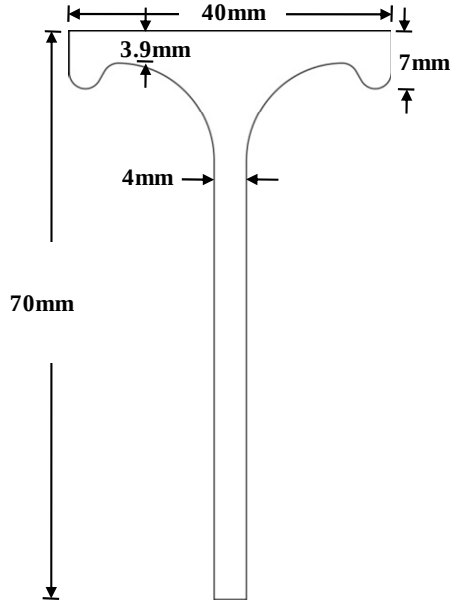

ST-2
35548-Type A

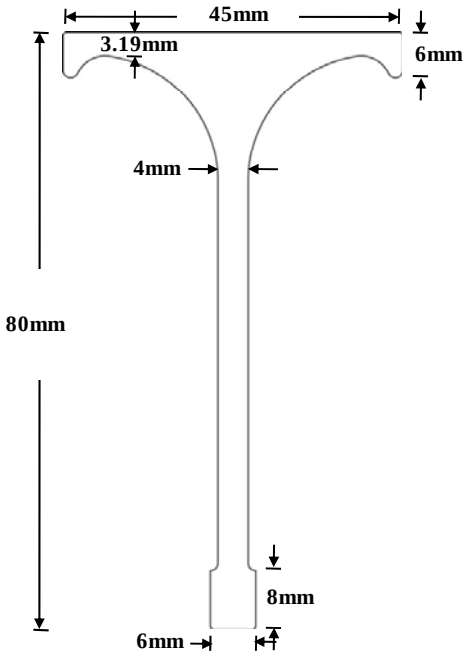

ST-3
35504-Type A

Figure 3.7 (*Continued*) Cross-sectional profiles of the extrusions

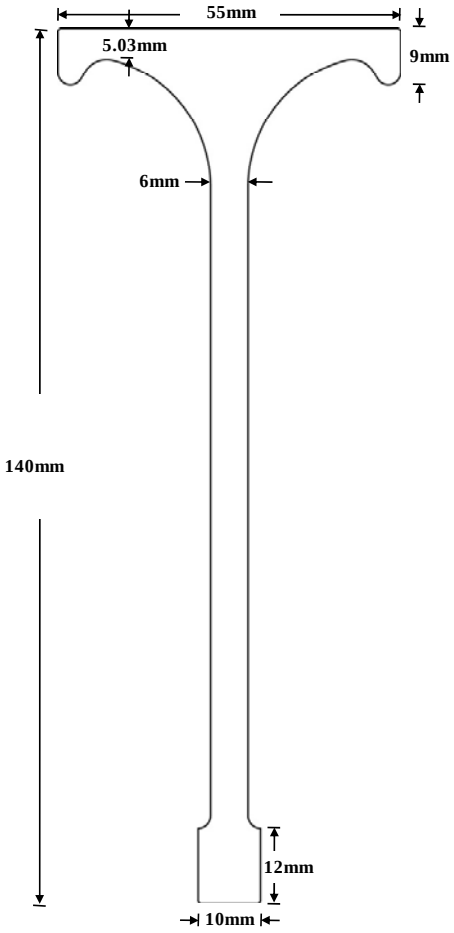

Figure 3.7 (*Continued*) Cross-sectional profiles of the extrusions

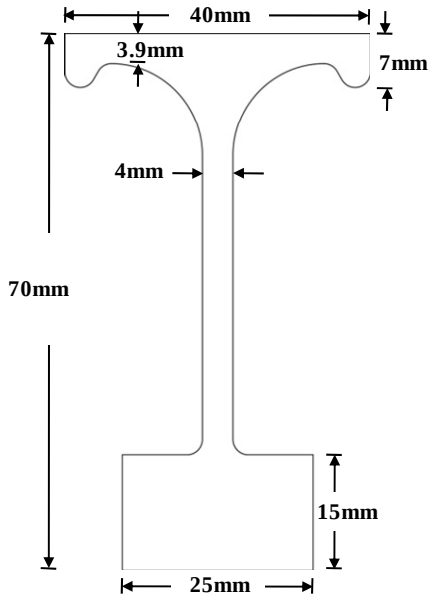

ST-6
35548-Type D

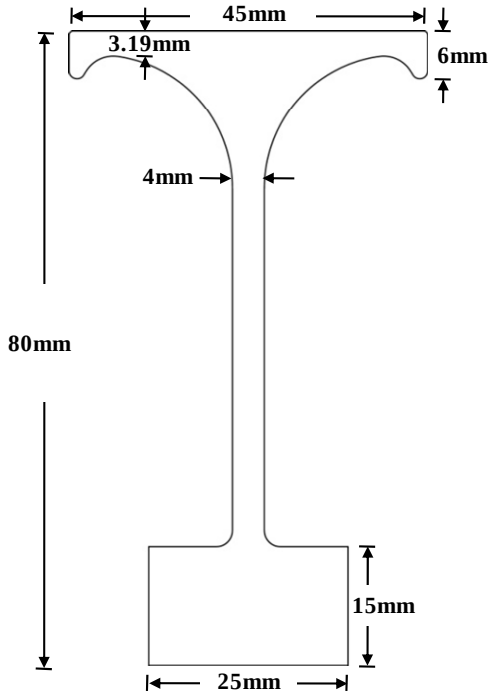

ST-7
35504-Type D

Figure 3.7 (*Continued*) Cross-sectional profiles of the extrusions

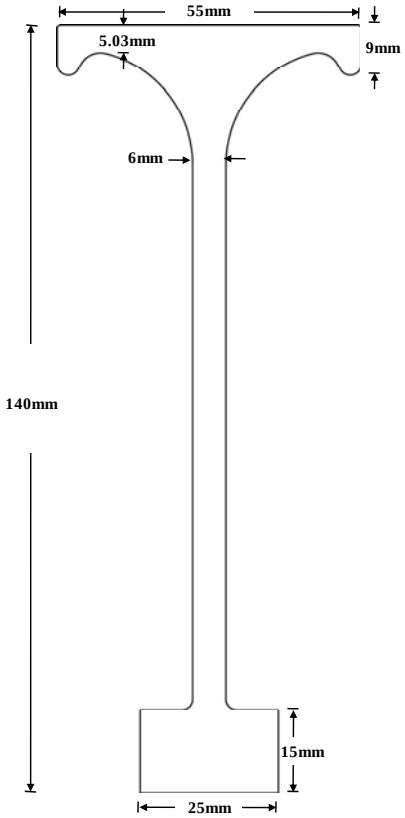

ST-8
35579-Type D

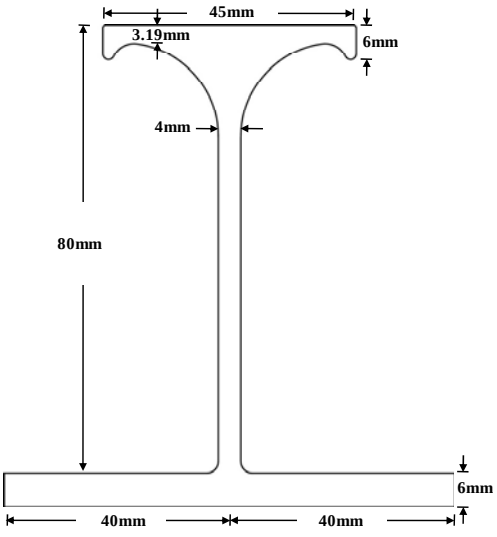

ST-9
35504-Type C

Figure 3.7 (*Continued*) Cross-sectional profiles of the extrusions

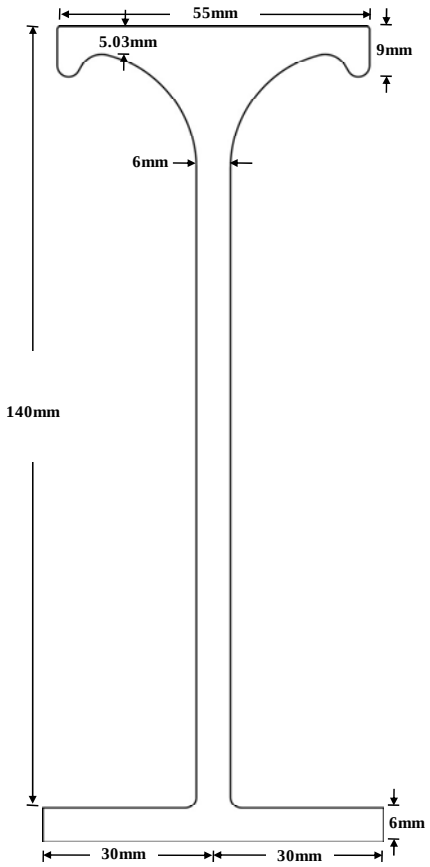

Figure 3.7 (*Continued*) Cross-sectional profiles of the extrusions

Table 3.7(a) Details of the cross-sectional properties for a single stiffener with attached plating of the present test structures

Model	σ_{Yp} (MPa)	σ_{Ys} (MPa)	σ_{Yeq1} (MPa)	σ_{Yeq2} (MPa)	A_p (mm^2)	A_{ep} (mm^2)	A_{es} (mm^2)	A_s (mm^2)	A_t (mm^2)	η (mm)	I (cm^4)	β	λ
19A	207.90	167.20	207.90	197.76	1800	0	597.42	597.42	2397.42	17.37	190.03	2.72	0.72
20A	207.90	167.20	207.90	190.57	1800	0	1334.21	1334.21	3134.21	42.21	944.56	2.72	0.36
17D	167.20	304.20	167.20	210.33	1800	0	826.95	826.95	2626.95	13.37	104.09	2.46	1.06
18D	167.20	304.20	167.20	210.16	1800	0	822.32	822.32	2622.32	14.31	131.96	2.46	0.94
19D1	167.20	304.20	167.20	212.79	1800	0	897.71	897.71	2697.71	16.97	190.95	2.46	0.80
19D2	207.90	167.20	207.90	194.36	1800	0	897.71	897.71	2697.71	16.97	190.95	2.72	0.76
20D1	167.20	342.90	167.20	249.15	1800	0	1573.61	1573.61	3373.61	40.29	965.78	2.46	0.43
20D2	207.90	167.20	207.90	188.92	1800	0	1573.61	1573.61	3373.61	40.29	965.78	2.72	0.37
19C	167.20	167.20	167.20	167.20	1320	480	582.71	1062.71	2382.71	17.42	189.95	2.45	0.66
20C	207.90	167.20	197.73	186.19	1440	360	1286.21	1646.21	3086.21	42.68	940.92	2.66	0.36

Table 3.7(b) Details of the cross-sectional properties for the entire stiffened panel cross section of the present test structures

Model	σ_{Yp} (MPa)	σ_{Ys} (MPa)	σ_{Yeq1} (MPa)	σ_{Yeq2} (MPa)	A_p (mm^2)	A_{ep} (mm^2)	A_{es} (mm^2)	A_s (mm^2)	A_t (mm^2)	η (mm)	I (cm^4)	β	λ
19A	207.90	167.20	207.90	196.31	6000	0	2389.68	2389.68	8389.68	19.43	731.40	2.72	0.68
20A	207.90	167.20	207.90	188.74	6000	0	5336.84	5336.84	11336.84	46.36	3576.80	2.72	0.35
17D	167.20	304.20	167.20	215.89	6000	0	3307.82	3307.82	9307.82	14.71	401.44	2.46	1.03
18D	167.20	304.20	167.20	215.71	6000	0	3289.26	3289.26	9289.26	15.77	510.16	2.46	0.91
19D1	167.20	304.20	167.20	218.49	6000	0	3590.83	3590.83	9590.83	18.72	737.10	2.46	0.77
19D2	207.90	167.20	207.90	192.66	6000	0	3590.83	3590.83	9590.83	18.72	737.10	2.72	0.72
20D1	167.20	342.90	167.20	257.15	6000	0	6294.45	6294.45	12294.45	43.93	3679.65	2.46	0.43
20D2	207.90	167.20	207.90	187.06	6000	0	6294.45	6294.45	12294.45	43.93	3679.65	2.72	0.36
19C	167.20	167.20	167.20	167.20	3960	1919.83	3591	5510.83	9470.83	19.75	727.43	2.45	0.67
20C	207.90	167.20	197.73	183.32	4320	1439.84	5145	6584.84	10904.84	47.92	3506.62	2.66	0.34

Table 3.8(a) Details of the cross-sectional properties for a single stiffener with attached plating of the SSC-451 test structures

Model	σ_{Yp} (MPa)	σ_{Ys} (MPa)	σ_{Yeq1} (MPa)	σ_{Yeq2} (MPa)	A_p (mm^2)	A_{ep} (mm^2)	A_{es} (mm^2)	A_s (mm^2)	A_t (mm^2)	η (mm)	I (cm^4)	β	λ
5	238.93	196.60	238.93	229.65	1800	0	505.74	505.74	2305.74	13.35	103.48	2.86	1.02
6	238.93	196.60	238.93	229.65	1800	0	505.60	505.60	2305.60	14.41	131.34	2.86	0.91
7	238.93	196.60	238.93	228.38	1800	0	597.42	597.42	2397.42	17.37	190.03	2.86	0.77
8	238.93	196.60	238.93	220.91	1800	0	1334.21	1334.21	3134.21	42.21	944.56	2.86	0.39
17	238.93	304.20	238.93	253.25	1800	0	505.74	505.74	2305.74	13.35	103.48	2.86	1.08
18	238.93	304.20	238.93	253.24	1800	0	505.60	505.60	2305.60	14.41	131.34	2.86	0.96
19	238.93	304.20	238.93	255.19	1800	0	597.42	597.42	2397.42	17.37	190.03	2.86	0.81
20	238.93	304.20	238.93	266.71	1800	0	1334.21	1334.21	3134.21	42.21	944.56	2.86	0.43
29	207.90	196.60	207.90	205.42	1800	0	505.74	505.74	2305.74	13.35	103.48	2.72	0.98
30	207.90	196.60	207.90	205.42	1800	0	505.60	505.60	2305.60	14.41	131.34	2.72	0.87
31	207.90	196.60	207.90	205.08	1800	0	597.42	597.42	2397.42	17.37	190.03	2.72	0.73
32	207.90	196.60	207.90	203.09	1800	0	1334.21	1334.21	3134.21	42.21	944.56	2.72	0.37

Table 3.8(b) Details of the cross-sectional properties for the entire stiffened panel cross section of the SSC-451 test structures

Model	σ_{Yp} (MPa)	σ_{Ys} (MPa)	σ_{Yeq1} (MPa)	σ_{Yeq2} (MPa)	A_p (mm^2)	A_{ep} (mm^2)	A_{es} (mm^2)	A_s (mm^2)	A_t (mm^2)	η (mm)	I (cm^4)	β	λ
5	238.93	196.60	238.93	228.26	6000	0	2022.95	2022.95	8022.95	14.90	398.79	2.86	0.98
6	238.93	196.60	238.93	228.26	6000	0	2022.39	2022.39	8022.39	16.12	507.02	2.86	0.87
7	238.93	196.60	238.93	226.87	6000	0	2389.68	2389.68	8389.68	19.43	731.40	2.86	0.74
8	238.93	196.60	238.93	219.00	6000	0	5336.84	5336.84	11336.84	46.36	3576.80	2.86	0.38
17	238.93	304.20	238.93	255.39	6000	0	2022.95	2022.95	8022.95	14.90	398.79	2.86	1.05
18	238.93	304.20	238.93	255.38	6000	0	2022.39	2022.39	8022.39	16.12	507.02	2.86	0.93
19	238.93	304.20	238.93	257.52	6000	0	2389.68	2389.68	8389.68	19.43	731.40	2.86	0.79
20	238.93	304.20	238.93	269.66	6000	0	5336.84	5336.84	11336.84	46.36	3576.80	2.86	0.43
29	207.90	196.60	207.90	205.05	6000	0	2022.95	2022.95	8022.95	14.90	398.79	2.72	0.93
30	207.90	196.60	207.90	205.05	6000	0	2022.39	2022.39	8022.39	16.12	507.02	2.72	0.82
31	207.90	196.60	207.90	204.68	6000	0	2389.68	2389.68	8389.68	19.43	731.40	2.72	0.70
32	207.90	196.60	207.90	202.58	6000	0	5336.84	5336.84	11336.84	46.36	3576.80	2.72	0.37

3.3 Fusion-welded Structures

Two of the test structure models, 19A and 20A, were fabricated via fusion welds. Figure 3.8 shows a schematic of fillet-type fusion welds. The welding conditions applied to fabricate these test structures were the same as those used to prepare the tensile coupon test specimens, as described in 3.1.3(b).

Figure 3.9 shows the layout of the fusion welds for test structures 19A and 20A. Figure 3.10 shows photos of the test structures during and after fusion fillet-weld fabrication. Test structure 20A is similar to 19A. Table 3.9 summarizes the weld types of the test structures in both the present study and SSC-451.

The fusion fillet-weld work of the present test structures was carried out by Best F.A Ltd. (www.best-fa.co.kr), Changwon, Korea, which is a company of professional fusion weld fabrication in Korea, while that of the SSC-451 test structures was performed by Hanjin Heavy Industries & Construction Co., Ltd. (www.hanjinsc.com), Busan, Korea.

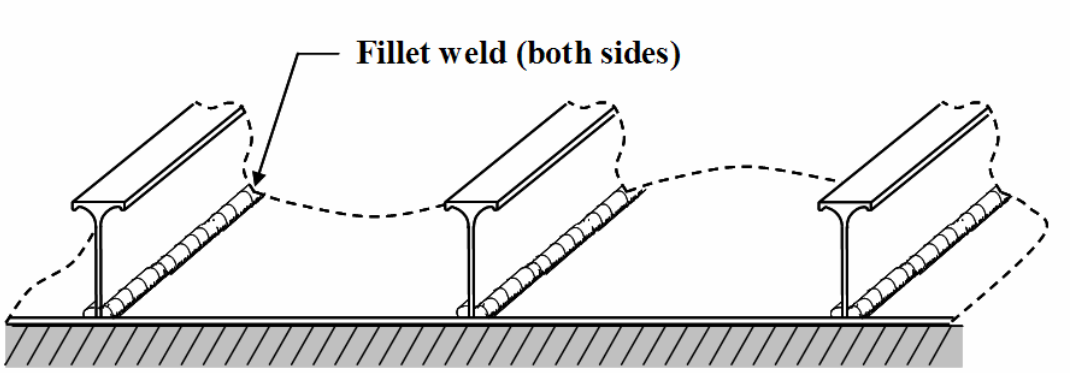

Figure 3.8 Schematic of fillet-type fusion weld (Fabrication method A)

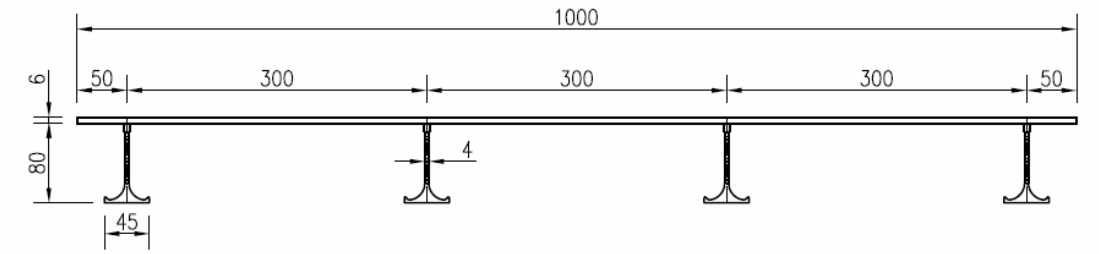

Figure 3.9(a) Layout of test structure 19A for fillet-type fusion weld in mm

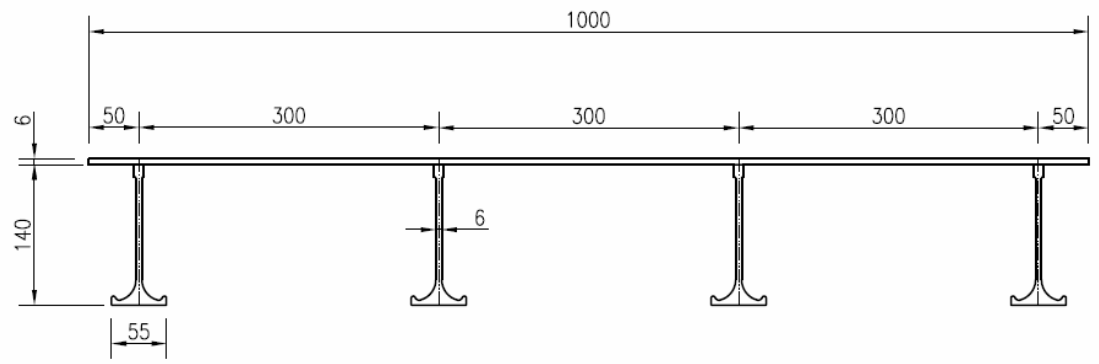

Figure 3.9(b) Layout of test structure 20A for fillet-type fusion weld in mm

Figure 3.10(a) Photo of one of the test structures during fusion-weld fabrication

Figure 3.10(b) Photo of test structure (19A) after fusion-weld fabrication

Table 3.9 Summary of fabrication methods applied in the test structures

The present test structures			The SSC-451 test structures		
Model	Weld method	Weld type	Model	Weld method	Weld type
19A	GMAW – Method A	Fillet weld	5	GMAW – Method A	Fillet weld
20A	GMAW – Method A	Fillet weld	6	GMAW – Method A	Fillet weld
17D	FSW – Method D	Lap weld	7	GMAW – Method A	Fillet weld
18D	FSW – Method D	Lap weld	8	GMAW – Method A	Fillet weld
19D1	FSW – Method D	Lap weld	17	GMAW – Method A	Fillet weld
19D2	FSW – Method D	Lap weld	18	GMAW – Method A	Fillet weld
20D1	FSW – Method D	Lap weld	19	GMAW – Method A	Fillet weld
20D2	FSW – Method D	Lap weld	20	GMAW – Method A	Fillet weld
19C	FSW – Method C-2	Butt weld	29	GMAW – Method A	Fillet weld
20C	FSW – Method C-2	Butt weld	30	GMAW – Method A	Fillet weld
			31	GMAW – Method A	Fillet weld
			32	GMAW – Method A	Fillet weld

Note: Schematic of weld configurations

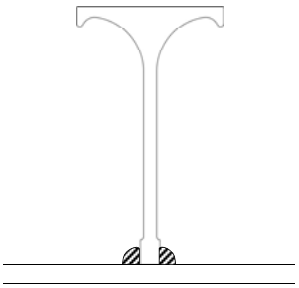

Fusion (GMAW) fillet-weld
(Fabrication method A)

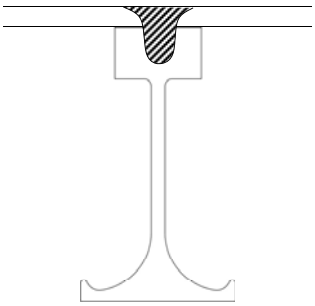

Friction stir lap-weld
(fabrication method D)

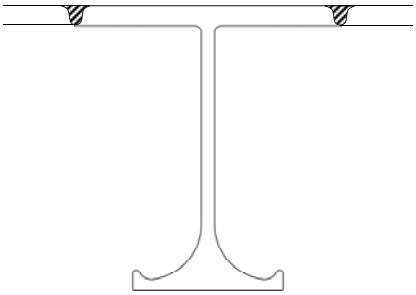

Friction stir butt-weld
(Fabrication method C-2)

3.4 Friction Stir-Welded Structures

3.4.1 Classification of Fabrication Methods

The application of various FSW methods may be appropriate, as shown in Figure 3.11, and Figure 3.12 shows possible applications of FSW for the fabrication of stiffened plate structures. Table 3.9 summarizes the weld methods applied to fabricate the test structures.

In reality, however, FSW applications have a number of limitations that are associated with the intervention of the FSW machine in the target structures (including the plate and extrusions) to be fabricated. For the application of Method A (fillet-welding), which is the most widely used method for fusion welding, either the target structure or the FSW machine needs to be tilted about 25 degrees from the upright position as shown in Figure 3.12(a), although Method A can of course become relevant in the future.

Method B applies the butt-joining technique, but it is appropriate only for assembling individual extrusions with large flanges. Method C also applies the butt-joining technique, but only between the narrow plate sheets and the flanges of the extrusions.

Two types of Method C may be considered, namely C-1 and C-2. The method C-1 applies the FSW on the side of the extrusions, whereas the method C-2 applies it on the side of the plate sheet. When the breadth of the extruded flanges on the unwelded side is relatively large, compared to the FSW machine, it is difficult to apply Method C-1 because of possible intervention between the flange and the machine. Method D applies the lap-joining technique between the continuous plate sheet and the short flanges of the extrusions, although a deep penetration weld may be required.

During the fabrication of the test structures used in this project, the following difficulties arose.

- The FSW machine was fixed in the upright position to provide sufficient downward force during welding. There was no facility to tilt the target structure for FSW fillet-joining.
- No supplier could provide extrusions with large flanges for the application of Method B.
- The breadth of the extruded flanges on the unwelded side was relatively large, meaning that the application of Method C-1 was not relevant.

For these reasons, this study adopted Method C-2 (butt-joining), as shown in Figure 3.12(c), and Method D (lap-joining), as shown in Figure 3.12(d). The welding conditions were similar to those applied to prepare the tensile coupon test specimens, as described in 3.1.3(b), but with different sizes of the FSW tool, as indicated in Table 3.10. The FSW fabrication work of the present test structures was carried out by Winxen Co., Ltd. (www.winxen.com), Changwon, Korea, which is a FSW machine supplier in Korea under the supervision of the Welding Institute in the U.K.

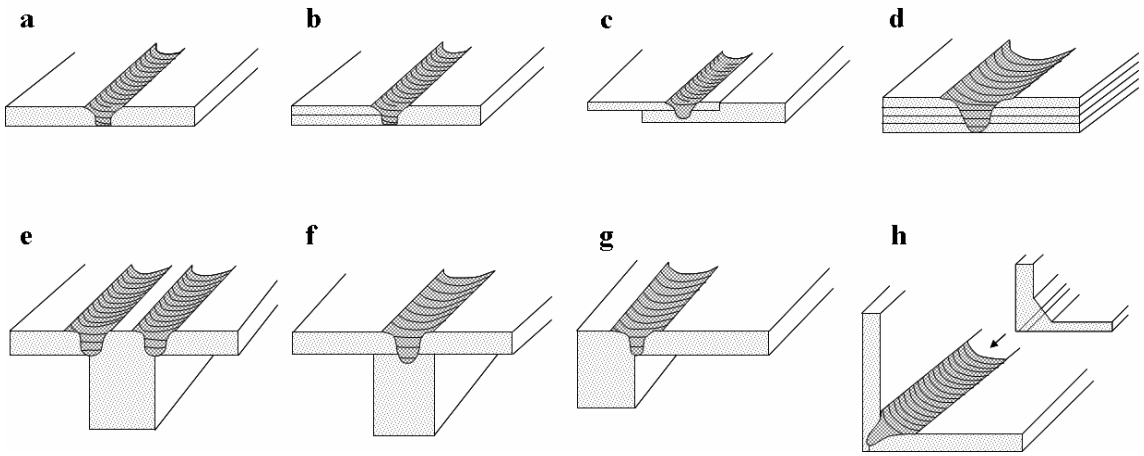

Figure 3.11 Various joint configurations for FSW (Kramer 2007)

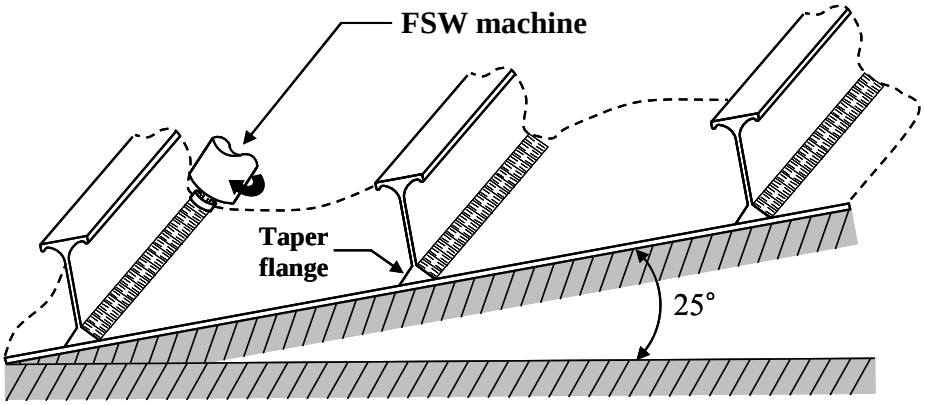

Figure 3.12(a) Schematic of FSW for fillet-joining between a continuous plate sheet and extrusions with taper flange (Method A)

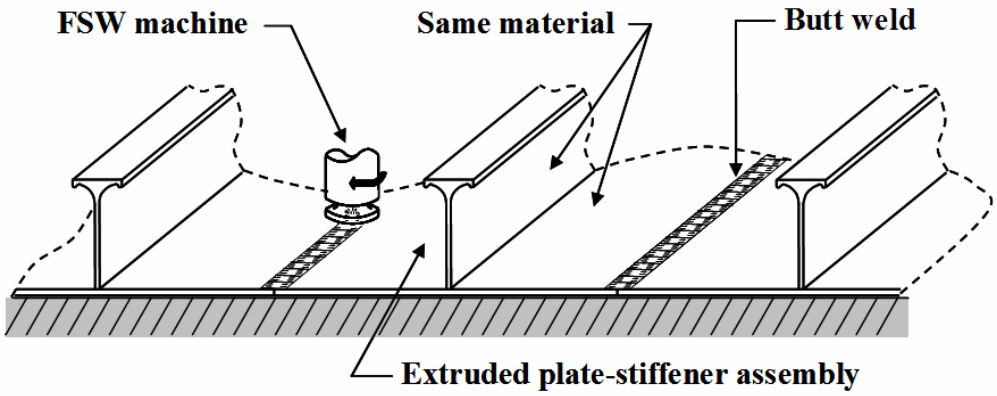

Figure 3.12(b) Schematic of FSW for butt-joining between large extrusions only (Method B)

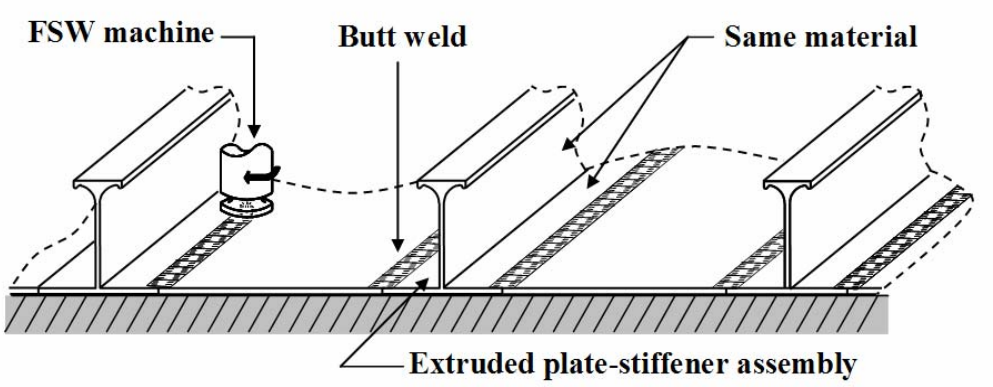

Figure 3.12(c) Schematic of FSW for butt-joining on the extrusion side between the plate sheet and the extrusion (Method C-1)

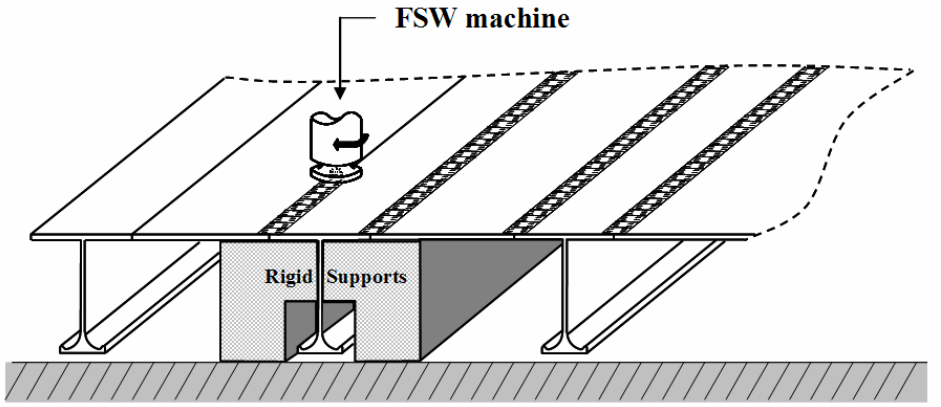

Figure 3.12(d) Schematic of FSW for butt-joining on the plate side between the plate sheet and the extrusion (Method C-2)

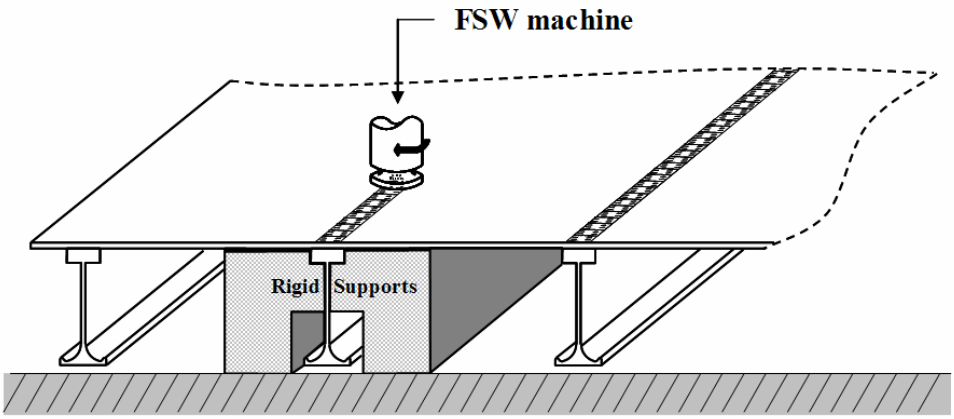

Figure 3.12(e) Schematic of FSW for lap-joining between the plate sheet and the extrusion (Method D)

Table 3.10 Sizes of the FSW tool applied to fabricate the test structures, with the nomenclature defined in Figure 3.4

Type	d_1	d_2	d_3	h
Butt-joining	4 mm	5 mm	15 mm	5.4 mm
Lap-joining	5 mm	8.9 mm	23 mm	8 mm

3.4.2 Butt-joining Methods

Figure 3.13 shows the layout of the friction stir welds for the butt-joining of test structures 19C and 20C. For the purposes of friction stir butt-welding, a specially designed jig was fabricated, as shown in Figure 3.14, in association with Method C-2. Figure 3.15 shows photos of one of the test structures during and after friction stir butt-joining.

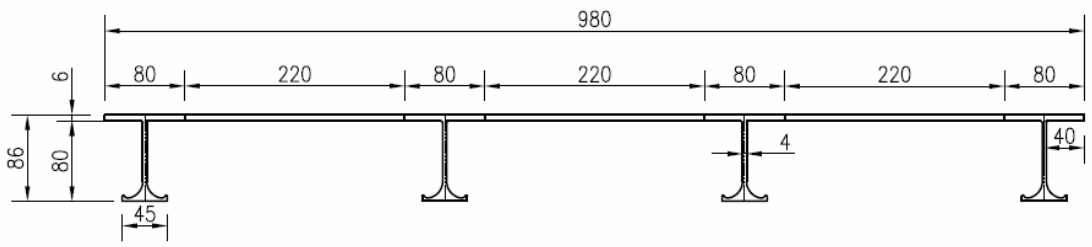

Figure 3.13(a) Layout of test structure 19C for friction stir butt-joining in mm

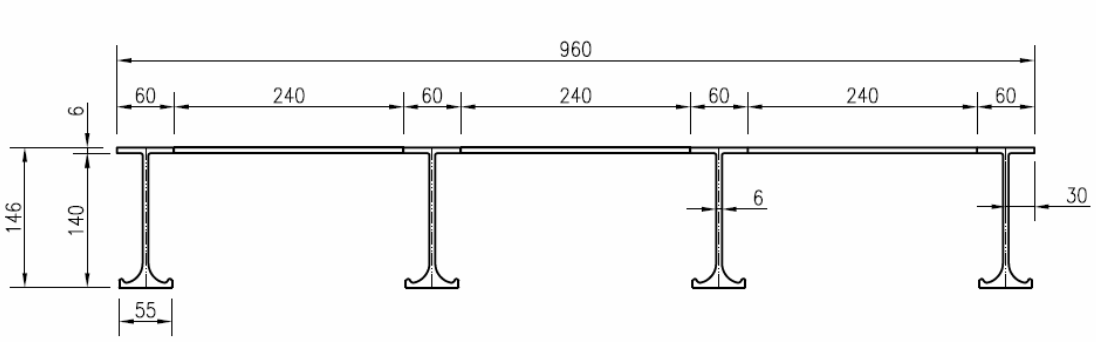

Figure 3.13(b) Layout of test structure 20C for friction stir butt-joining in mm

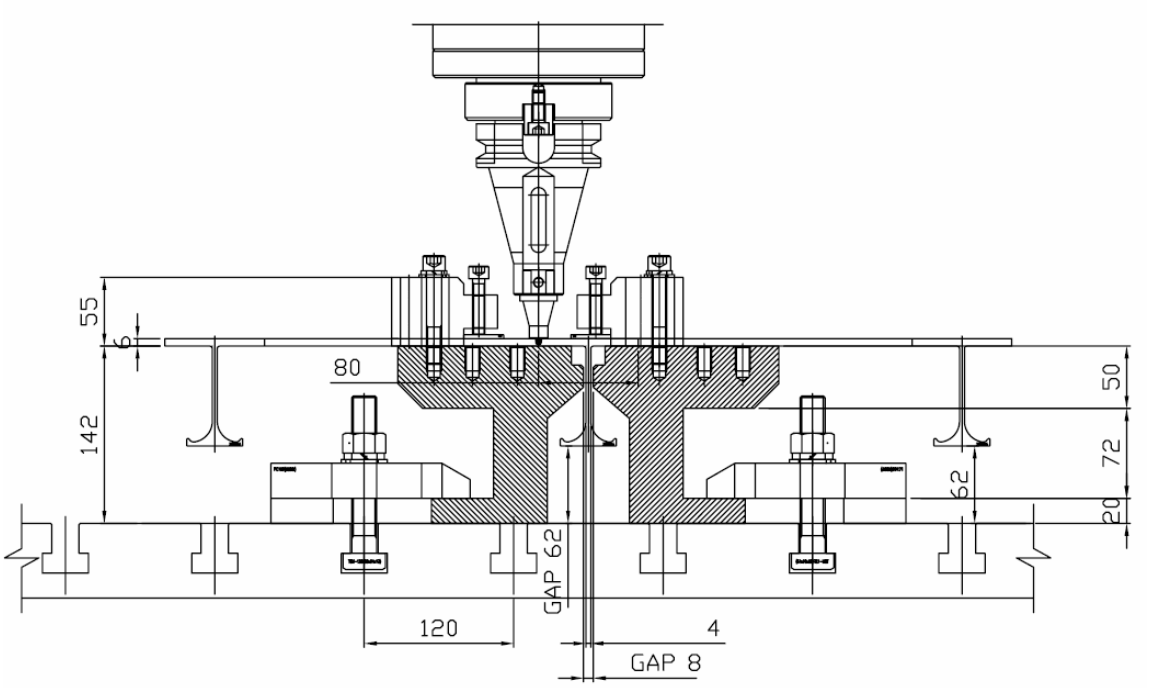

Figure 3.14 Support jig design for FSW butt-joining in association with Method C-2 in mm

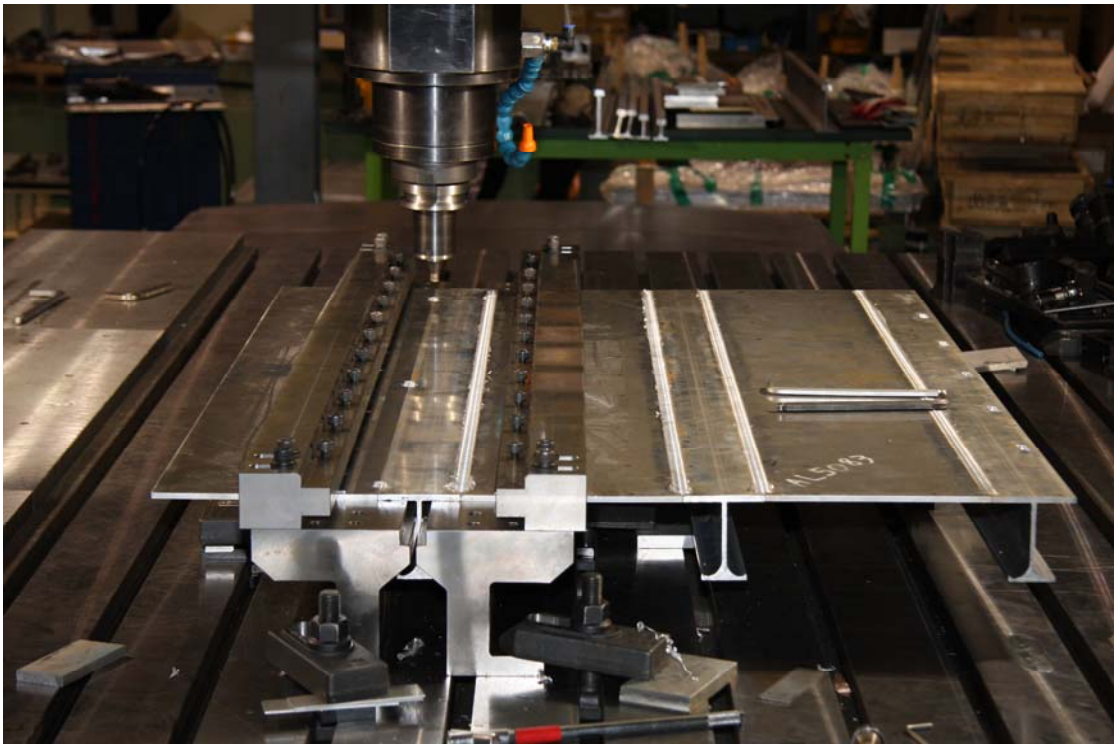

Figure 3.15(a) Photo of one of the test structures during friction stir butt-joining

Figure 3.15(b) Photo of test structure 19C after friction stir butt-joining

3.4.3 Lap-joining Methods

Figure 3.16 shows the layout of the friction stir welds for the lap-joining of test structures 17D, 18D, 19D1, 19D2, 20D1 and 20D2. Figure 3.17 presents the design of the support jig for the friction stir lap-joining applied during fabrication of the test structures. Figure 18 shows a photo of test structure 17D after the completion of friction stir lap-joining.

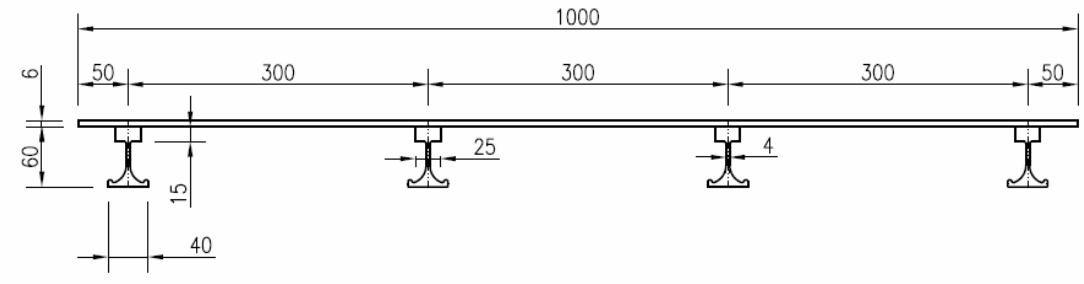

Figure 3.16(a) Layout of test structure 17D for friction stir lap-joining in mm

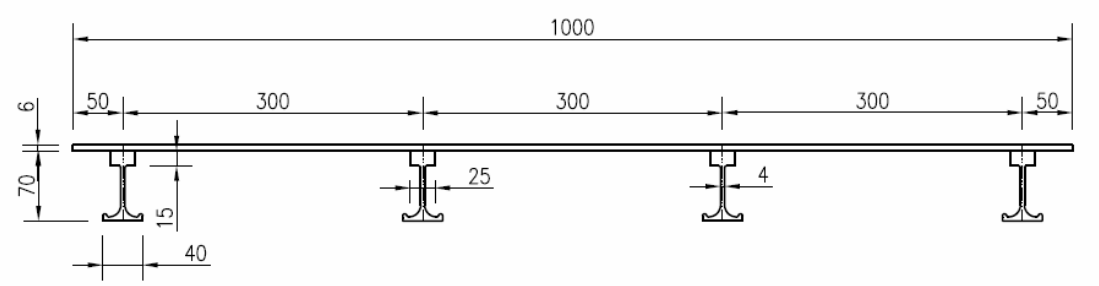

Figure 3.16(b) Layout of test structure 18D for friction stir lap-joining in mm

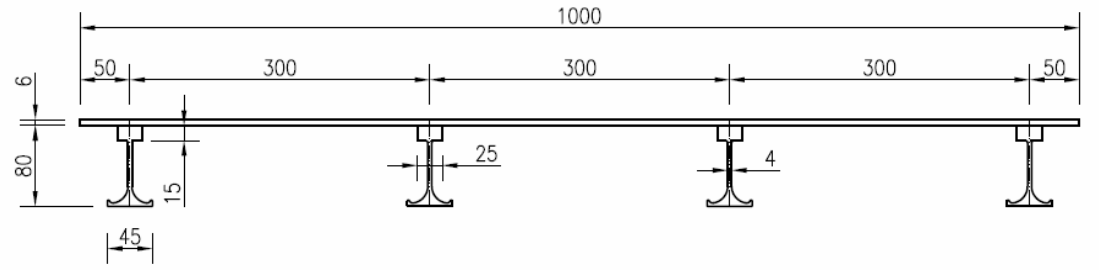

Figure 3.16(c) Layout of test structure 19D1 for friction stir lap-joining in mm

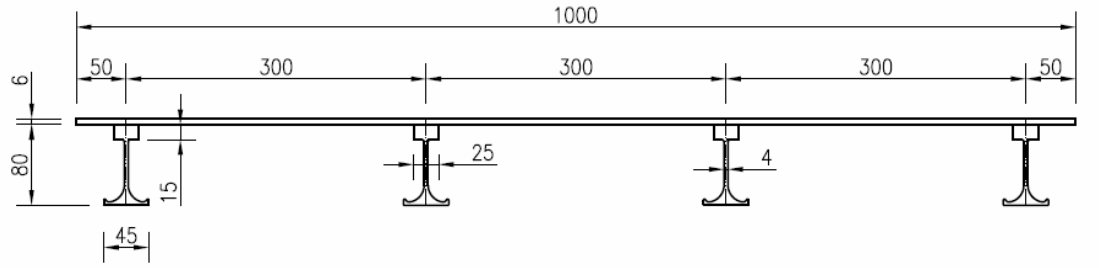

Figure 3.16(d) Layout of test structure 19D2 for friction stir lap-joining in mm

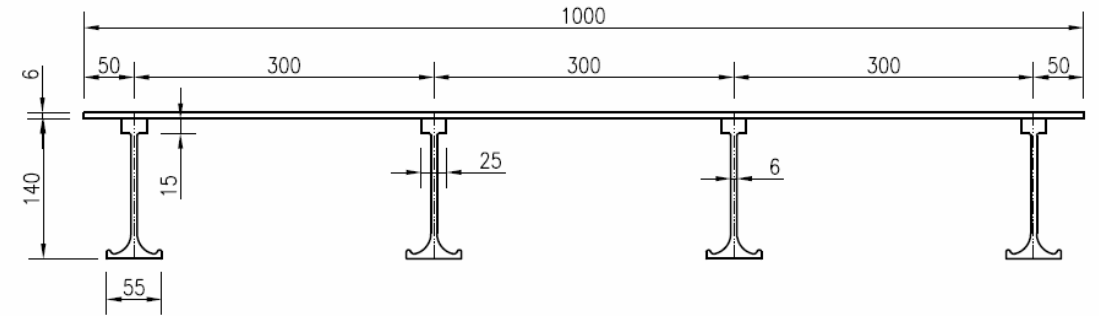

Figure 3.16(e) Layout of test structure 20D1 for friction stir lap-joining in mm

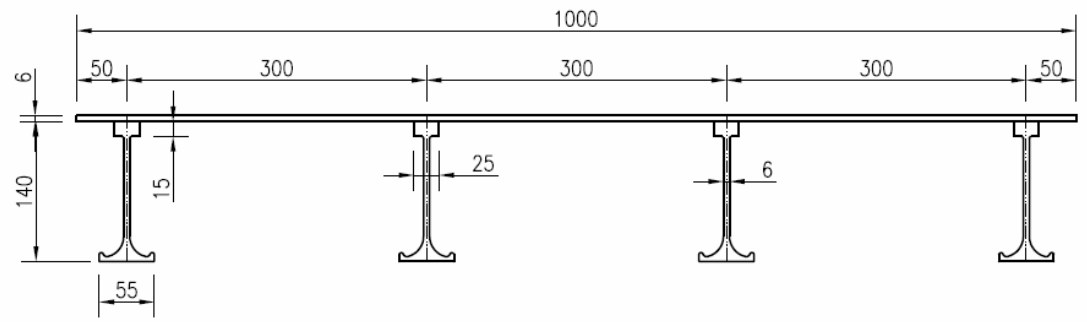

Figure 3.16(f) Layout of test structure 20D2 for friction stir lap-joining in mm

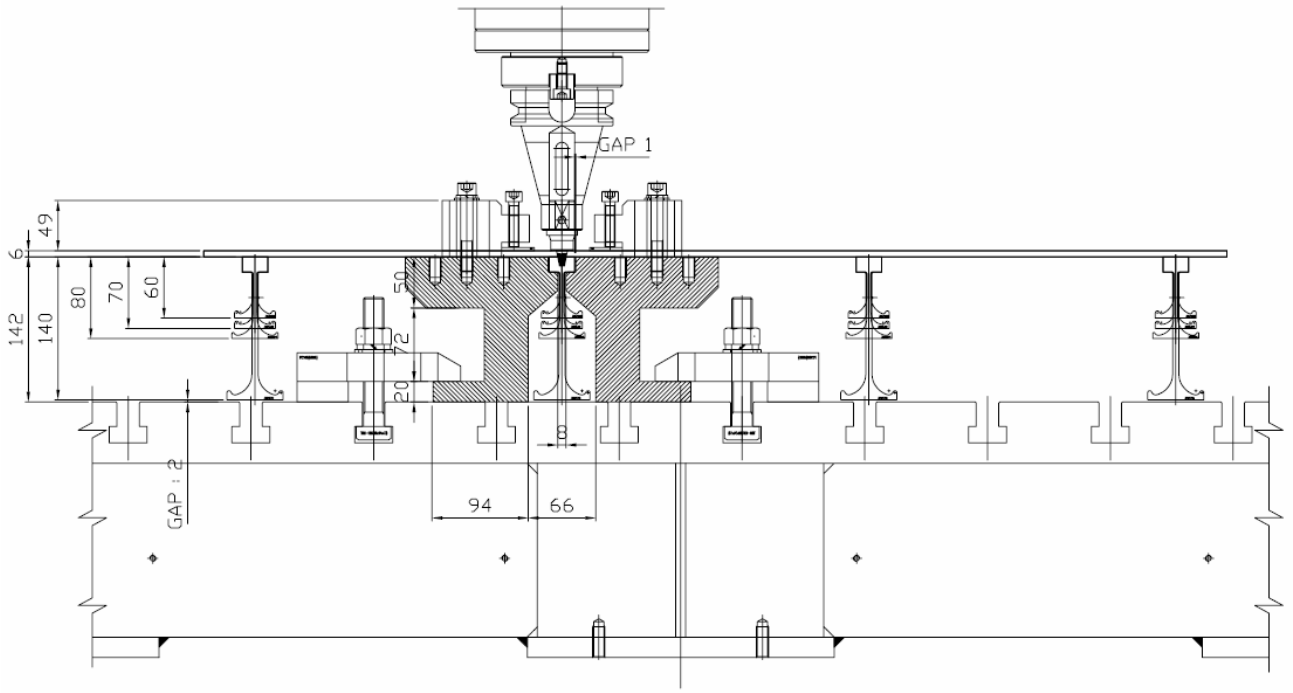

Figure 3.17 Support jig design for FSW lap-joining in association with Method D in mm

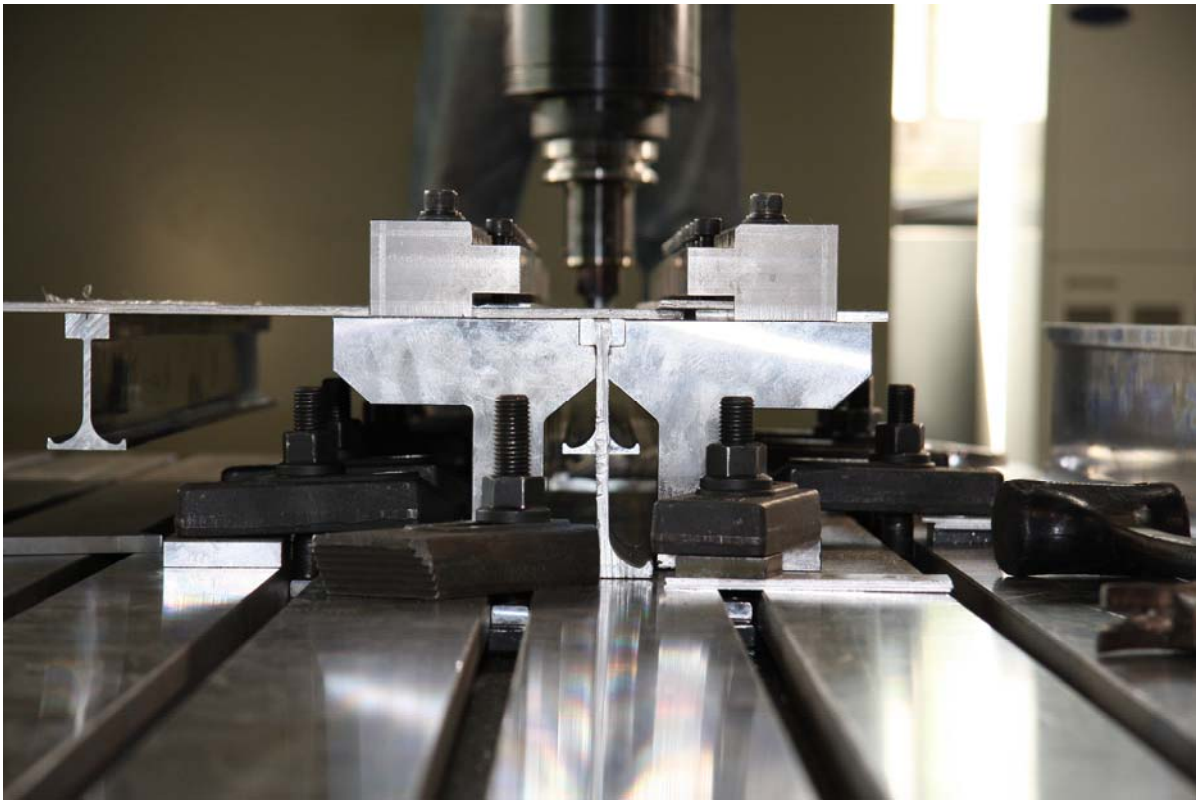

Figure 3.18(a) Photo of a test structure during friction stir lap-joining

Figure 3.18(b) Photo of test structure 17D after friction stir lap-joining

Chapter 4 Weld-induced Initial Imperfections of Test Structures

4.1 Types of Weld-induced Initial Imperfections

Welding may induce the following six types of initial imperfections in aluminum structures.

- Initial deflection of the plating between the stiffeners (see Figure 4.1)
- Column-type initial distortion of the stiffener (see Figure 4.1)
- Sideways initial distortion of the stiffener (see Figure 4.1)
- Residual stress in the plating between the stiffeners (see Figure 4.2)
- Residual stress in the stiffener web (see Figure 4.2)
- Softening in the thermo-mechanically affected zone (TMAZ) and the heat-affected zone (HAZ)

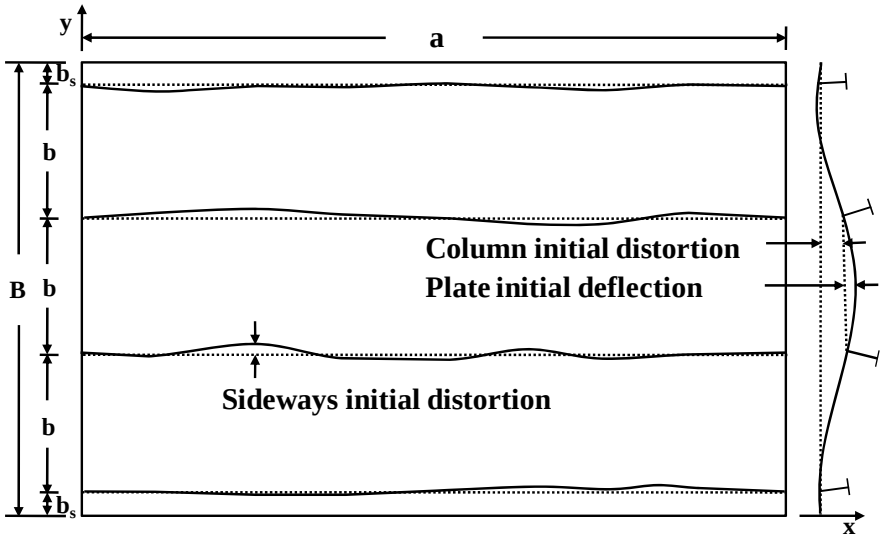

Figure 4.1 Schematic of weld-induced initial distortions

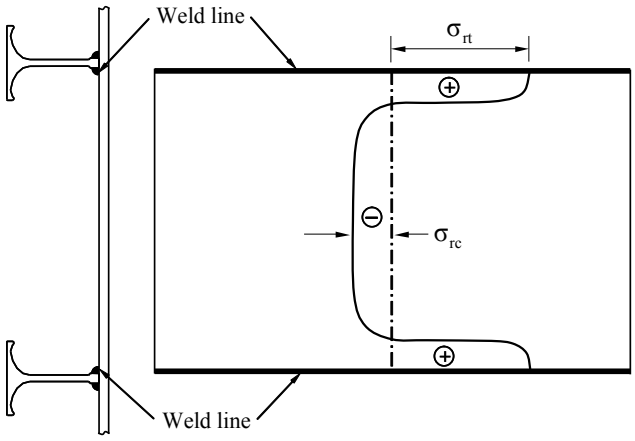

Figure 4.2(a) Schematic of fillet weld-induced residual stresses in the plating

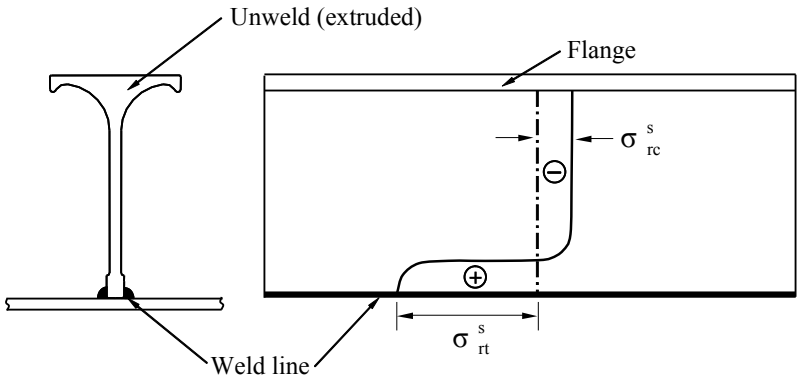

Figure 4.2(b) Schematic of fillet weld-induced residual stresses in the stiffener web

It should be noted that the first five types of initial imperfections are also of primary concern in welded steel structures, although the softening phenomenon in the softened zone of these structures is usually insignificant and thus ignored in terms of ultimate compressive strength performance. The properties in the softened zone are often formulated in association with the reduced yield strength and breadth of this zone.

These weld-induced initial imperfections affect (reduce) the ultimate compressive strength performance of structures in a sensitive manner, and thus they must be dealt with as important parameters of influence in structural design and strength assessment.

The SSC-451 report (Paik et al. 2008b) presents an extensive set of initial imperfection measurements in aluminum stiffened plate structures fabricated by fusion welding. The fusion weld-induced initial imperfection measurements presented in SSC-451 are here compared with the database obtained from the present study by friction stir welding (FSW). The details of extrusion profiles and dimensions, and weld methods used to fabricate the present test structures are summarized in Tables 3.6(a) to 3.8(a) and Table 3.9.

4.2 SSC-451 Database

A total of 78 aluminum stiffened plate structures fabricated by fusion welding were studied in SSC-451 (Paik et al. 2008b), as indicated in Tables 3.6(b) to 3.8(b) and Table 3.9. The six types of weld-induced initial imperfections were measured for all of that study's test structures, and the resulting database of measurements was then analyzed to obtain the statistical characteristics in terms of the means and standard deviations at the three levels of initial imperfections, i.e., slight, average and severe.

The following are the mean values of the initial imperfections obtained from the statistical analysis in SSC-451.

- Maximum initial deflection of the plating between longitudinal stiffeners:

$$w_{opl} = \begin{cases} 0.018\beta^2 t & \text{for slight level} \\ 0.096\beta^2 t & \text{for average level} \\ 0.252\beta^2 t & \text{for severe level} \end{cases} . \tag{4.1}$$

- Maximum column-type initial distortion of the stiffener:

$$w_{oc} = \begin{cases} 0.00016a & \text{for slight level} \\ 0.0018a & \text{for average level} \\ 0.0056a & \text{for severe level} \end{cases} . \tag{4.2}$$

- Maximum sideways initial distortion of the stiffener:

$$w_{os} = \begin{cases} 0.00019a & \text{for slight level} \\ 0.001a & \text{for average level} \\ 0.0024a & \text{for severe level} \end{cases} . \tag{4.3}$$

- Compressive residual stress in the plating:

$$\sigma_{rcx} = \begin{cases} -0.110\sigma_{Yp} & \text{for slight level} \\ -0.161\sigma_{Yp} & \text{for average level} \\ -0.216\sigma_{Yp} & \text{for severe level} \end{cases} . \tag{4.4}$$

- Compressive residual stress in the stiffener web:

$$\sigma_{rcx} = \begin{cases} -0.078\sigma_{Ys} & \text{for slight level} \\ -0.137\sigma_{Ys} & \text{for average level} \\ -0.195\sigma_{Ys} & \text{for severe level} \end{cases} . \tag{4.5}$$

- Reduced yield strength in the softened zone (5083-H116):

$$\frac{\sigma_{YHAZ}}{\sigma_Y} = \begin{cases} 0.906 & \text{for slight level} \\ 0.777 & \text{for average level} \\ 0.437 & \text{for severe level} \end{cases} . \tag{4.6}$$

- Reduced yield strength in the softened zone (5383-H112):

$$\frac{\sigma_{YHAZ}}{\sigma_Y} = 0.891 \text{ for average level.} \tag{4.7}$$

- Reduced yield strength in the softened zone (5383-H116):

$$\frac{\sigma_{YHAZ}}{\sigma_Y} = \begin{cases} 0.820 \text{ for slight level} \\ 0.774 \text{ for average level.} \\ 0.640 \text{ for severe level} \end{cases} \tag{4.8}$$

- Reduced yield strength in the softened zone (6082-T6):

$$\frac{\sigma_{YHAZ}}{\sigma_Y} = 0.703 \text{ for average level.} \tag{4.9}$$

- Half of the softened zone breadth:

$$b_{HAZ} = b_t = \begin{cases} 11.3\,\text{mm for slight level} \\ 23.1\,\text{mm for average level.} \\ 29.9\,\text{mm for severe level} \end{cases} \tag{4.10}$$

4.3 Initial Distortions

The three types of initial distortions, i.e., plate initial deflections, column-type initial distortions of the stiffeners, and sideways initial distortions of the stiffeners, were measured at various locations on the structures at intervals of 50 mm.

Figure 4.3 shows photos of the initial distortion measurements. Figure 4.4 presents three-dimensional displays of the initial distortion measurements for the plating and stiffeners in the test structures, where the measured values of the initial distortions were amplified by 30 times. Figure 4.5 depicts the initial distortion patterns for the plating and stiffeners at y = 0mm (the end of the structure) and y = 600mm (mid-span). It can be observed from Figure 4.5 that the initial distortions in the fusion-welded structures (19A, 20A) generally tended to be more severe than those in the FSW structures. It is also interesting to note that the initial distortions of the FSW butt-joined structures (19C, 20C) were more severe than those of the FSW lap-joined structures.

Figure 4.6 presents the details of the initial distortion measurements, and Table 4.1 lists the maximum values of the initial distortions in the plating and stiffeners. The acceptance tolerances of the weld-induced initial distortions in aluminum structures, as specified by classification society rules (ABS 2006), are also compared in this table, indicating that the maximum initial distortions in the test structures were within these tolerances.

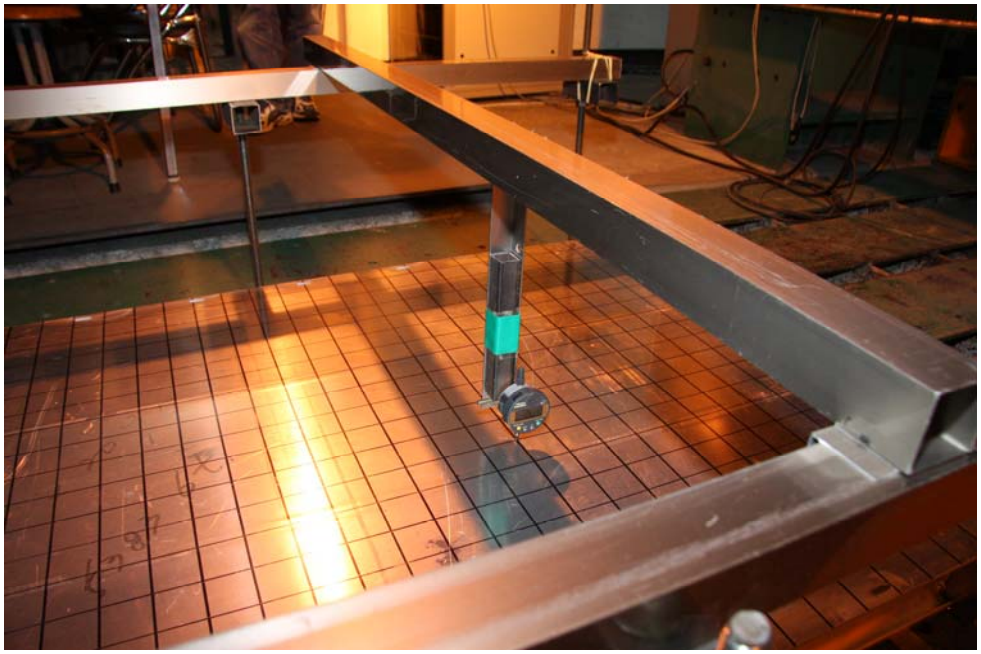

Figure 4.3 (a) Photo of the set-up for the plate initial deflection measurements

Figure 4.3(b) Photo of the set-up for the stiffener initial distortion measurements

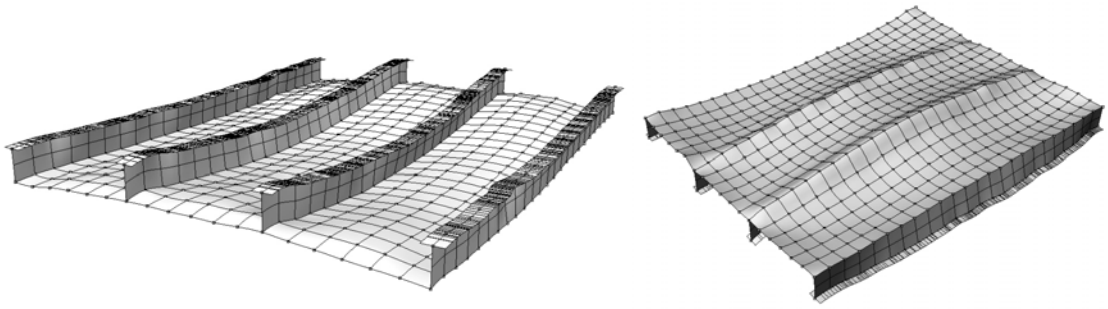

Figure 4.4(a) Three-dimensional display of initial distortions (amplified by 30 times) in test structure 19A

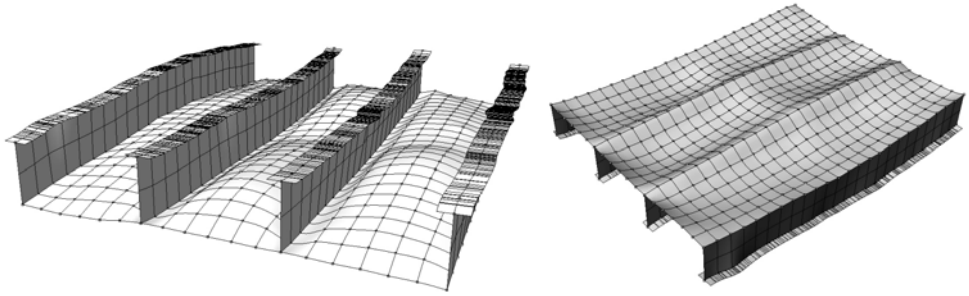

Figure 4.4(b) Three-dimensional display of initial distortions (amplified by 30 times) in test structure 20A

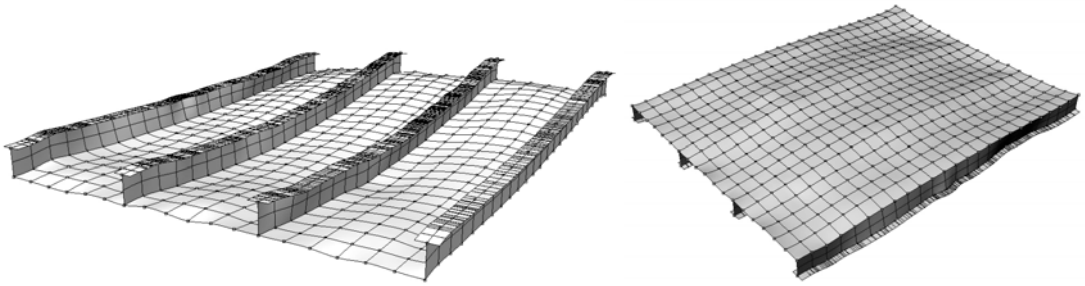

Figure 4.4(c) Three-dimensional display of initial distortions (amplified by 30 times) in test structure 17D

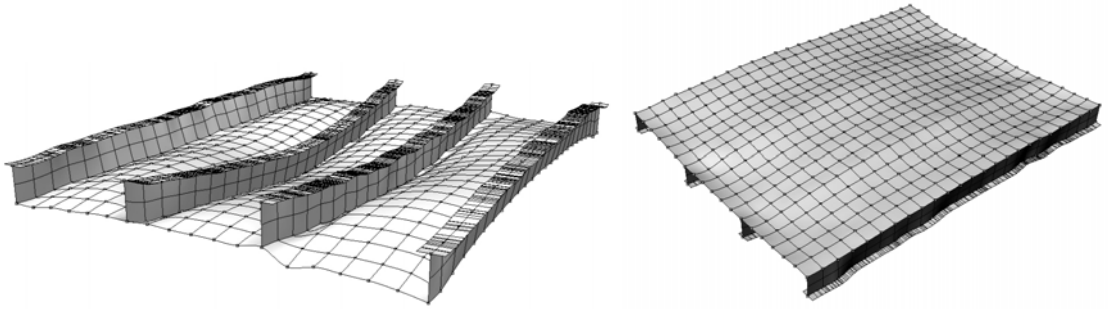

Figure 4.4(d) Three-dimensional display of initial distortions (amplified by 30 times) in test structure 18D

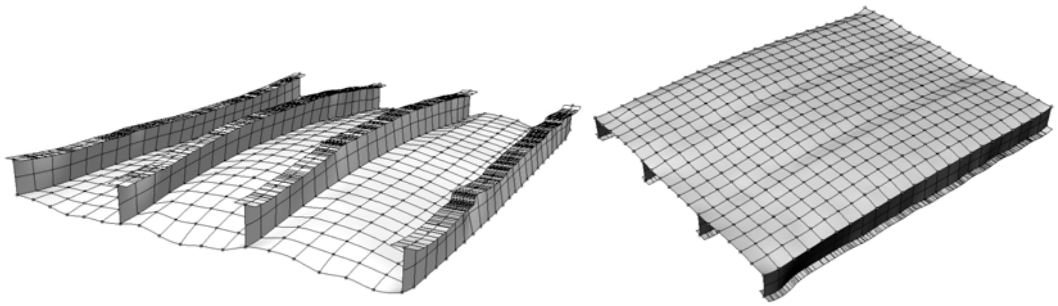

Figure 4.4(e) Three-dimensional display of initial distortions (amplified by 30 times) in test structure 19D1

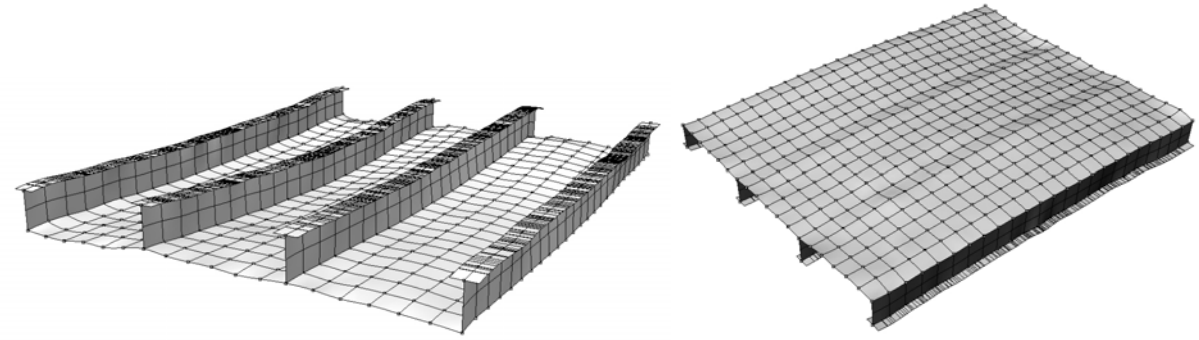

Figure 4.4(f) Three-dimensional display of initial distortions (amplified by 30 times) in test structure 19D2

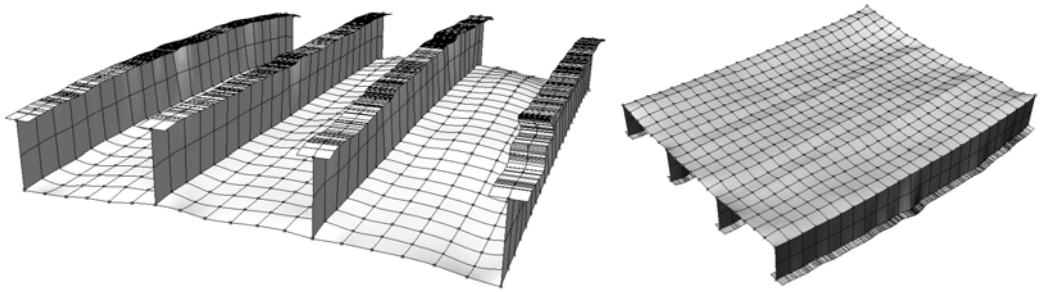

Figure 4.4(g) Three-dimensional display of initial distortions (amplified by 30 times) in test structure 20D1

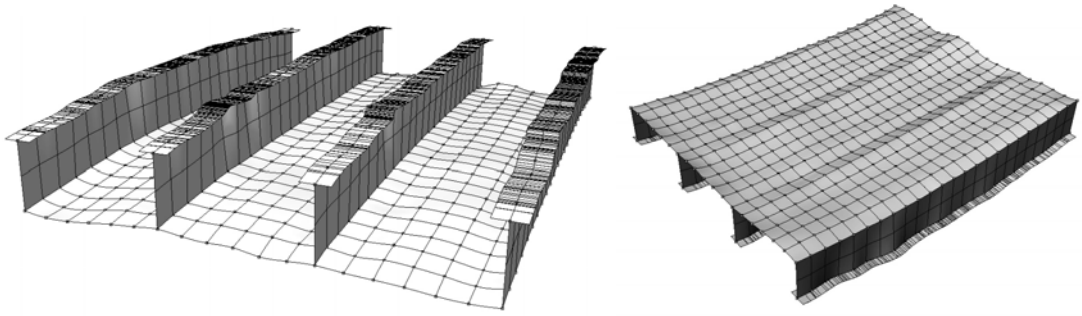

Figure 4.4(h) Three-dimensional display of initial distortions (amplified by 30 times) in test structure 20D2

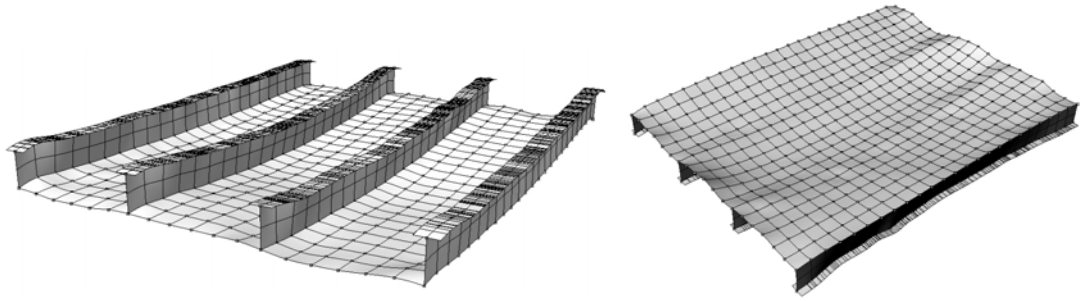

Figure 4.4(i) Three-dimensional display of initial distortions (amplified by 30 times) in test structure 19C

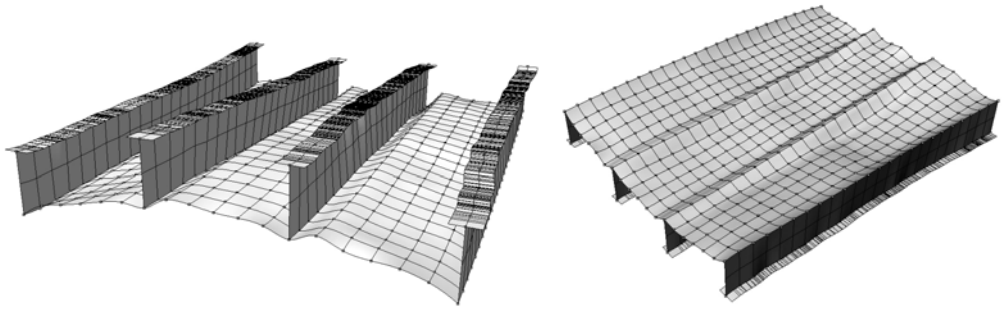

Figure 4.4(j) Three-dimensional display of initial distortions (amplified by 30 times) in test structure 20C

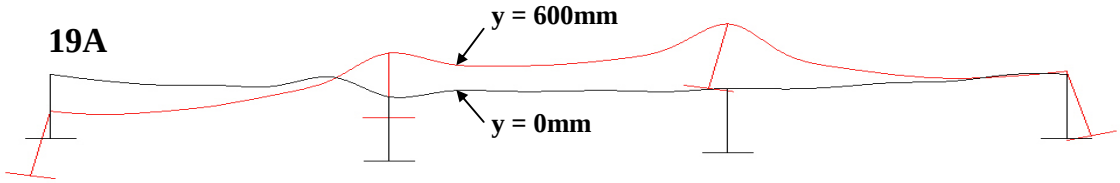

Figure 4.5(a) Shape of initial distortions (amplified by 30 times) for the plating and stiffeners in test structure 19A

Figure 4.5(b) Shape of initial distortions (amplified by 30 times) for the plating and stiffeners in test structure 20A

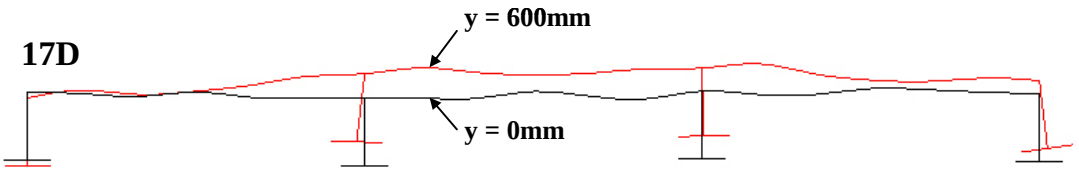

Figure 4.5(c) Shape of initial distortions (amplified by 30 times) for the plating and stiffeners in test structure 17D

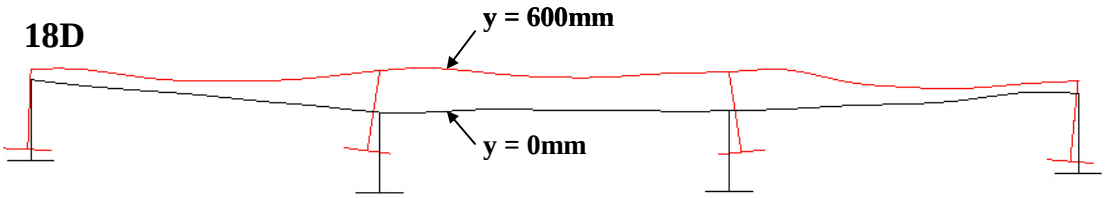

Figure 4.5(d) Shape of initial distortions (amplified by 30 times) for the plating and stiffeners in test structure 18D

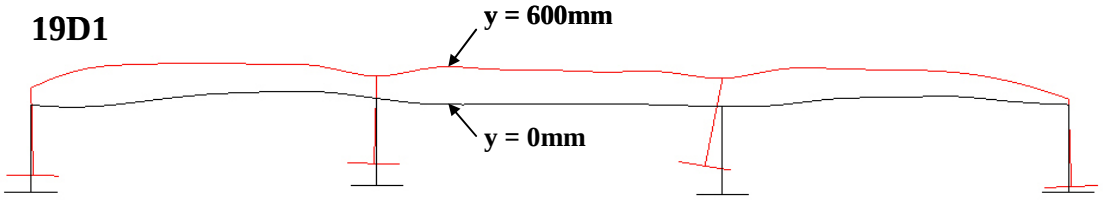

Figure 4.5(e) Shape of initial distortions (amplified by 30 times) for the plating and stiffeners in test structure 19D1

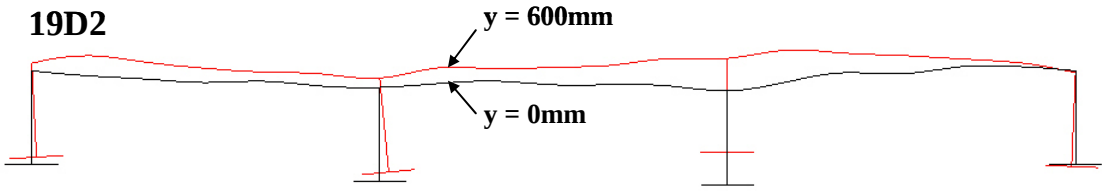

Figure 4.5(f) Shape of initial distortions (amplified by 30 times) for the plating and stiffeners in test structure 19D2

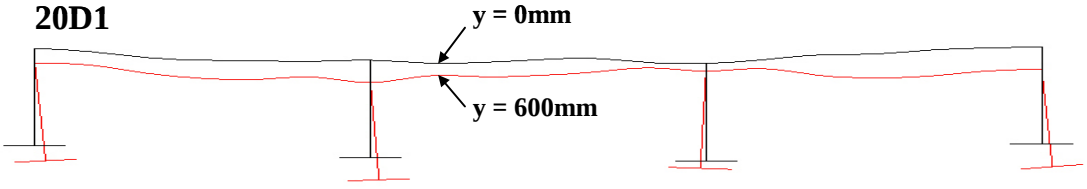

Figure 4.5(g) Shape of initial distortions (amplified by 30 times) for the plating and stiffeners in test structure 20D1

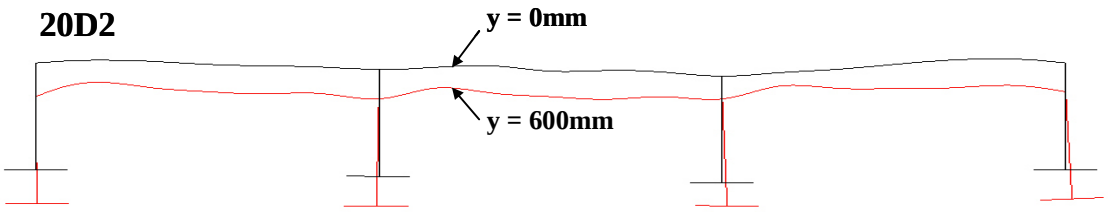

Figure 4.5(h) Shape of initial distortions (amplified by 30 times) for the plating and stiffeners in test structure 20D2

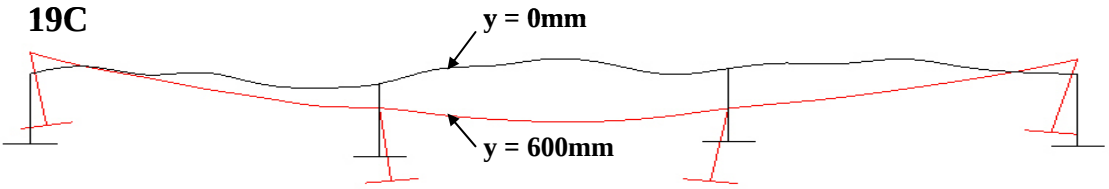

Figure 4.5(i) Shape of initial distortions (amplified by 30 times) for the plating and stiffeners in test structure 19C

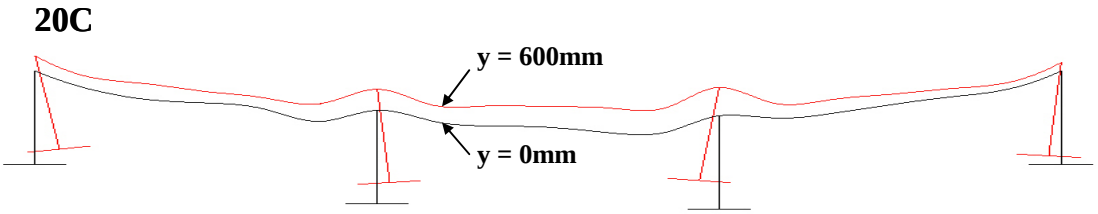

Figure 4.5(j) Shape of initial distortions (amplified by 30 times) for the plating and stiffeners in test structure 20C

Table 4.1 Maximum values of the initial distortion measurements in the plating and stiffeners, together with the ABS rule requirements for tolerance

Model	w_{opl} (mm)	w_{oc} (mm)	w_{os} (mm)	Tolerance (mm)	
				Plate	Stiffener
19A	-1.254	-1.527	-0.635	4.76	7.95
	0.899	1.710	-0.252		
	-0.751	2.457	-0.629		
		0.190	0.950		
20A	-1.825	-0.882	-0.554	4.76	4.54
	-1.474	0.801	-0.600		
	-1.471	0.841	0.357		
		-1.568	-0.295		
17D	0.722	-1.428	0.171	4.76	10.6
	1.123	-0.832	-0.316		
	0.702	0.988	0.287		
		-0.544	0.539		
18D	0.834	-0.614	0.426	4.76	9.09
	1.110	1.396	-0.455		
	0.573	1.064	0.485		
		-0.475	-0.433		
19D1	1.098	0.561	0.227	4.76	7.95
	1.180	1.120	-0.300		
	0.934	-0.779	-0.542		
		-0.384	-0.412		
19D2	-1.153	-0.731	0.739	4.76	7.95
	-0.471	-0.773	0.565		
	-0.920	-0.356	-0.309		
		-1.163	0.714		
20D1	0.692	-0.469	0.262	4.76	4.54
	0.823	0.452	0.380		
	0.878	1.222	0.091		
		-0.976	-0.234		
20D2	-0.831	-1.640	0.294	4.76	4.54
	-0.702	-1.281	0.419		
	-0.723	-0.666	0.471		
		-1.290	0.432		
19C	-0.68	0.867	0.742	4.76	7.95
	-2.053	-1.077	0.444		
	-1.104	-1.525	-0.583		
		0.579	-0.774		
20C	-0.381	0.802	0.862	4.76	4.54
	-0.753	-0.459	0.589		
	-0.872	-0.250	-0.682		
		0.466	-0.448		

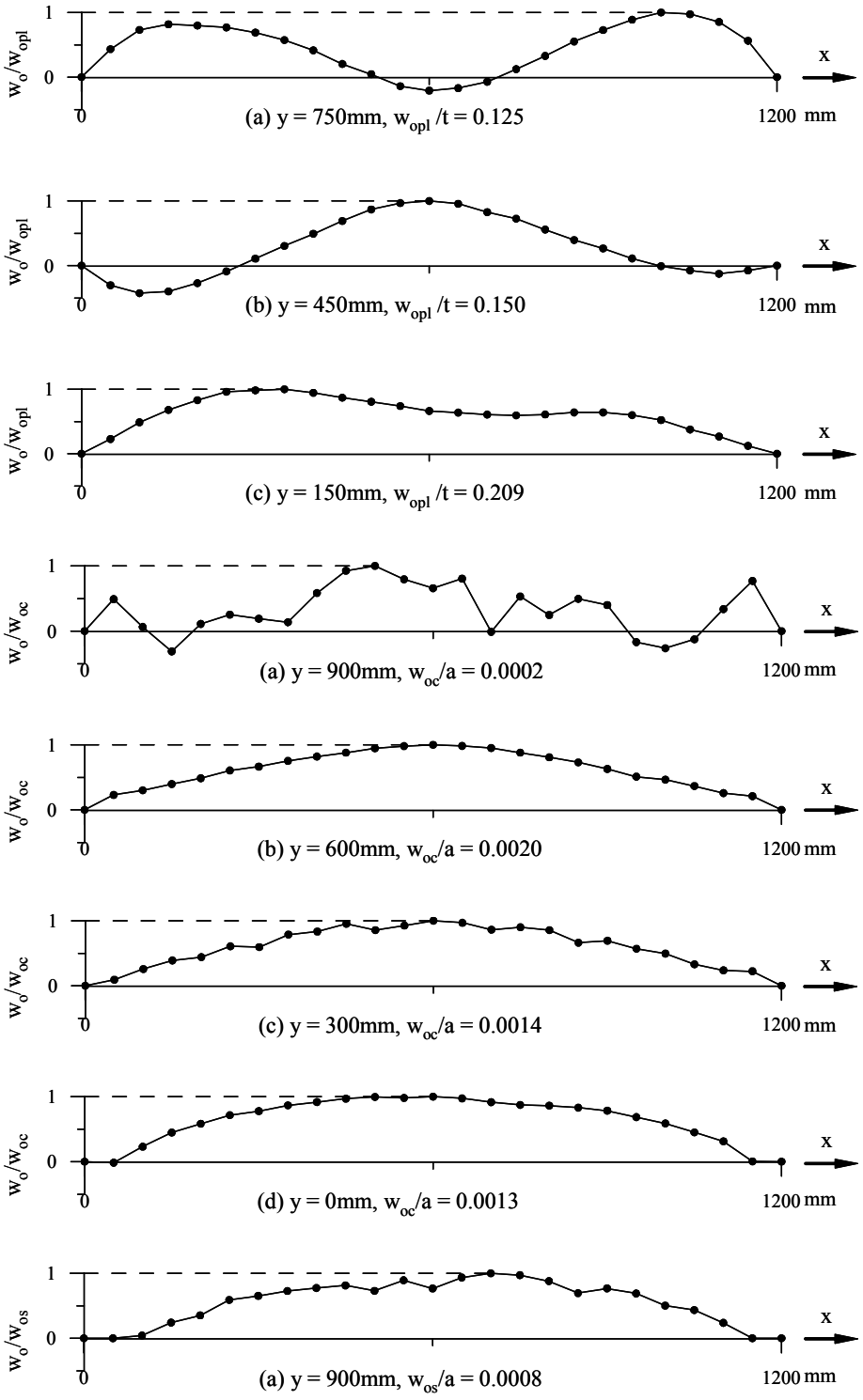
1
0
w_o/w_{opl}
x
0
1200 mm
(a) y = 750mm, w_{opl} /t = 0.125
(b) y = 450mm, w_{opl} /t = 0.150
(c) y = 150mm, w_{opl} /t = 0.209
w_o/w_{oc}
(a) y = 900mm, w_{oc}/a = 0.0002
(b) y = 600mm, w_{oc}/a = 0.0020
(c) y = 300mm, w_{oc}/a = 0.0014
(d) y = 0mm, w_{oc}/a = 0.0013
w_o/w_{os}
(a) y = 900mm, w_{os}/a = 0.0008

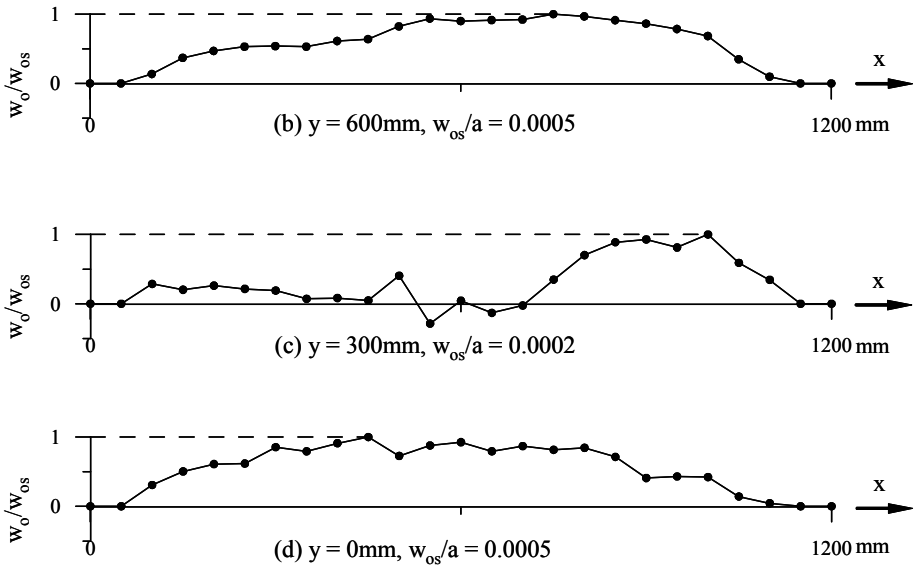

Figure 4.6(a) Details of initial distortion measurements in test structure 19A

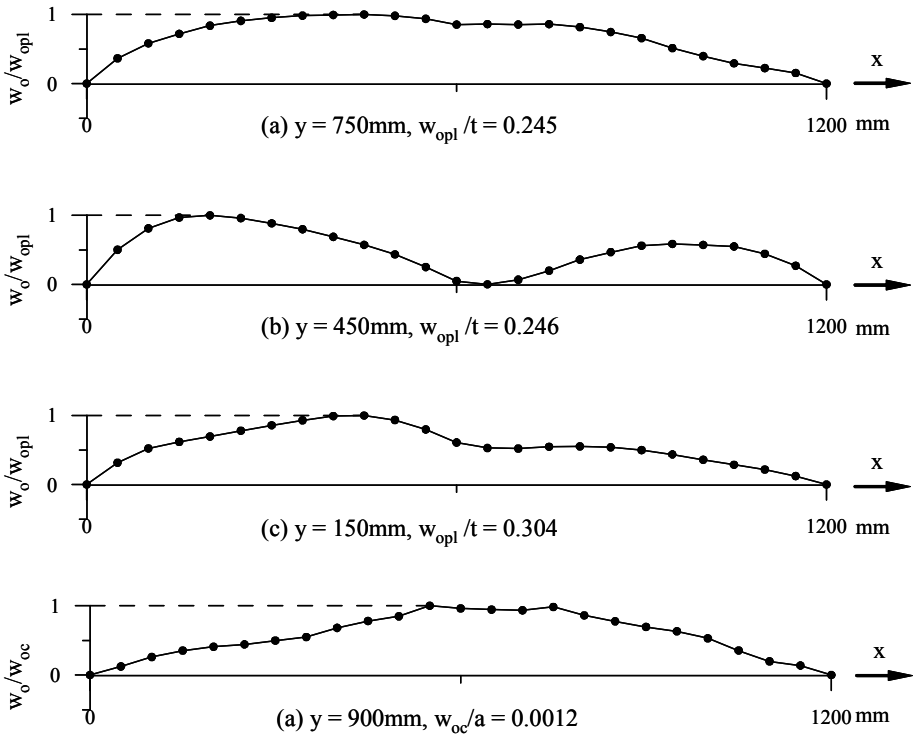

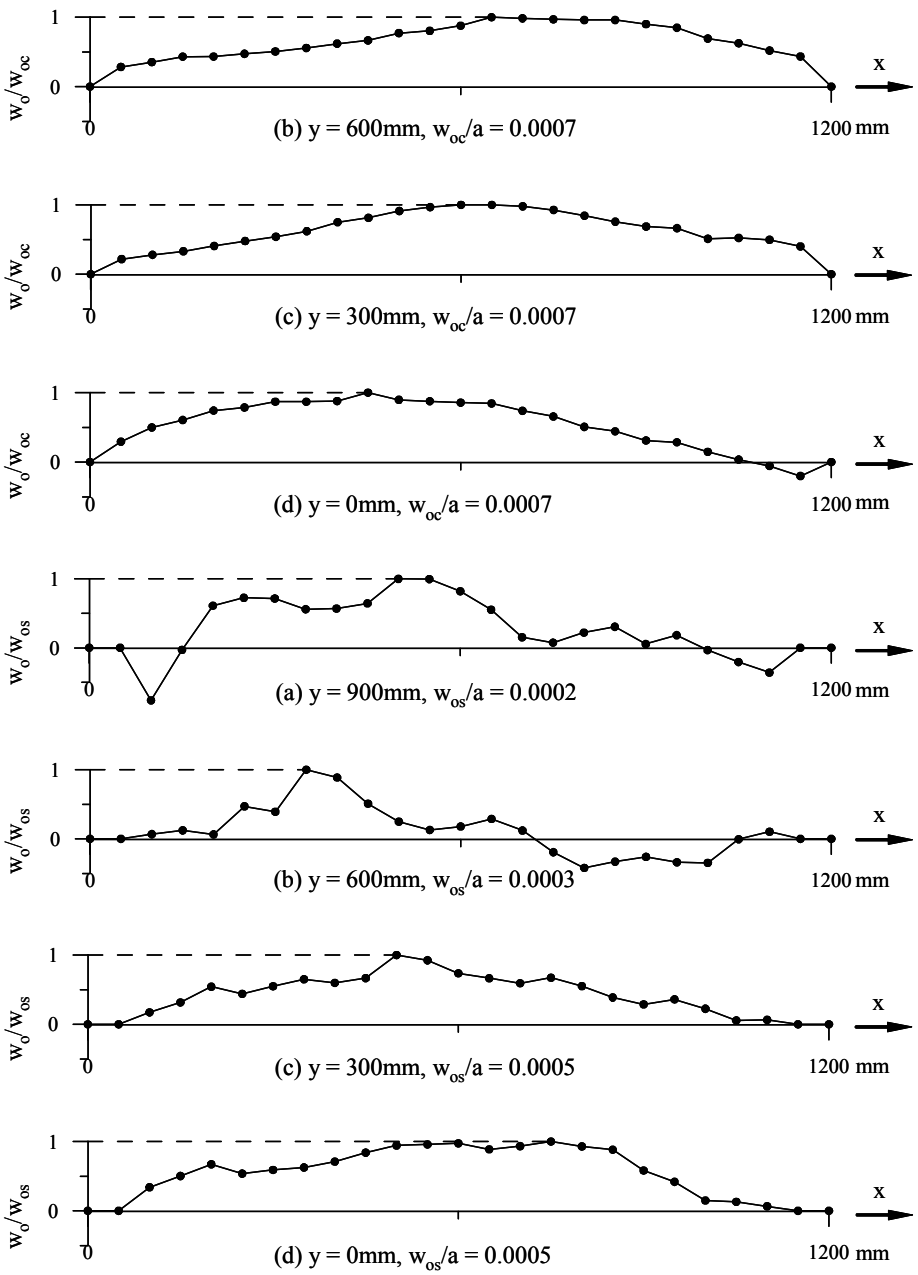

Figure 4.6(b) Details of initial distortion measurements in test structure 20A

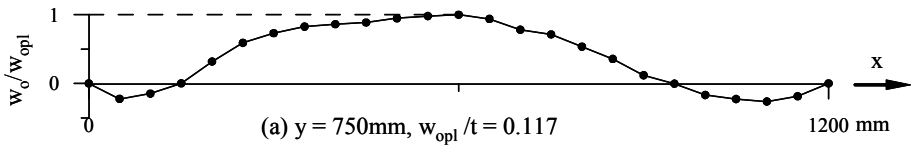

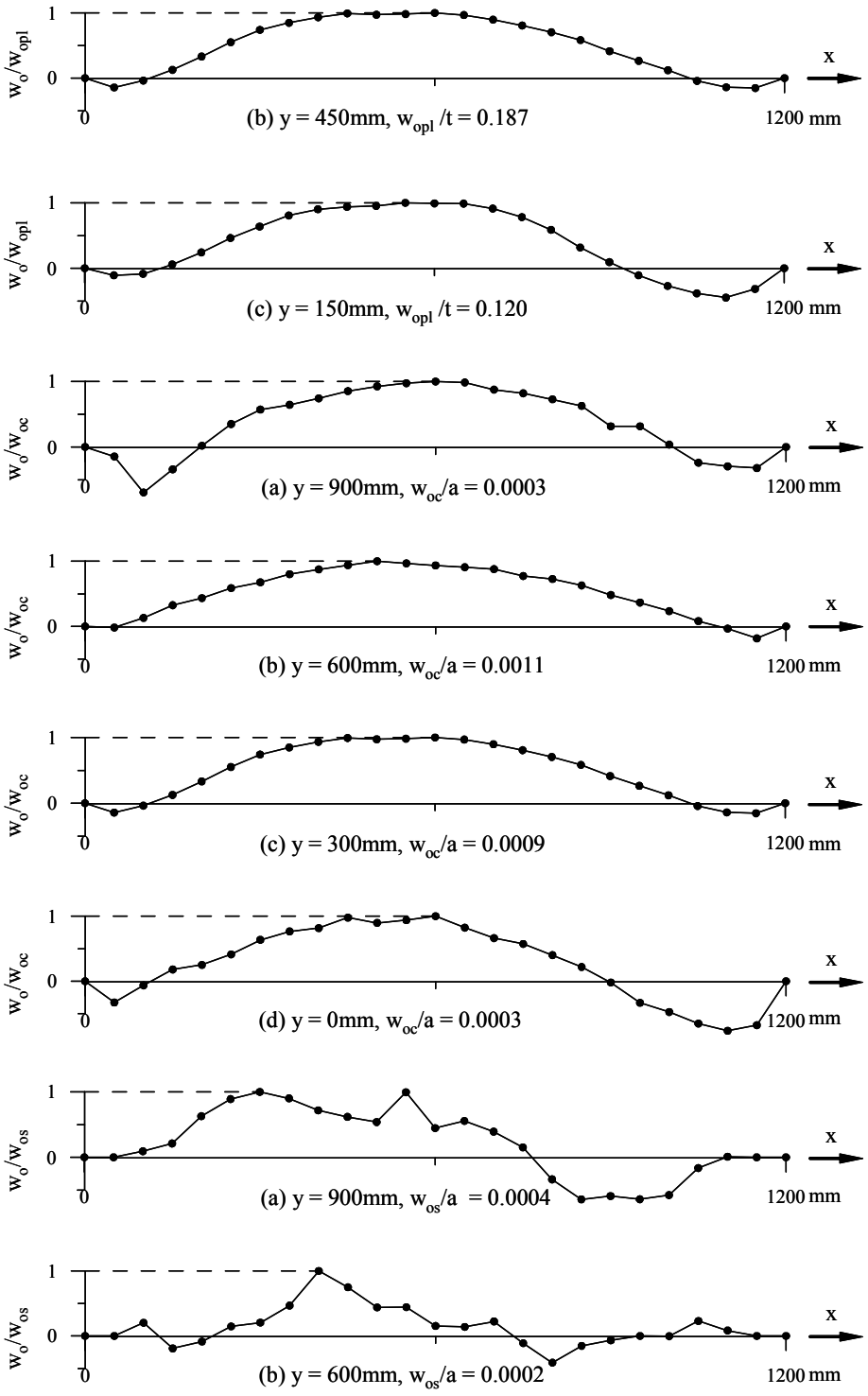
1
0
w_o/w_{opl}
x
0
1200 mm
(b) y = 450mm, $w_{opl}/t = 0.187$
(c) y = 150mm, $w_{opl}/t = 0.120$
w_o/w_{oc}
(a) y = 900mm, $w_{oc}/a = 0.0003$
(b) y = 600mm, $w_{oc}/a = 0.0011$
(c) y = 300mm, $w_{oc}/a = 0.0009$
(d) y = 0mm, $w_{oc}/a = 0.0003$
w_o/w_{os}
(a) y = 900mm, $w_{os}/a = 0.0004$
(b) y = 600mm, $w_{os}/a = 0.0002$

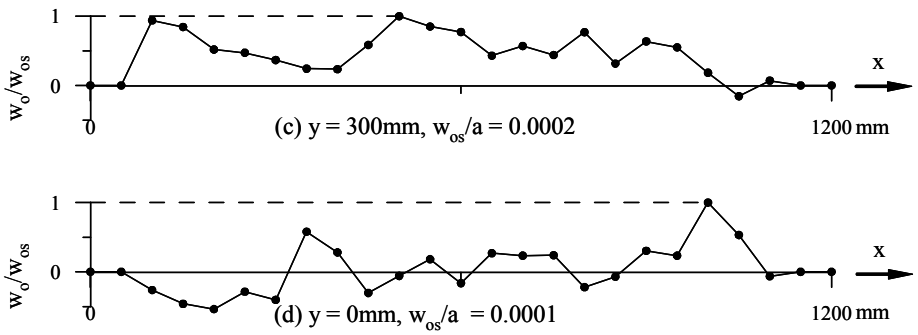

Figure 4.6(c) Details of initial distortion measurements in the test structure 17D

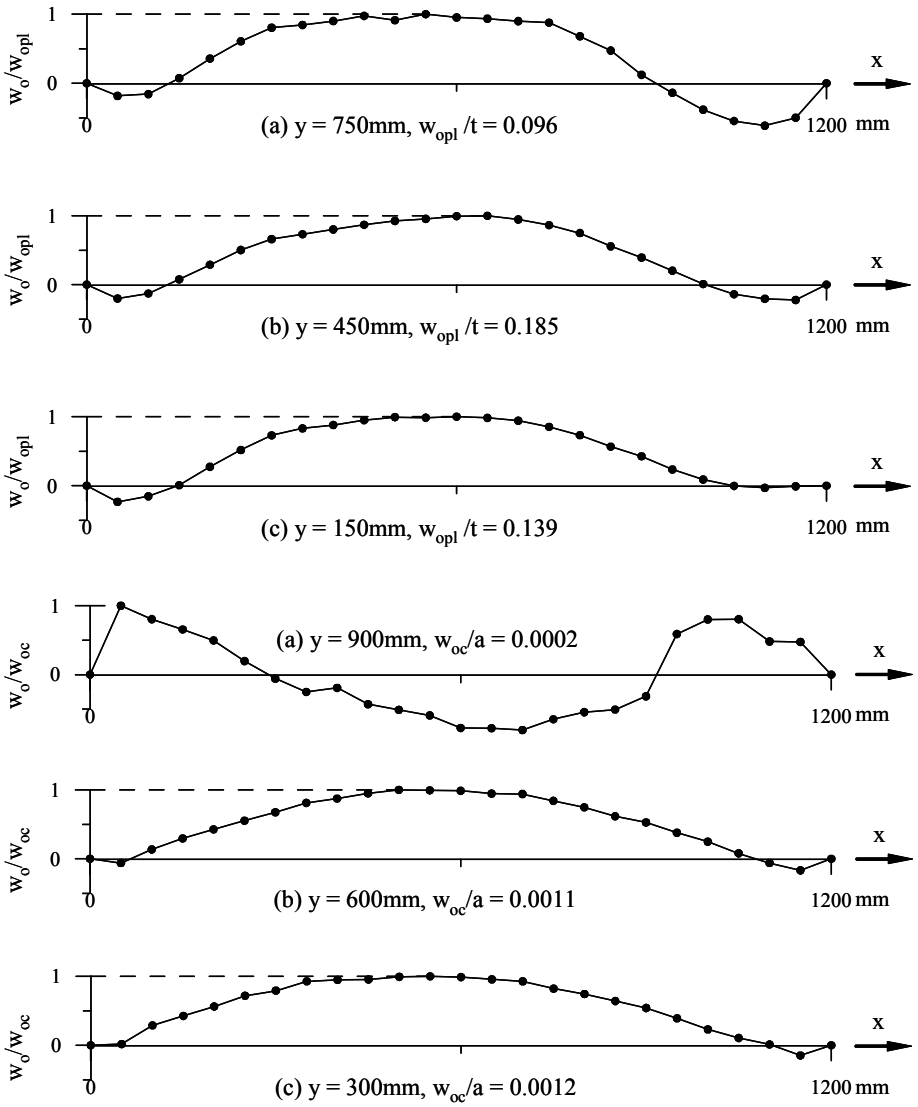

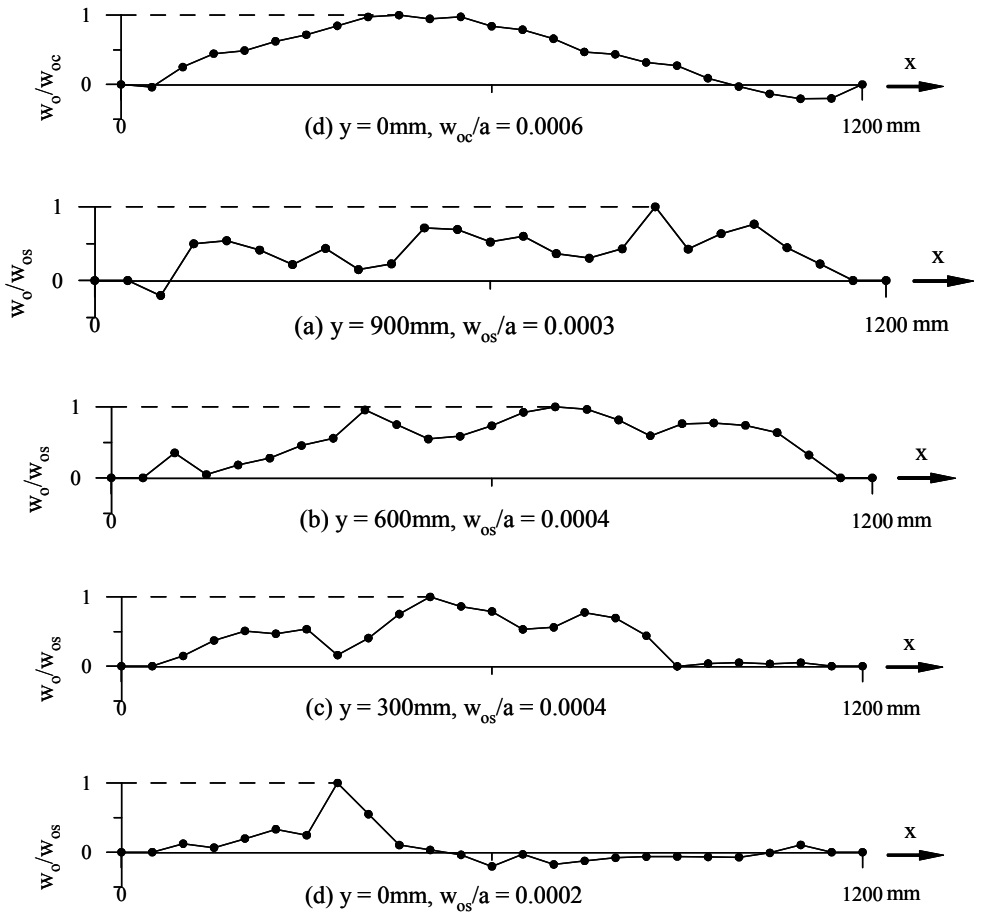

Figure 4.6(d) Details of initial distortion measurements in test structure 18D

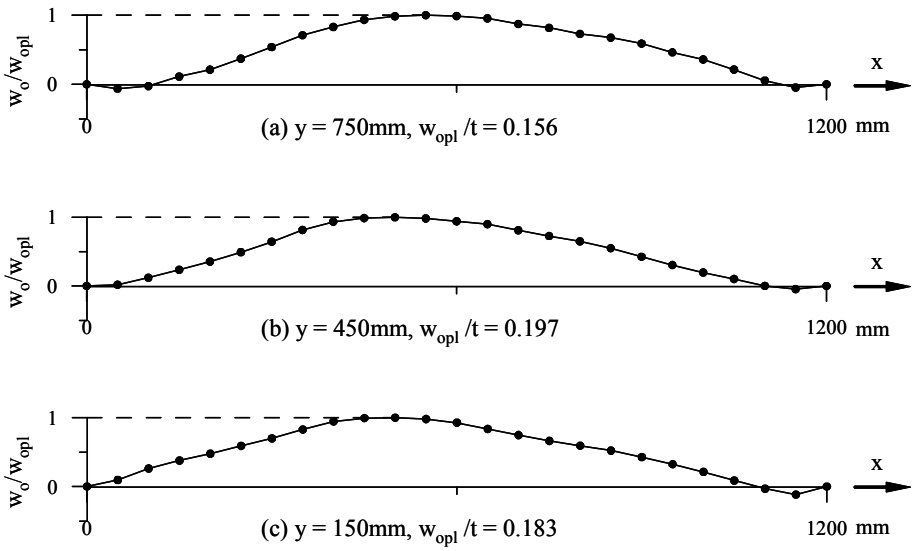

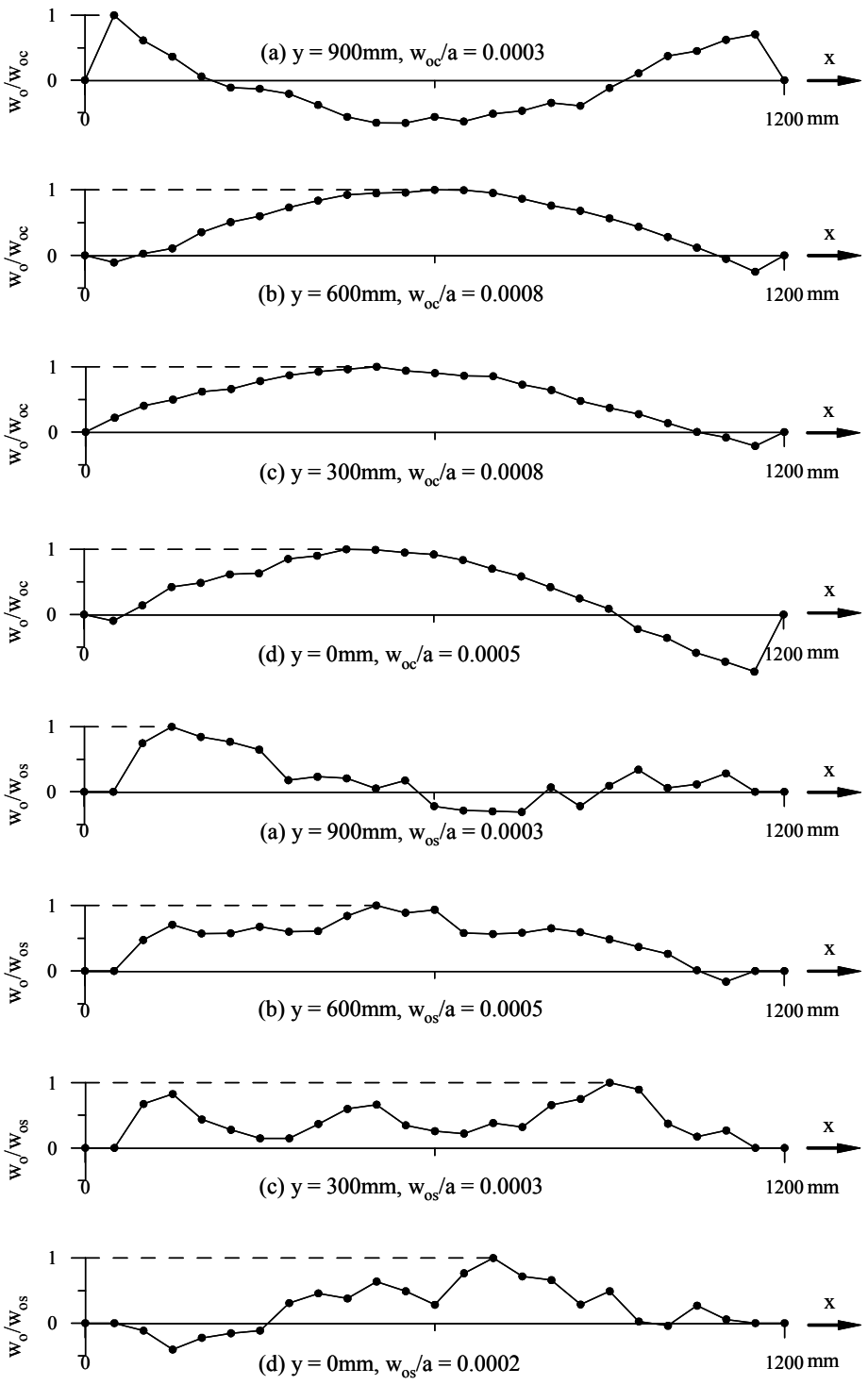

Figure 4.6(e) Details of initial distortion measurements in test structure 19D1

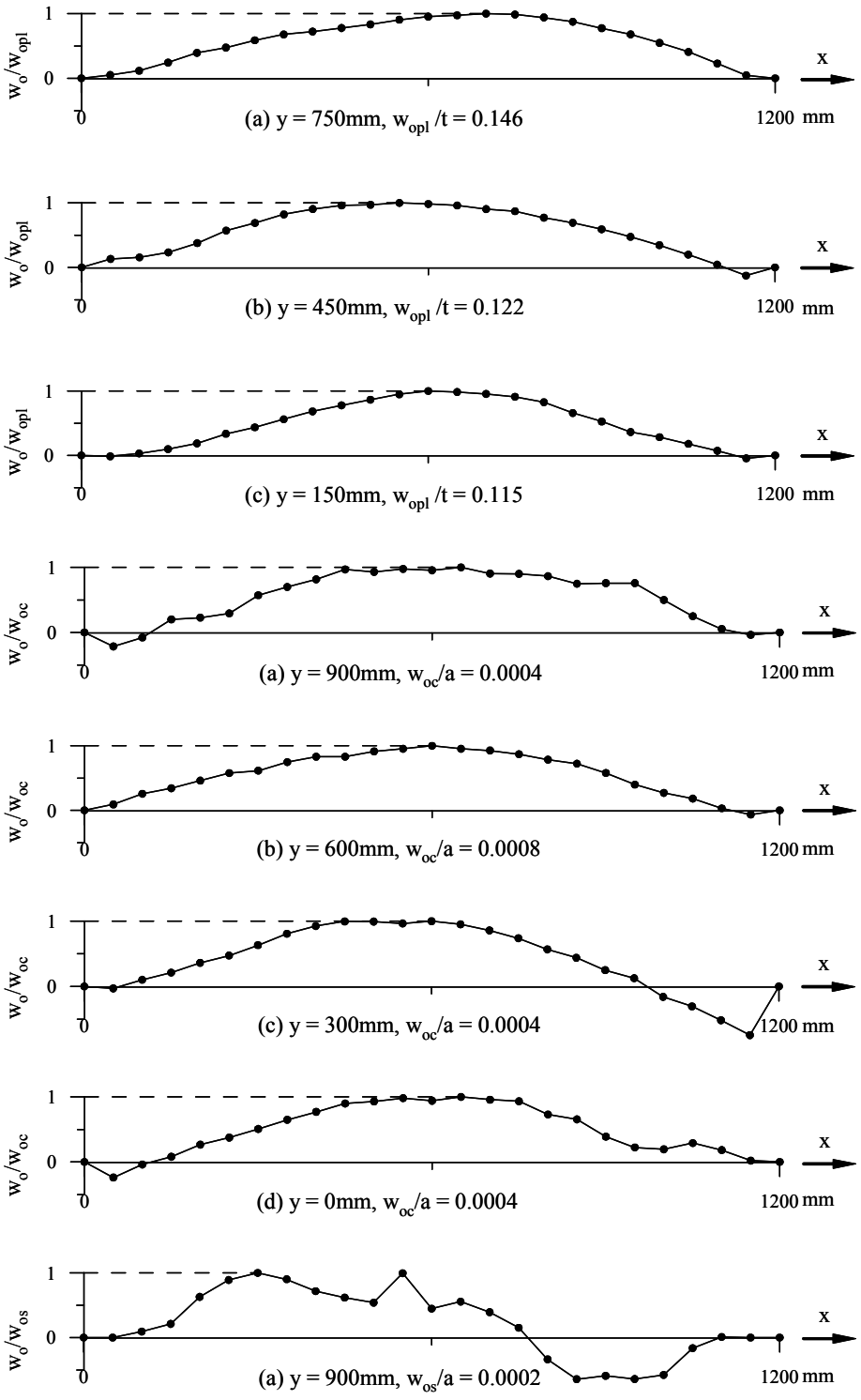
1
0
w_o/w_{opl}
x
0
1200 mm
(a) y = 750mm, w_{opl} /t = 0.146
(b) y = 450mm, w_{opl} /t = 0.122
(c) y = 150mm, w_{opl} /t = 0.115
w_o/w_{oc}
(a) y = 900mm, w_{oc}/a = 0.0004
(b) y = 600mm, w_{oc}/a = 0.0008
(c) y = 300mm, w_{oc}/a = 0.0004
(d) y = 0mm, w_{oc}/a = 0.0004
w_o/w_{os}
(a) y = 900mm, w_{os}/a = 0.0002

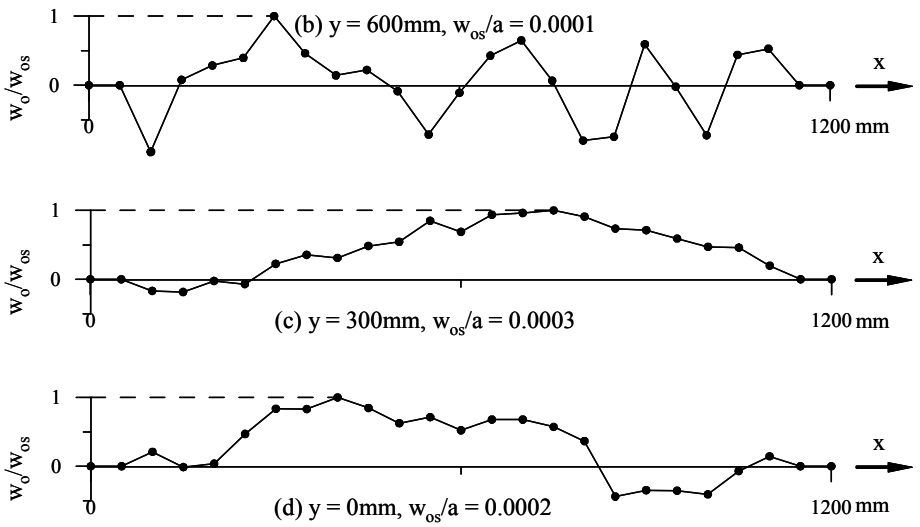

Figure 4.6(f) Details of initial distortion measurements in test structure 19D2

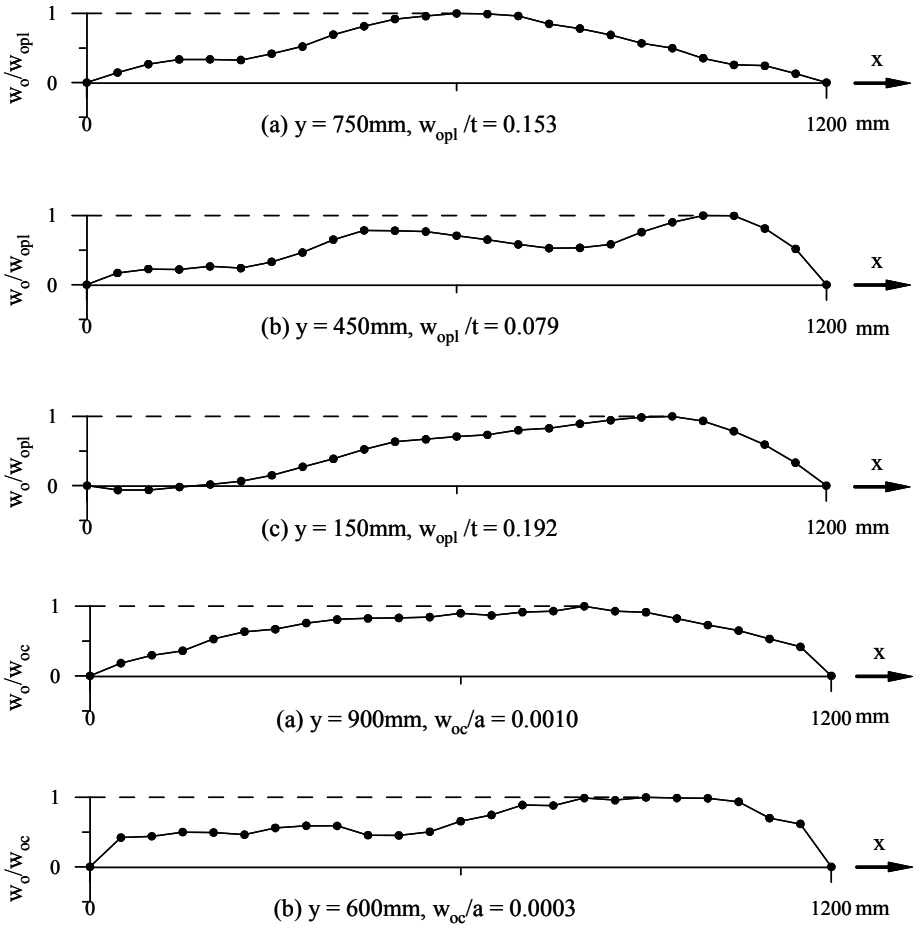

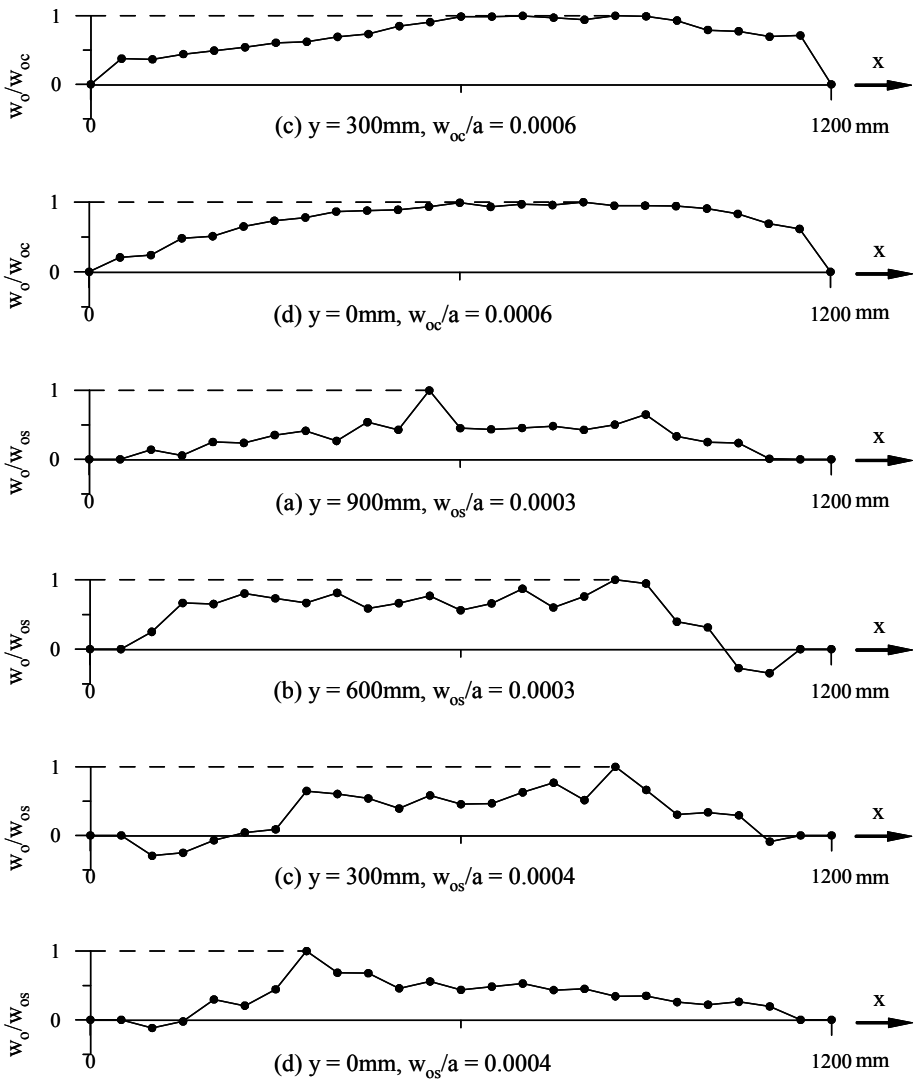

Figure 4.6(g) Details of initial distortion measurements in test structure 20D1

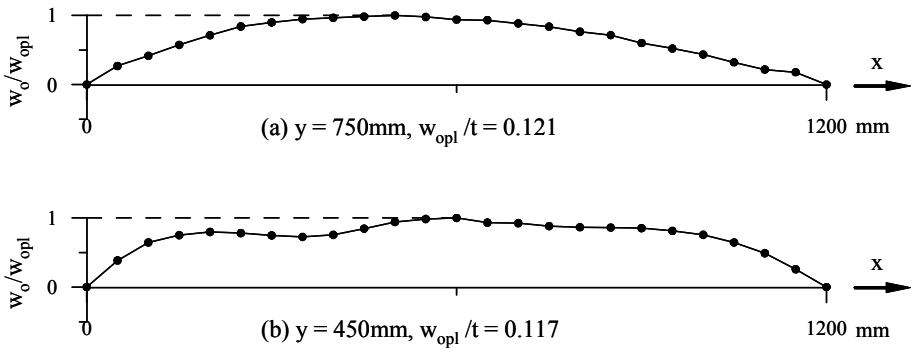

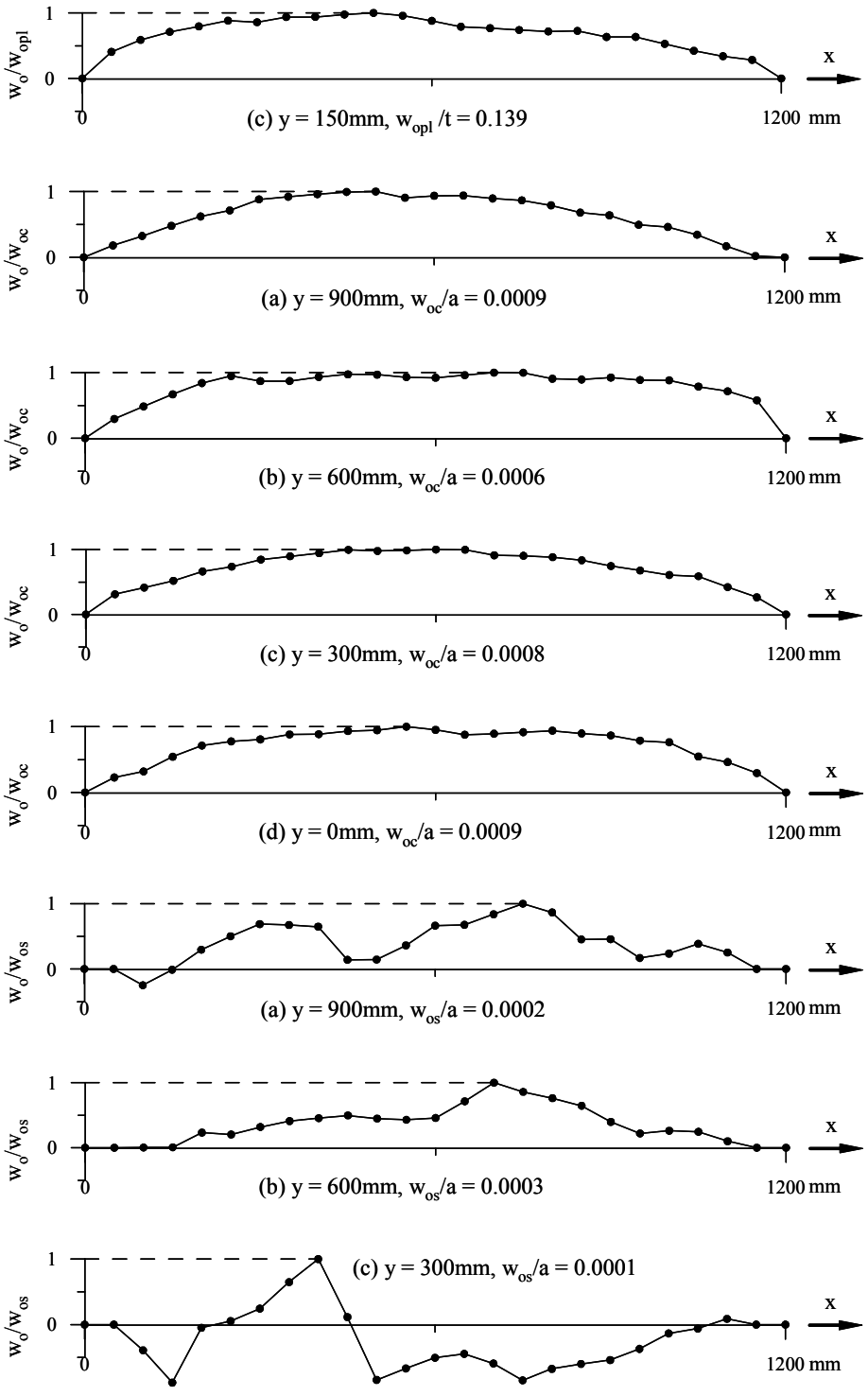
1
0
w_o/w_{opl}
x
0
1200 mm
(c) y = 150mm, w_{opl} /t = 0.139
w_o/w_{oc}
(a) y = 900mm, w_{oc}/a = 0.0009
(b) y = 600mm, w_{oc}/a = 0.0006
(c) y = 300mm, w_{oc}/a = 0.0008
(d) y = 0mm, w_{oc}/a = 0.0009
w_o/w_{os}
(a) y = 900mm, w_{os}/a = 0.0002
(b) y = 600mm, w_{os}/a = 0.0003
(c) y = 300mm, w_{os}/a = 0.0001

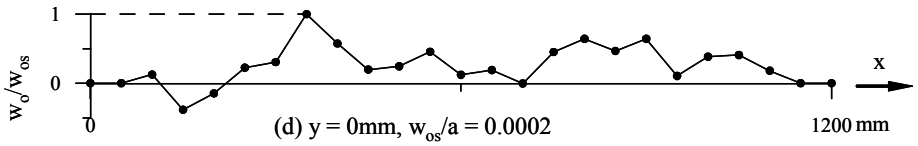

Figure 4.6(h) Details of initial distortion measurements in test structure 20D2

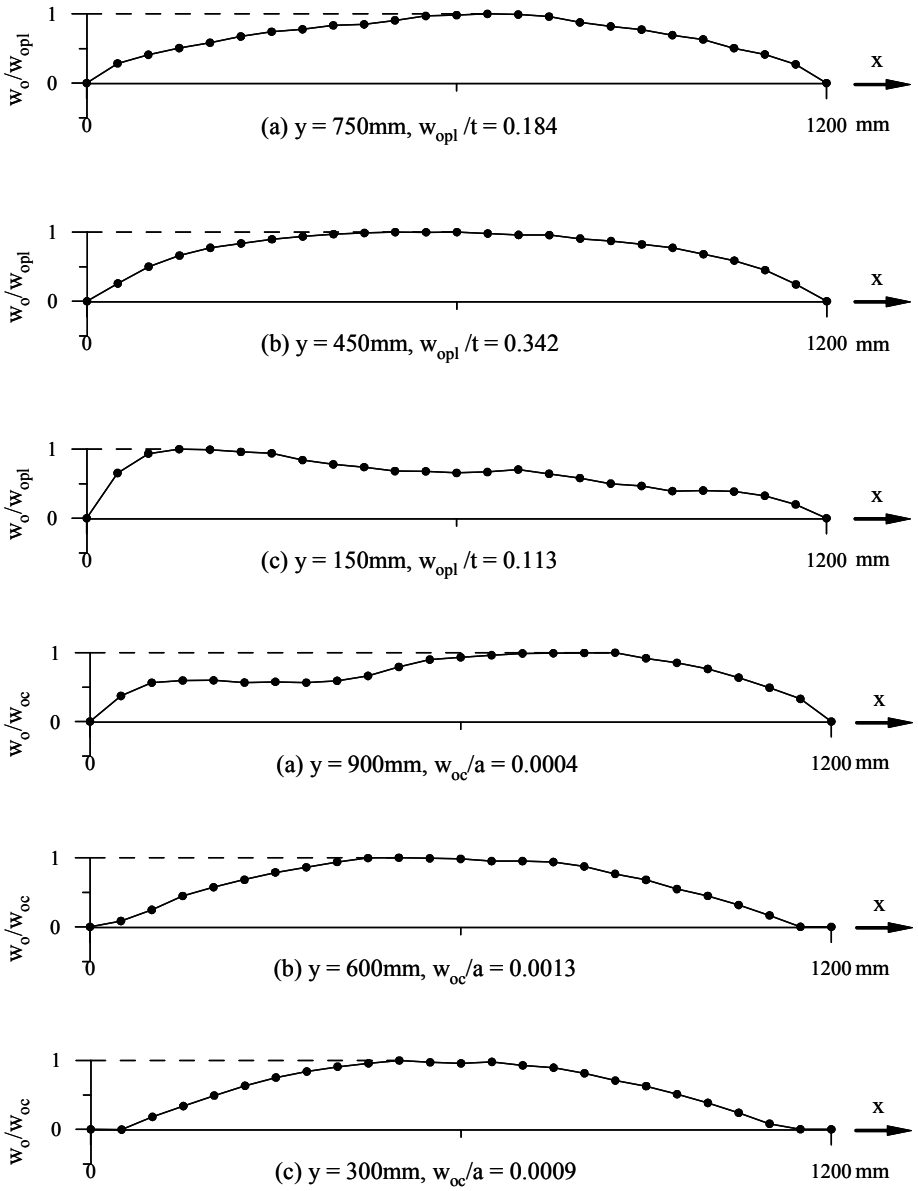

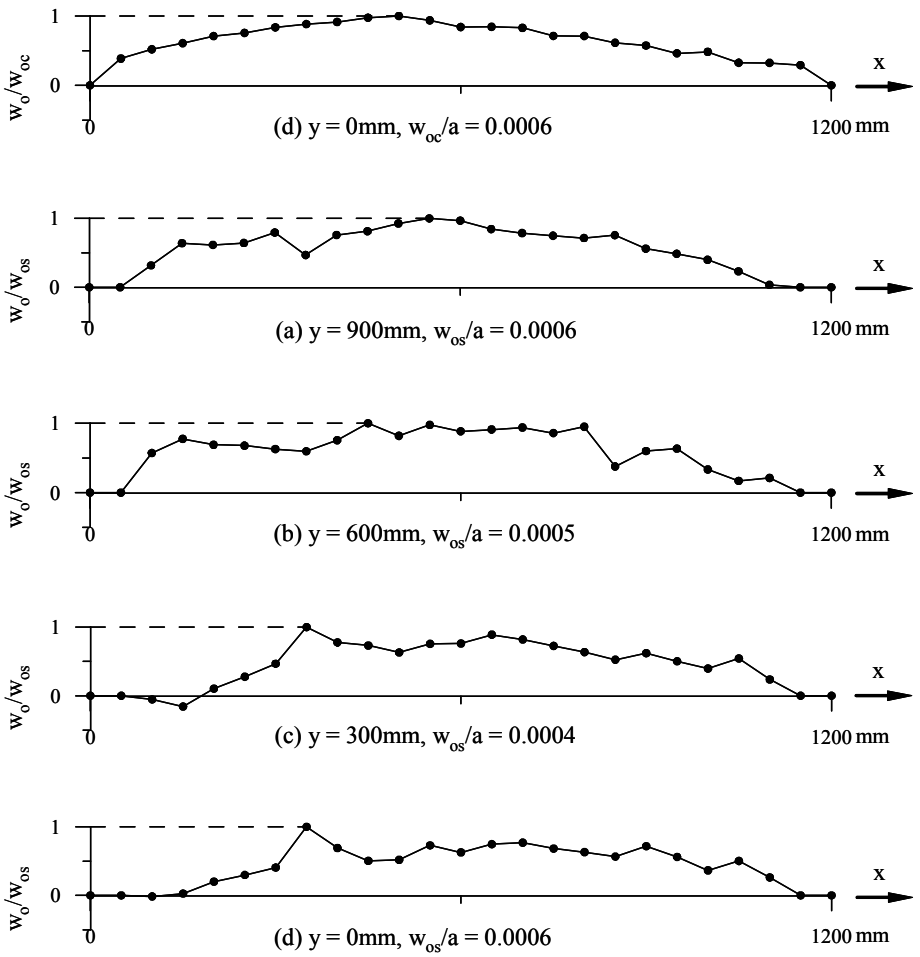

Figure 4.6(i) Details of initial distortion measurements in test structure 19C

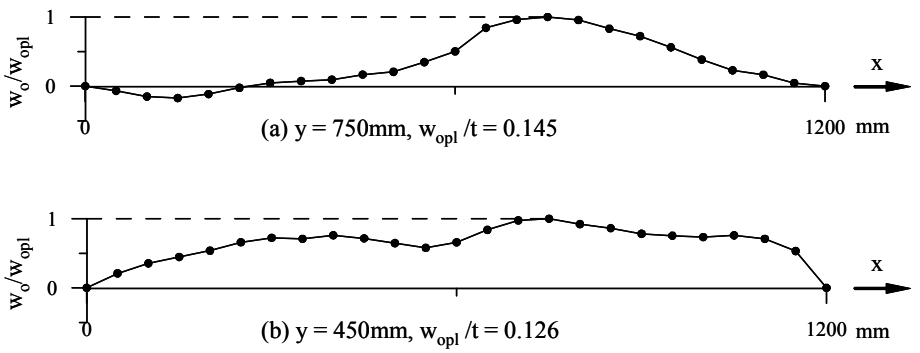

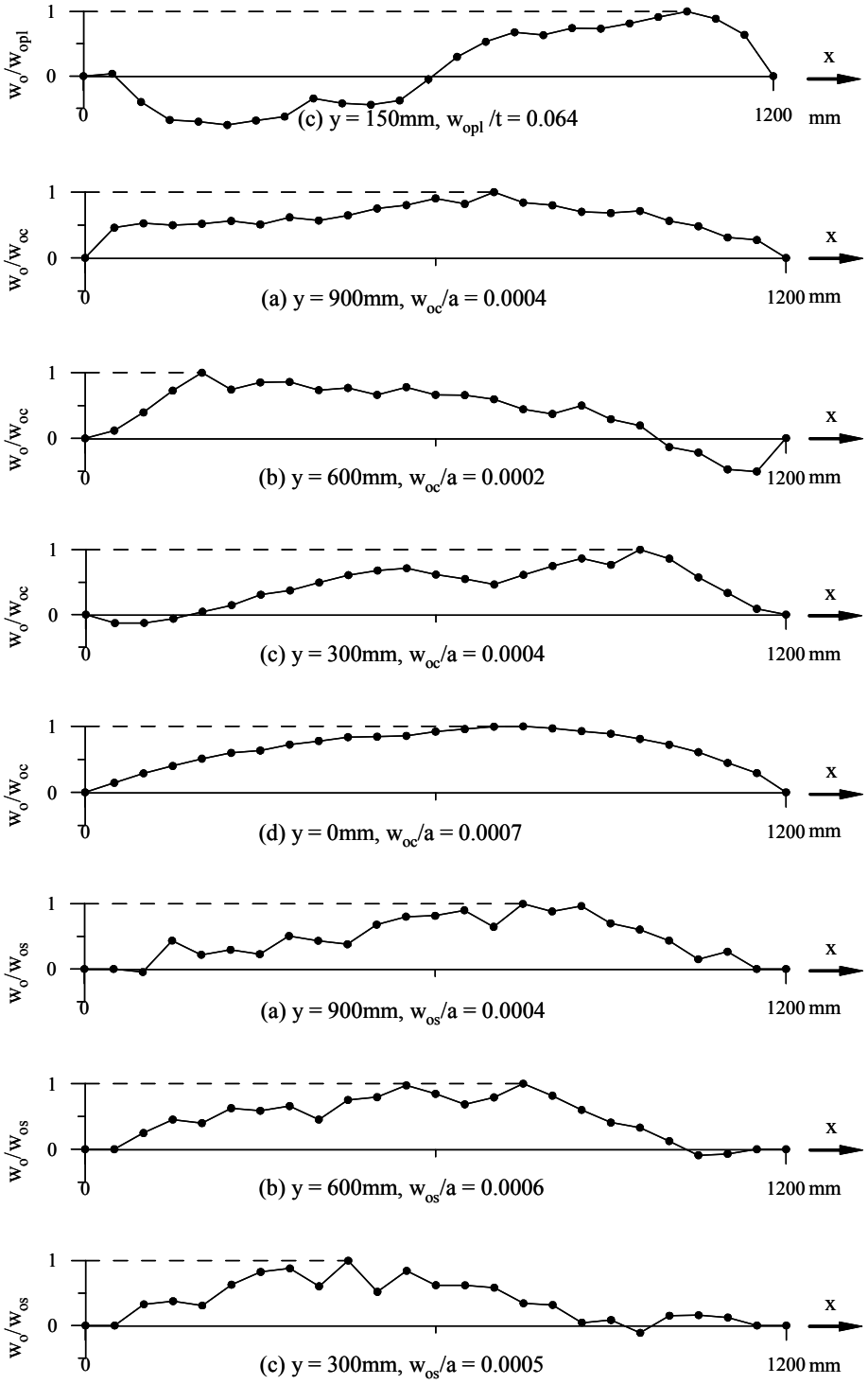
1
0
w_o/w_{opl}
x
0
1200 mm
(c) y = 150mm, w_{opl} /t = 0.064
w_o/w_{oc}
(a) y = 900mm, w_{oc}/a = 0.0004
(b) y = 600mm, w_{oc}/a = 0.0002
(c) y = 300mm, w_{oc}/a = 0.0004
(d) y = 0mm, w_{oc}/a = 0.0007
w_o/w_{os}
(a) y = 900mm, w_{os}/a = 0.0004
(b) y = 600mm, w_{os}/a = 0.0006
(c) y = 300mm, w_{os}/a = 0.0005

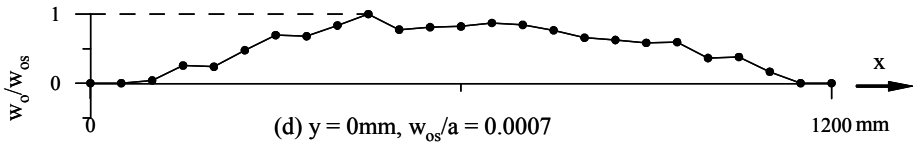

Figure 4.6(j) Details of initial distortion measurements in test structure 20C

4.4 Residual Stresses

The hole-drilling strain-gauge method (Inter Technology 2005) is the most widely-used modern technique applied today to measure residual stresses. Therefore, this method was employed to measure the weld-induced residual stresses in the test structures in the present study and those in SSC-451.

The residual stress measurement procedure involves the following six steps (Inter Technology 2005).

- Step 1: A special three- (or six-) element strain-gauge rosette is installed at the target location where the residual stresses are to be measured.
- Step 2: The gauge grids are wired and connected to a multi-channel static strain indicator or through a switch-and-balance unit (six-element gauge).
- Step 3: A precision milling guide is attached to the test part and accurately centered over a drilling target on the rosette.
- Step 4: After zero-balancing the gauge circuits, a small, shallow hole is drilled through the geometric center of the rosette.
- Step 5: Readings are taken of the relaxed strains that correspond to the residual stress.
- Step 6: Using special data-reduction relationships, the principal residual stresses and their angular orientations are calculated from these measured strains.

Figure 4.7 shows the residual stress measurement set-up using the hole-drilling strain-gauge method. With regard to Step 4, the hole was drilled in the target location up to a depth of 2.3 mm in the plate thickness direction where the released strain became almost constant. Figure 4.8 shows typical examples of the relationship between the drilling depth and the released strain in the panel longitudinal direction at a location in the compressive residual stress zone.

It was found that there is no change in the released strain after a drilling depth of 2.0 mm, regardless of the fabrication method used. It is also interesting to note that this strain (and the subsequent compressive residual stress) was greater in the following order: GMAW (19A), FSW (19D2) and FSW (19C).

Figure 4.9 shows the residual stress distributions, both measured and as idealized for the test structures. The idealized distributions of the residual stress were determined based on the hypothesis that the compressive residual stress must be in equilibrium with the tensile residual stress over the cross-sectional area in the plating or stiffener web.

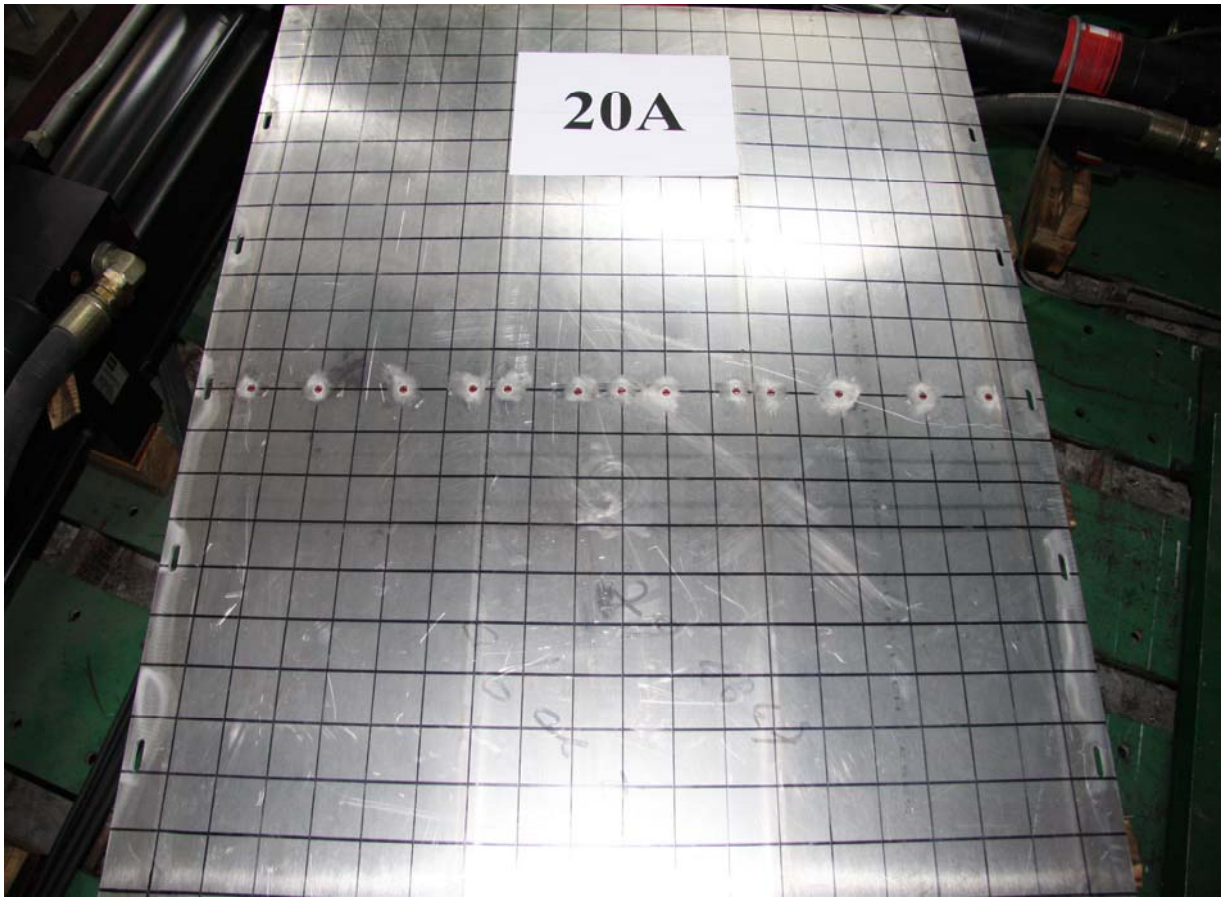

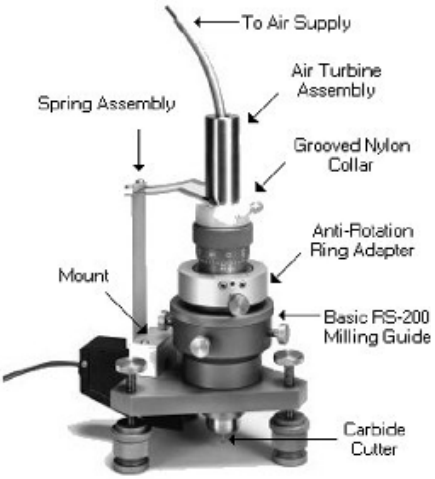

Figure 4.7 Set-up for residual stress measurement using the hole-drilling strain-gauge method

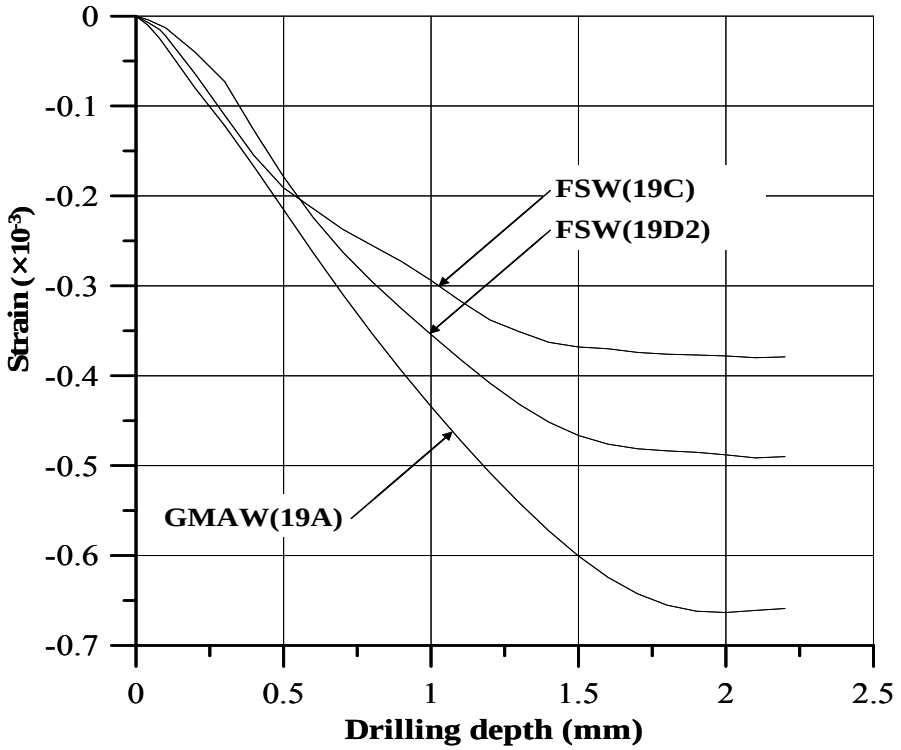

Figure 4.8 Relationships between drilling depth and released strain in the panel longitudinal direction at a location in the compressive residual stress zone

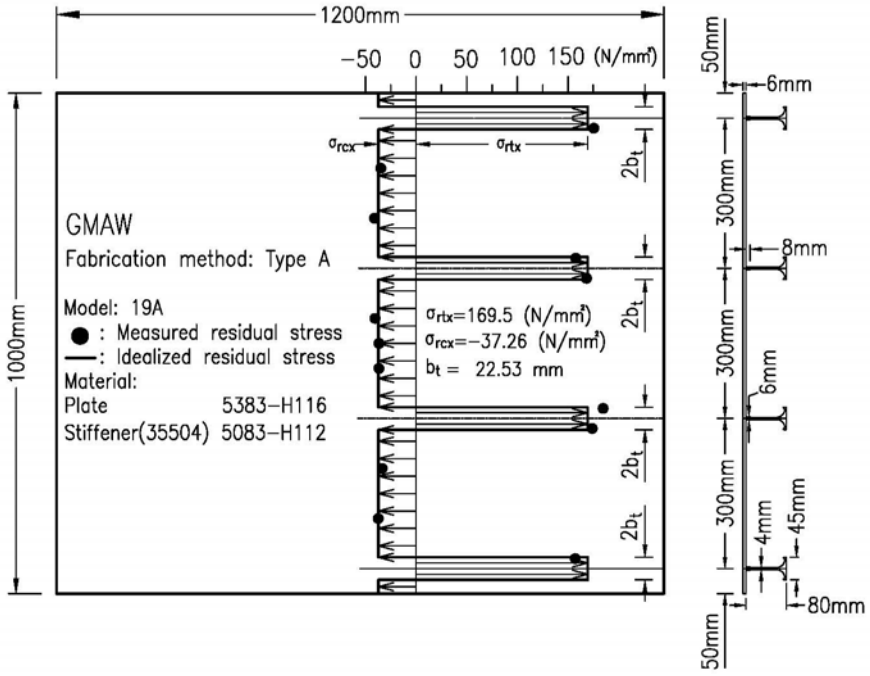

Figure 4.9(a) Distribution of residual stress in test structure 19A

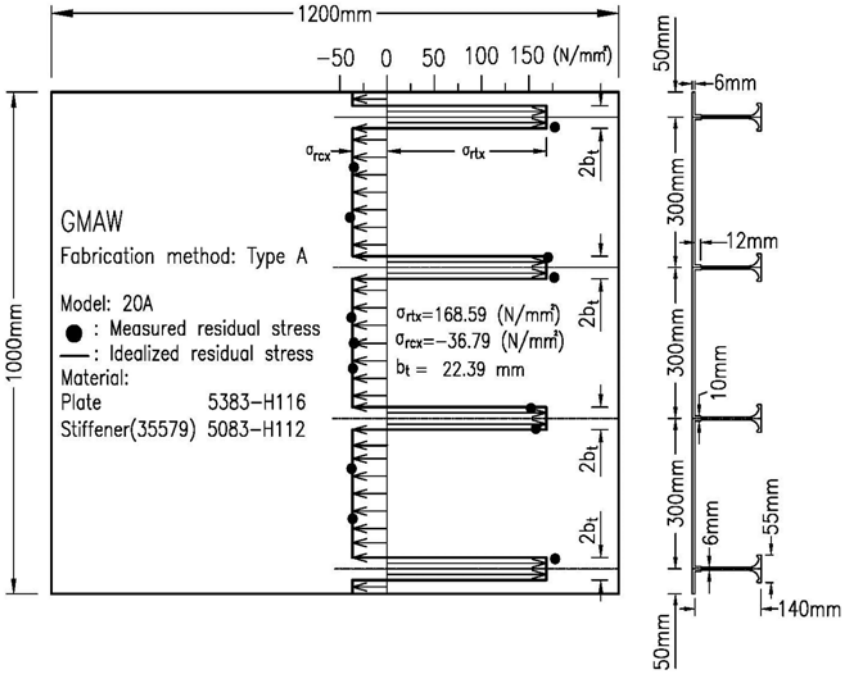

(a)

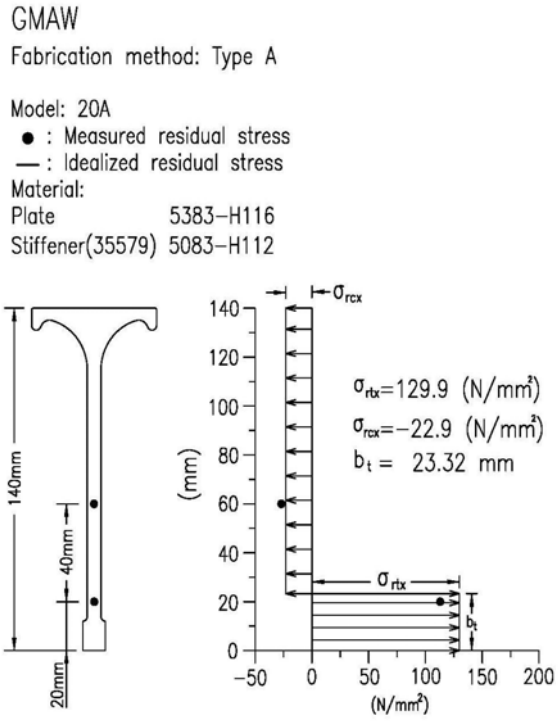

(b)

Figure 4.9(b) Distribution of residual stress in test structure 20A: (a) plate, (b) stiffener web

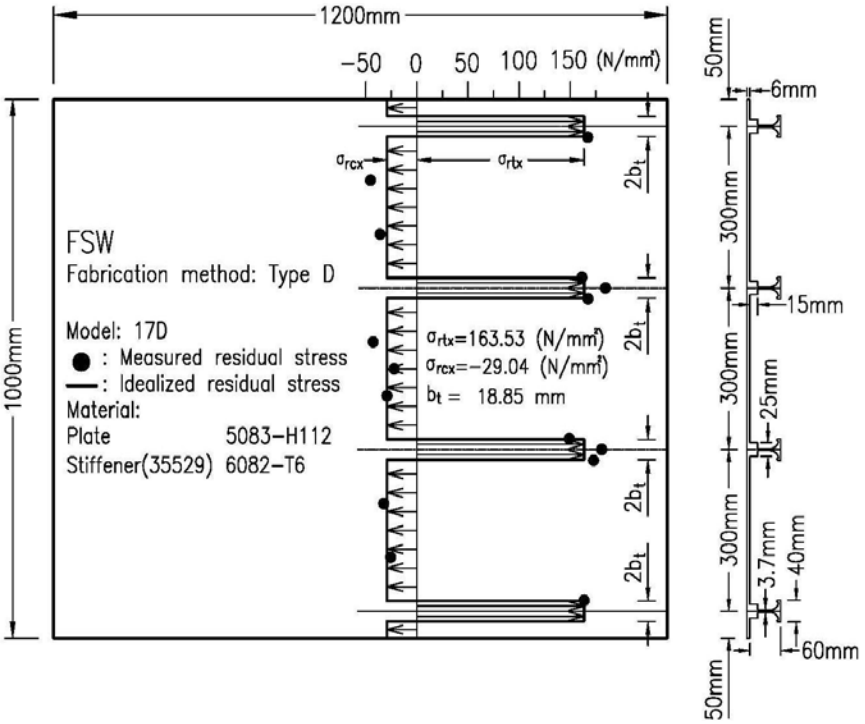

Figure 4.9(c) Distribution of residual stress in test structure 17D

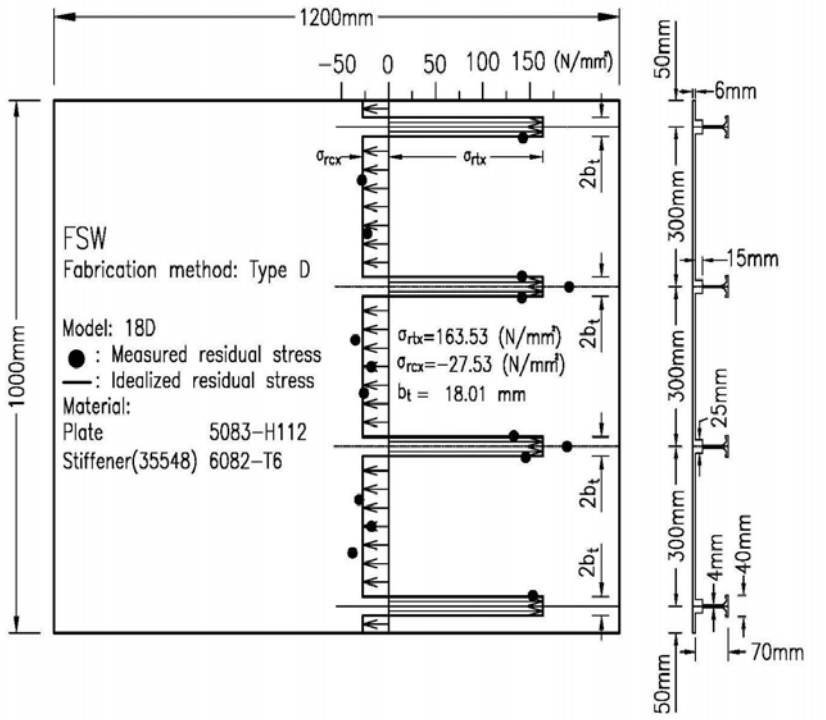

Figure 4.9(d) Distribution of residual stress in test structure 18D

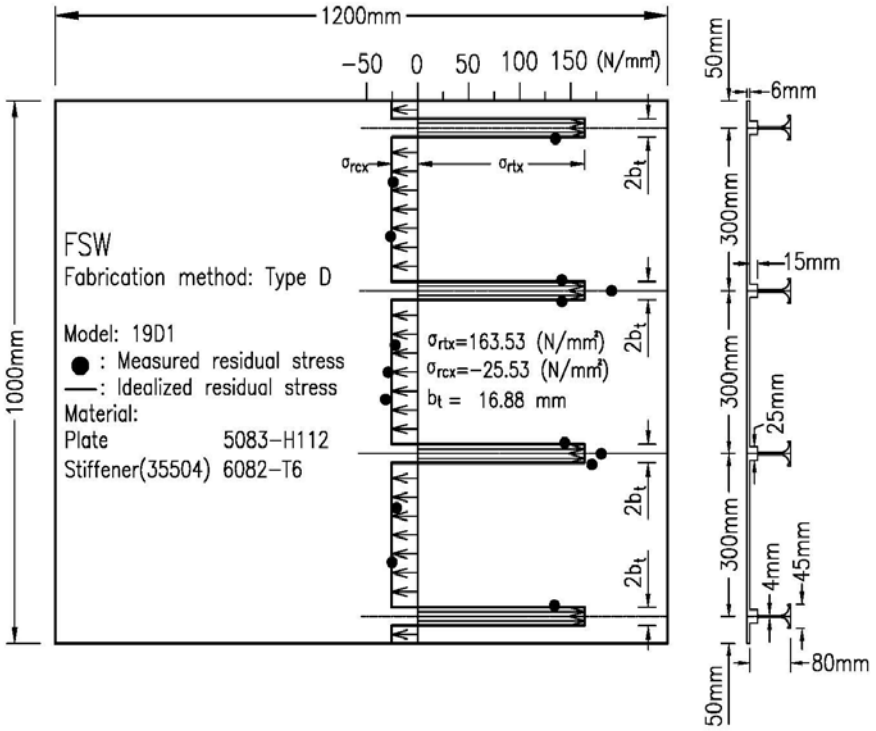

Figure 4.9(e) Distribution of residual stress in test structure 19D1

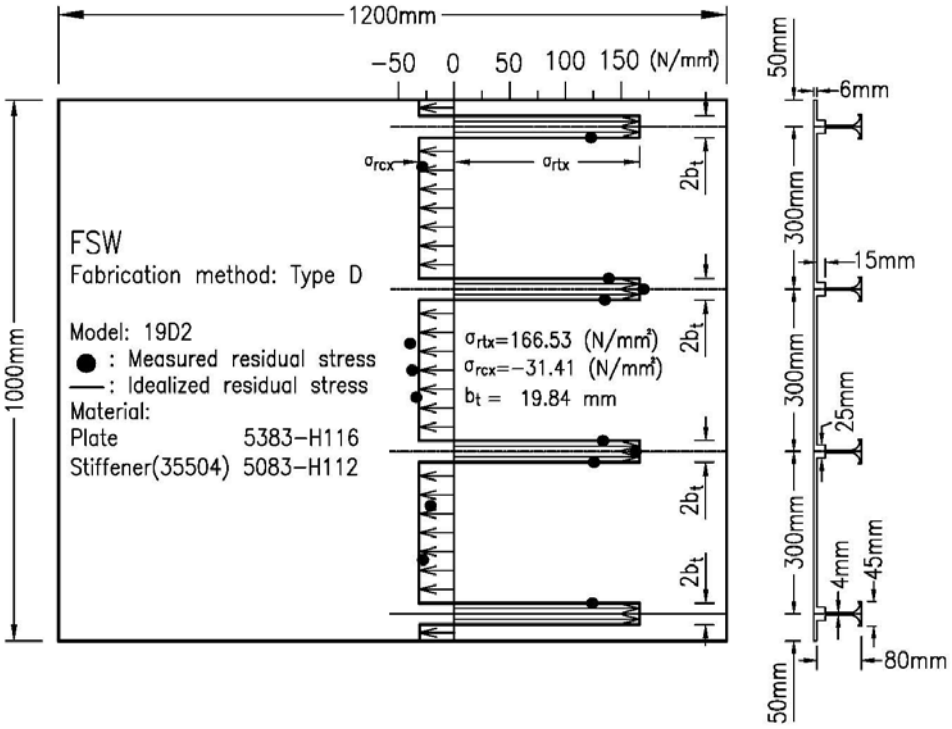

Figure 4.9(f) Distribution of residual stress in test structure 19D2

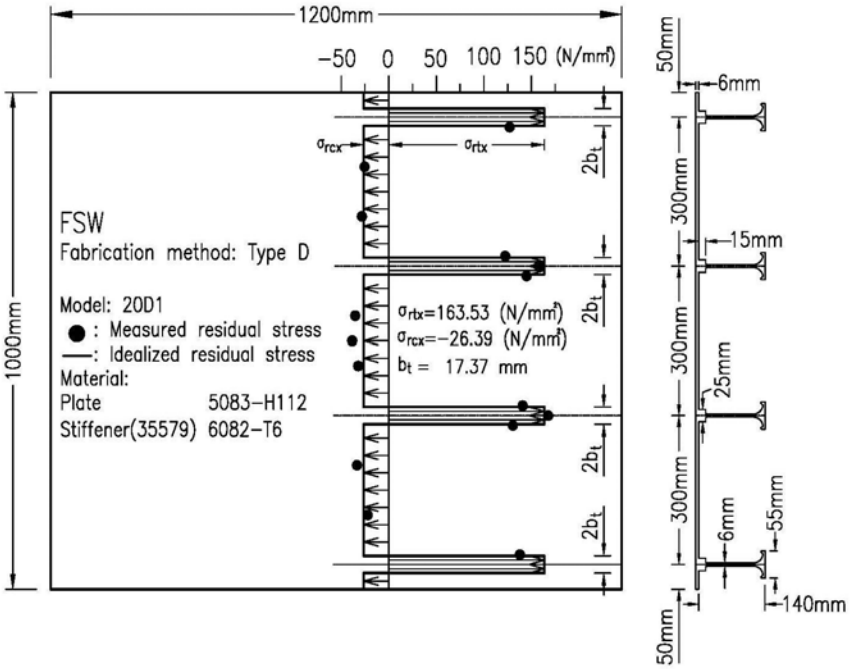

(a)

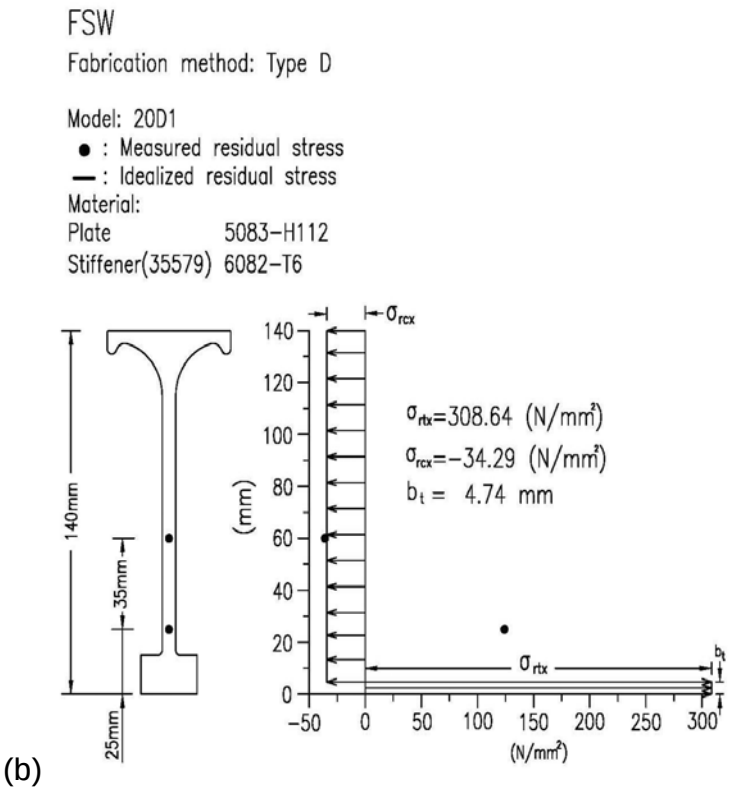

(b)

Figure 4.9(g) Distribution of residual stress in test structure 20D1: (a) plate, (b) stiffener web

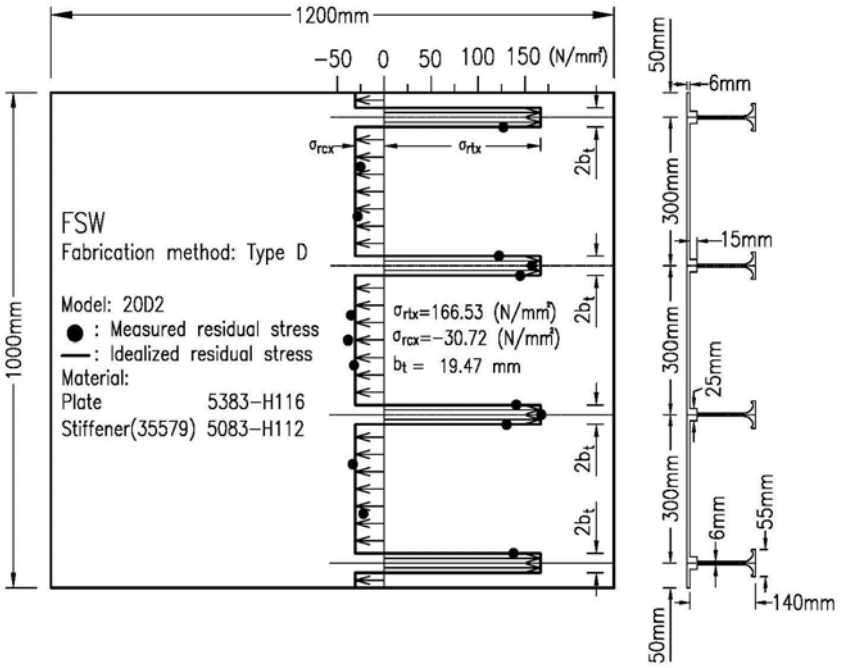

(a)

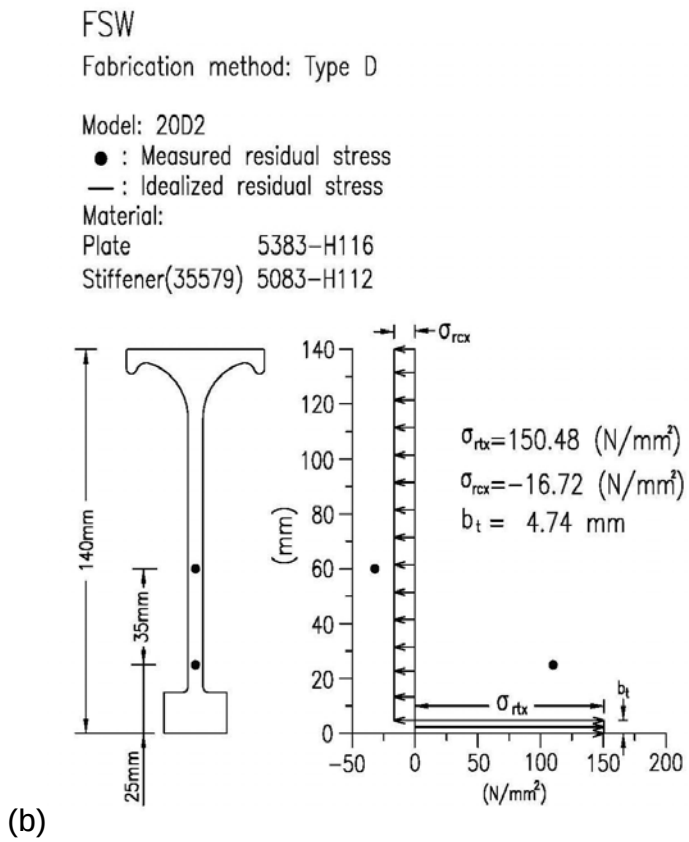

(b)

Figure 4.9(h) Distribution of residual stress in test structure 20D2: (a) plate, (b) stiffener web

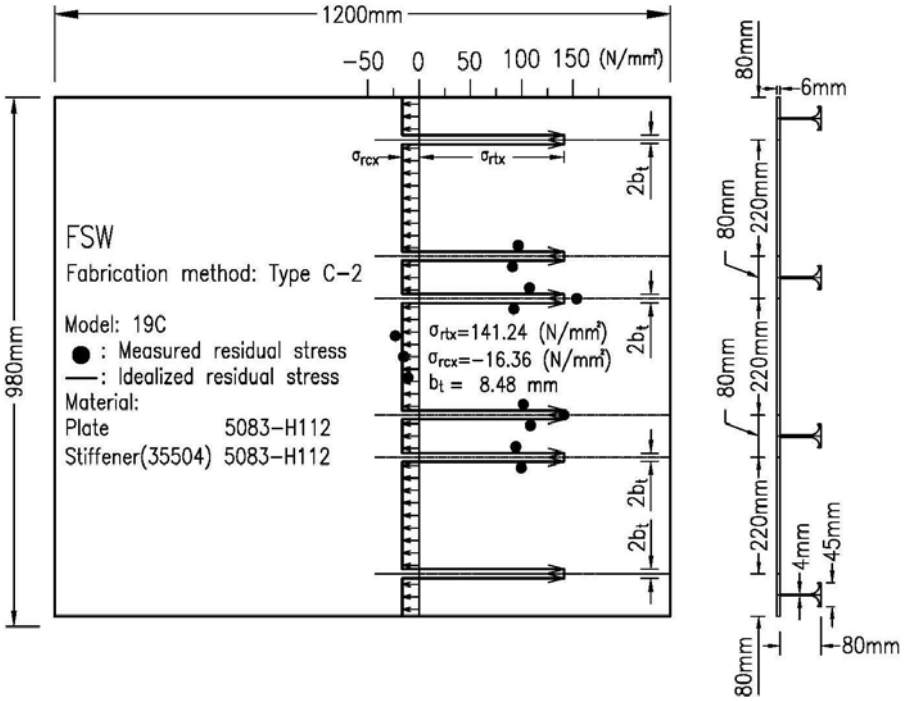

Figure 4.9(i) Distribution of residual stress in test structure 19C

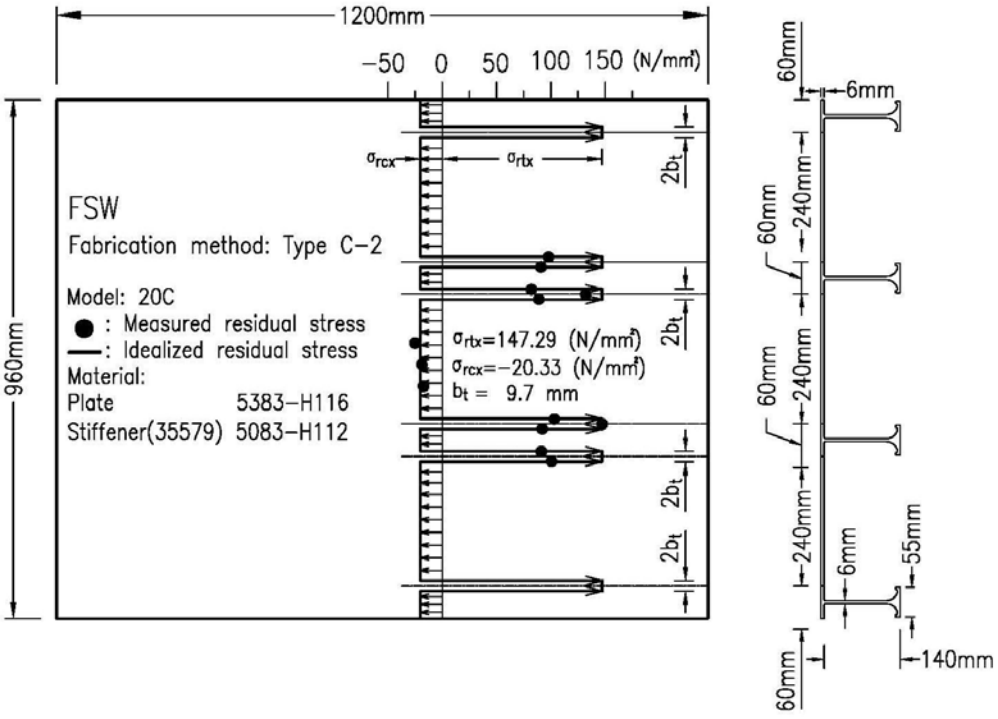

Figure 4.9(j) Distribution of residual stress in test structure 20C

4.5 Properties of the Softened Zone

The micro-structural characteristics of the TMAZ may differ from those of the HAZ, as is illustrated in Figure 2.7 in Chapter 2. For the sake of simplicity, however, the present study applies the following hypotheses.

- The properties of the TMAZ are similar to those of the HAZ. This is because the two zones exhibit a similar tendency in terms of reduced yield strength, which is of primary concern when evaluating ultimate compressive strength performance.
- The yield strength in the softened zone is equivalent to the tensile residual stress in the corresponding zone. This is based on the fact that the tensile residual stress in the HAZ easily reaches the material yield stress in the case of mild steel (Masubuchi 1980, Paik & Thayamballi 2003).
- The compressive residual stress is in equilibrium with the tensile residual stress over the plate cross-sectional area.

Table 4.2 Mechanical properties of the softened zone in terms of breadth and reduced yield strength

Model	Full breadth of the softened zone (mm)		Reduced yield strength (MPa)	
	Plate	Web	Plate	Web
19A	45.06	23.32*	169.50	129.90*
20A	44.78	23.32	168.59	129.90
17D	37.70	2.67*	163.53	273.78*
18D	36.02	2.49*	163.53	273.78*
19D1	33.76	2.69*	163.53	273.78*
19D2	39.68	2.69*	166.53	150.48*
20D1	34.74	4.74	163.53	308.64
20D2	38.94	4.74	166.53	150.48
19C	16.96	0.0*	141.24	0.0*
20C	19.40	0.0*	147.29	0.0*

Note: *Assumed values; the rest are measured values.

Table 4.2 summarizes the mechanical properties of the softened zone in terms of breadth and reduced yield strength. All of the properties of the plate part are obtained from direct measurements. The properties of the stiffener web are mostly

assumed where the reduced yield strength in the softened zone of the stiffener web is considered to be 90% of the yield strength of the base material from the measurements indicated in Figures 4.9(g) and 4.9(h).

Table 4.3 Comparison of initial imperfections in fusion welds versus friction stir welds

Model	$w_{opl}/(\beta^2 t)$	w_{oc}/a	w_{os}/a	$\sigma_{rcx} / \sigma_{Yp}$	$\sigma_{YHAZ} / \sigma_{Yp}$	b_{HAZ}
19A	0.022	0.0012	0.00051	-0.179	0.815	22.53
20A	0.036	0.0009	0.00038	-0.177	0.811	22.39
17D	0.023	0.0008	0.00027	-0.174	0.978	18.85
18D	0.023	0.0007	0.00037	-0.165	0.978	18.01
19D1	0.029	0.0006	0.00031	-0.153	0.978	16.88
19D2	0.019	0.0006	0.00048	-0.151	0.801	19.84
20D1	0.022	0.0006	0.00020	-0.158	0.978	17.37
20D2	0.017	0.0010	0.00034	-0.148	0.801	19.47
19C	0.036	0.0008	0.00053	-0.098	0.845	8.48
20C	0.016	0.0004	0.00054	-0.098	0.708	9.70
SSC-451[1)]	0.096	0.0018	0.001	-0.161	0.7~0.9	23.10

Note: [1)] Indicates the average values of initial imperfections due to fusion fillet-welds, obtained from SSC-451.

It is confirmed that the *1 inch rule* applies in terms of the breadth of the softened zone for fusion welds (Models 19A and 20A), as is also indicated in Equation (4.10). For FSW structures, however, it is found that the breadth of the softened zone is equivalent to approximately two times the width of the FSW tool shoulder for lap-joining, where the width of the FSW tool shoulder is denoted by d_3, as defined in Figure 3.4 in Chapter 3, and the breadth of this zone for butt-joining is equivalent to the width of the FSW tool shoulder.

It should be noted that the softened zone properties presented in Table 4.2 are used for the nonlinear finite element method computations of ultimate strength that are discussed in Chapter 6.

4.6 Comparison between Fusion Welds and Friction Stir Welds

The weld-induced initial imperfections of FSW aluminum structures are here compared with those of fusion fillet-welded aluminum structures.

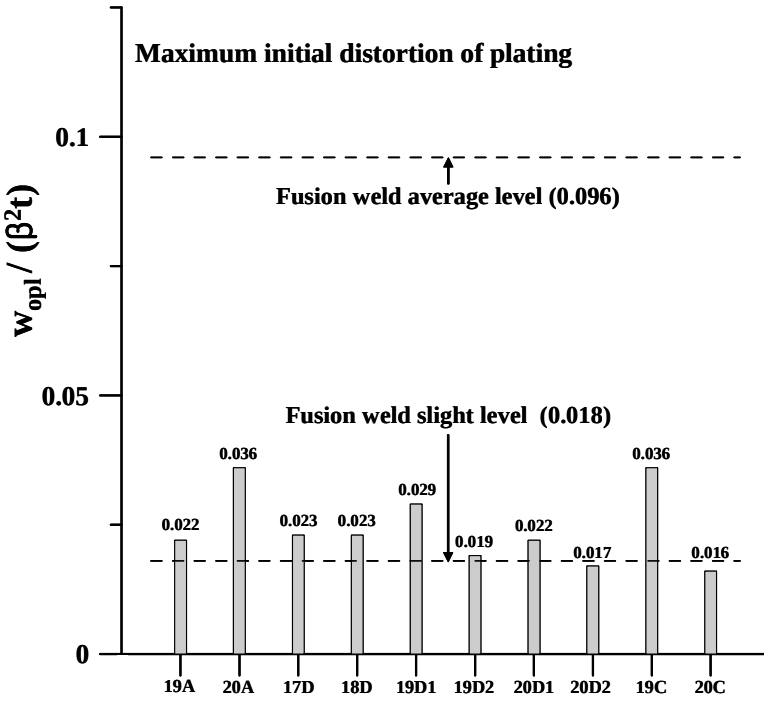

Figure 4.10(a) Comparison of the maximum initial distortion of the plating in fusion welds versus friction stir welds

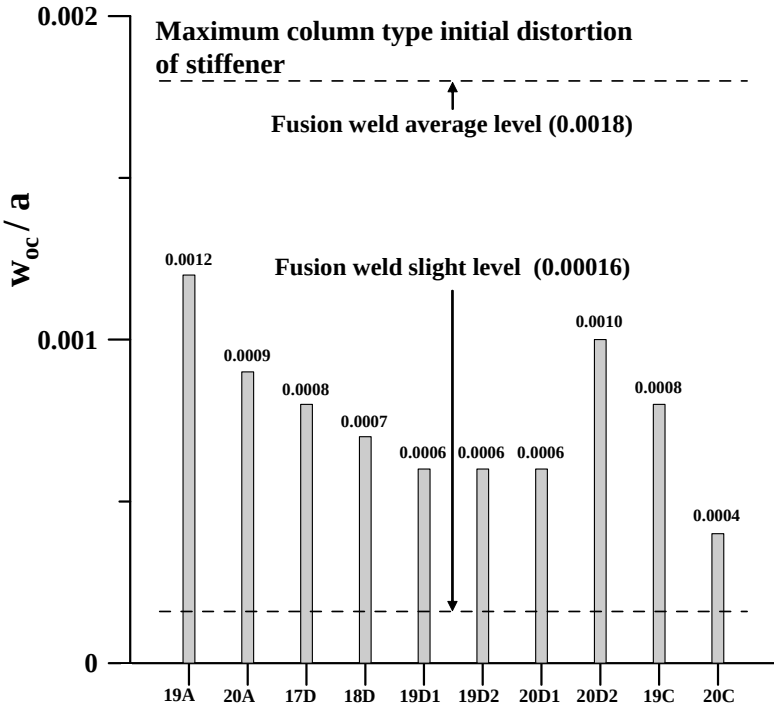

Figure 4.10(b) Comparison of the maximum column-type initial distortion of the stiffener in fusion welds versus friction stir welds

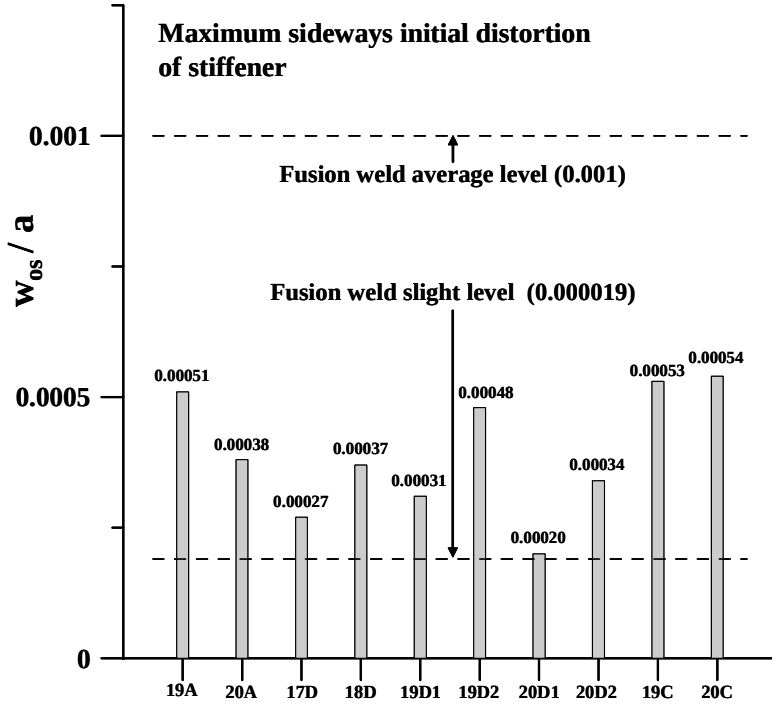

Figure 4.10(c) Comparison of the maximum sideways initial distortion of the stiffener in fusion welds versus friction stir welds

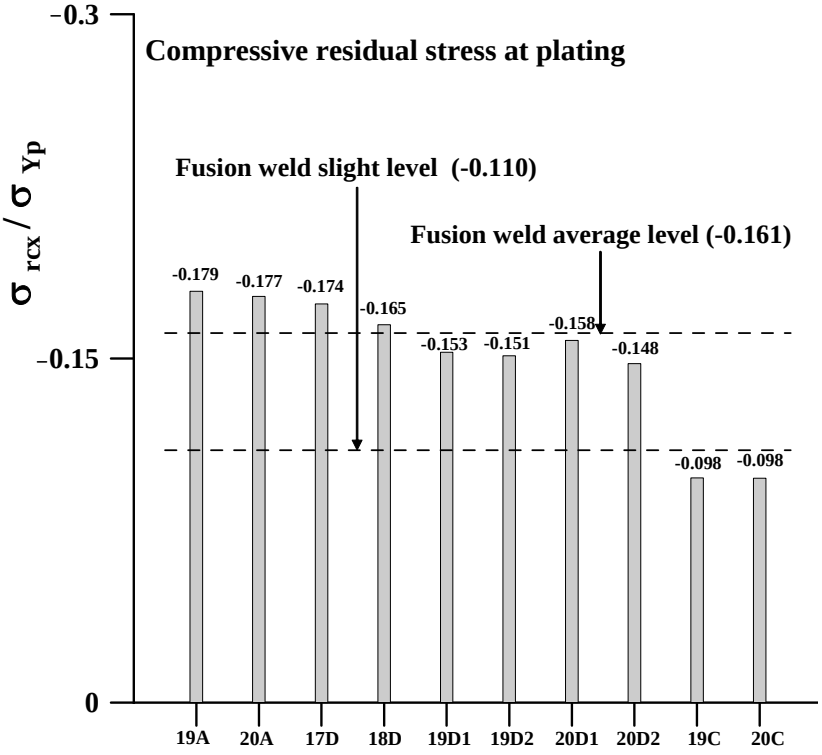

Figure 4.10(d) Comparison of the compressive residual stress at the plating in fusion welds versus friction stir welds

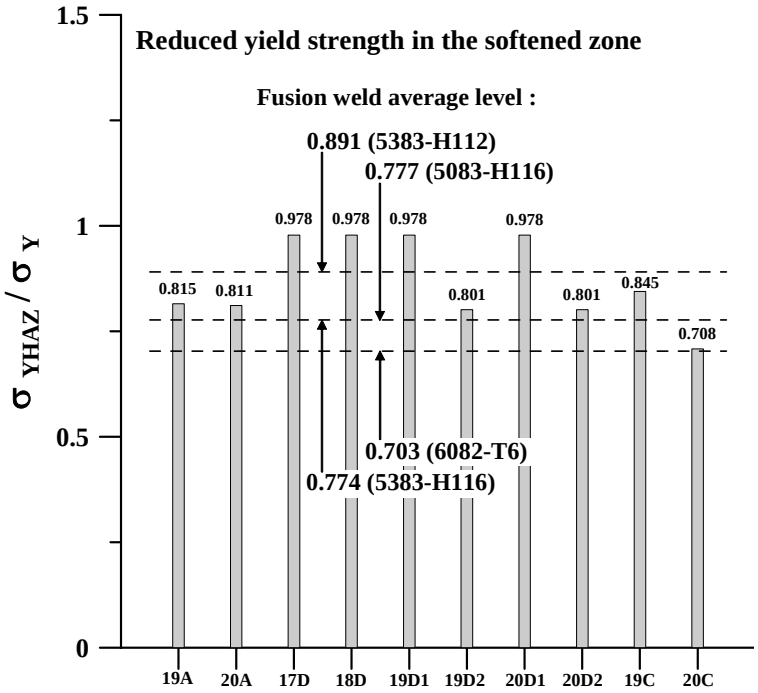

Figure 4.10(e) Comparison of the reduced yield strength in the softened zone in fusion welds versus friction stir welds

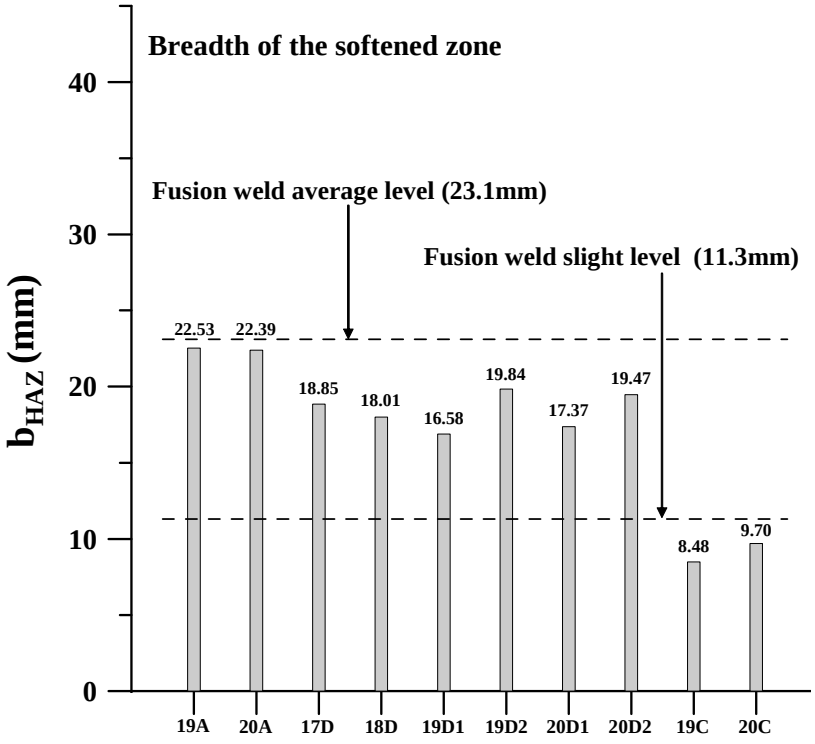

Figure 4.10(f) Comparison of the softened zone breadth (half value) in fusion welds versus friction stir welds

Table 4.3 and Figure 4.10 present the average values of these initial imperfections, as obtained from the measurements of the test structures in the present study, as well as the slight and average values of the initial imperfections obtained from SSC-451 by fusion fillet-welds (GMAW).

The insights and findings obtained from this comparison of the initial imperfections in fusion fillet-welds versus friction stir lap- and butt-welds are as follows.

- The FSW-induced initial distortions are, in general, smaller than the fusion-weld induced initial distortions. The plate initial deflection due to friction stir welds is close to the slight level of such deflection due to fusion fillet-welds. The column-type or sideways initial distortion of the stiffeners due to friction stir welds is some 50% of that due to fusion fillet-welds.
- It is observed that the level of the sideways initial distortions of the stiffeners due to FSW butt-joining for test structures 19C and 20C appears to be comparatively large. It is thought, however, that these distortions were inherent in the extrusion production process for these structures rather than arising during FSW. The extrusions of test structures 19C and 20C had wide flanges that may exhibit non-uniform temperature distribution over the flange and web during the cooling process, thus causing larger sideways initial distortions than those in extruded short flanges.
- The level of the compressive residual stress in FSW lap-welds is similar to that in fusion fillet-welds, but the level of the compressive residual in FSW butt-welds is closer to the slight level in fusion fillet-welds.
- The trend in the yield strength reduction in the softened zone depends on the material type. The reduction in this zone due to friction stir welds is similar to that due to fusion welds.
- The breadth of the softened zone in FSW aluminum structures is equal to approximately two times the width of the FSW tool shoulder for lap-joining, but approximately equal to the width of the FSW tool shoulder for butt-joining. This may be because the lap-joining process requires a deeper penetration of the FSW pin than does the butt-joining process, and, subsequently, the HAZ tends to be more likely to expand.

Chapter 5 Buckling Collapse Testing

5.1 Test Facilities and Their Set-up

Buckling collapse testing on the stiffened plate structures was performed in a test frame that facilitates a 2000 kN loading actuator at the Ship and Offshore Structural Mechanics Laboratory, the Lloyd's Register Educational Trust (LRET) Research Centre of Excellence at Pusan National University.

Figure 5.1 shows a typical test structure set-up using this facility. The target structure was positioned vertically in the test frame. The loading actuator generated axial compressive forces in the longitudinal direction of the test plate panels. To apply these forces uniformly over the cross-sectional area of the loaded panel edges, a rigid steel plate was attached to each of the loaded panel edges.

Both the loaded and unloaded edges of the test structures were kept straight and in a simply supported condition, i.e., with zero lateral deflection and zero rotational restraints, during testing.

To accomplish the simply supported condition at the loaded edges, a rigid solid bar with a circular cross section was inserted into each edge, as shown in Figure 5.2. The unloaded edges were supported by a set of two rigid strips bolted to the test panels, as shown in Figure 5.3.

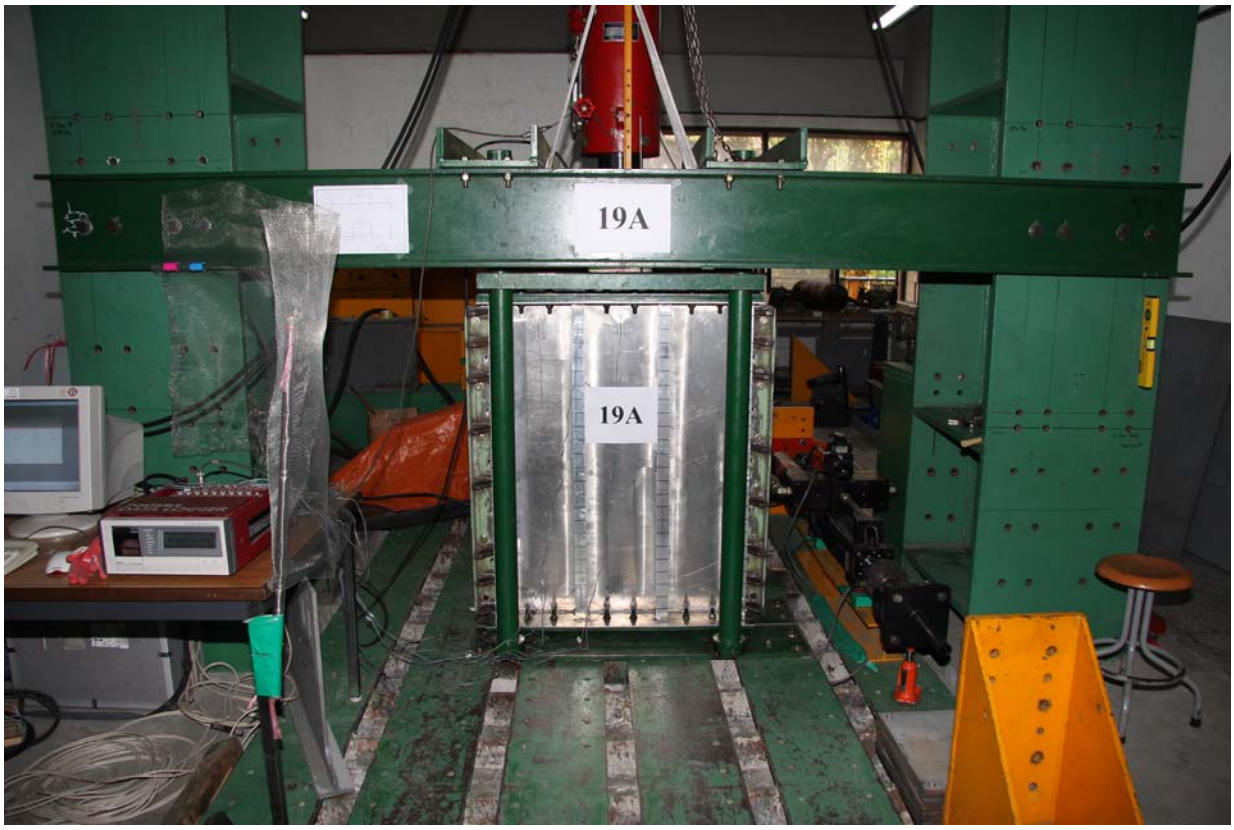

Figure 5.1 Photo of the test set-up for buckling collapse testing

Figure 5.2 Photo of the rigid solid bar inserted into the loaded edge

Figure 5.3 Photo of the rigid strips bolted to the test panel at the unloaded edge

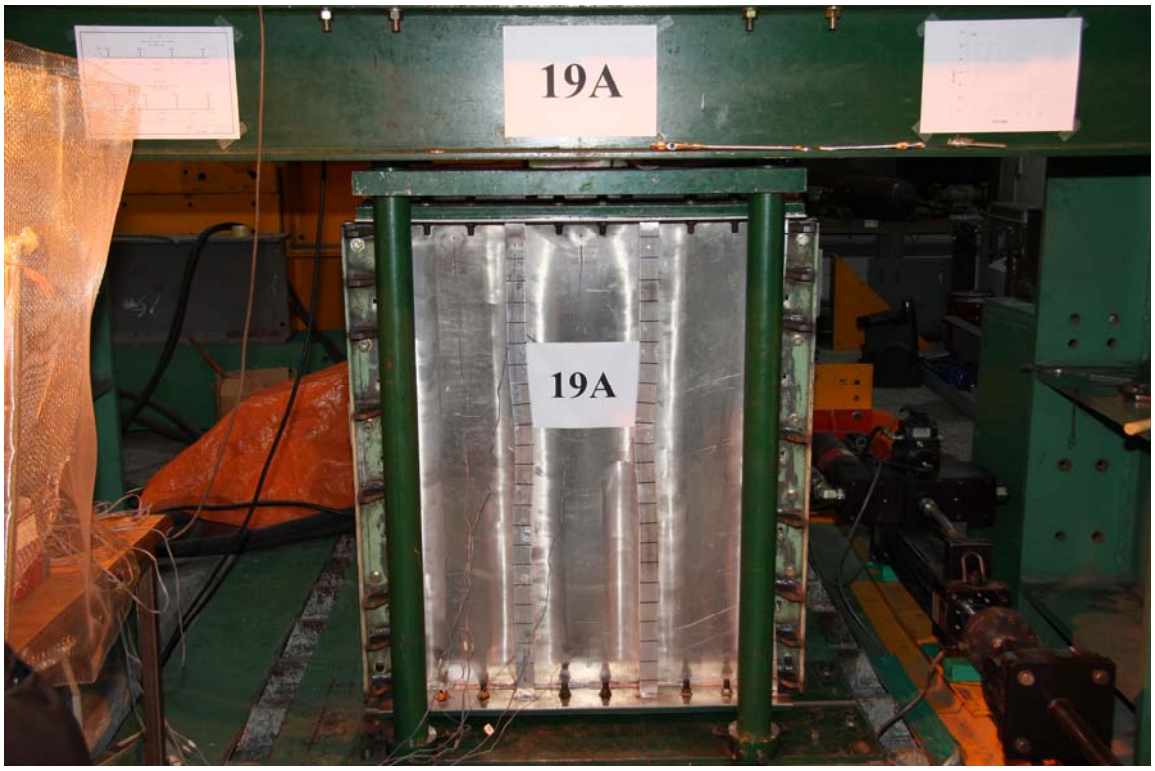

Figure 5.4 Photo of the strain gauges attached at both the lower and upper ends of the test structure

The axial compressive forces were applied at the neutral axis of the panel cross section, as shown in Figure 5.2, until and after the test structure had reached its ultimate strength. This was important in avoiding any unnecessary eccentricity-causing additional end moments and ensuring that pure axial compressive forces could be applied. The neutral axis of each test structure was determined using structural mechanics before the start of buckling collapse testing.

It was also important to confirm the precision of the test set-up for each of the test structures in which the test plate panels were subjected to pure and uniform axial compressive forces. For this purpose, a total of eight strain gauges were attached to the plating and stiffeners at both the lower and upper ends of each structure, as shown in Figure 5.4. The axial strains of the structures were measured until axial compressive forces of some 150 kN had been reached, with comparisons made among them, and the neutral axis position of each of those in the test frame was readjusted until the axial strains become almost identical. This was repeated prior to starting the actual buckling collapse testing. However, it was impossible to adjust the change of the neutral axis position in the middle of buckling collapse testing, which can occur due to the local failure of test structures.

The relationships between the axial force and axial displacement of the test structures were recorded with a personal computer. Photographs of the test structures were taken before, during and after ultimate strength was reached.

5.2 Test Results and Discussions

It is recognized that the following six types of collapse modes are relevant to stiffened plate structures until ultimate strength is reached (Paik & Thayamballi 2003, Paik & Thayamballi 2007).

- Mode I: Overall collapse after overall buckling, see Figure 5.5(a)
- Mode II: Collapse of plating between stiffeners without failure of stiffeners, see Figure 5.5(b)
- Mode III: Beam-column type collapse as a plate-stiffener combination, see Figure 5.5(c)
- Mode IV: Local buckling of stiffener web, see Figure 5.5(d)
- Mode V: Flexural-torsional buckling (tripping) of stiffener, see Figure 5.5(e)
- Mode VI: Gross yielding without local buckling

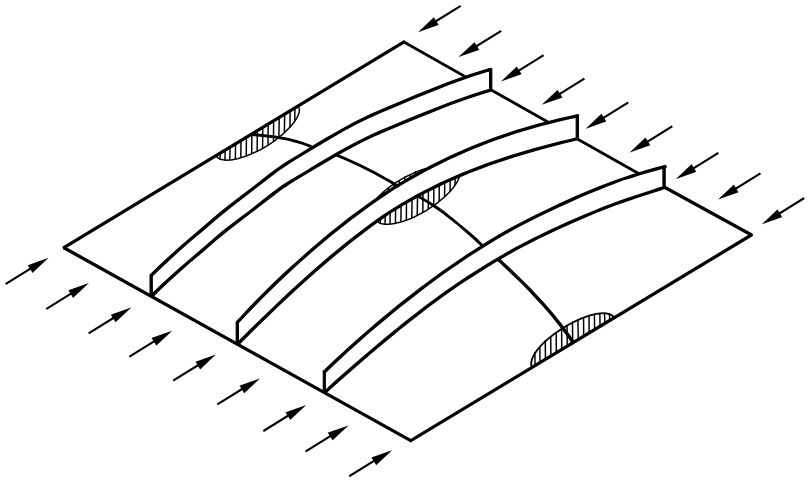

Figure 5.5(a) Mode I: Overall collapse after overall buckling

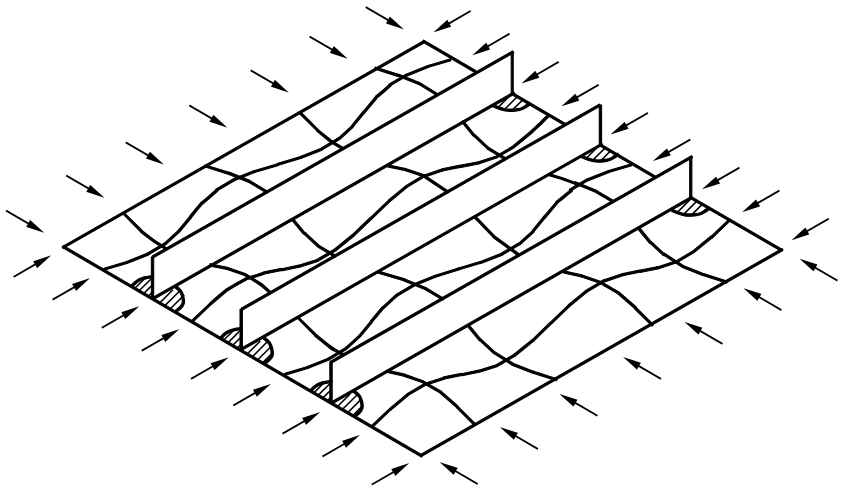

Figure 5.5(b) Mode II: Collapse of plating without failure of stiffeners

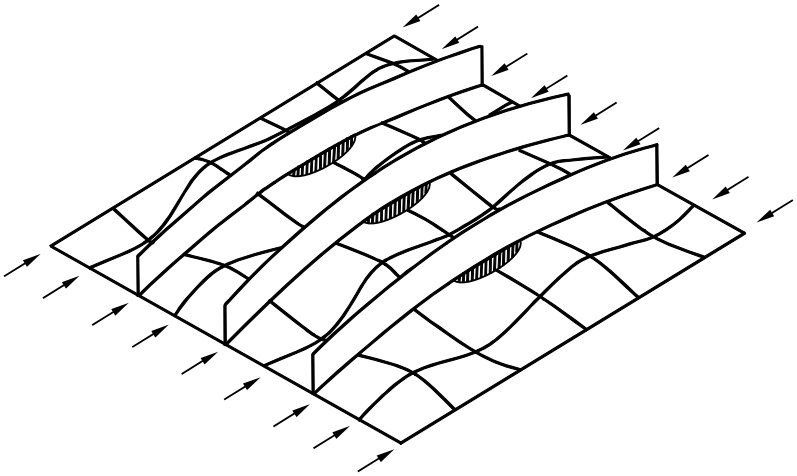

Figure 5.5(c) Mode III: Beam-column type collapse as a plate-stiffener combination

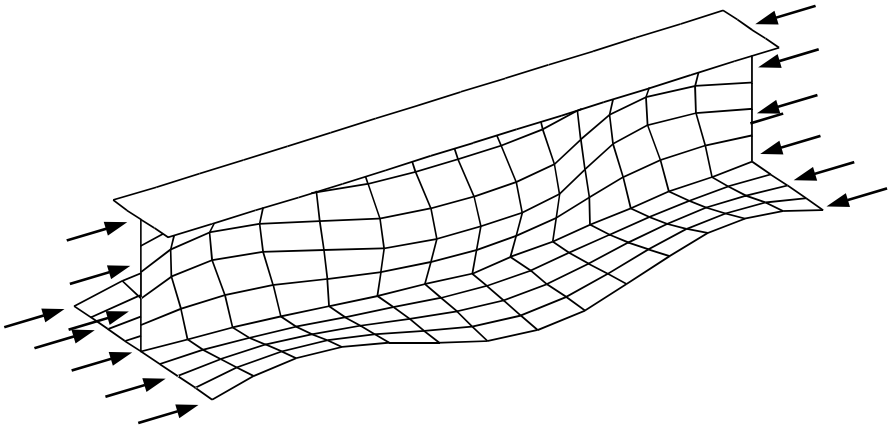

Figure 5.5(d) Mode IV: Local buckling of stiffener web

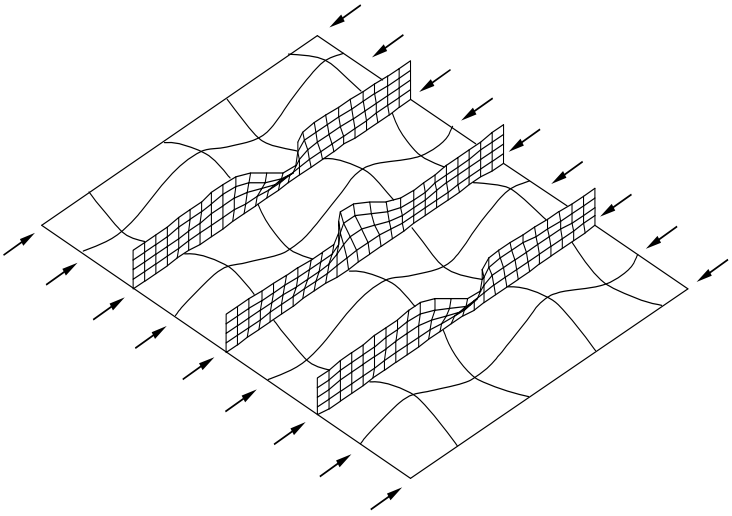

Figure 5.5(e) Mode V: Flexural-torsional buckling (tripping) of stiffener

Table 5.1 Summary of the ultimate compressive strength and associated collapse mode of the present test structures

Model (Fig. No.)	P_p (kN)	Experiment			
		P_u (kN)	P_u/P_p	Collapse mode	Delamination failure
19A (5.6)	1646.9	697.1	0.423	V	No delam
20A (5.7)	2139.7	1401.1	0.655	IV	No delam
17D (5.8)	2009.4	1006.4	0.501	III	One severe delam in post-ULS
18D (5.9)	2003.8	1036.2	0.517	III	Two severe delams in post-ULS
19D1 (5.10)	2095.5	1111.9	0.531	III	Two severe and one slight delams in post-ULS
19D2 (5.11)	1847.8	939.7	0.509	IV	One slight delam in post-ULS
20D1 (5.12)	3161.6	1563.7	0.495	V	Two severe delams before ULS
20D2 (5.13)	2299.8	1561.9	0.679	IV	Three slight delams in post-ULS
19C (5.14)	1583.5	784.6	0.495	II	Two severe and one slight delams in post-ULS
20C (5.15)	1999.1	1166.0	0.583	IV	Two severe and one slight delams before ULS

Note: P_u = ultimate compressive force; P_p = fully plastic axial force = $\sum_i A_i \sigma_{Yi}$, with A_i = area of (i)th cross-section and σ_{Yi} = material yield strength of the (i)th cross-section.

In the following sections, the buckling collapse strength characteristics of each of the test structures are described, where the details of extrusion profiles and dimensions, and weld methods are indicated in Tables 3.6(a) to 3.8(a) and Table 3.9. Table 5.1 summarizes the ultimate compressive strength and associated collapse mode of the test structures obtained from the buckling collapse testing.

5.2.1 Fusion Fillet-welded Structures 19A and 20A

Figures 5.6(a) and 5.7(a) show the relationships between the axial compressive

force and axial compressive displacement for test structures 19A and 20A, respectively. The fully plastic axial force of each structure without consideration of buckling is also plotted. The details of the test structures in terms of material type, extrusion type, and weld method together with the structural dimensions are described in Chapter 3.

The ultimate compressive strength (P_u) normalized by the fully plastic force (P_p) is indicated in Table 5.1. The ultimate strength ratio to the fully plastic axial force is an indicator of representing the severity of local failures in which the ultimate strength ratio becomes smaller as local failure occurs earlier and/or more severely.

Test structure 19A reached its ultimate strength via Collapse Mode V (tripping), as shown in Figure 5.6(b), while test structure 20A collapsed via Mode IV (local buckling of stiffener web), as shown in Figure 5.7(b). No local failure including delamination in the fusion welded area occurred in both 19A and 20A until and after ultimate strength had been reached.

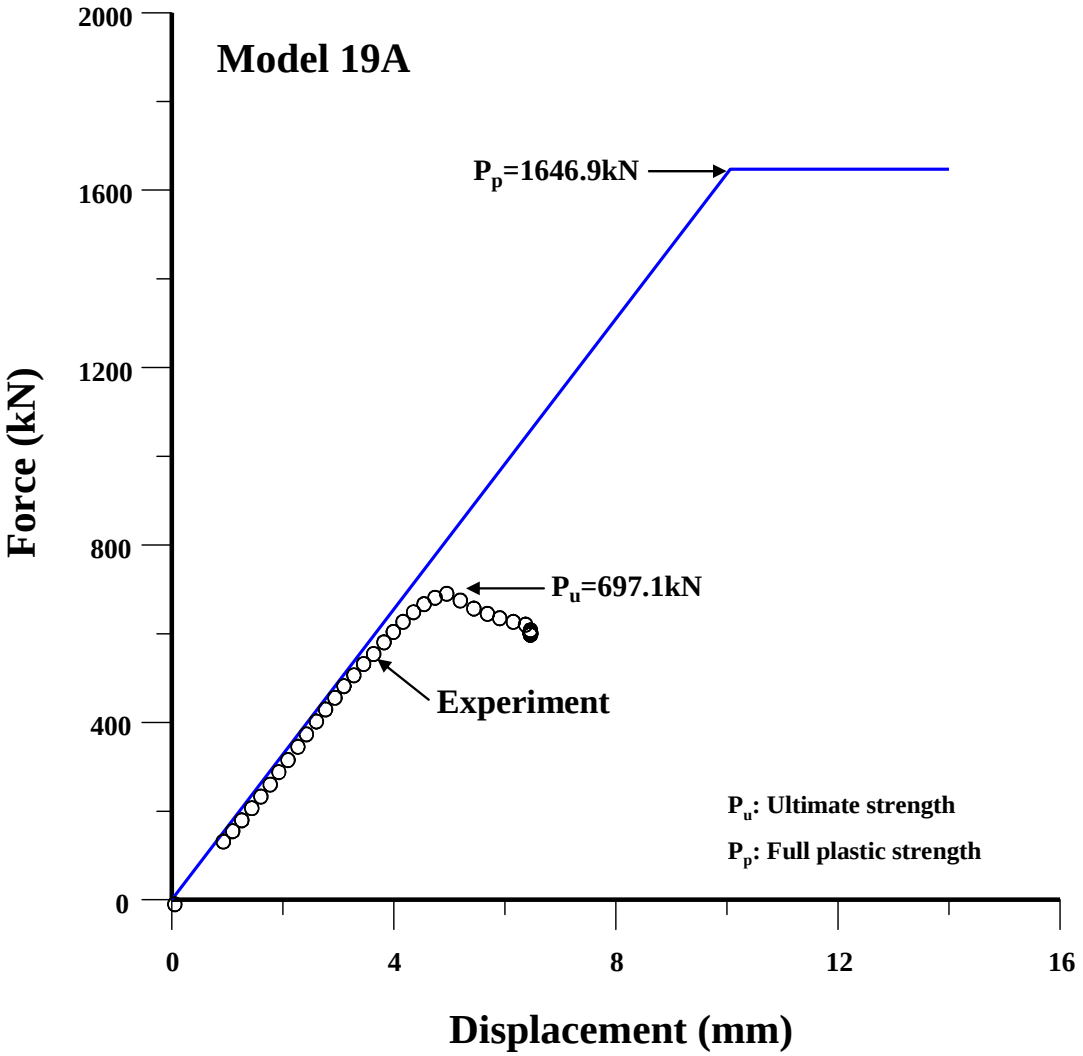

Figure 5.6(a) Relationship between axial compressive force and axial compressive displacement for test structure 19A

Figure 5.6(b) Photo of Collapse Mode V in test structure 19A

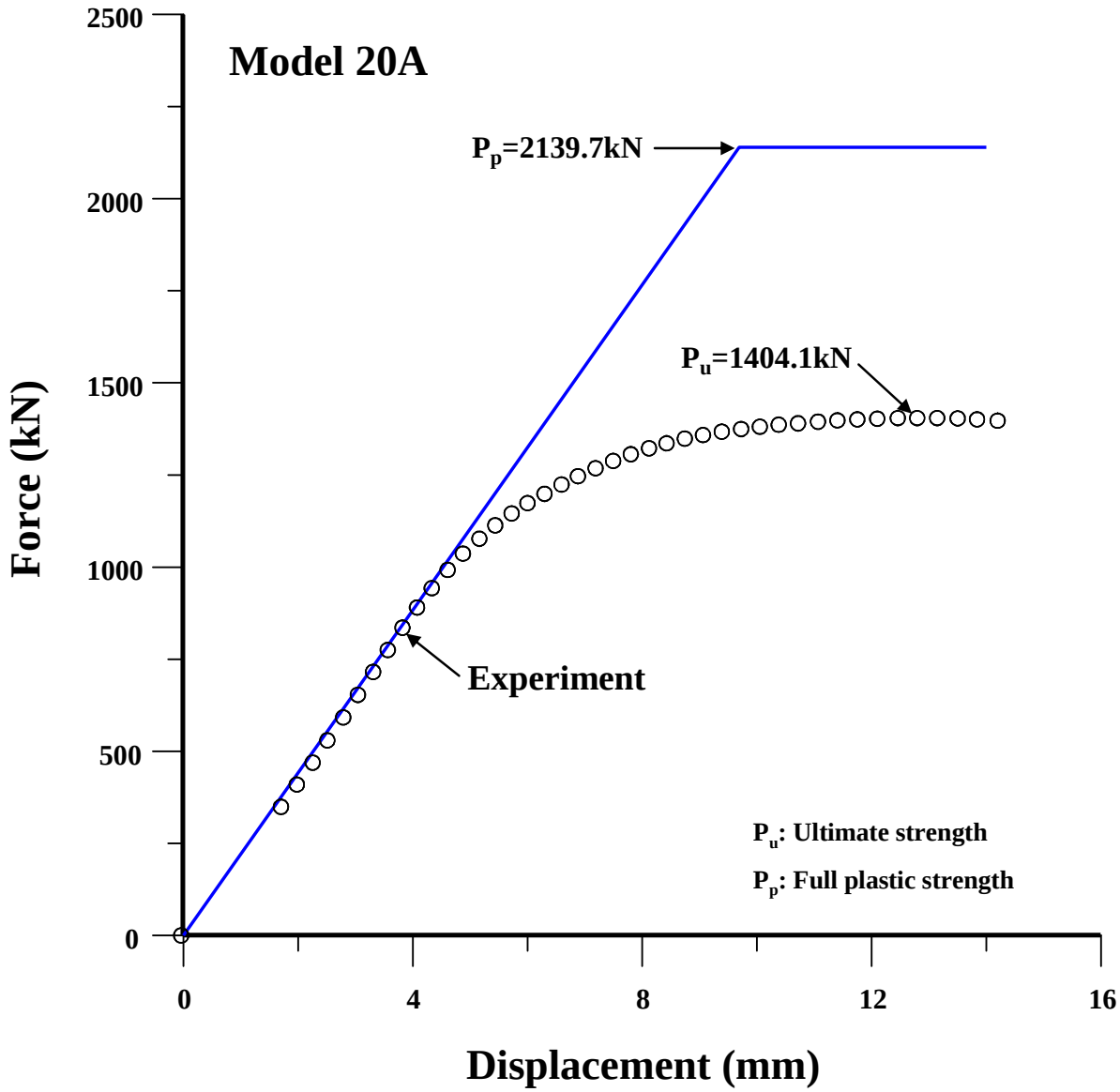

Figure 5.7(a) Relationship between axial compressive force and axial compressive displacement for test structure 20A

Figure 5.7(b) Photo of Collapse Mode IV in test structure 20A

5.2.2 FSW Lap-joined Structures 17D, 18D, 19D1, 19D2, 20D1 and 20D2

Figures 5.8(a) to 5.13(a) show the relationships between the axial compressive force and axial compressive displacement for test structures 17D, 18D, 19D1, 19D2, 20D1, and 20D2, respectively. The fully plastic axial force of each structure without consideration of buckling is also plotted. The ultimate strength of each structure normalized by the fully plastic capacity is presented in Table 5.1.

Each of three test structures 17D, 18D and 19D1 reached its ultimate strength via Collapse Mode III (beam column-type collapse), as shown in Figure 5.8(b). Test structure 20D1 showed Collapse Mode V (flexural-torsional buckling of the stiffener) similar to that as shown in Figure 5.6(b), while test structures 19D2 and 20D2 reached their ultimate strength via Collapse Mode IV (local buckling of stiffener web) similar to that as shown in Figure 5.7(b).

For all the FSW lap-joined test structures, delamination occurred across the entire width of the friction stir-welded area of stiffeners, as those shown in Figures 5.8(b) to 5.13(b) which are photos taken at the end of testing. Most structures showed the delamination failure after ultimate strength had been reached. However, in test structure 20D1, severe delamination in two stiffeners occurred, starting before the ultimate compressive strength had been reached.

It is surmised that such a delamination must have contributed to the collapse of this structure to some large extent. In fact, the ultimate strength ratio of test structure 20D1 to the fully plastic axial force is unusually small as will be discussed in Chapter 6, by a comparison with nonlinear finite element method computations.

This caused speculation about the quality of the friction stir-welding (FSW) lap-

joining technology, although the delamination mostly occurred after the structures had reached ultimate strength, except for one structure, i.e., 20D1.

The post-collapse delamination in lap-welded structures, i.e., with base plate and extruded stiffeners, may not be of major concern because it can still maintain the water tightness of the stiffened plate structures. However, the pre-collapse delamination can reduce the ultimate compressive strength significantly.

It is recognized that the performance of friction stir-welded region is significantly affected by the welding parameters such as width and depth of molten metal thin layer, molten temperature, rotating and forwarding speeds, and possible quick cooling, etc. (Cavaliere et al. 2009, Lombard et al. 2009, Zhang & Zhang 2009a, 2009b). Therefore, further study is required to establish optimum parameters of the FSW process and also investigate the compressive strength properties and delamination in the friction stir lap-welded region.

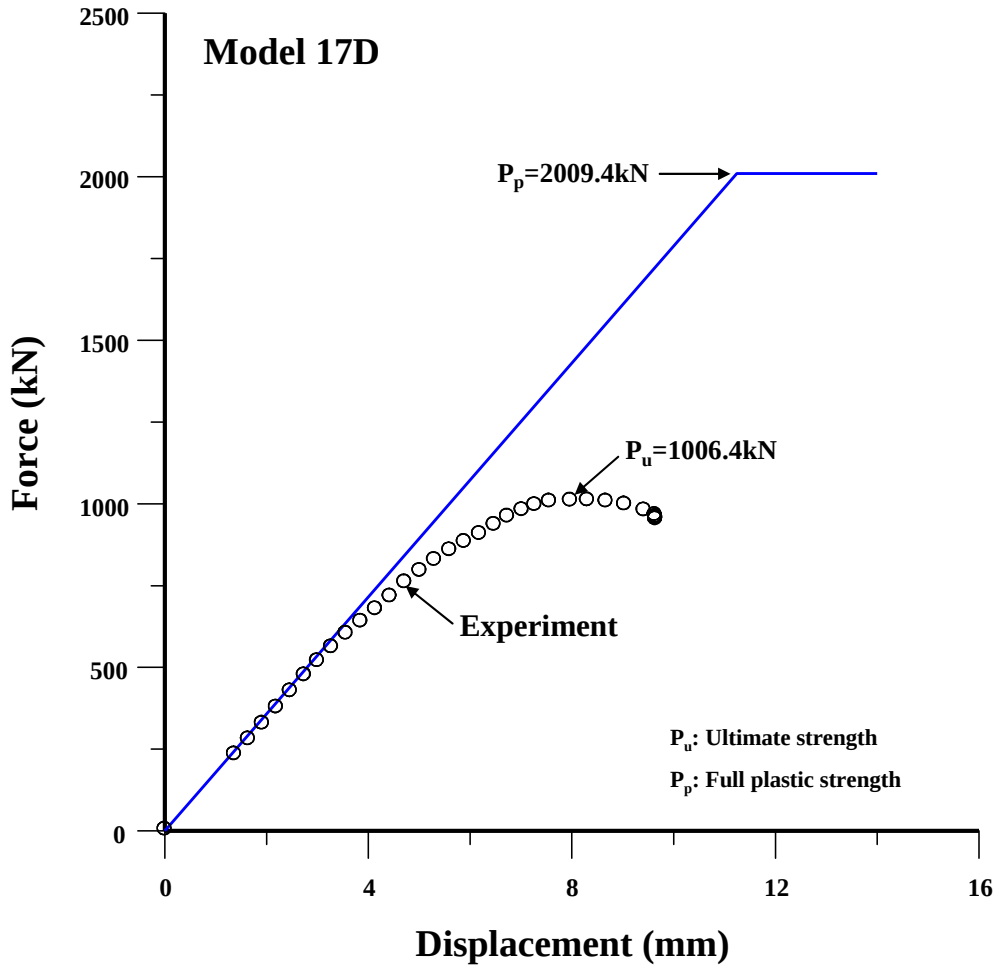

Figure 5.8(a) Relationship between axial compressive force and axial compressive displacement for test structure 17D

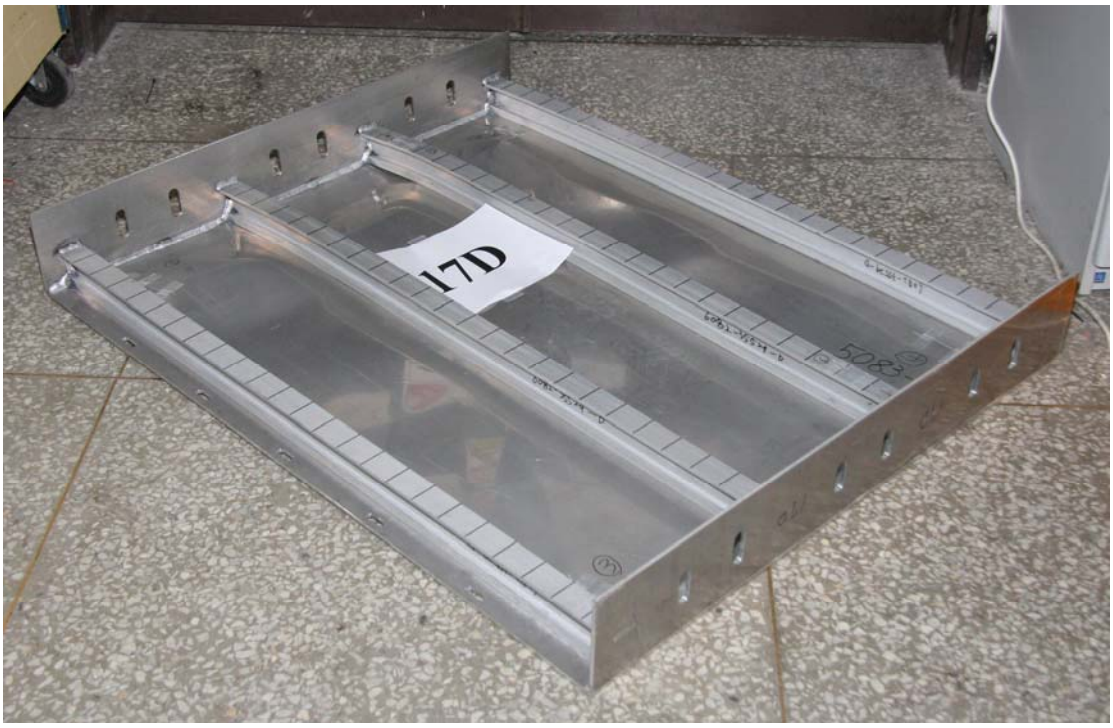

Figure 5.8(b) Photo of Collapse Mode III in test structure 17D

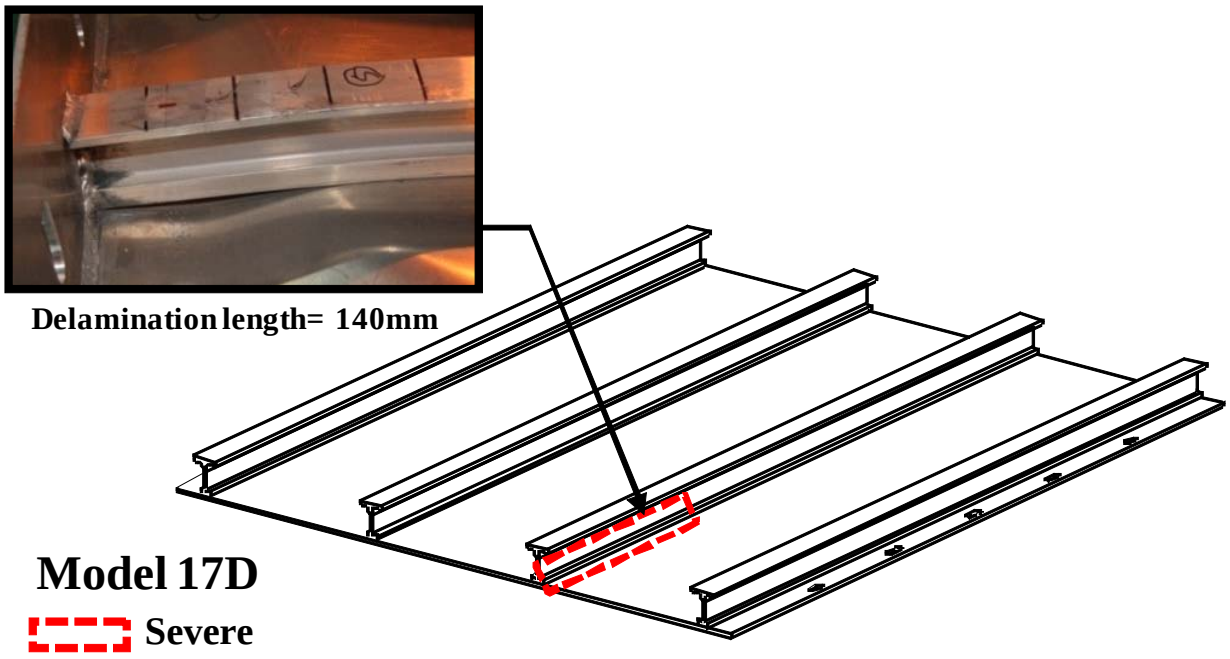

Figure 5.8(c) Photo of the delamination failure in test structure 17D, taken at the end of testing

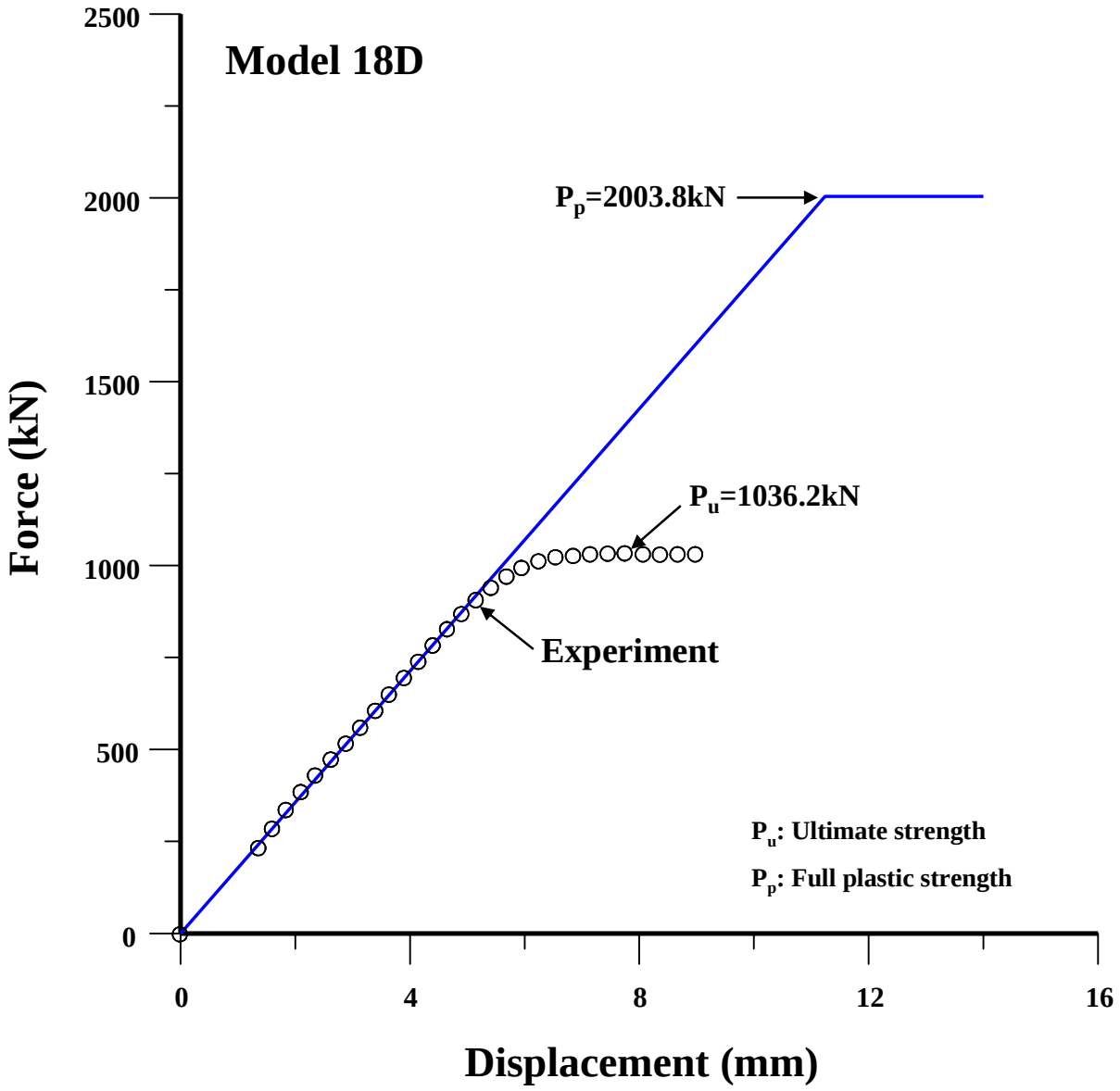

Figure 5.9(a) Relationship between axial compressive force and axial compressive displacement for test structure 18D

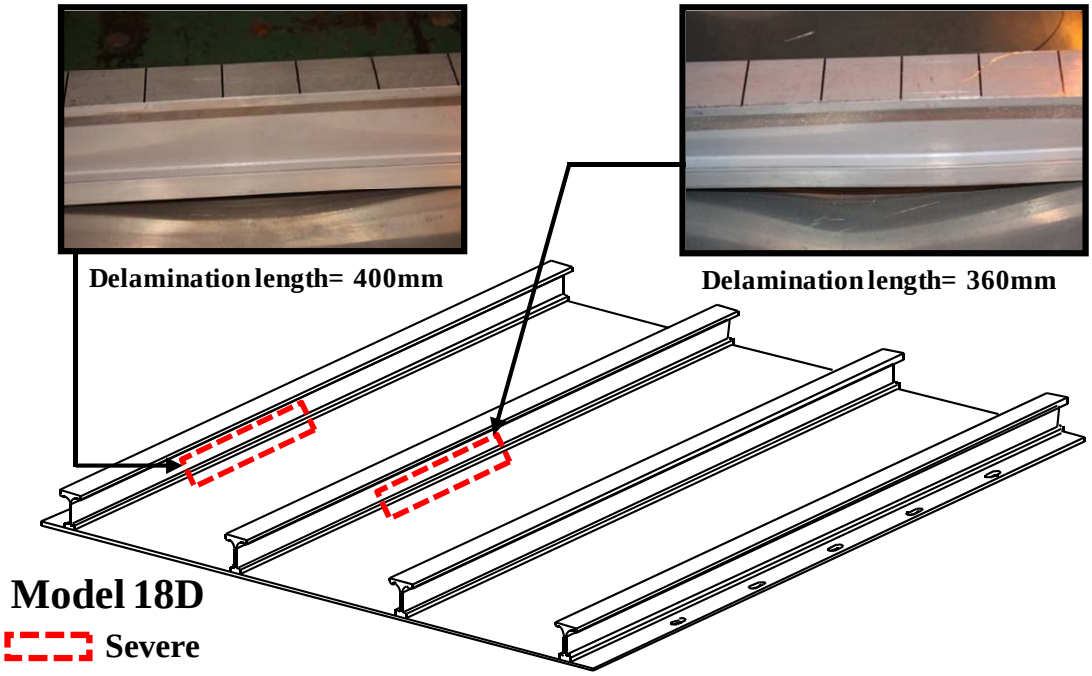

Figure 5.9(b) Photo of the delamination failure in test structure 18D, taken at the end of testing

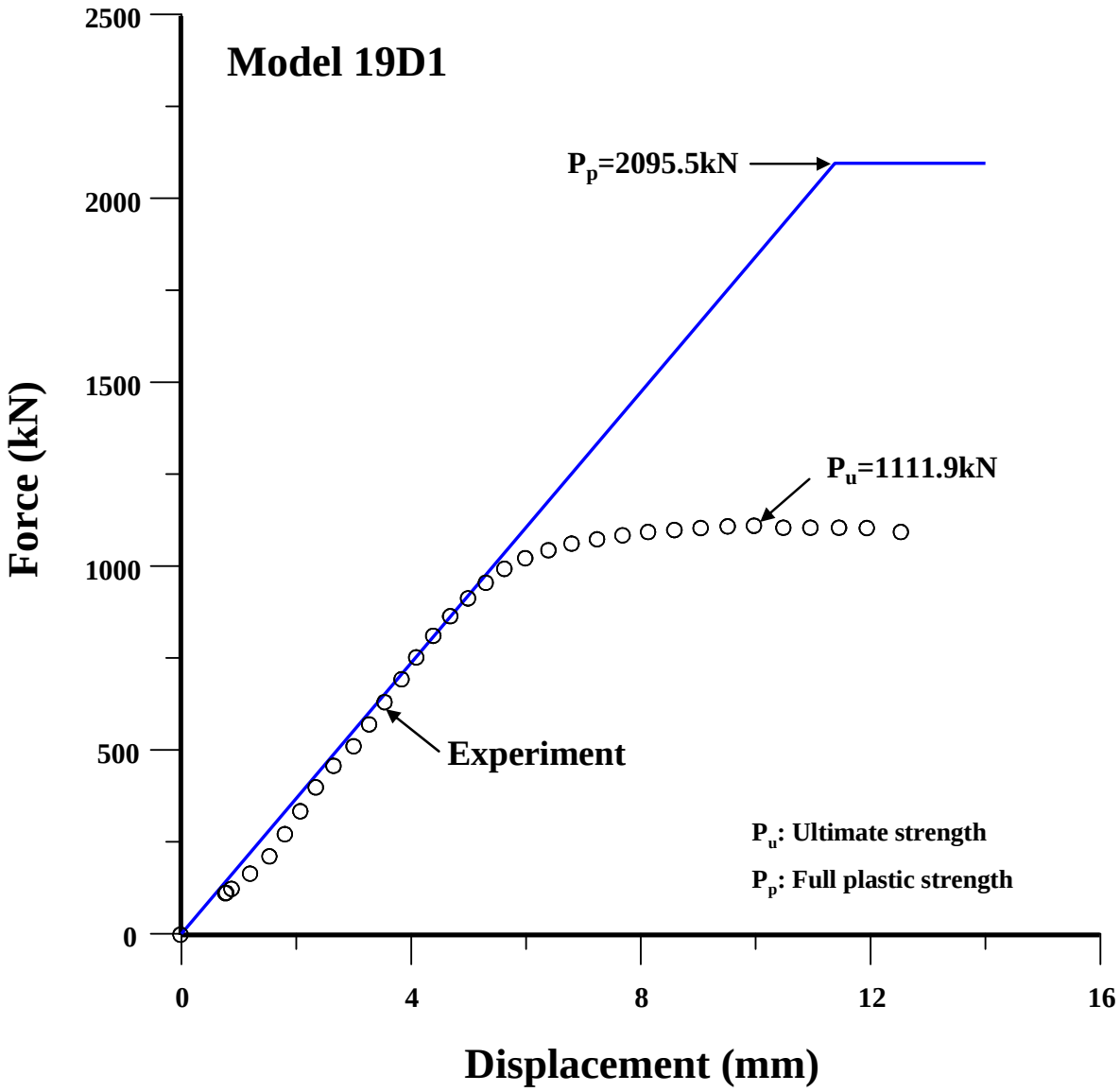

Figure 5.10(a) Relationship between axial compressive force and axial compressive displacement for test structure 19D1

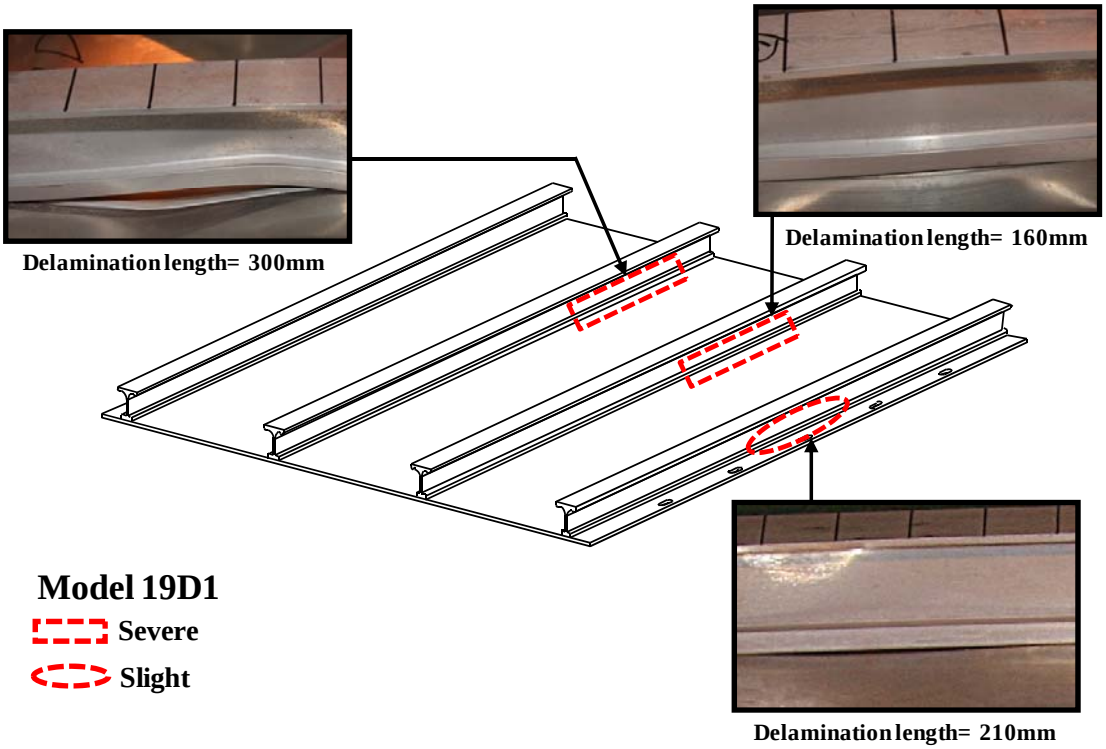

Figure 5.10(b) Photo of the delamination failure in test structure 19D1, taken at the end of testing

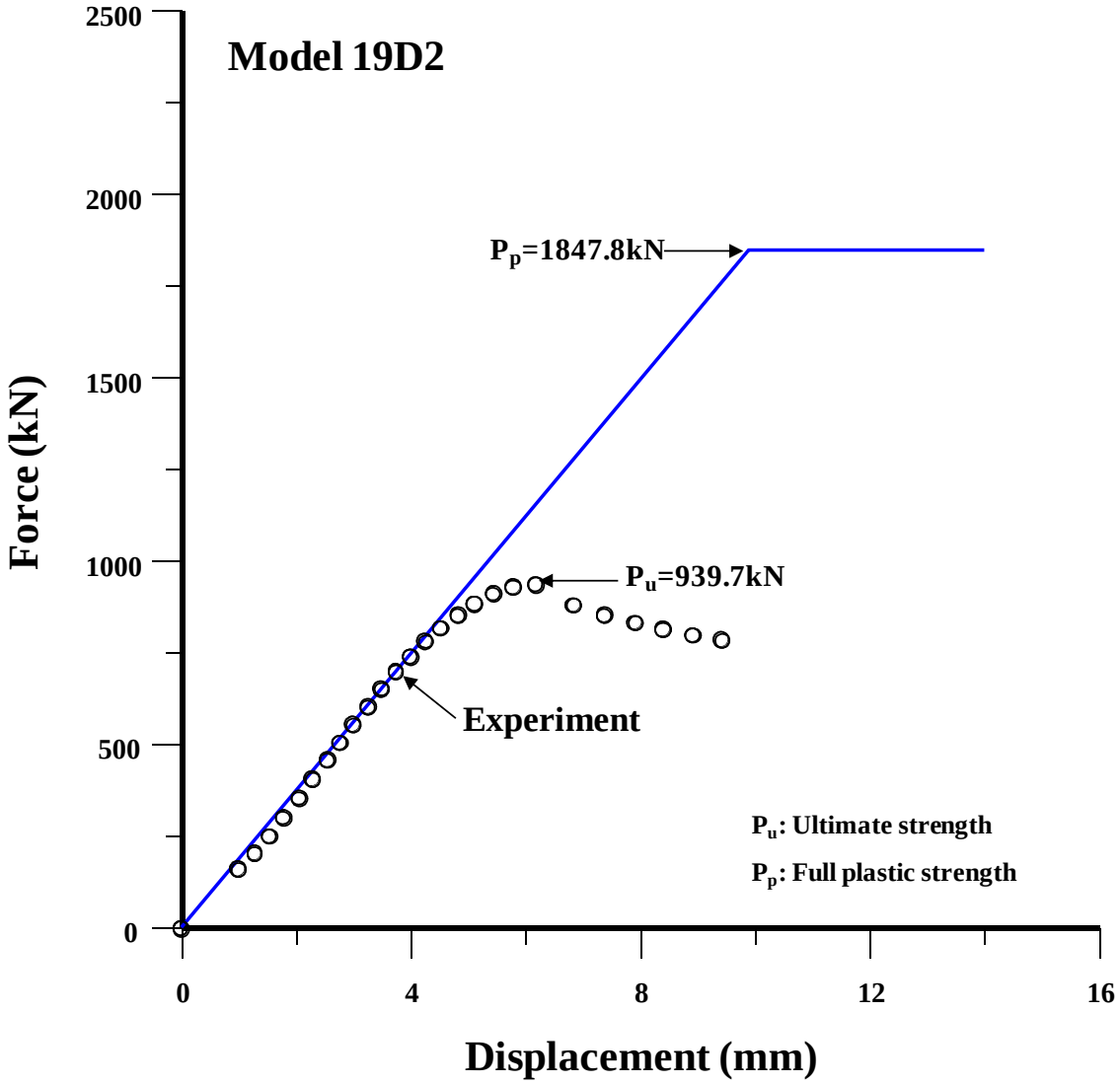

Figure 5.11(a) Relationship between axial compressive force and axial compressive displacement for test structure 19D2

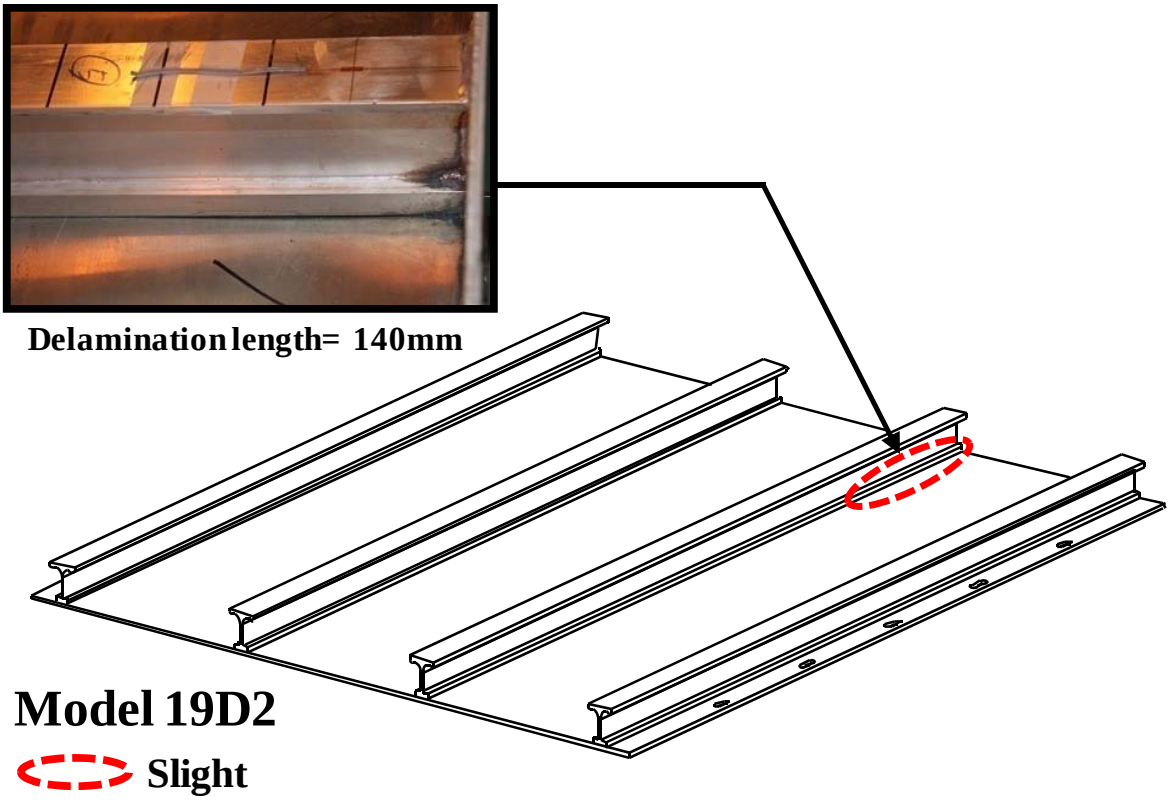

Figure 5.11(b) Photo of the delamination failure in test structure 19D2, taken at the end of testing

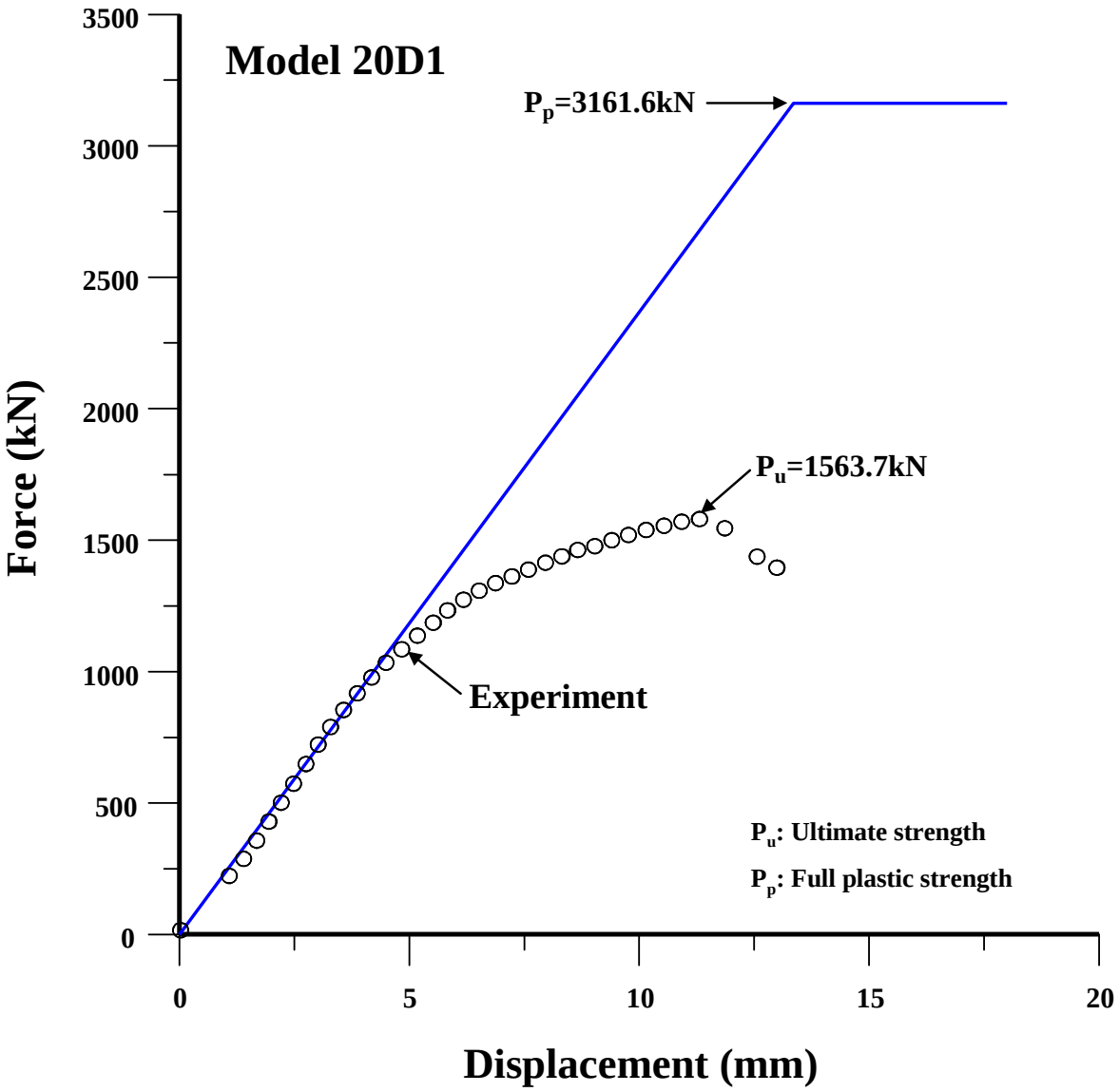

Figure 5.12(a) Relationship between the axial compressive force and axial compressive displacement for test structure 20D1

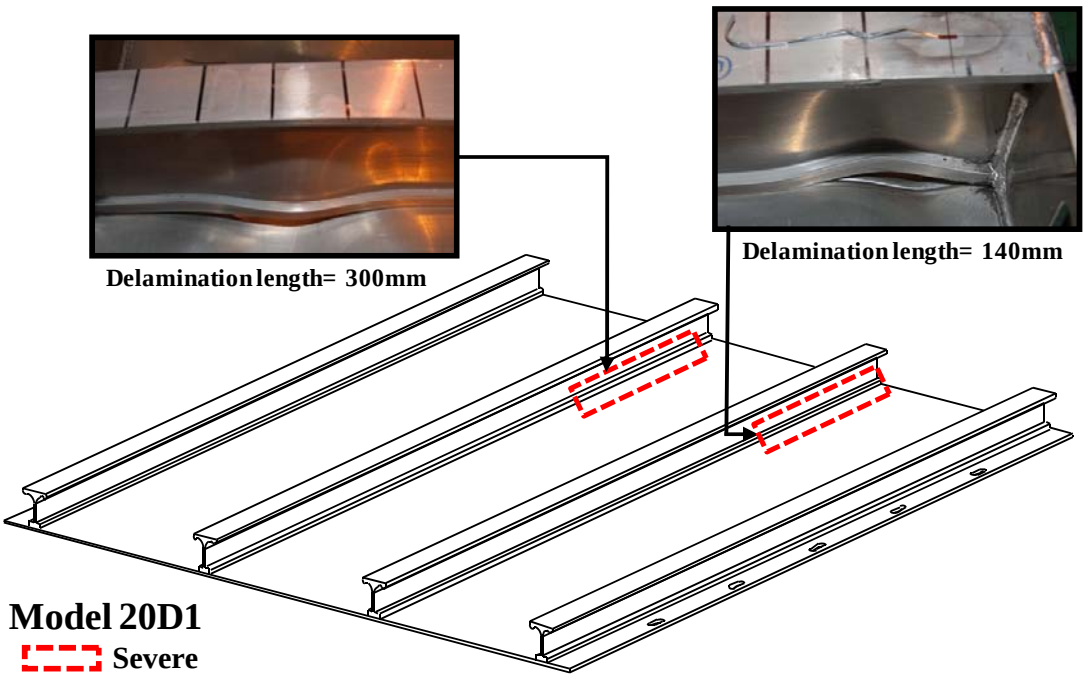

Figure 5.12(b) Photo of the delamination failure in test structure 20D1, taken at the end of testing

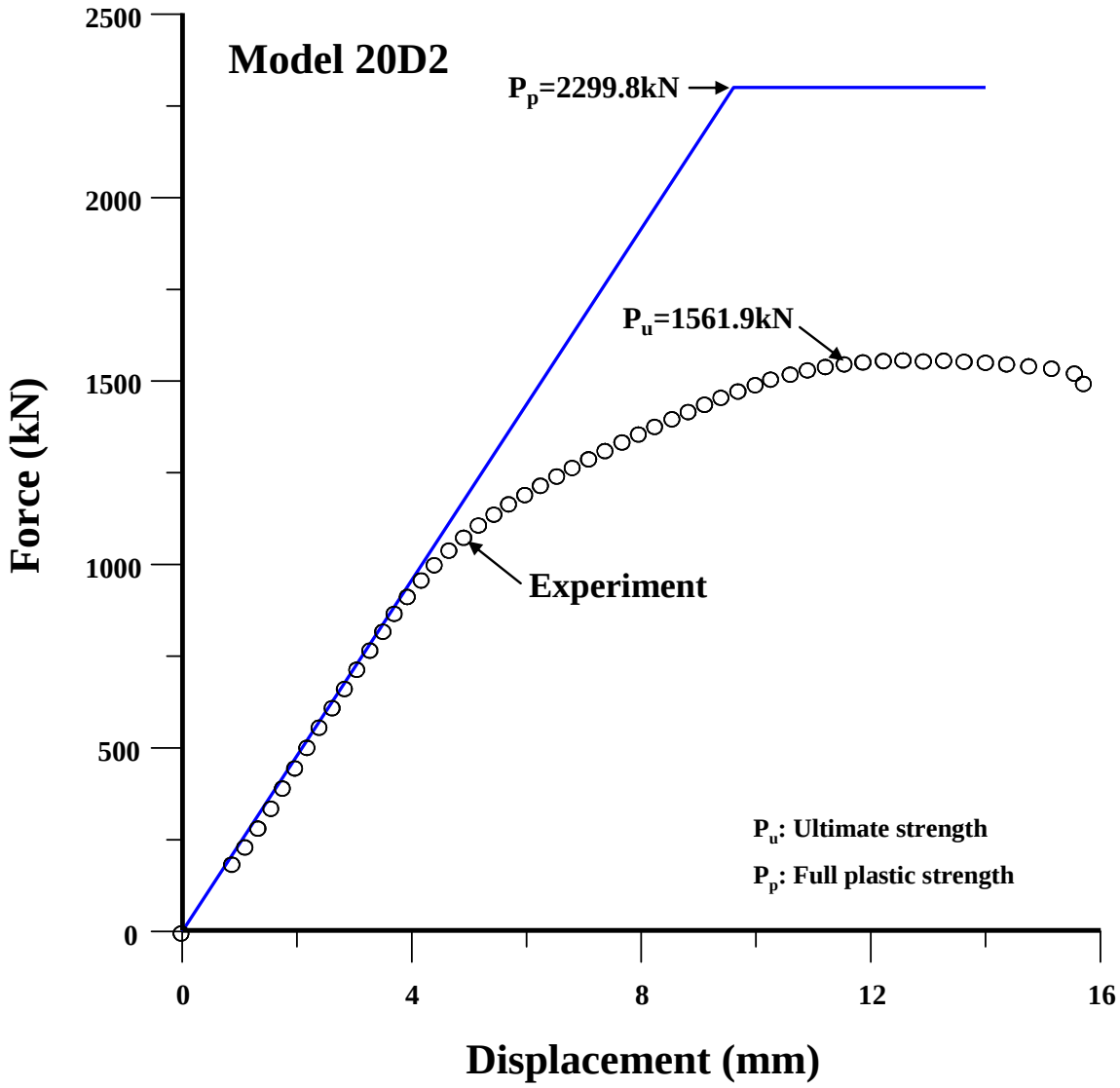

Figure 5.13(a) Relationship between axial compressive force and axial compressive displacement for test structure 20D2

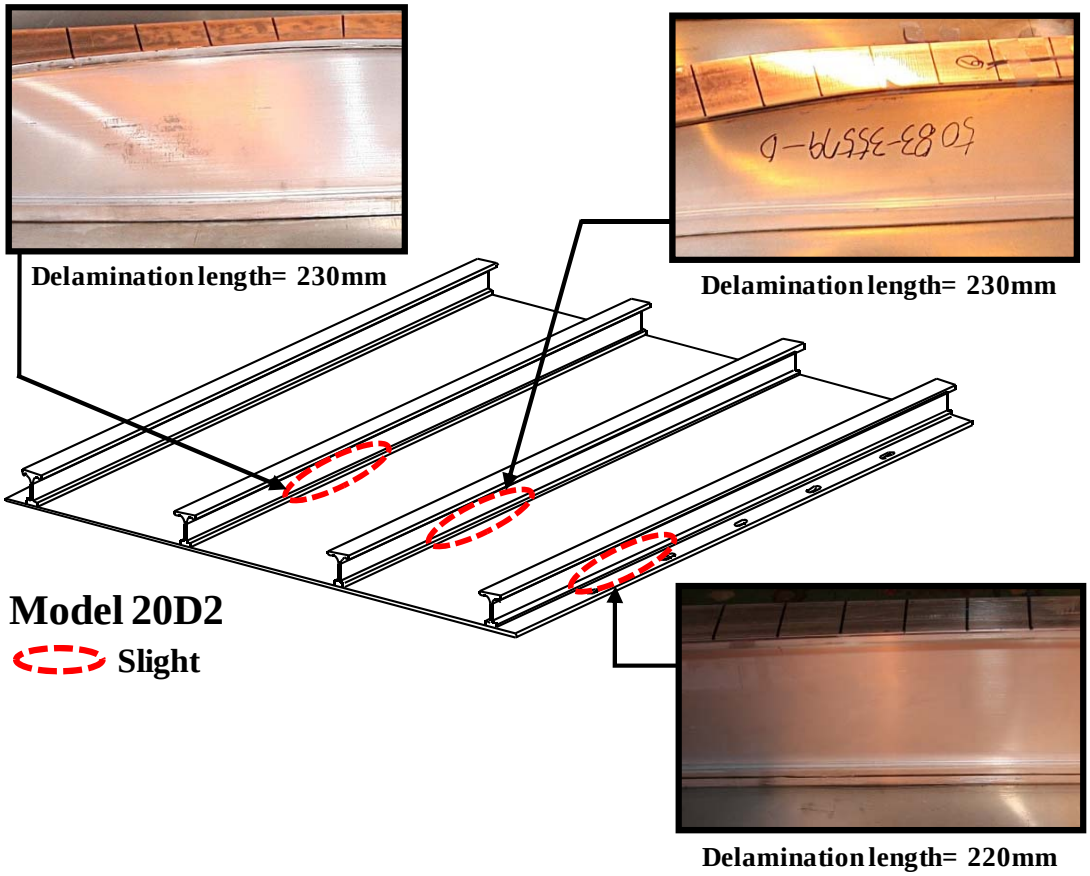

Figure 5.13(b) Photo of the delamination failure in test structure 20D2, taken at the end of testing

5.2.3 FSW Butt-joined Structures 19C and 20C

Figures 5.14(a) and 5.15(a) show the relationships between the axial compressive force and axial compressive displacement for test structures 19C and 20C, respectively. The fully plastic axial force without consideration of buckling is also plotted. The ultimate strength of these structures normalized by the fully plastic capacity is indicated in Table 5.1. Test structure 19C reached its ultimate strength via Collapse Mode II (collapse of the plating without failure of the stiffeners), as shown in Figure 5.14(b), while test structure 20C showed Collapse Mode IV (local buckling of stiffener web), as shown in Figure 5.15(b).

Delamination also occurred in the FSW butt-joined area between plates, as those shown in Figure 5.14(c) and 5.15(b). Test structure 19C showed delamination after the ultimate strength had been reached, but delamination occurred in test structure 20C prior to the ultimate strength. Again, it is thought that the ultimate strength of test structure 20C is unusually small compared to nonlinear finite element computations presented in Chapter 6.

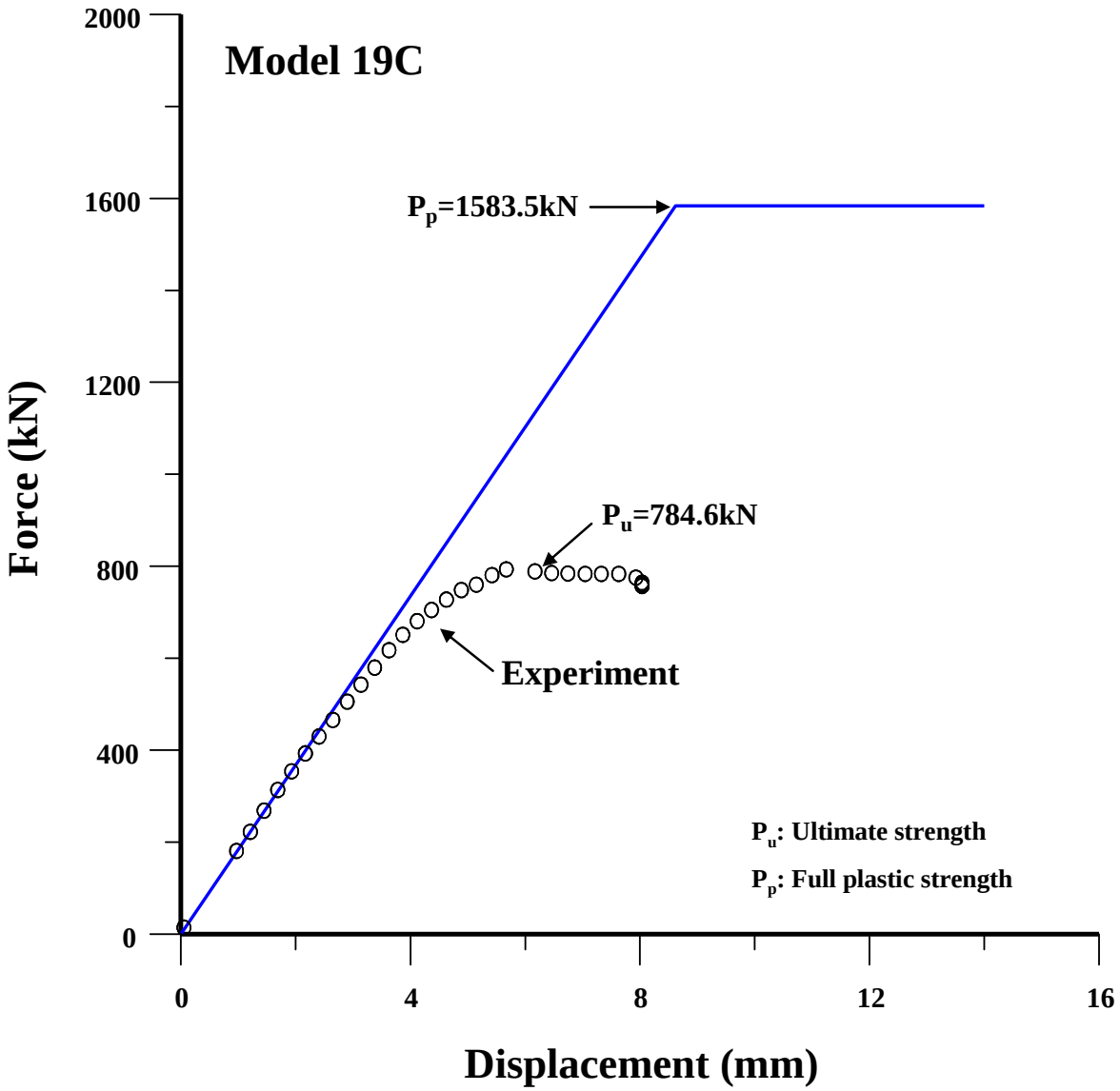

Figure 5.14(a) Relationship between axial compressive force and axial compressive displacement for test structure 19C

It is interesting to note that the delaminations in the friction stir butt-welds have occurred only at one free edge of the butt joint but not at both free edges, with the configuration of the butt welds described in Table 3.9 of Chapter 3.

The pre-collapse delamination in friction stir butt-welded structures can of course reduce the ultimate compressive strength performance significantly. Also, the pre- or post-collapse delamination in friction stir butt-welded structures should be of great concern because the water tightness of the stiffened plate structure can not be assured anymore. In this regard, the friction stir lap-weld method may be more promising than the friction stir butt-weld method, because the post-collapse delamination is not of major concern in the friction stir lap-welded structures.

Further study is recommended to manage the quality assurance in the friction stir butt-welded region in association with the mechanical property and delamination, similar to the friction stir lap-welded region as described in Section 5.2.2.

Figure 5.14(b) Photo of Collapse Mode II in test structure 19C

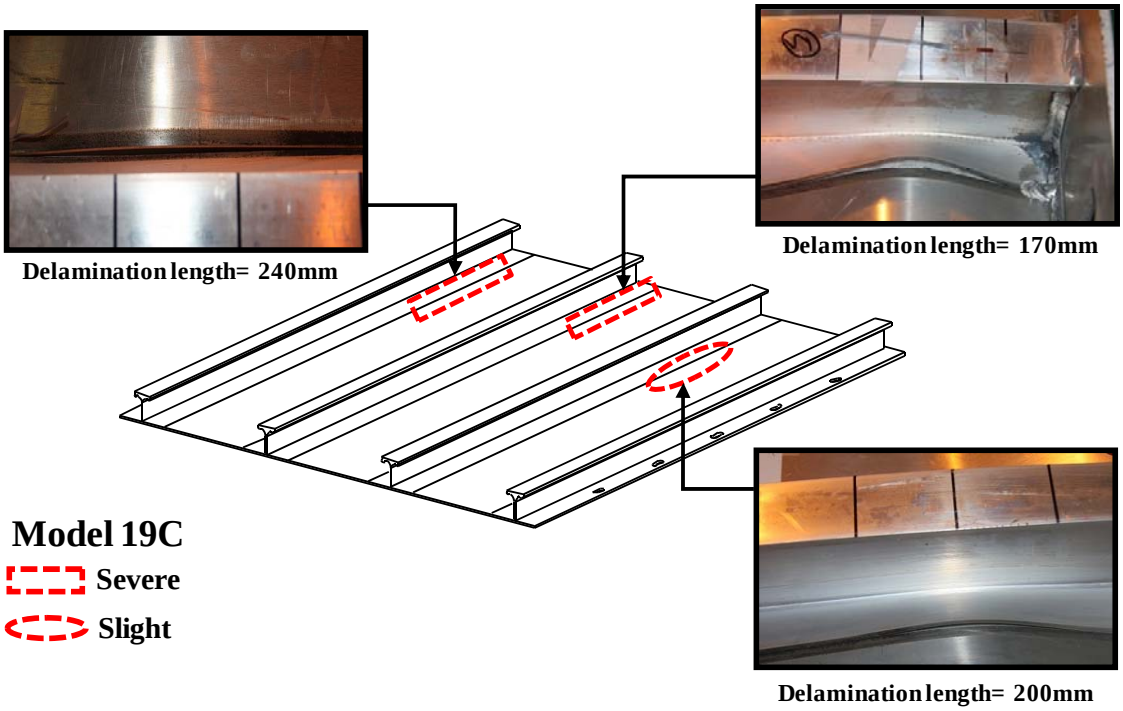

Figure 5.14(c) Photo of the delamination failure in test structure 19C, taken at the end of testing

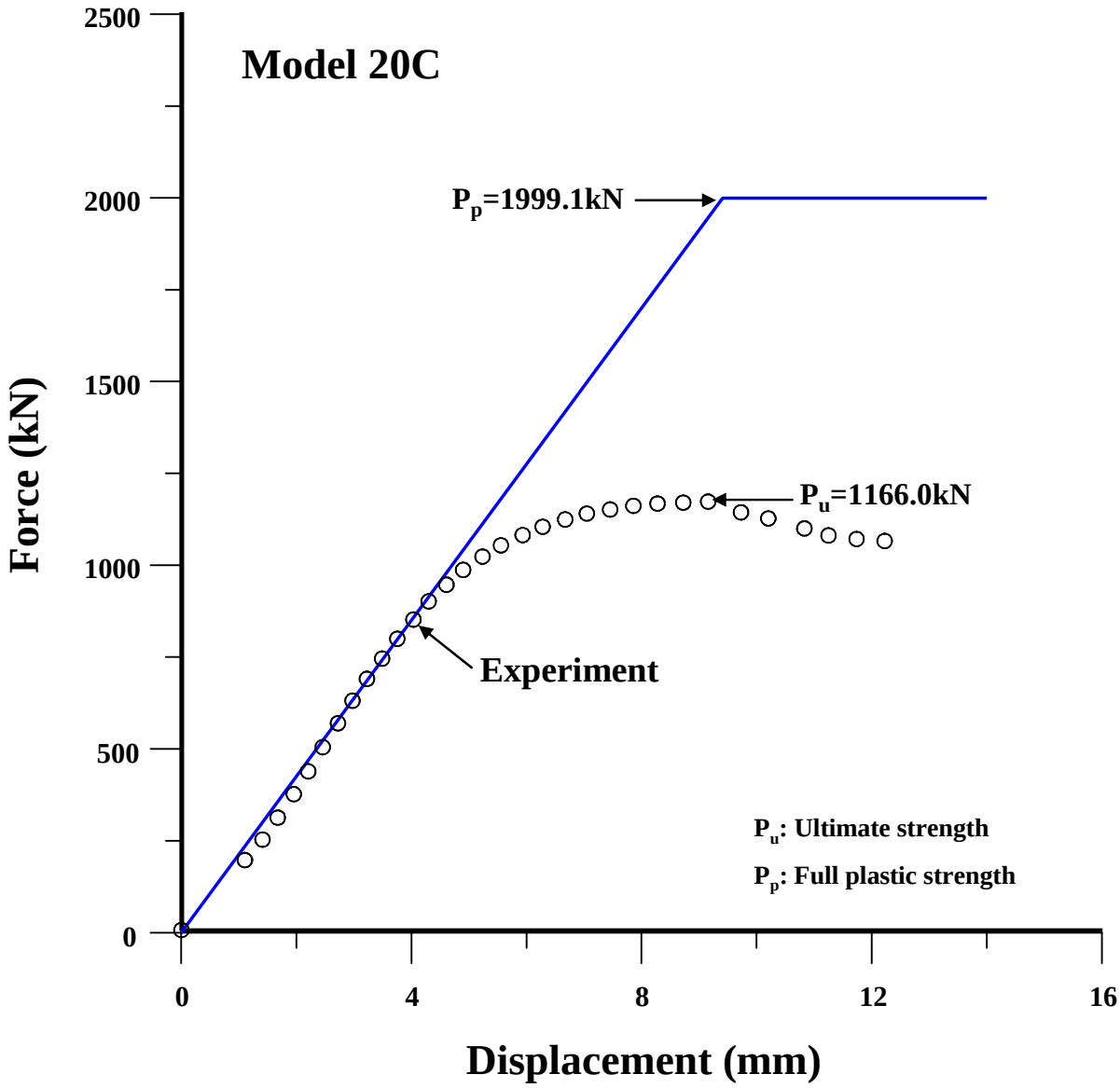

Figure 5.15(a) Relationship between axial compressive force and axial compressive displacement for test structure 20C

Figure 5.15(b) Photo of Collapse Mode IV in test structure 20C

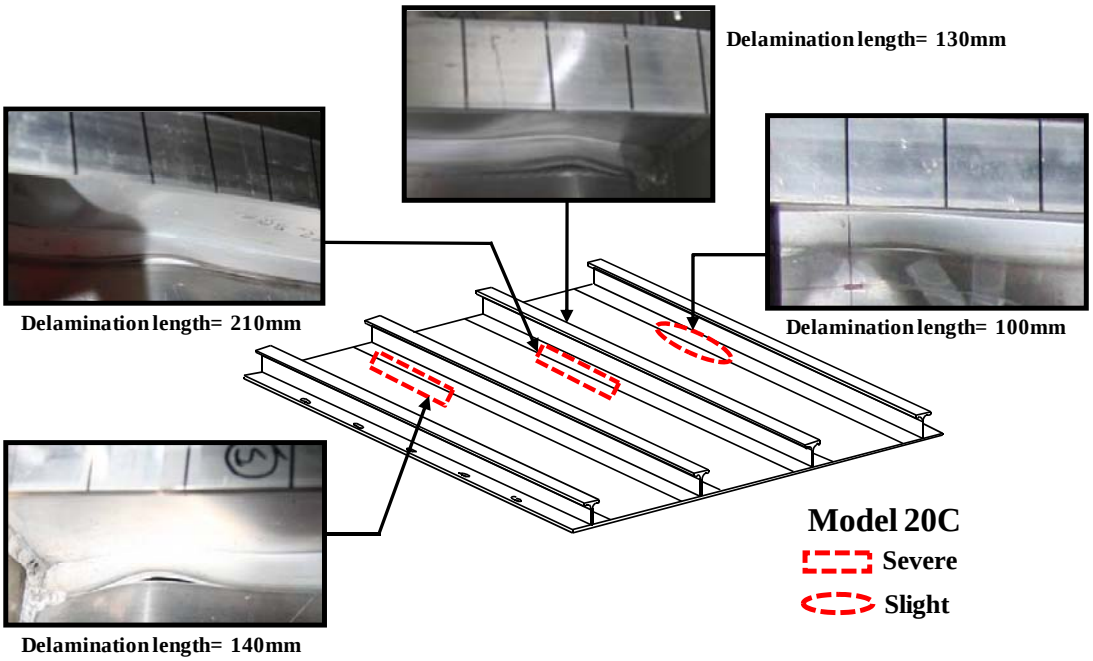

Figure 5.15(c) Photo of the delamination failure in test structure 20C, taken at the end of testing

5.3 SSC-451 Database

Figures 5.16 to 5.27 show the relationships between the axial compressive force and axial compressive displacement for the fusion-welded test structures in SSC-451, until and after ultimate strength had been reached, where the details of the extrusion profiles and dimensions, and weld methods are indicated in Tables 3.6(b) to 3.8(b) and Table 3.9. Table 5.2 summarizes the ultimate compressive strength and associated collapse mode of the structures.

Table 5.2 Summary of the ultimate compressive strength and associated collapse mode for the SSC-451 test structures

Model (Fig. No.)	P_p (kN)	Experiment			
		P_u (kN)	P_u/P_p	Collapse mode	Delamination failure
5 (5.16)	1831.3	777.8	0.425	III	No
6 (5.17)	1831.2	918.0	0.501	III	No
7 (5.18)	1903.4	931.8	0.490	III	No
8 (5.19)	2482.8	1513.8	0.610	V	No
17 (5.20)	2049.0	778.0	0.380	III	No
18 (5.21)	2048.8	829.6	0.405	III	No
19 (5.22)	2160.5	970.5	0.449	III,IV	No
20 (5.23)	3057.1	1659.2	0.543	III,IV	No
29 (5.24)	1645.1	791.0	0.481	V	No
30 (5.25)	1645.0	908.7	0.552	V	No
31 (5.26)	1717.2	895.9	0.522	III,IV	No
32 (5.27)	2296.6	1367.3	0.595	III,IV	No

Note: P_u = ultimate compressive force; P_p = fully plastic axial force = $\sum_i A_i \sigma_{Yi}$ where A_i = area of the (i)the cross-section and σ_{Yi} = material yield strength of the (i)th cross-section.

All the test structures reached the ultimate strength by an anticipated collapse mode. Most structures showed one distinct collapse mode until ultimate strength had been reached, but test structures 19, 20, 31 and 32 collapsed via combined modes of III (beam-column type collapse) and IV (local buckling of stiffener web). No delamination failure occurred in the fusion welded area of all the SSC-451 test structures.

The ultimate compressive strength performance of these test structures was then compared with that for the FSW test structures investigated in the present project as discussed in Chapters 6 and 7.

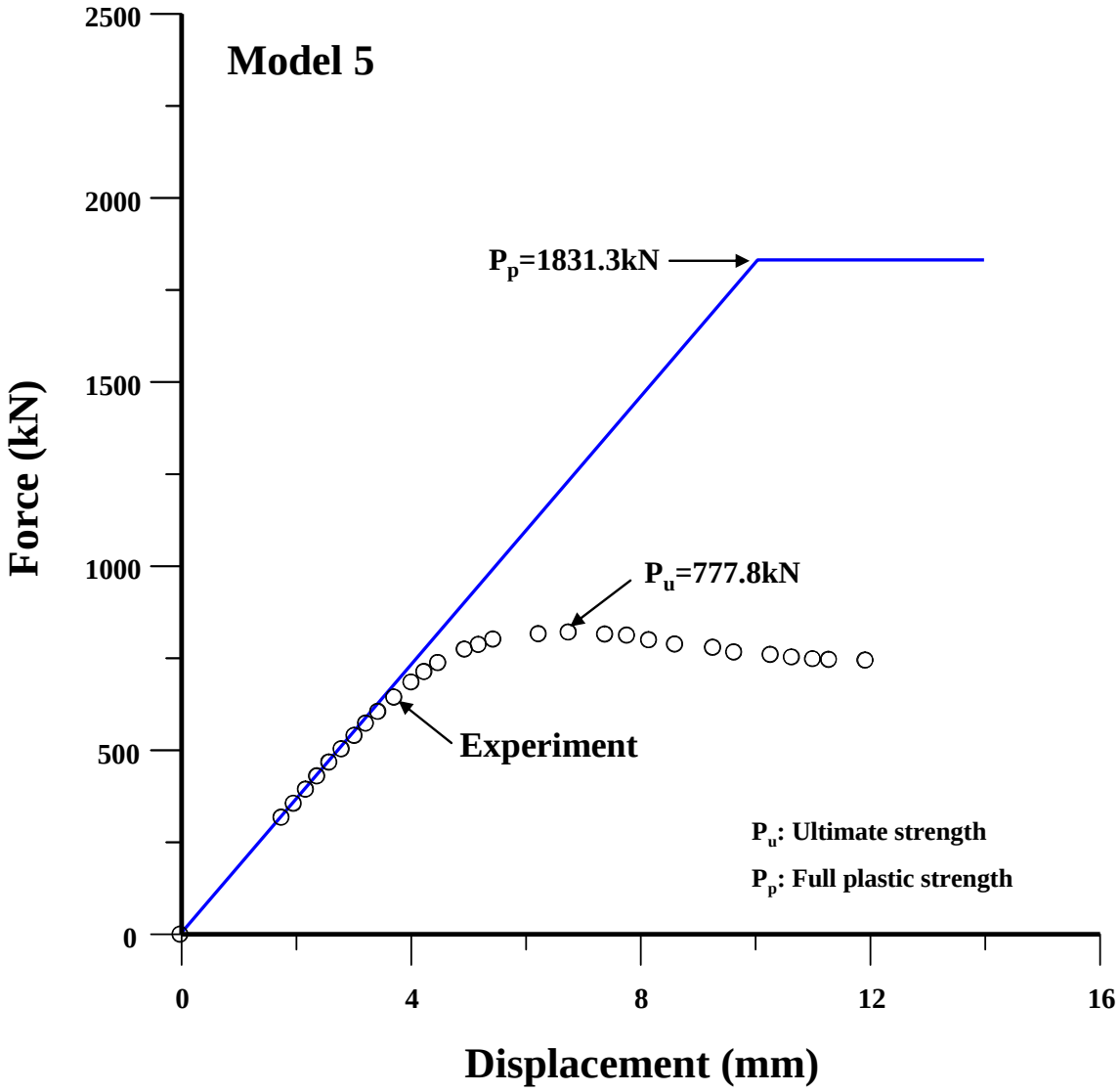

Figure 5.16 Relationship between axial compressive force and axial compressive displacement for test structure 5 in SSC-451

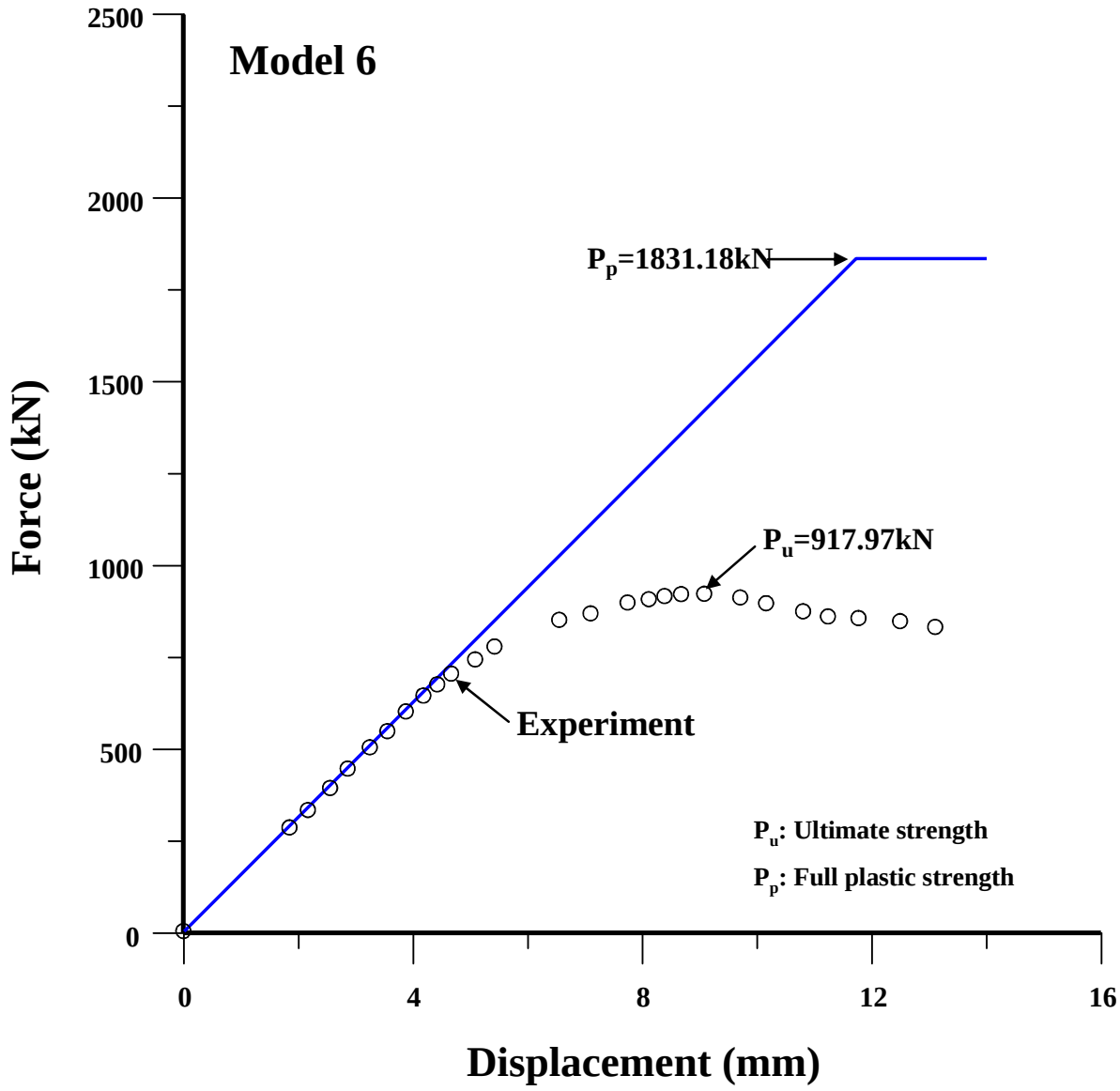

Figure 5.17 Relationship between axial compressive force and axial compressive displacement for test structure 6 in SSC-451

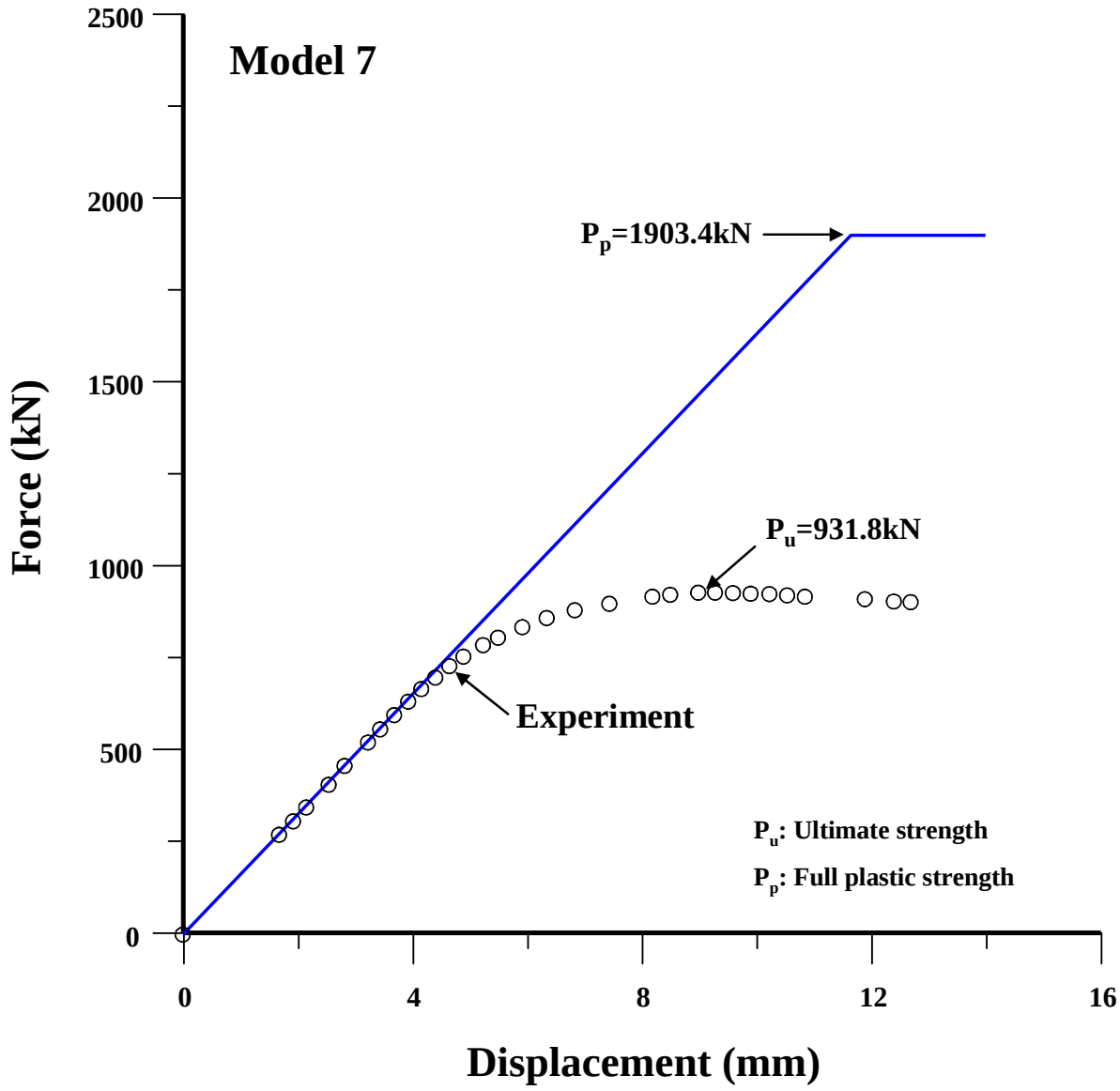

Figure 5.18 Relationship between axial compressive force and axial compressive displacement for test structure 7 in SSC-451

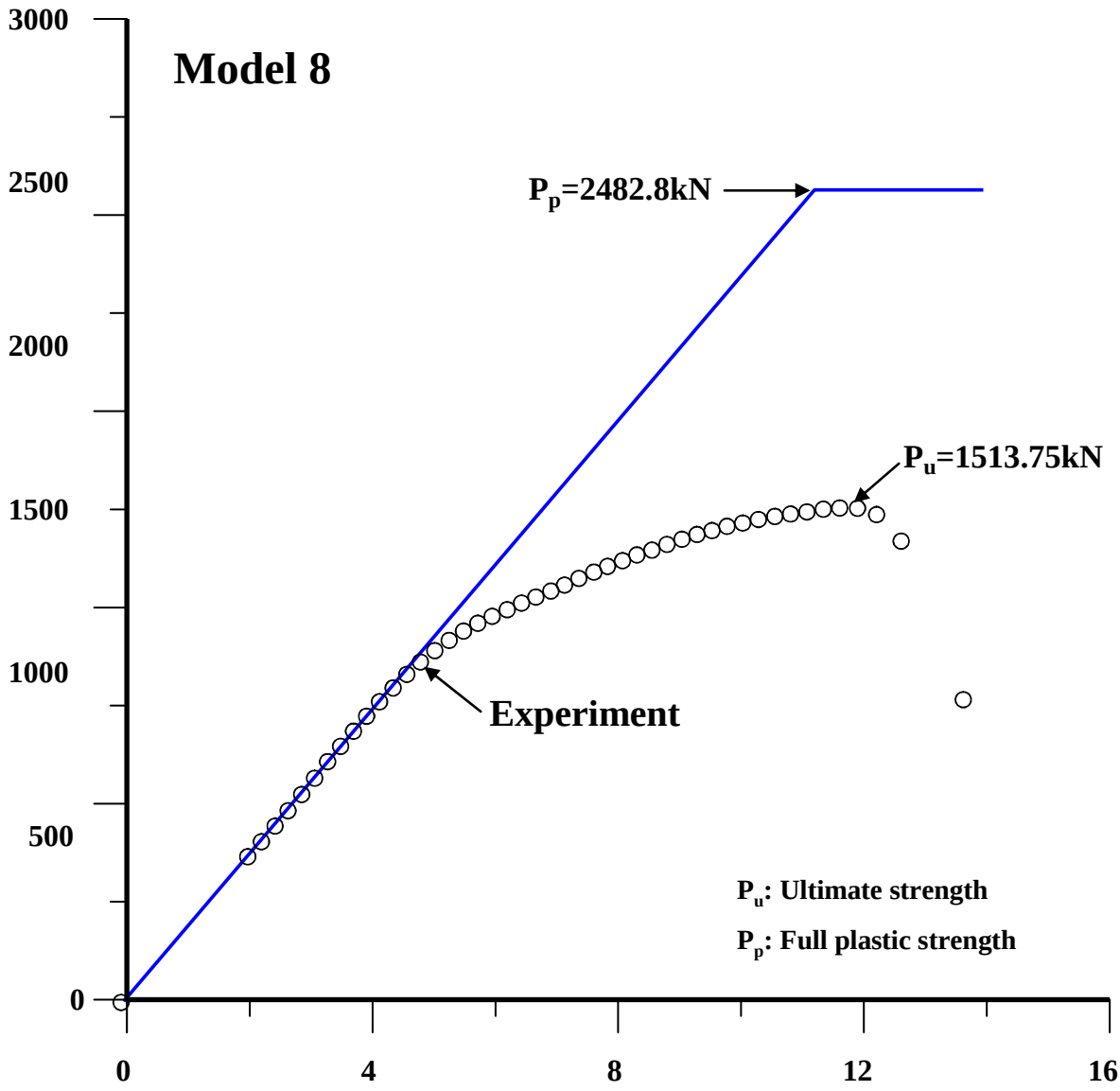

Figure 5.19 Relationship between axial compressive force and axial compressive displacement for test structure 8 in SSC-451

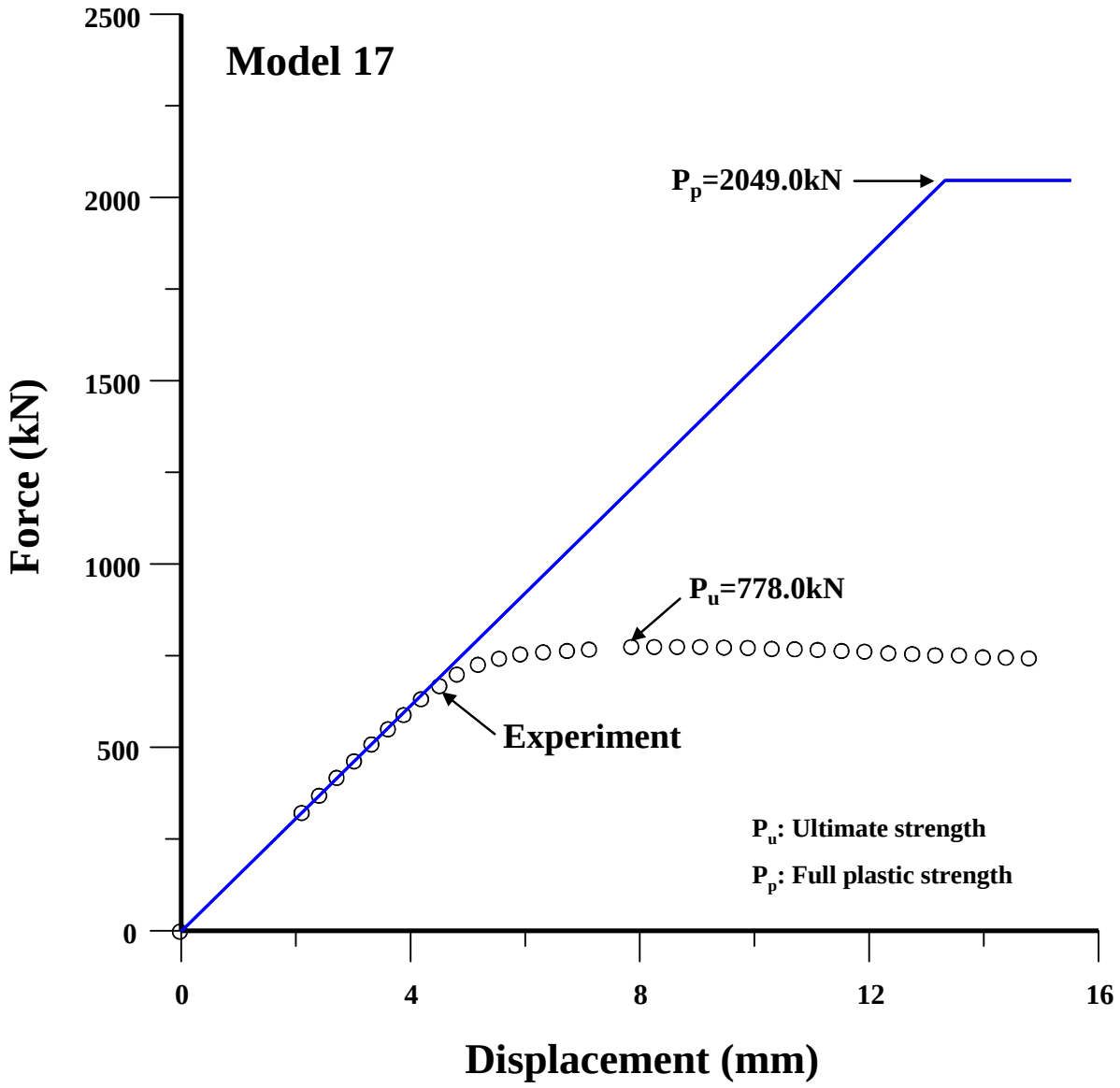

Figure 5.20 Relationship between axial compressive force and axial compressive displacement for test structure 17 in SSC-451

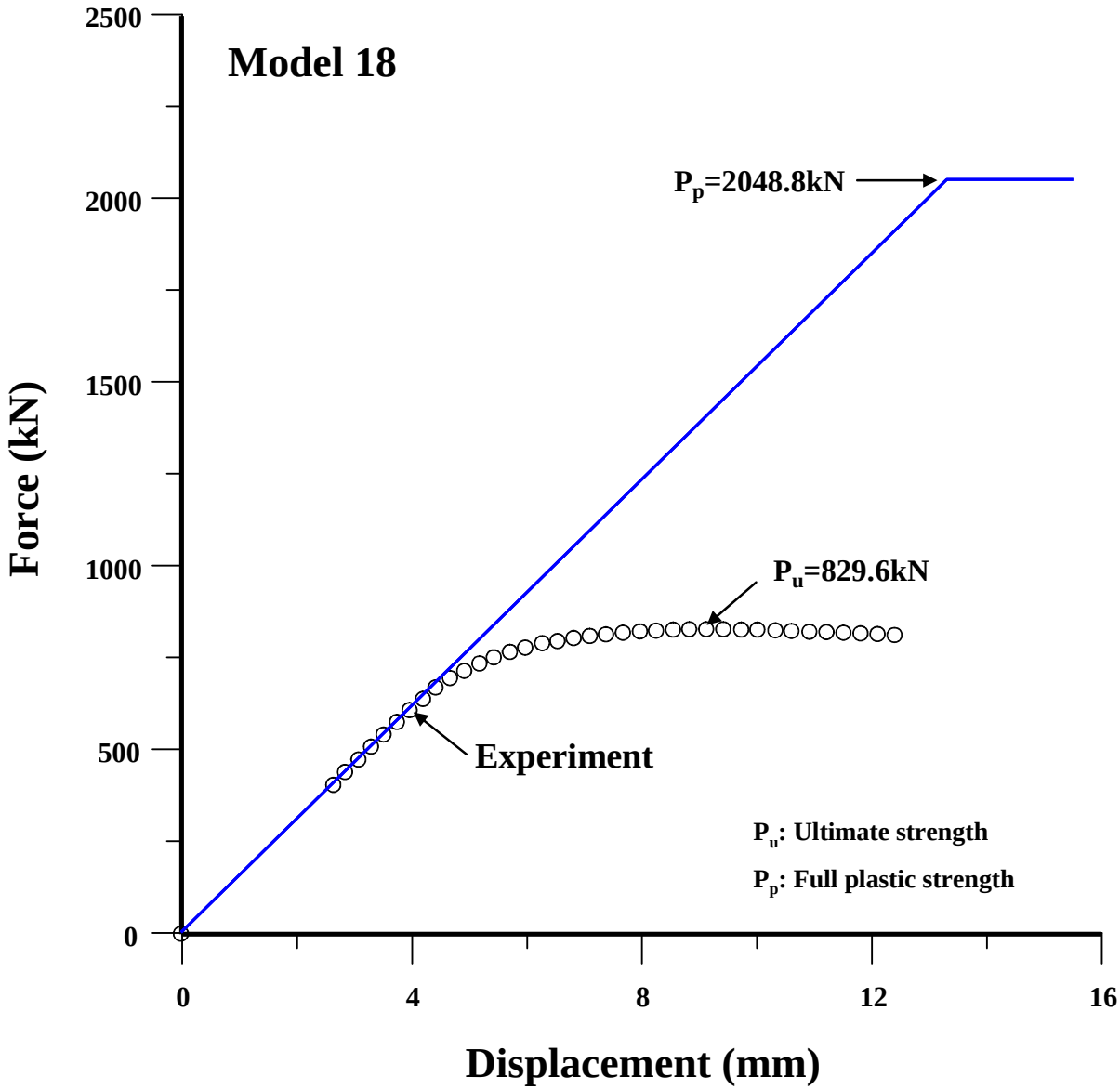

Figure 5.21 Relationship between axial compressive force and axial compressive displacement for test structure 18 in SSC-451

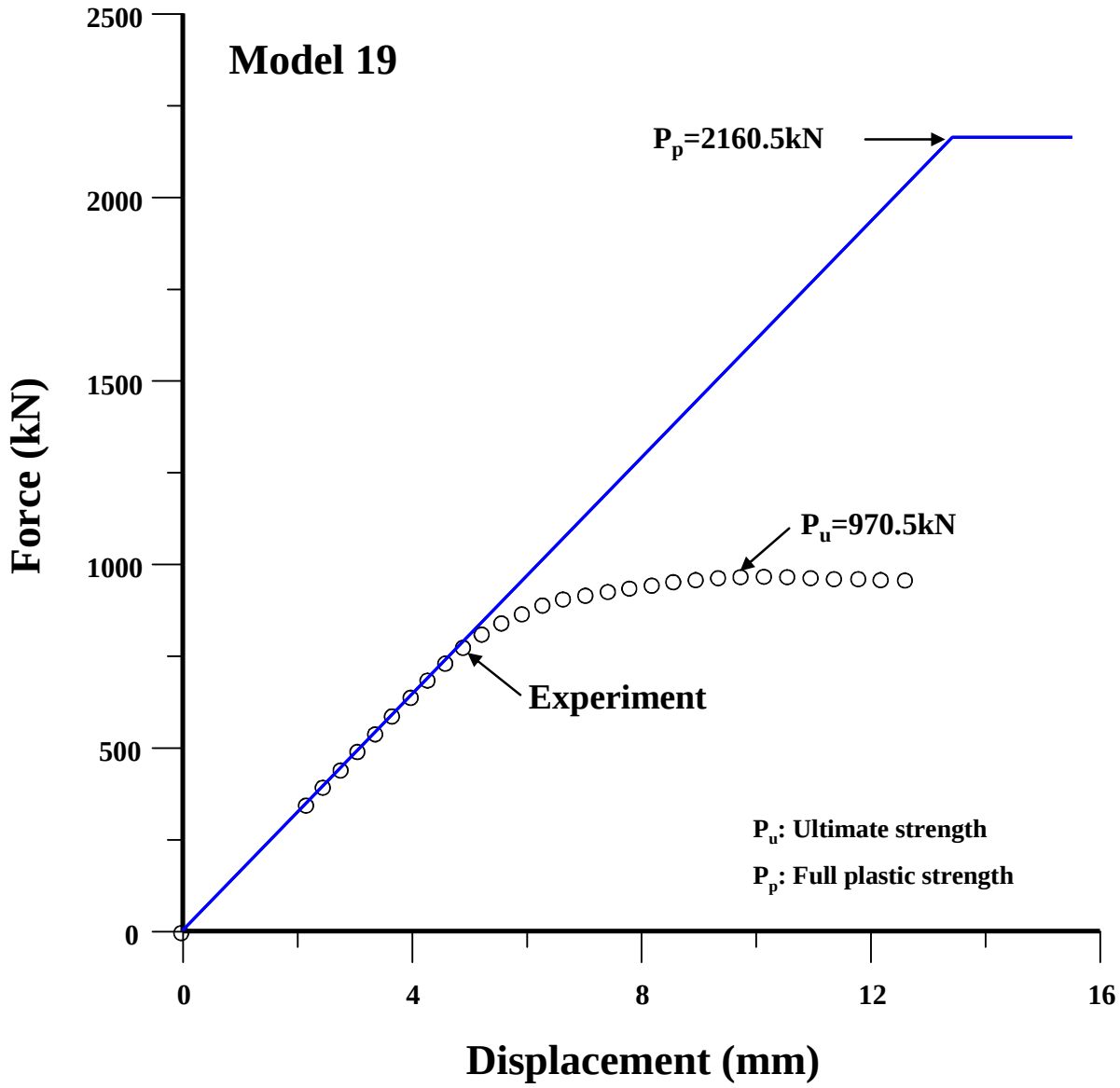

Figure 5.22 Relationship between axial compressive force and axial compressive displacement for test structure 19 in SSC-451

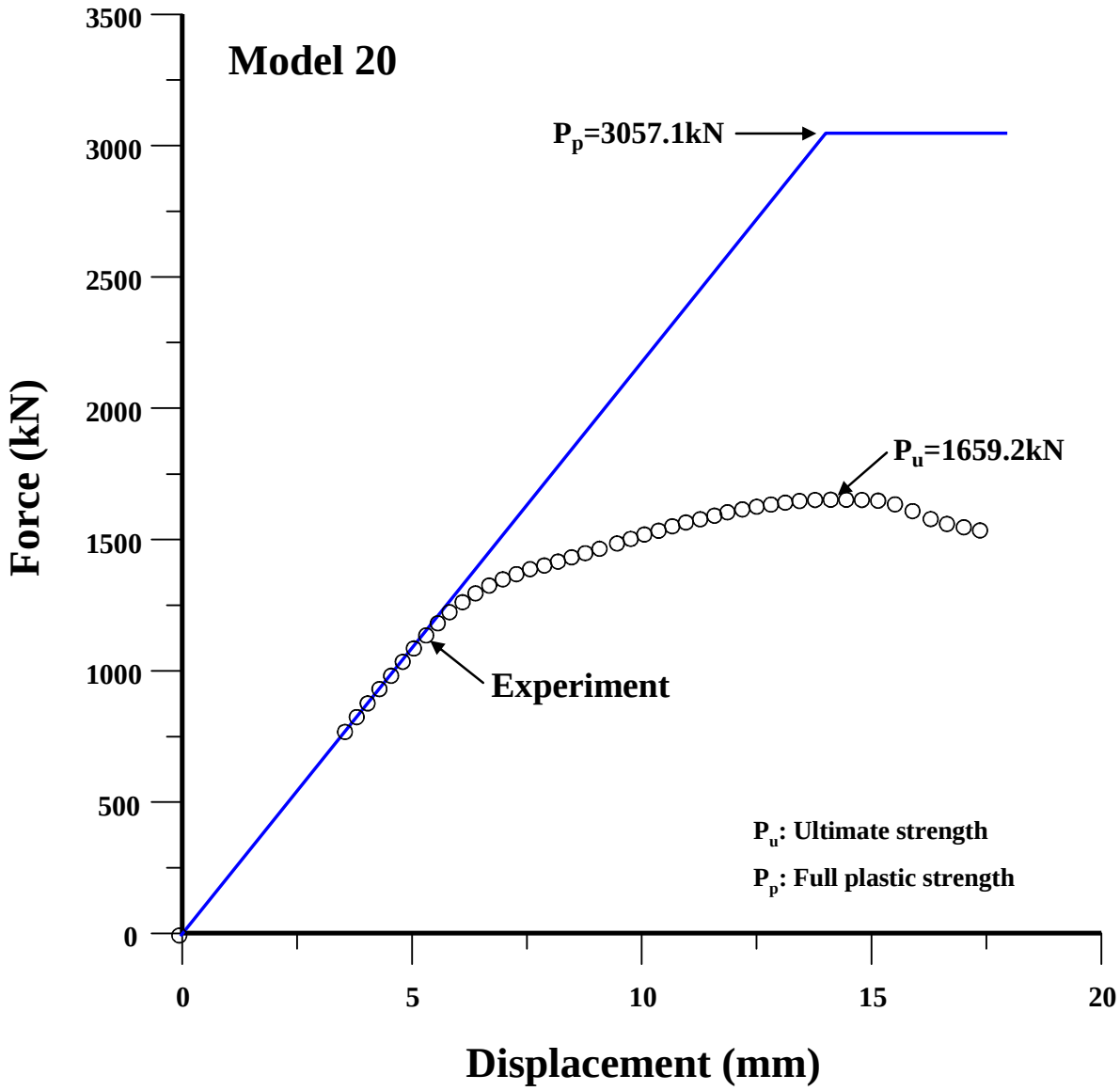

Figure 5.23 Relationship between axial compressive force and axial compressive displacement for test structure 20 in SSC-451

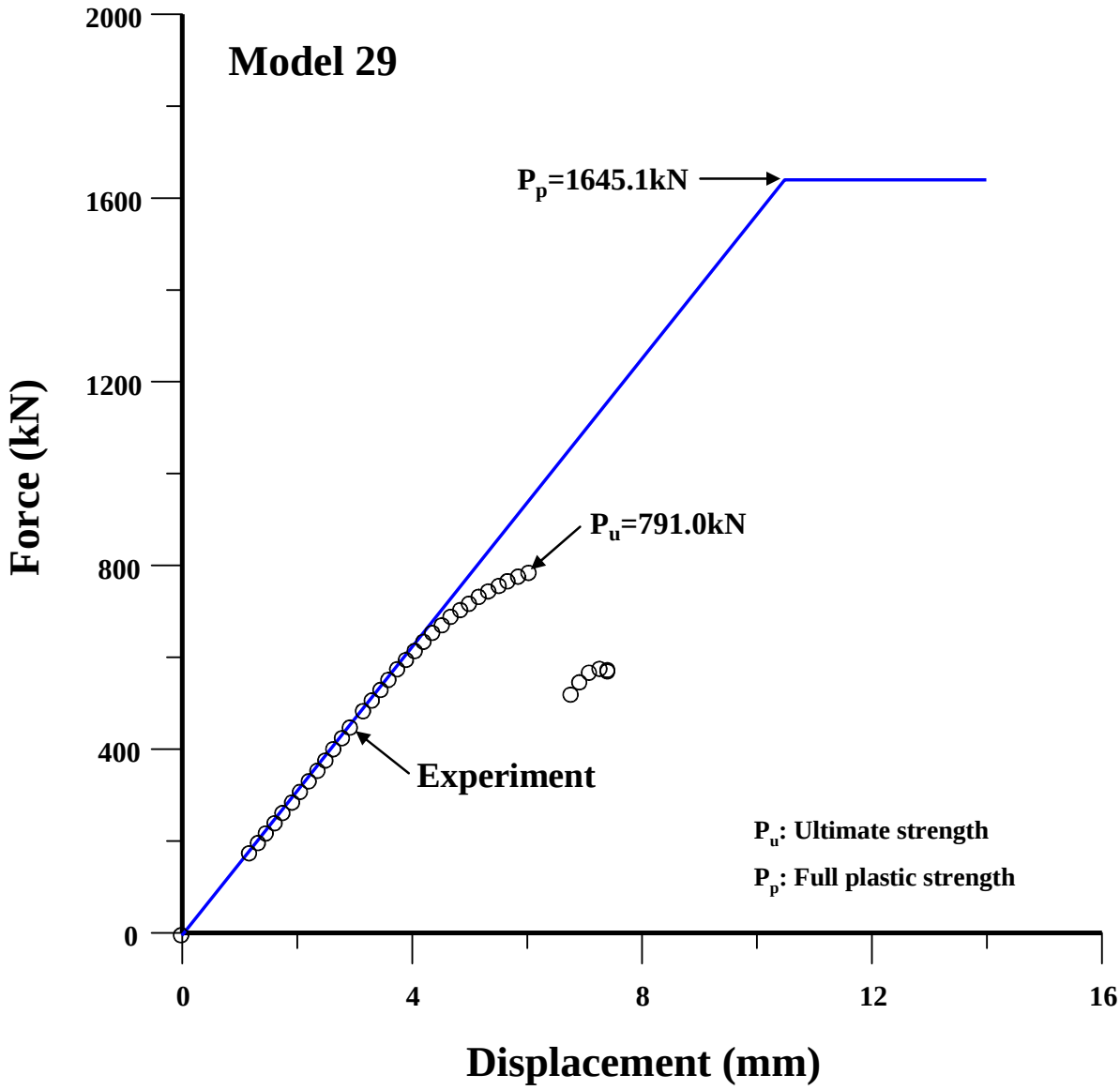

Figure 5.24 Relationship between axial compressive force and axial compressive displacement for test structure 29 in SSC-451

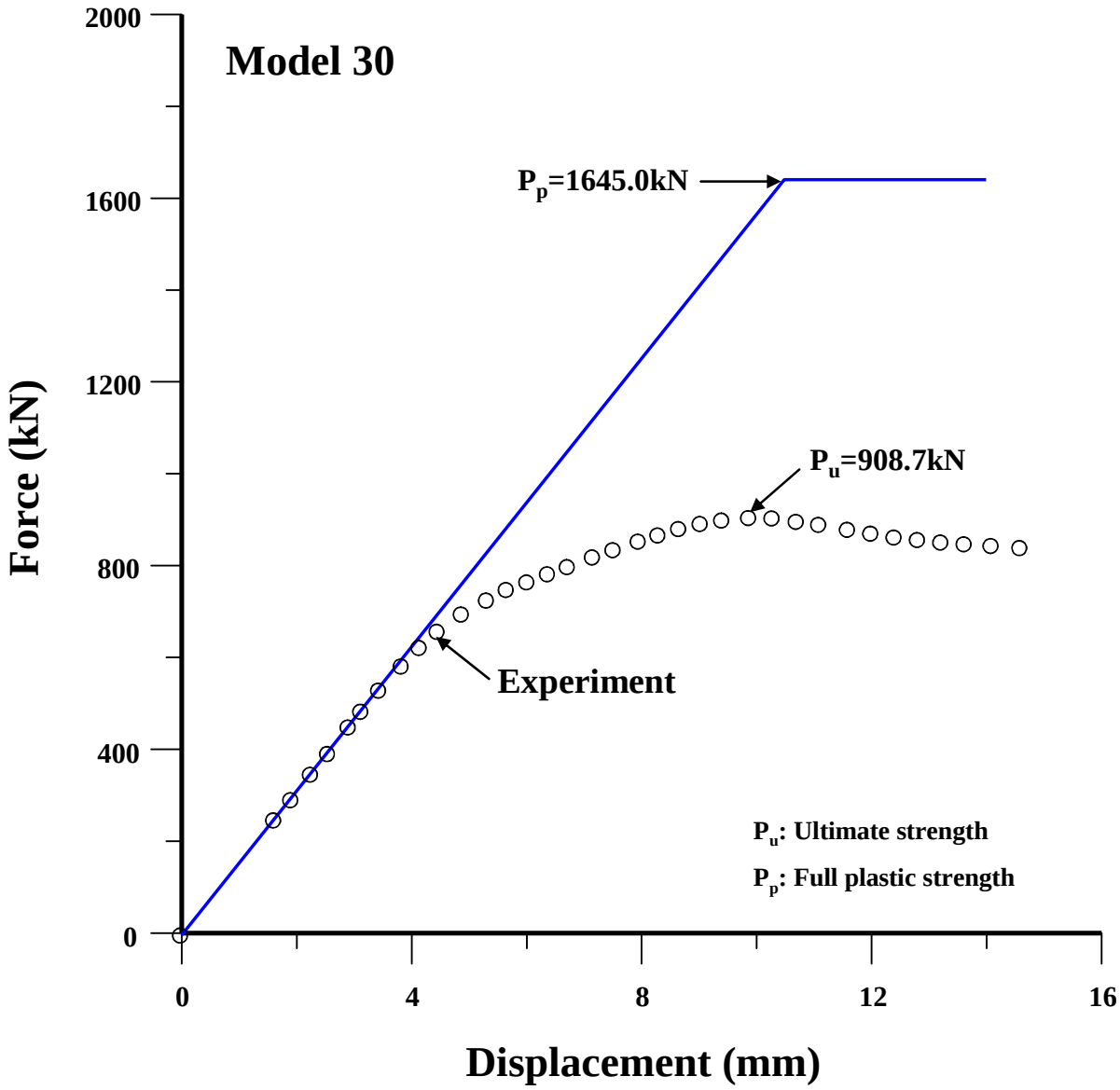

Figure 5.25 Relationship between axial compressive force and axial compressive displacement for test structure 30 in SSC-451

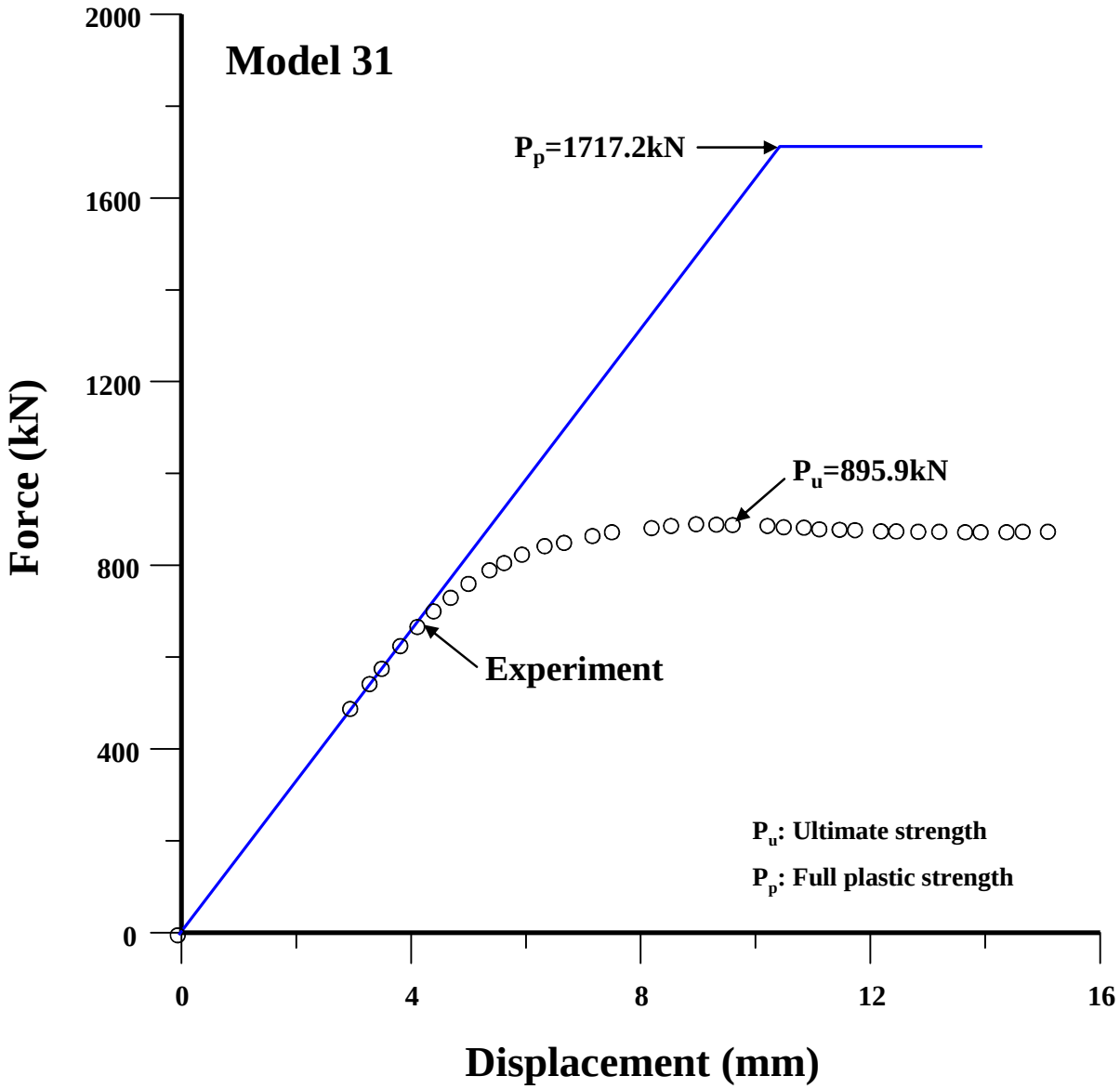

Figure 5.26 Relationship between axial compressive force and axial compressive displacement for test structure 31 in SSC-451

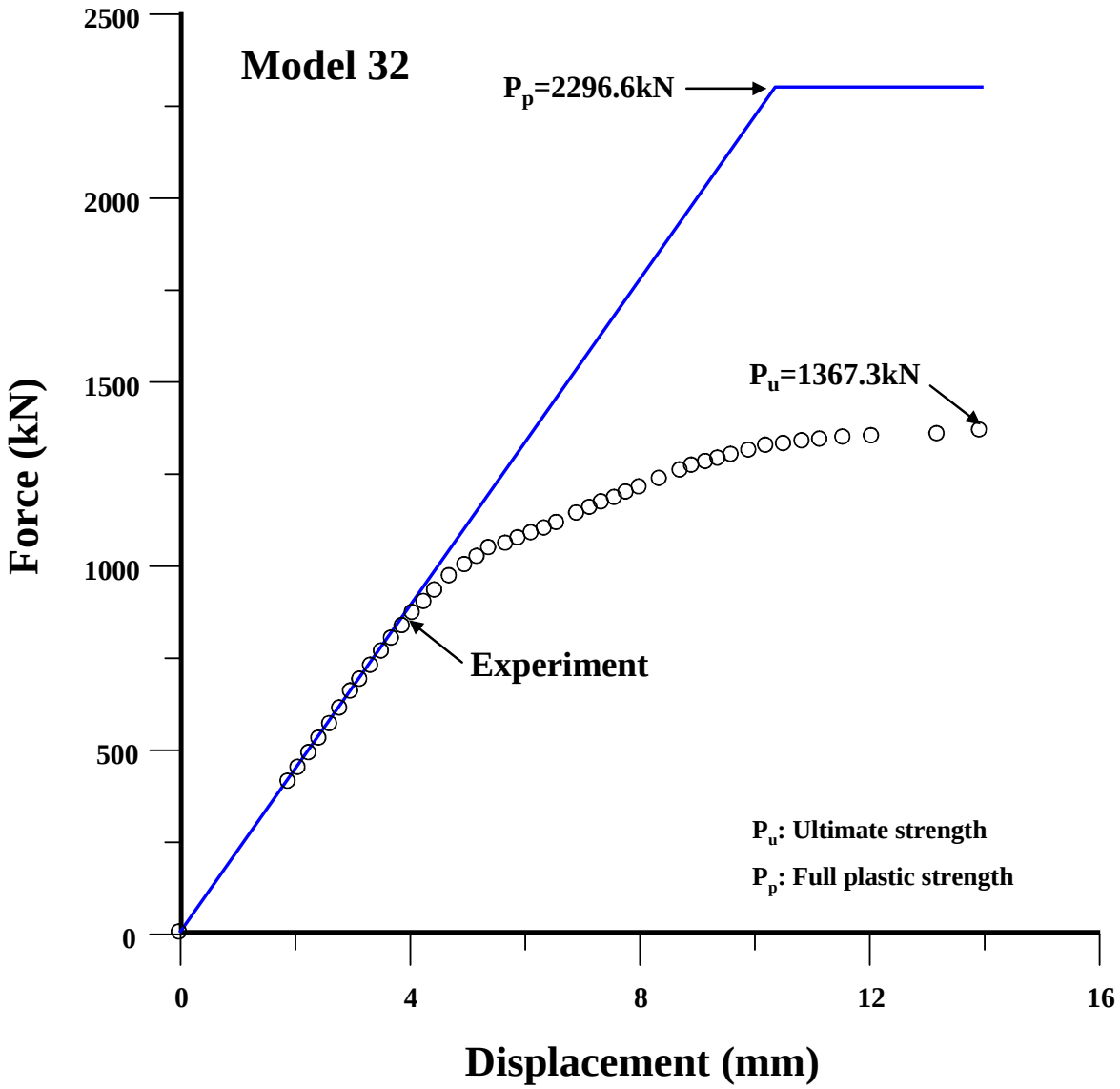

Figure 5.27 Relationship between axial compressive force and axial compressive displacement for test structure 32 in SSC-451

Chapter 6 Nonlinear Finite Element Method Computations

6.1 Structural Modeling

The ANSYS (2008) nonlinear finite element method was employed to compute the ultimate strength behavior of the test structures. The following describes the structural modeling technique applied in the present study.

6.1.1 Extent of the Analysis

It is desirable to extend the extent of the analysis to the entire structure under consideration. If the funds available for structural modeling and computation are limited, however, only a part of the target structure may be included in the finite element modeling.

If only a partial structure is involved in the analysis, then it is important to realize that an artificial boundary is often formed for the target structure, and thus it must be modeled as appropriate in conjunction with mathematics and engineering.

Current practices in the maritime industry show that structural modeling with analysis to a partial extent provides reasonable solutions that are good enough for the practical purposes of structural design and strength assessment as long as the boundary conditions among the other factors are idealized in a relevant way.

The analysis of a partial structure usually involves a cut out of the target structure with respect to the symmetric boundary in terms of structural deformations and failure modes. The extent of the analysis should, in fact, be expanded if possible to reflect the boundary conditions of the target structure more realistically.

Figure 6.1 presents some examples that show the extent of the analysis for the plates and stiffened plate structures. In SSC-451, the two-bay plate-stiffener combination model shown in Figure 6.1(c) was employed to save computational efforts on the 78 test structures.

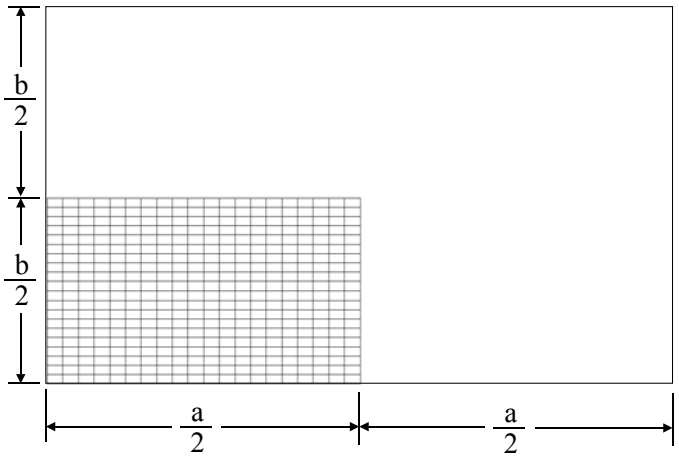

Figure 6.1(a) A quarter model for a rectangular plate under uniaxial compression

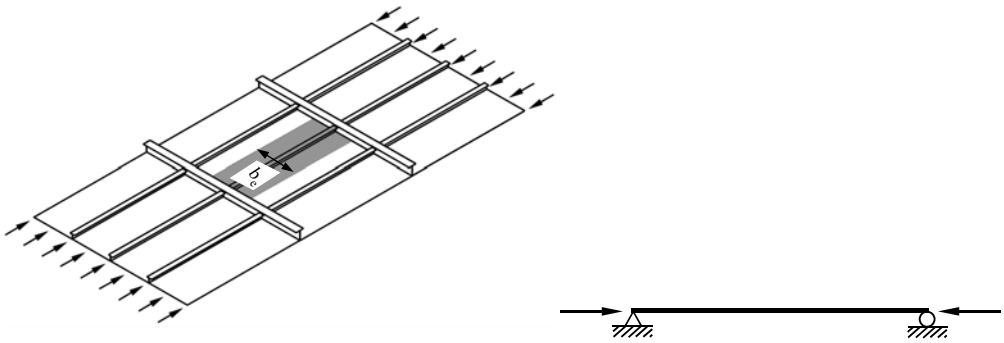

Figure 6.1(b) A one-bay plate-stiffener combination model for a stiffened plate structure under uniaxial compression

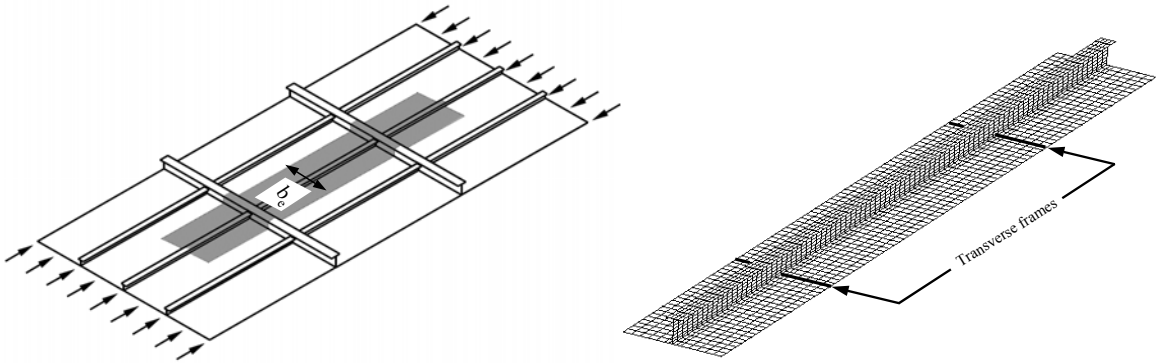

Figure 6.1(c) A two-bay plate-stiffener combination model for a stiffened plate structure under uniaxial compression

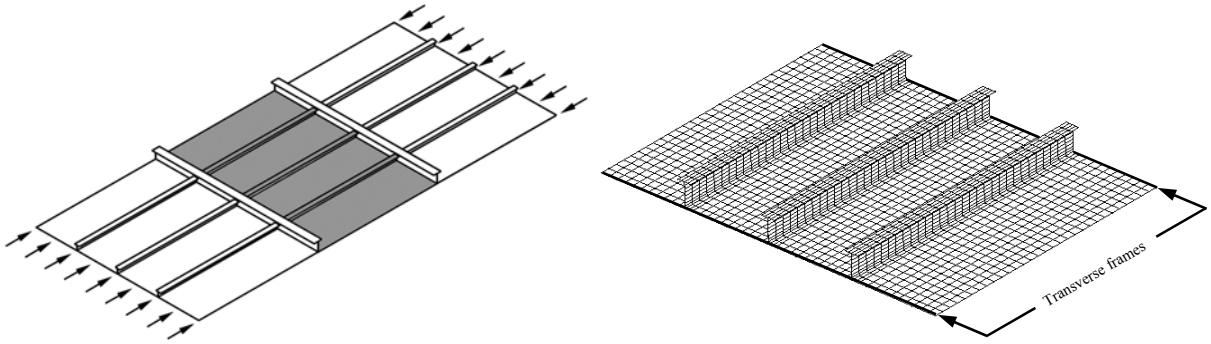

Figure 6.1(d) A one-bay stiffened panel model for a stiffened plate structure under uniaxial compression

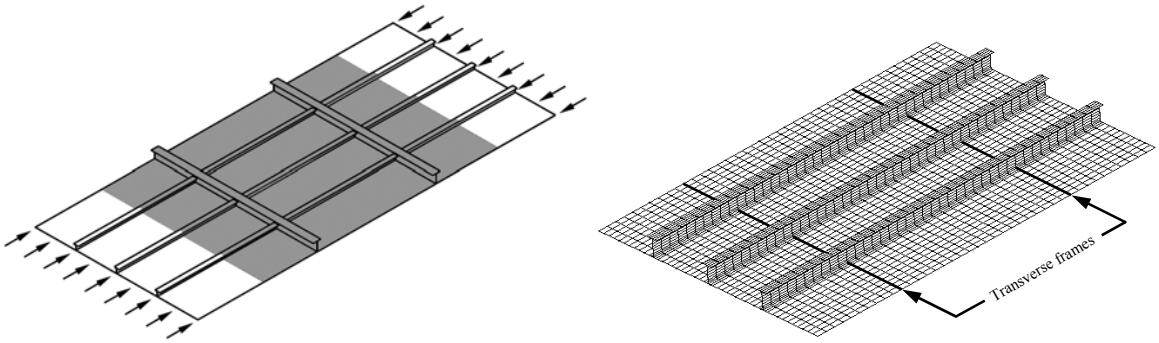

Figure 6.1(e) A two-bay stiffened panel model for a stiffened plate structure under uniaxial compression

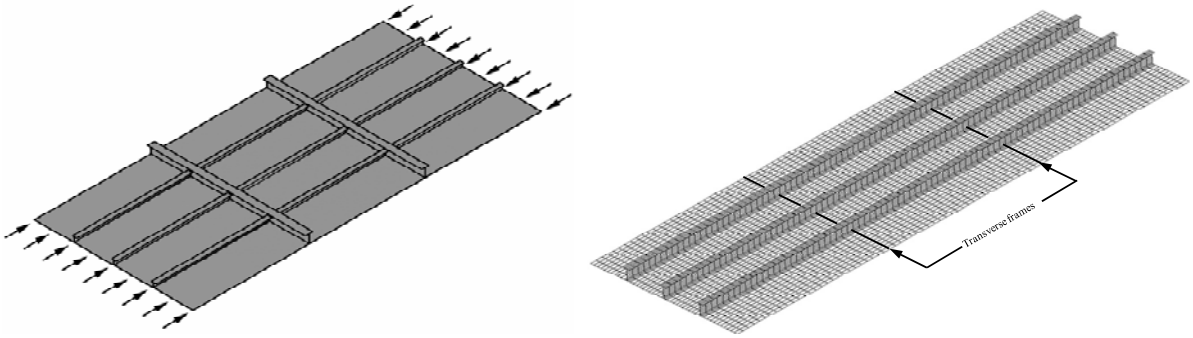

Figure 6.1(f) A three-bay stiffened panel model for a stiffened plate structure under uniaxial compression

In the present study, the three-bay stiffened panel model shown in Figure 6.1(f) was employed, although the target structure is the plate panel in the middle. This model was adopted because it was able to reflect the nonlinear behavior of the entire stiffened plate structure more realistically. However, transverse frames were not included in the structural modeling, although the support condition at the transverse frames was modeled as appropriate, as will be described in Section 6.1.7.

6.1.2 Types of Finite Elements

A variety of finite element types are available in practice, but it is difficult to establish specific guidelines about which types of finite elements are the best to apply. For the nonlinear analysis of thin-walled or plated structures, however, current practice indicates that the rectangular type of plate-shell elements is more appropriate than the triangular type, because this type more easily defines the membrane stress components inside each element when the Cartesian coordinate system is applied.

For the nonlinear analysis of ships and offshore structures, in association with ultimate limit states and structural crashworthiness, therefore, four-node plate-shell elements are more often employed, in which the nodal points in the plate thickness direction are located in the mid-thickness of each element, thus indicating that no

element mesh is assigned to the thickness layers.

To reflect nonlinear behavior more accurately, the use of plate-shell elements is desirable in the modeling of support members, including both webs and flanges as well as plate parts, although beam elements are sometimes more efficient for modeling these members or at least the flanges.

In the present study, four-node plate-shell elements were employed for the structural modeling. The stiffener web and flange and the plating were all modeled using four-node plate-shell elements.

Figure 6.2 represents a view of the finite element models of all the test structures at the y-z plane. It is noted that the sectional profile of extruded stiffener web has non-uniform wall thickness as shown in Figure 3.9 of Chapter 3, and thus it is modeled by multiple elements with a uniform-thickness per each element as shown in Figure 6.2. Also, a single element is allocated for the softened zone of the stiffener web as of the plate part.

Model 19A

Figure 6.2(a) A view of the finite element model of test structure 19A in the y-z plane

Model 20A

Figure 6.2(b) A view of the finite element model of test structure 20A in the y-z plane

Model 17D

Figure 6.2(c) A view of the finite element model of test structure 17D in the y-z plane

Model 18D

Figure 6.2(d) A view of the finite element model of test structure 18D in the y-z plane

Model 19D1

Figure 6.2(e) A view of the finite element model of test structure 19D1 in the y-z plane

Model 19D2

Figure 6.2(f) A view of the finite element model of test structure 19D2 in the y-z plane

Model 20D1

Figure 6.2(g) A view of the finite element model of test structure 20D1 in the y-z plane

Model 20D2

Figure 6.2(h) A view of the finite element model of test structure 20D2 in the y-z plane

Model 19C

Figure 6.2(i) A view of the finite element model of test structure 19C in the y-z plane

Model 20C

Figure 6.2(j) A view of the finite element model of test structure 20C in the y-z plane

6.1.3 Size of the Finite Elements

Although finer mesh modeling certainly results in more accurate solutions, it is not necessarily the best practice. A similar degree of accuracy can actually be attained with coarser mesh modeling, which requires less computational cost.

A convergence study is usually required to determine the 'best size' for the finite element mesh by balancing computational cost with the resulting accuracy. In such a study, sample applications of the corresponding nonlinear analysis are made by varying the element mesh size and searching for the largest finite element size that provides a sufficient level of accuracy.

Although a convergence study is often able to provide best practice for nonlinear finite element modeling in terms of a determination of the relevant mesh size, such a study itself sometimes requires a lot of computational effort. Therefore, useful guidance is necessary to define the finite element mesh size without a convergence

study.

Current practice for the ultimate strength analysis of stiffened plate structures that involve an elastic-plastic large deflection response indicates that at least eight four-node plate-shell elements are required to model the plating in between the small support members (e.g., the longitudinal stiffeners). The size of these plate-shell elements is assigned in the plate length direction so that the aspect ratio of each finite element is almost unity, which is desirable. The number of stiffener webs in the web height direction may be more than six using four-node plate-shell elements, and the number of stiffener flanges in the flange breadth direction may be at least two.

In the present study, a total of 16 four-node plate-shell elements were allocated for the plating between the longitudinal stiffeners in the transverse direction. For the stiffener web, a total of eight four-node plate-shell elements were assigned in the stiffener height direction for test structures 20D1 and 20D2, which had a deeper web height. For the remaining test structures, a total of six elements were employed. The stiffener flanges were modeled using four plate-shell elements, i.e., there were two elements on each side of the flanges with respect to the center line. Figure 6.2 also represents the size of the finite elements for the test structures.

As also discussed in Section 6.1.6, non-continuity or a sharp change in the material properties and residual stresses occurs around the softened zone. This may cause additional nonlinearity, and therefore a finer set of finite elements may need to be assigned in this region. However, it has been found that the finite element method model with a single element in the softened zone in the transverse (panel-breadth) direction gives sufficiently good computations within 0.5% deviations in terms of the ultimate strength behavior. Thus, the present study assigned a single element in the softened zone for the nonlinear finite element method computations.

6.1.4 Material Models – Base Material and Softened Zone

The ultimate strength behavior of structures almost always involves material nonlinearity in association with plasticity or yielding, among other factors. For nonlinear finite element analysis, therefore, the characteristics of material behavior should be modeled as appropriate in terms of the stress versus strain relationship.

It is, of course, desirable to employ a realistic relationship between the stresses and strains of the materials that is obtained by a direct test program that covers pre-yielding behavior, yielding, post-yielding behavior, including the strain-hardening effect, ultimate strength, and post-ultimate strength behavior, including the necking effect. This is particularly important for the analysis of structural crashworthiness made necessary by accidental events.

In the present study, the stress-strain curves of the base materials used for the test structures were obtained by tensile coupon tests, as described in Chapter 3. These data were used directly for the finite element analyses presented here, i.e., the entire history of the stress-strain relationship, including the strain-hardening effect, is considered.

However, it was not possible to obtain test results for the stress-strain curves of the materials in the softened zone, although their reduced yield strength was approximately defined, as described in Chapter 4. For the finite element method computations presented here, therefore, the material model illustrated in Figure 6.3

was applied to the materials in the softened zone. In this model, the post-yield behavior of these materials was considered to be similar to that of the base material, whereas the elastic modulus remained unchanged and the yield strength was reduced.

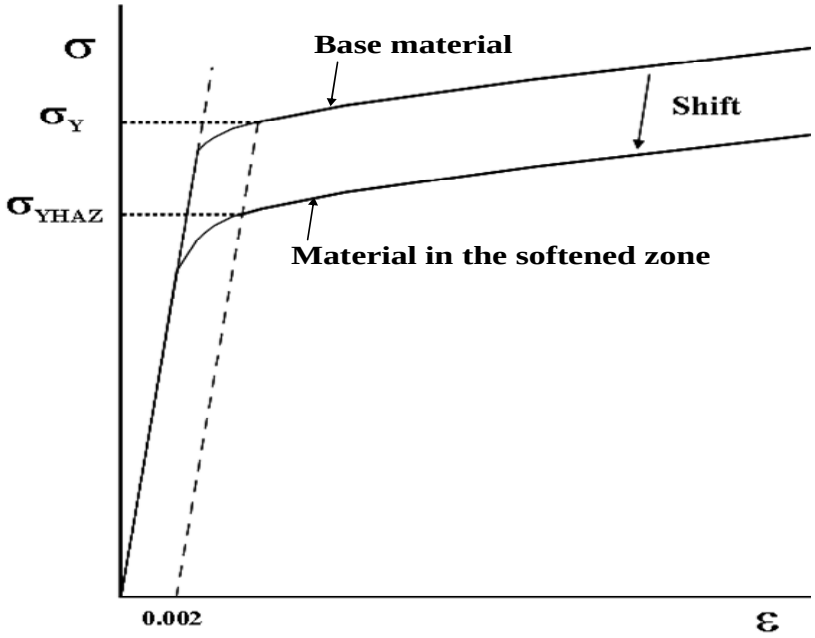

Figure 6.3 A material model for materials in the softened zone in terms of the relationship between the stress (σ) and the strain (ε)

6.1.5 Conditions at the Boundaries and Supports

Figure 6.4 shows the nonlinear finite element model applied to compute the ultimate strength behavior of the test structures.

The boundary and support conditions applied in the numerical computations are as follows.

- Loaded edges (AB, GH): These remain straight in both the x and z directions over their entirety, including the plate part and the extruded stiffeners. The extruded stiffeners remain upright in both the x and y directions, although they are able to move in parallel in the transverse (y) direction. The deformations in the z direction, i.e., the lateral deflections, are unrestrained.
- Unloaded edges (ACEG, BDFH): These remain straight in the y direction over their entirety. The deformations in the z direction are unrestrained.
- Supports at the transverse frames (CD, EF): The deformations of the plate part in the z direction are restrained. The extruded stiffeners remain upright in the y direction, and may or may not rotate about the y axis, i.e., at the transverse frames in the x direction. For the long and slender stiffeners with a relatively large column slenderness ratio (λ) value, the transverse frames may keep them upright in both the x and y directions. The extruded stocky-stiffeners with a relatively small column slenderness ratio value, however, are able to rotate in the x direction, but remain upright in the y direction. Test structures 17D and 18D, which have a column

slenderness ratio greater than 0.9, are modeled such that the extruded stiffeners at the transverse frames keep them upright in both the x and y directions. For the remainder of the test structures, the extruded stiffeners at the transverse frames are able to rotate about the y axis, although they remain upright in the y direction. To resolve this issue more satisfactorily, it is desirable to include the transverse frames themselves in the finite element modeling, but allow the rotational degree of freedom associated with the upright condition of the stiffeners at the transverse frames in both the x and y directions. Further studies are recommended in this regard.

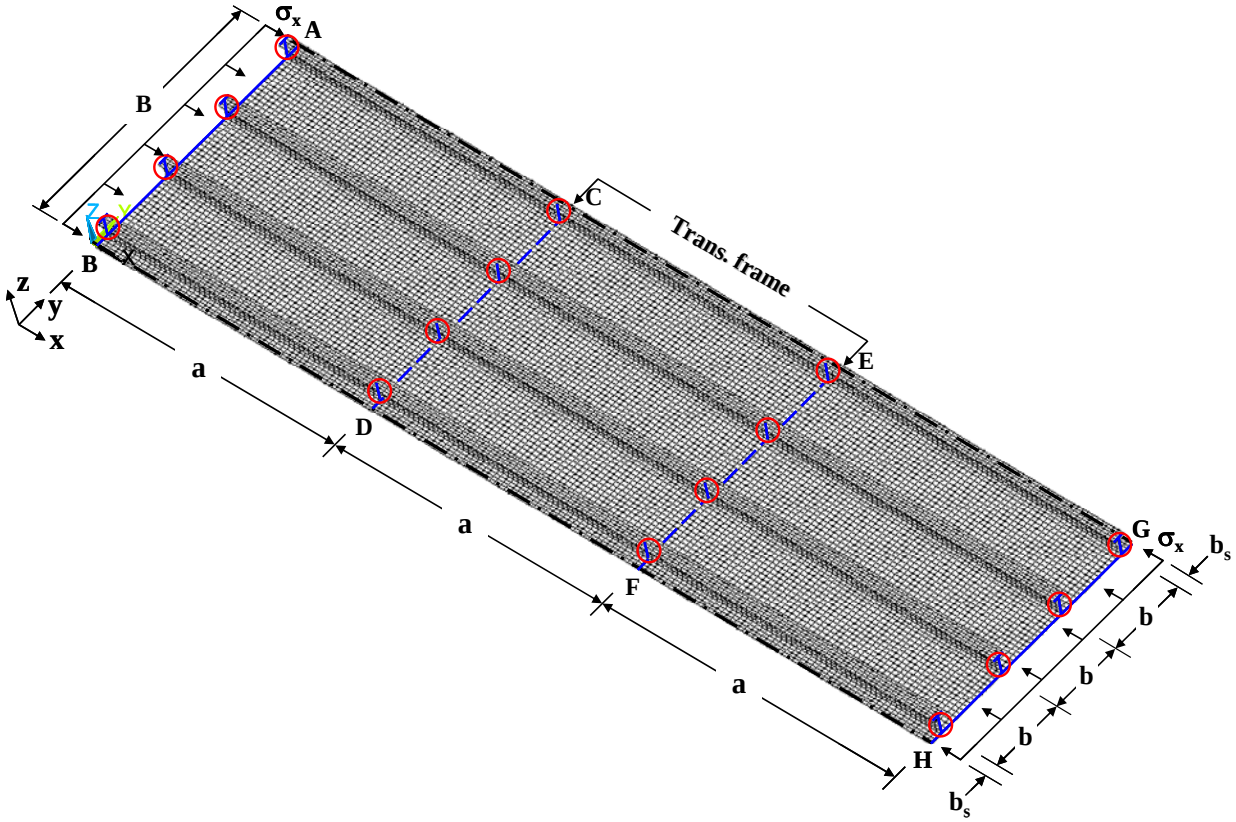

Figure 6.4 Nonlinear finite element model for the test structures

6.1.6 Loading Condition

Longitudinal axial compressive actions are applied via the nodal points at the two loaded edges, thus generating uniformly distributed axial compressive stresses in the x direction.

6.1.7 Initial Distortions

Three types of initial distortions, namely, plate initial deflection, the column-type initial distortion of the stiffener, and the sideways initial distortion of the stiffener are considered here. For plate initial deflection, the maximum value of the initial deflection on the three plates of each test structure is taken as the reference initial

deflection value w_{opl}^{*}, and the shape of the initial deflection for each plate is assumed to be as follows.

$$w_{opl} = w_{opl}^{*} \sin\frac{m\pi x}{a} \sin\frac{\pi y}{b}, \tag{6.1}$$

where m is the buckling half-wave number of the plate, which is taken as 4 for the test structures.

The maximum value of the column-type initial distortions on the four stiffeners of each test structure is taken as the reference initial distortion value w_{oc}^{*}, and the shape of the initial distortion for the entire plate panel is assumed to be as follows.

$$w_{oc} = w_{oc}^{*} \sin\frac{\pi x}{a} \sin\frac{\pi y}{B}. \tag{6.2}$$

Finally, the maximum value of the sideways initial distortions of the four stiffeners of each test structure is taken as the reference initial distortion value w_{os}^{*}, and the shape of the initial distortion for each stiffener is assumed to be as follows.

$$w_{os} = w_{os}^{*} \frac{z}{h_w} \sin\frac{\pi x}{a}, \tag{6.3}$$

where z is the coordinate in the stiffener height direction.

These three types of initial distortions are superimposed on the target structures and allocated in the coordinates via the nodal points, as appropriate.

Directions of column-type initial distortions of stiffeners can govern the stiffened panel collapse patterns and result in the plate-induced failure or stiffener-induced failure. In this regard, two types of the column-type initial distortion direction of stiffeners, i.e., compression in plate (CIP) and compression in stiffener (CIS), are considered in the present finite element method computations.

The CIP type represents the column-type initial distortion of stiffeners in the central panel of the structure in which the plate part is subjected to compression and the stiffener side is subjected to tension. The CIS type indicates an opposite situation to that of the CIP type. Figure 6.5 represents schematics of the abovementioned CIP and CIS types of the column initial distortion of stiffeners, which reflect the conditions at the boundaries and supports as described in Section 6.1.5. While the cross sections of the structure at the loaded edges are kept both plane and upright, the cross sections of the structure at the transverse frames may or may not keep upright, that is, may not or may rotate with regard to the y axis, although they still remain plane.

As discussed in Section 6.1.5, the nonlinear finite element method computations of test structures 17D and 18D with the slender stiffeners presume the condition in that the cross sections at the transverse frames remain upright.

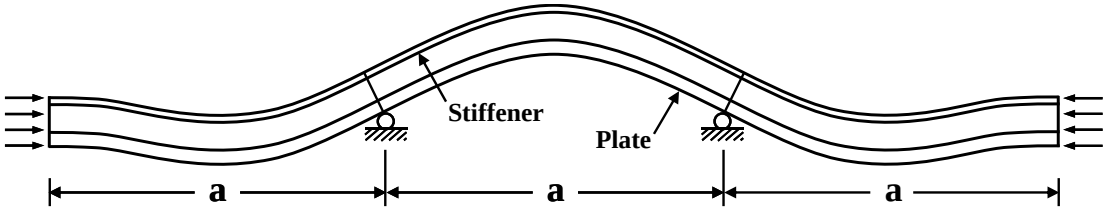

Figure 6.5(a) The CIP type of the column initial distortion of stiffeners in the central panel of the structure, with the cross sections at the transverse frames rotating with regard to the y axis

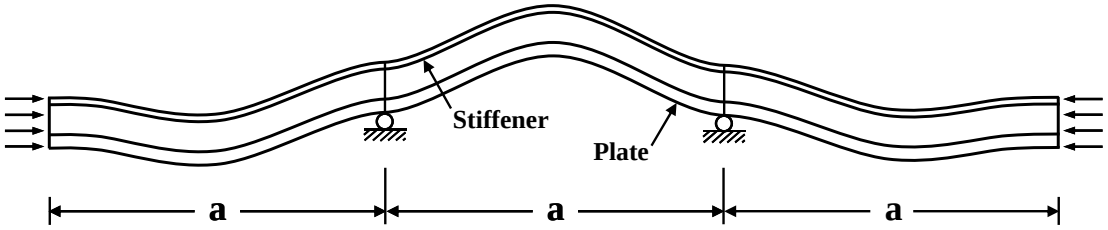

Figure 6.5(b) The CIP type of the column initial distortion of stiffeners in the central panel of the structure, with the cross sections at the transverse frames keeping upright

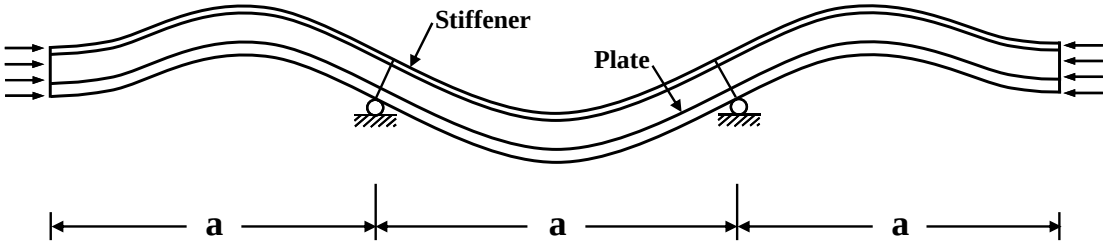

Figure 6.5(c) The CIS type of the column initial distortion of stiffeners in the central panel of the structure, with the cross sections at the transverse frames rotating with regard to the y axis

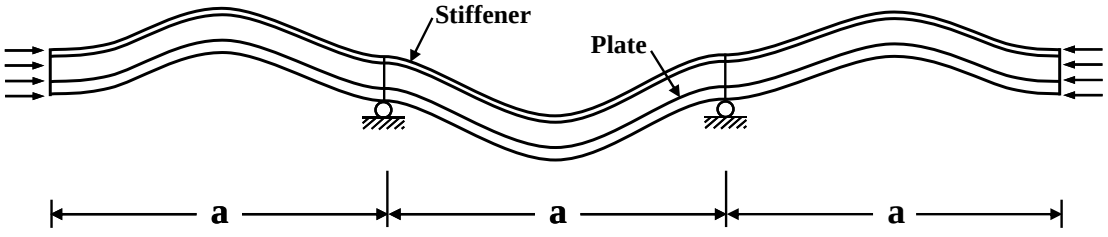

Figure 6.5(d) The CIP type of the column initial distortion of stiffeners in the central panel of the structure, with the cross sections at the transverse frames keeping upright

6.1.8 Welding Residual Stresses

Welding residual stresses, which are composed of tensile residual stress blocks and compressive residual stress blocks, were dealt with as initial stresses in the structures.

Initial strains, which are possibly caused by heating and cooling down in association with residual stresses, may or may not affect the ultimate strength behavior, but the present study neglects the effects of such strains. Further studies are recommended to consider this issue.

One remaining issue is how to allocate the number of finite elements in the region of the tensile residual stress blocks that corresponds to the softened zone. This is important, because non-continuity or a sharp change in the residual stress distribution occurs around this zone. However, it was found that a single finite element in the softened zone was sufficient for the nonlinear finite element method computations, as described in Section 6.2. This finding is also available for steel-plated structures (Paik & Sohn 2009).

In the present study, the idealized distributions of the residual stresses described in Chapter 4 were applied for the numerical computations.

6.2 Computational Results and Discussions

Figures 6.6 to 6.15 show the relationships between the axial compressive force and the axial compressive displacement of the test structures.

The results of the CIS computations indicate an opposite condition to those of the CIP, that is, the stiffener flange side is subjected to compression while the plate side is subjected to tension. These computations were also carried out both with and without residual stresses and softening effects.

Tables 6.1 and 6.2 summarize the ultimate compressive strength computations by a comparison with experimental results. In Table 6.2, the ultimate compressive forces P_u obtained by FEA indicates a smaller value of the ultimate compressive forces computed by either CIP or CIS with the residual stress and softening effects. The ultimate strength ratio to the fully plastic force indicates the severity of local failures in the structures until the ultimate strength reached. In other words, the ultimate strength ratio becomes smaller as the local failures occur earlier and/or more severely. In general, more stocky structures will have a larger value of the ultimate strength ratio or more slender structures will have a smaller value of the ultimate strength ratio. This is because the stocky structures may buckle involving a certain degree of plasticity although the slender structures may buckle in the elastic regime.

It is found from Figures 6.6 to 6.15 that the residual stresses and softening phenomena significantly reduce the ultimate strength performance. The nonlinear finite element method computations for both the CIP and CIS column-type initial distortions of the stiffeners taking into account the effects of residual stresses and softening provide good agreement with the experimental results, except for structures 20D1 and 20C, which unintentionally collapsed earlier through delamination in the friction stir-welded region rather than via buckling collapse. However, it is important to realize that the nonlinear finite element method computations depend significantly on the structural modeling techniques applied.

Table 6.1 Summary of the ultimate compressive strength computations for the test structures in terms of the ultimate compressive stress normalized by the equivalent yield stress

Model (Fig. No.)	Experiment		FEA			
			Without residual stress and softening		With residual stress and softening	
			CIP	CIS	CIP	CIS
	σ_{xu}/σ_{Yeq}	Collapse mode	σ_{xu}/σ_{Yeq}	σ_{xu}/σ_{Yeq}	σ_{xu}/σ_{Yeq}	σ_{xu}/σ_{Yeq}
19A (6.6)	0.429	V	0.514	0.512	0.433	0.433
20A (6.7)	0.649	IV	0.759	0.745	0.692	0.663
17D (6.8)	0.512	III	0.616	0.609	0.549	0.536
18D (6.9)	0.531	III	0.649	0.649	0.599	0.590
19D1 (6.10)	0.545	III	0.572	0.569	0.500	0.499
19D2 (6.11)	0.504	V	0.591	0.588	0.530	0.529
20D1[1)] (6.12)	0.511	IV	0.837	0.835	0.779	0.779
20D2 (6.13)	0.673	IV	0.837	0.823	0.753	0.733
19C (6.14)	0.571	II	0.612	0.621	0.598	0.606
20C[1)] (6.15)	0.577	IV	0.780	0.777	0.753	0.749

Note: [1)] Test structure that unintentionally collapsed through delamination in the friction stir-welded region; Collapse mode is as defined in Section 5.1; CIP = column-type initial distortion of the stiffeners in the x direction with compression on the plate side; CIS = column-type initial distortion of the stiffeners in the x direction with compression on the stiffener side; $\sigma_{xu} = P_u / A_t$ where A_t = total cross-sectional area of the entire stiffened panel.

Table 6.2 Summary of the ultimate compressive strength computations for the test structures in terms of the ultimate compressive force normalized by the fully plastic force

Model (Fig. No.)	P_p (kN)	Experiment		FEA	
		P_u (kN)	P_u/P_p	P_u (kN)	P_u/P_p
19A (6.6)	1646.9	697.1	0.423	715.4	0.434
20A (6.7)	2139.7	1401.1	0.655	1382.9	0.646
17D (6.8)	2009.4	1006.4	0.501	1053.2	0.524
18D (6.9)	2003.8	1036.2	0.517	1152.5	0.575
19D1 (6.10)	2095.5	1111.9	0.531	1109.1	0.529
19D2 (6.11)	1847.8	939.7	0.509	987.2	0.534
20D1[1)] (6.12)	3161.6	1563.7	0.495	2382.1	0.753
20D2 (6.13)	2299.8	1561.9	0.679	1700.3	0.739
19C (6.14)	1583.5	784.6	0.495	821.5	0.519
20C[1)] (6.15)	1999.1	1166.0	0.583	1517.3	0.759

Note: [1)] Test structure that unintentionally collapsed through delamination in the friction stir-welded region; Collapse mode is as defined in Section 5.1; P_u = ultimate compressive force; P_p = fully plastic axial force; $\sigma_{xu} = P_u / A_t$ where A_t = total cross-sectional area of the entire stiffened panel.

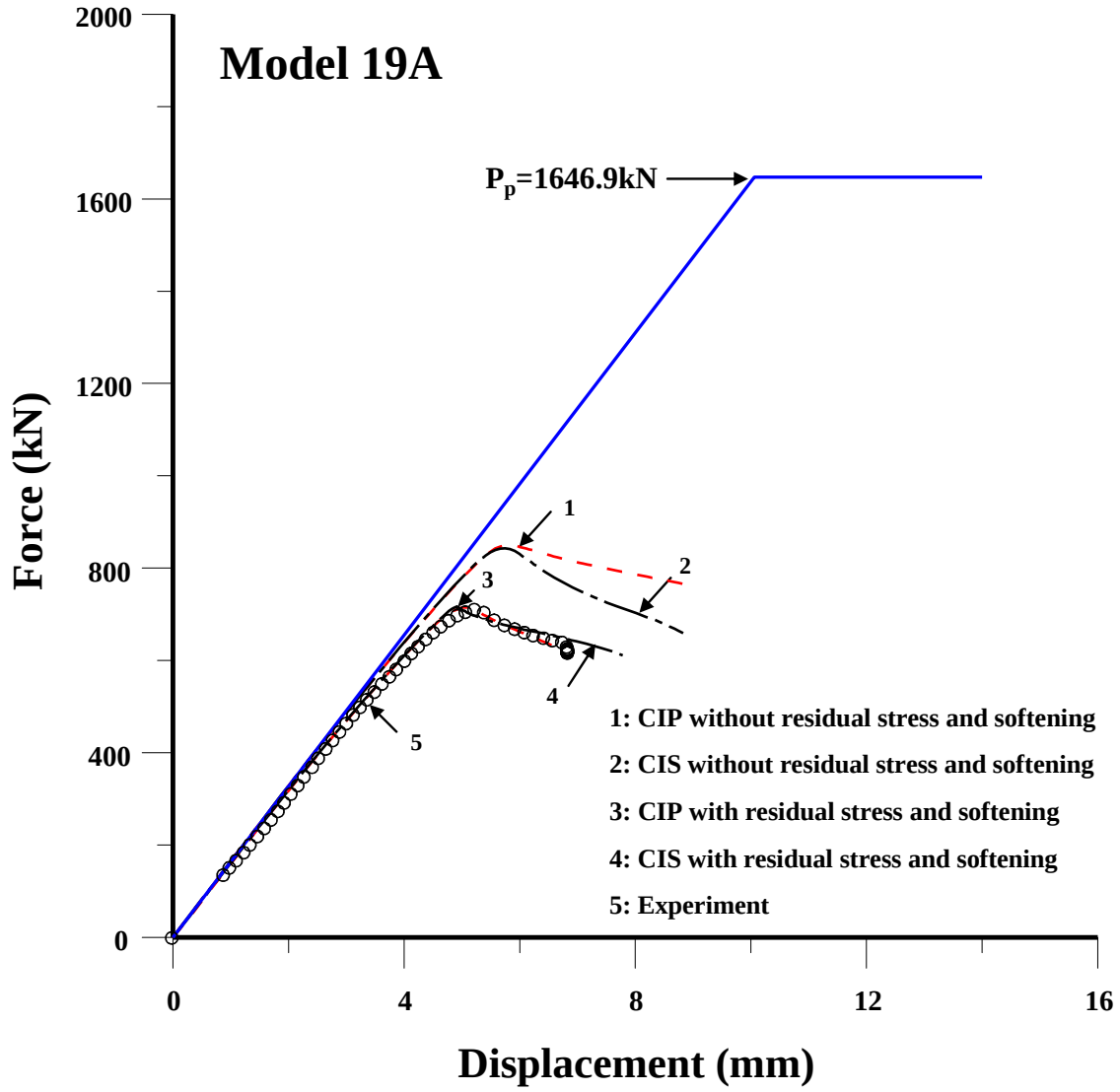

Figure 6.6 The axial compressive force versus the axial compressive displacement of test structure 19A

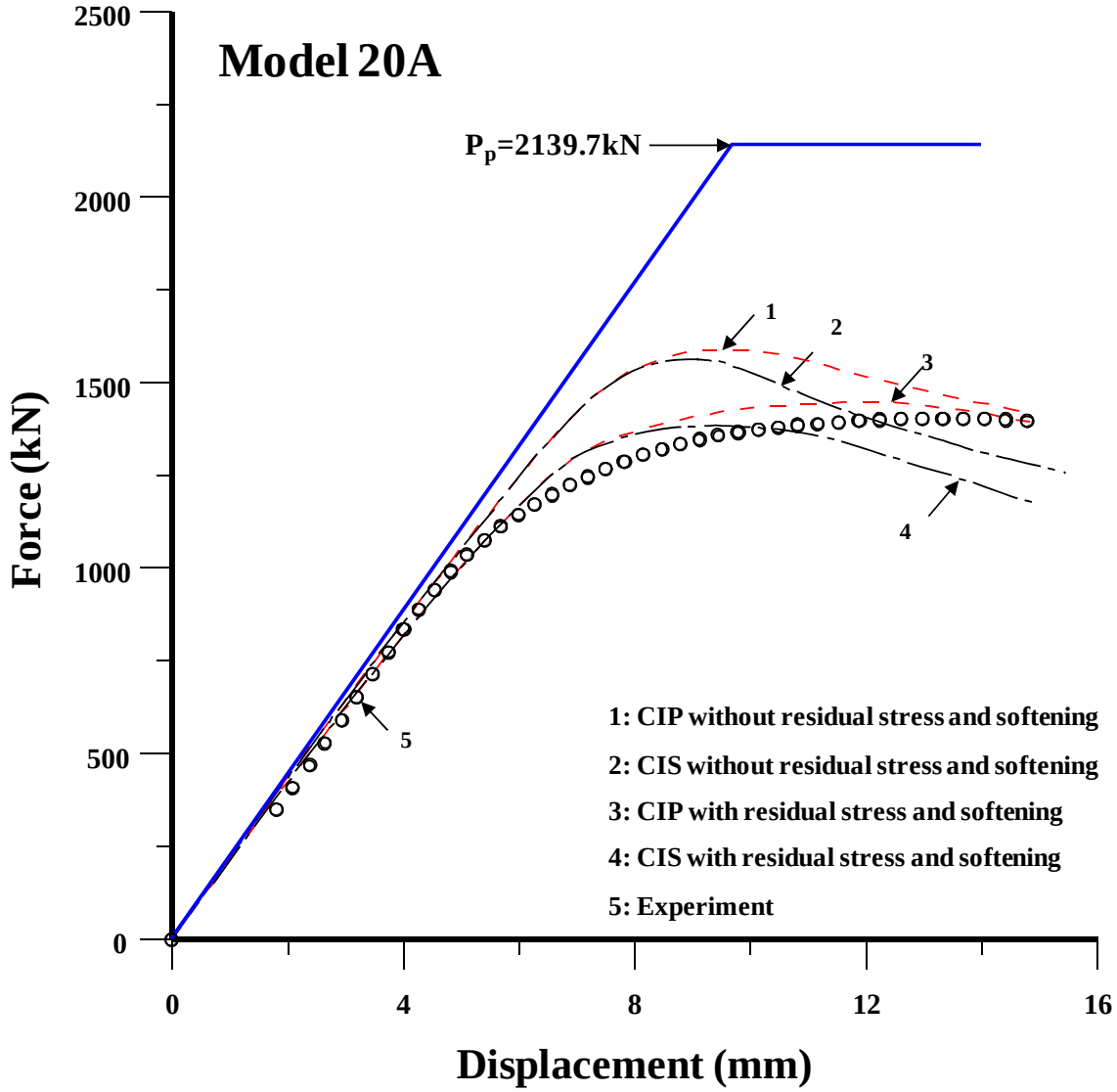

Figure 6.7 The axial compressive force versus the axial compressive displacement of test structure 20A

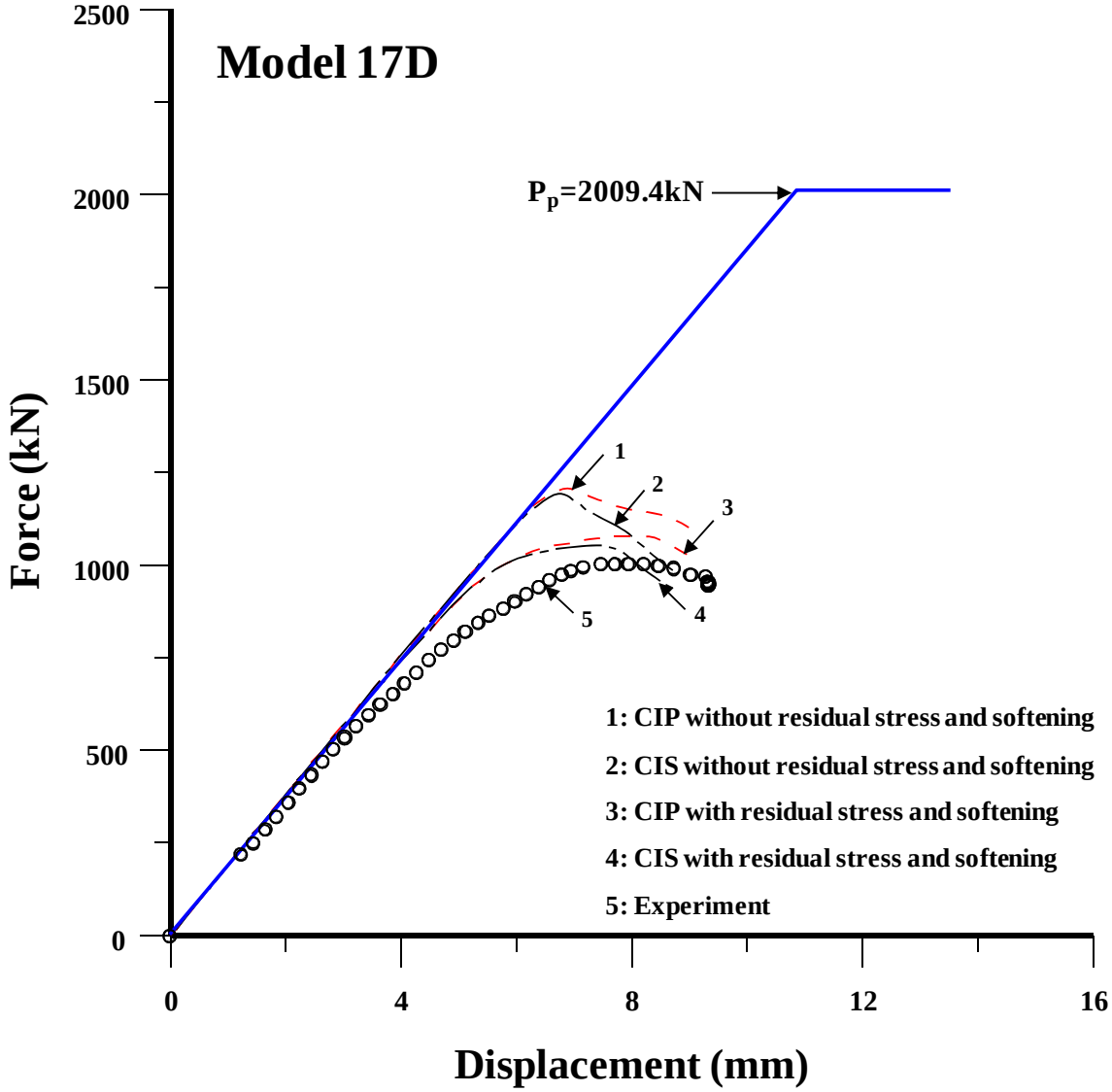

Figure 6.8 The axial compressive force versus the axial compressive displacement of test structure 17D

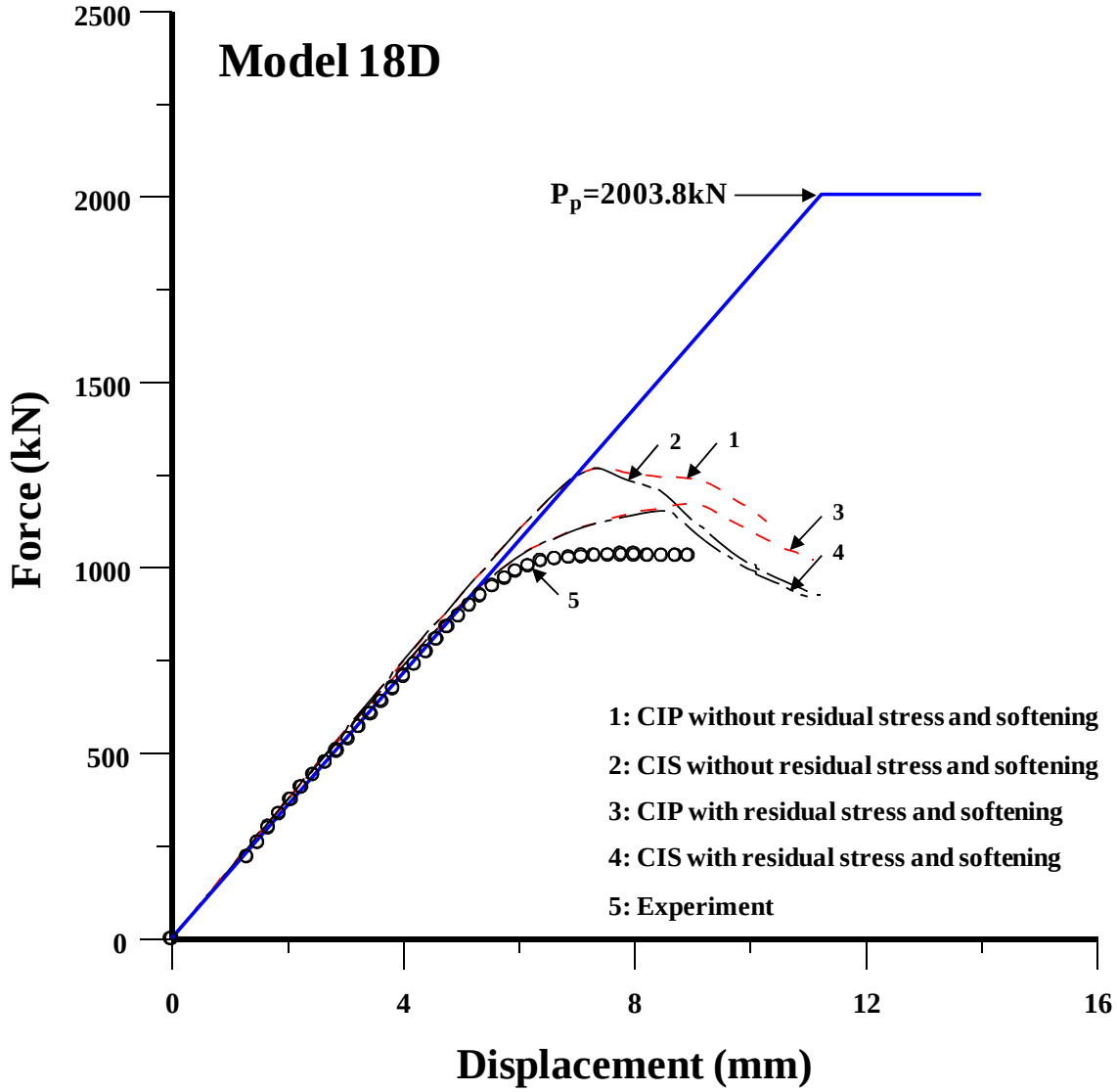

Figure 6.9 The axial compressive force versus the axial compressive displacement of test structure 18D

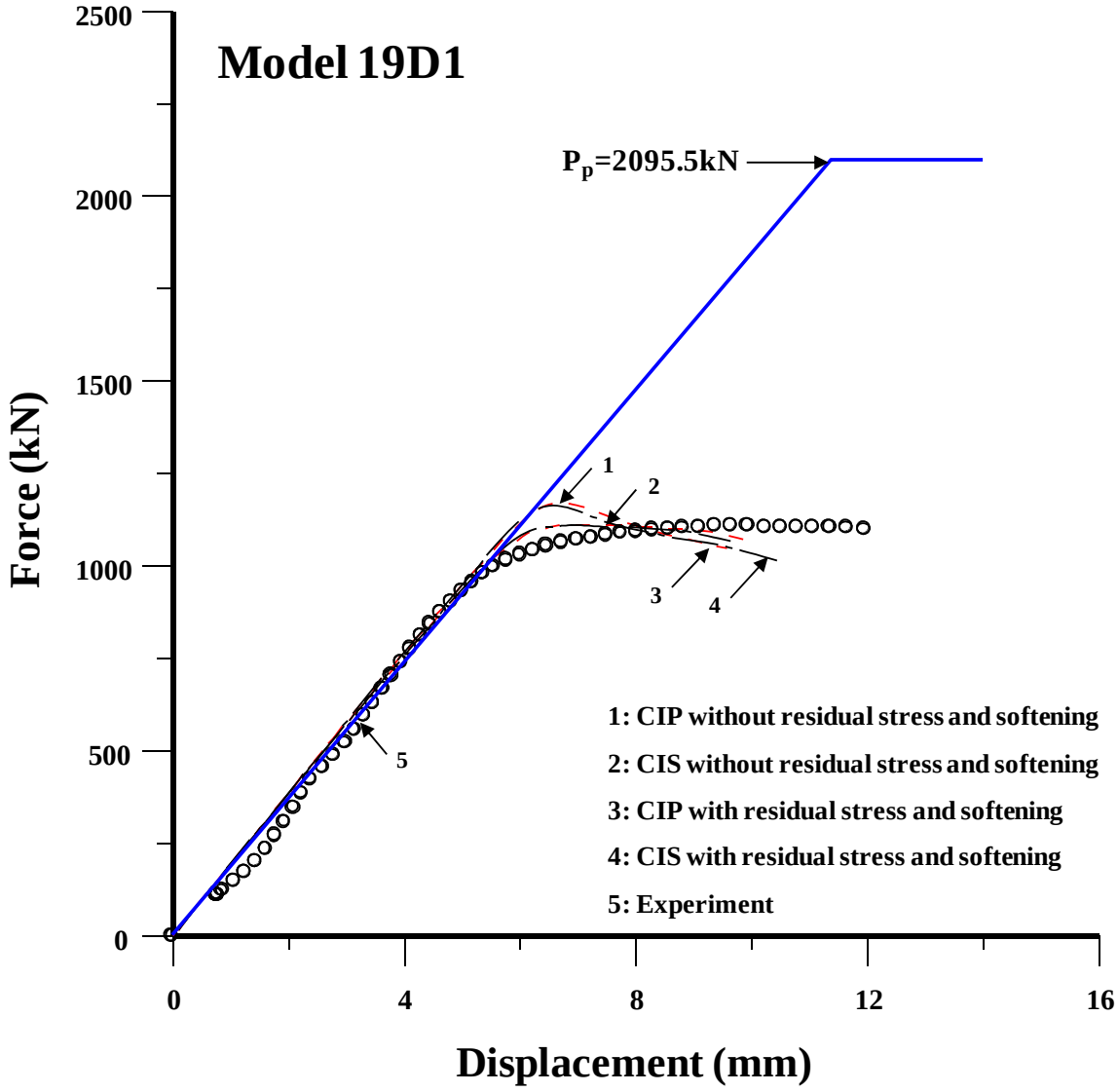

Figure 6.10 The axial compressive force versus the axial compressive displacement of test structure 19D1

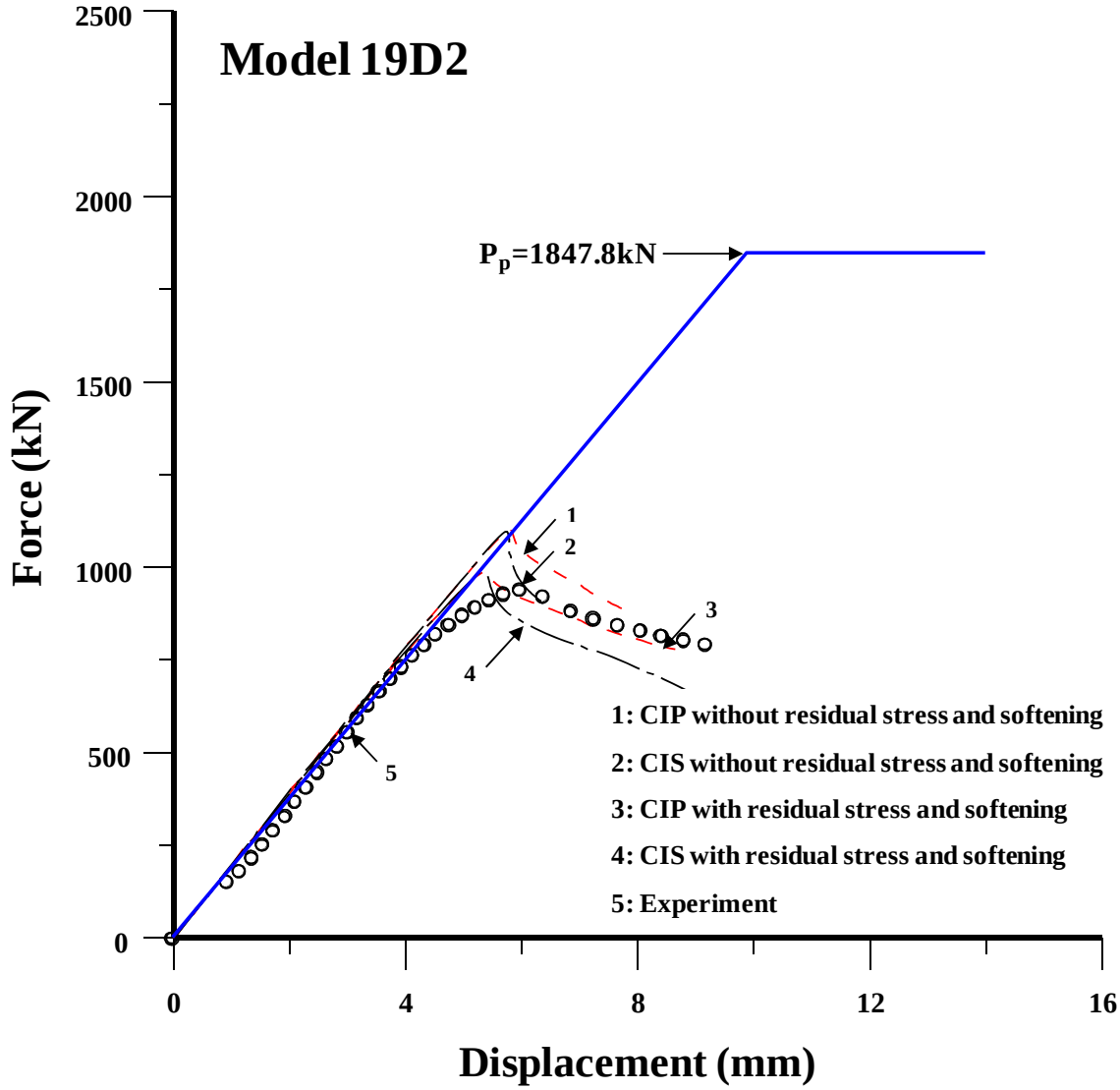

Figure 6.11 The axial compressive force versus the axial compressive displacement of test structure 19D2

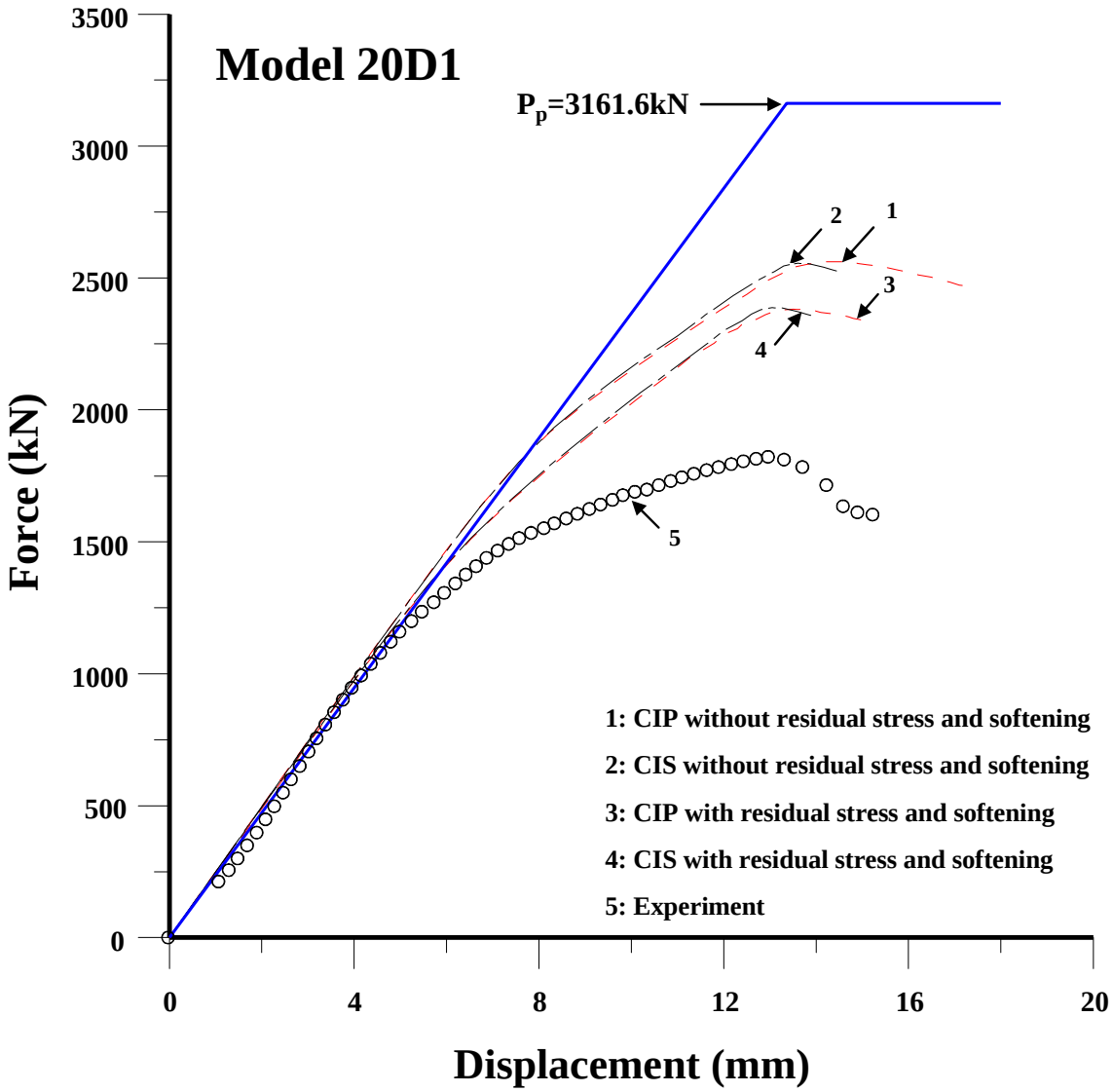

Figure 6.12 The axial compressive force versus the axial compressive displacement of test structure 20D1

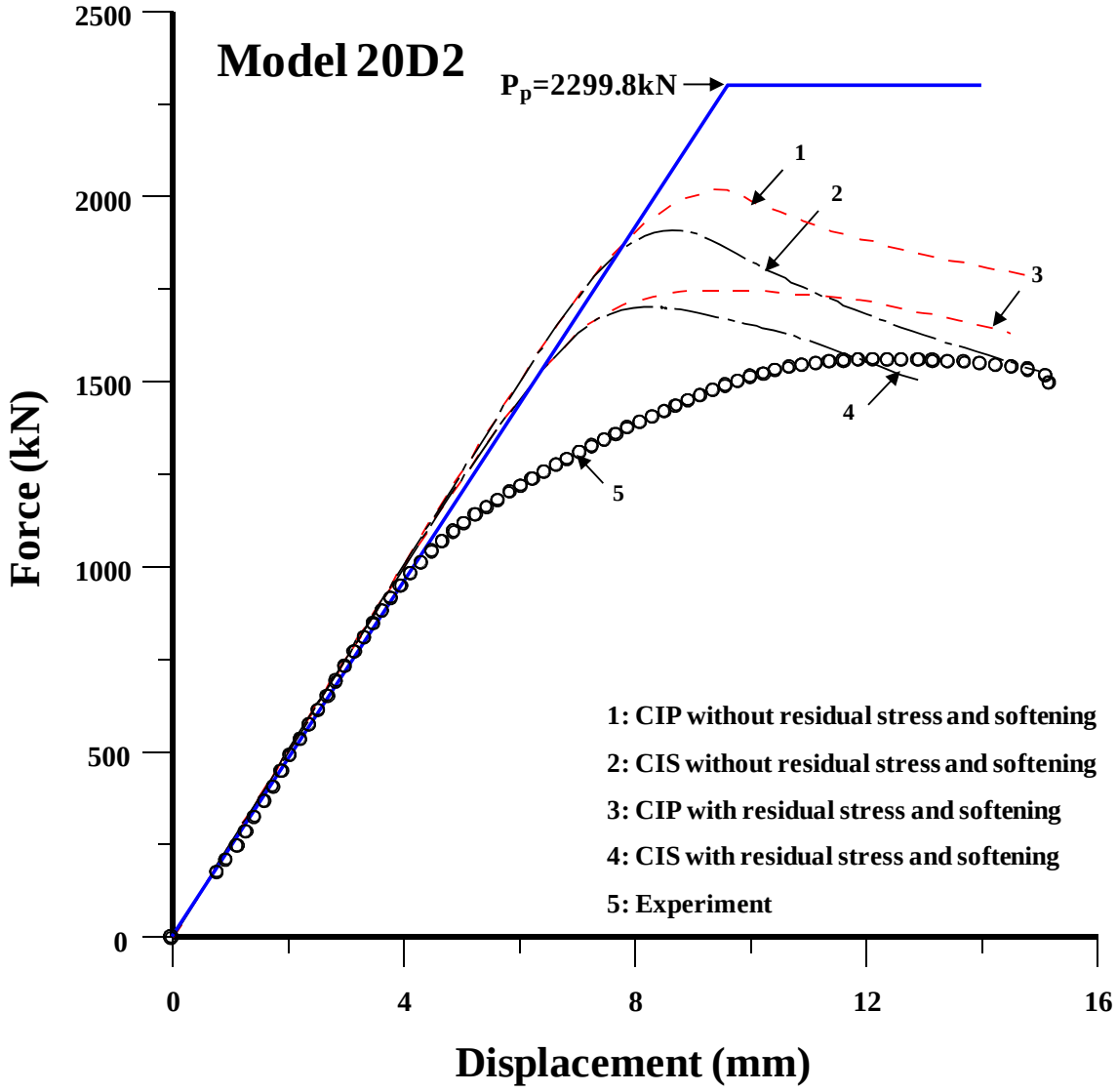

Figure 6.13 The axial compressive force versus the axial compressive displacement of test structure 20D2

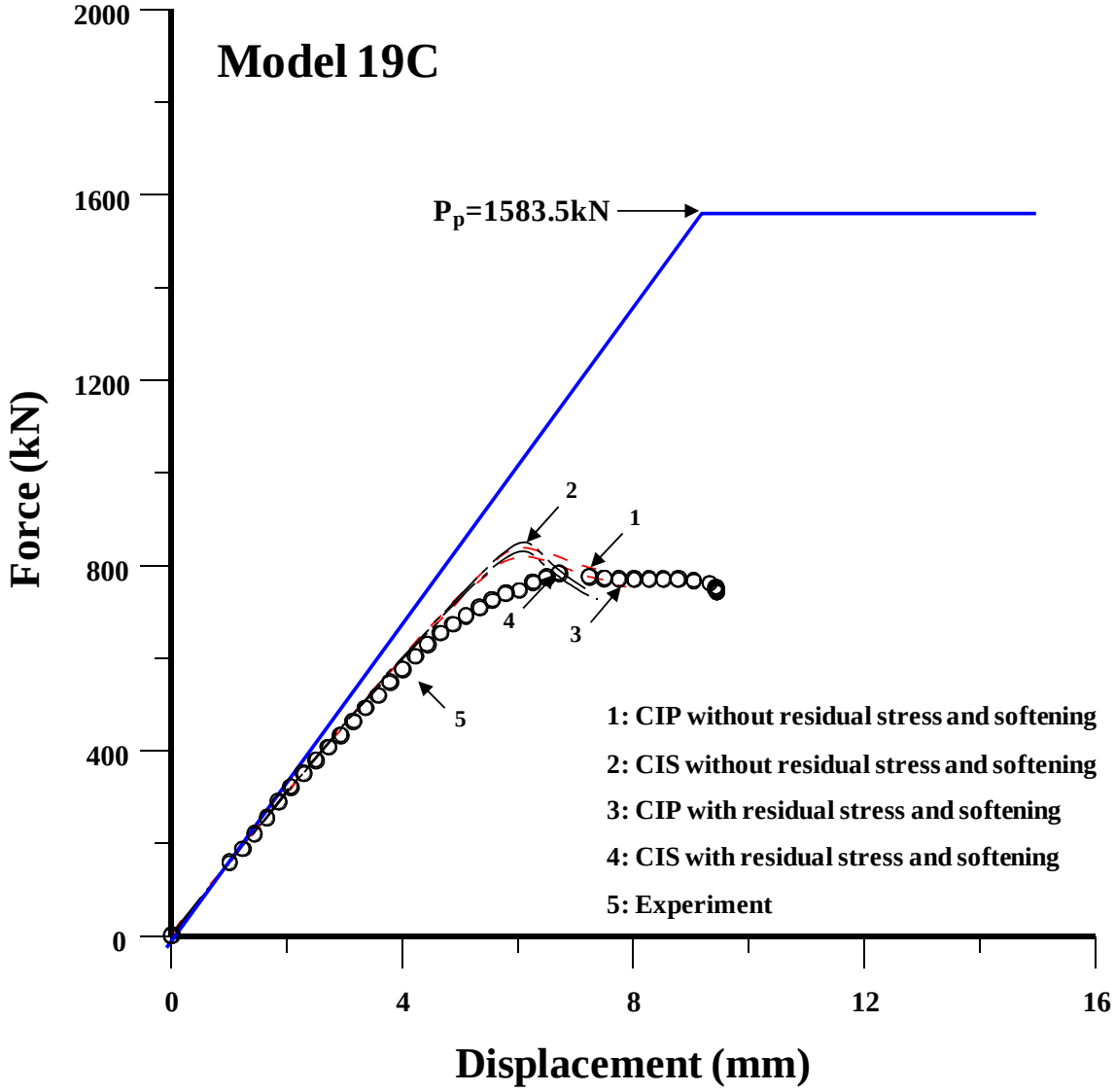

Figure 6.14 The axial compressive force versus the axial compressive displacement of test structure 19C

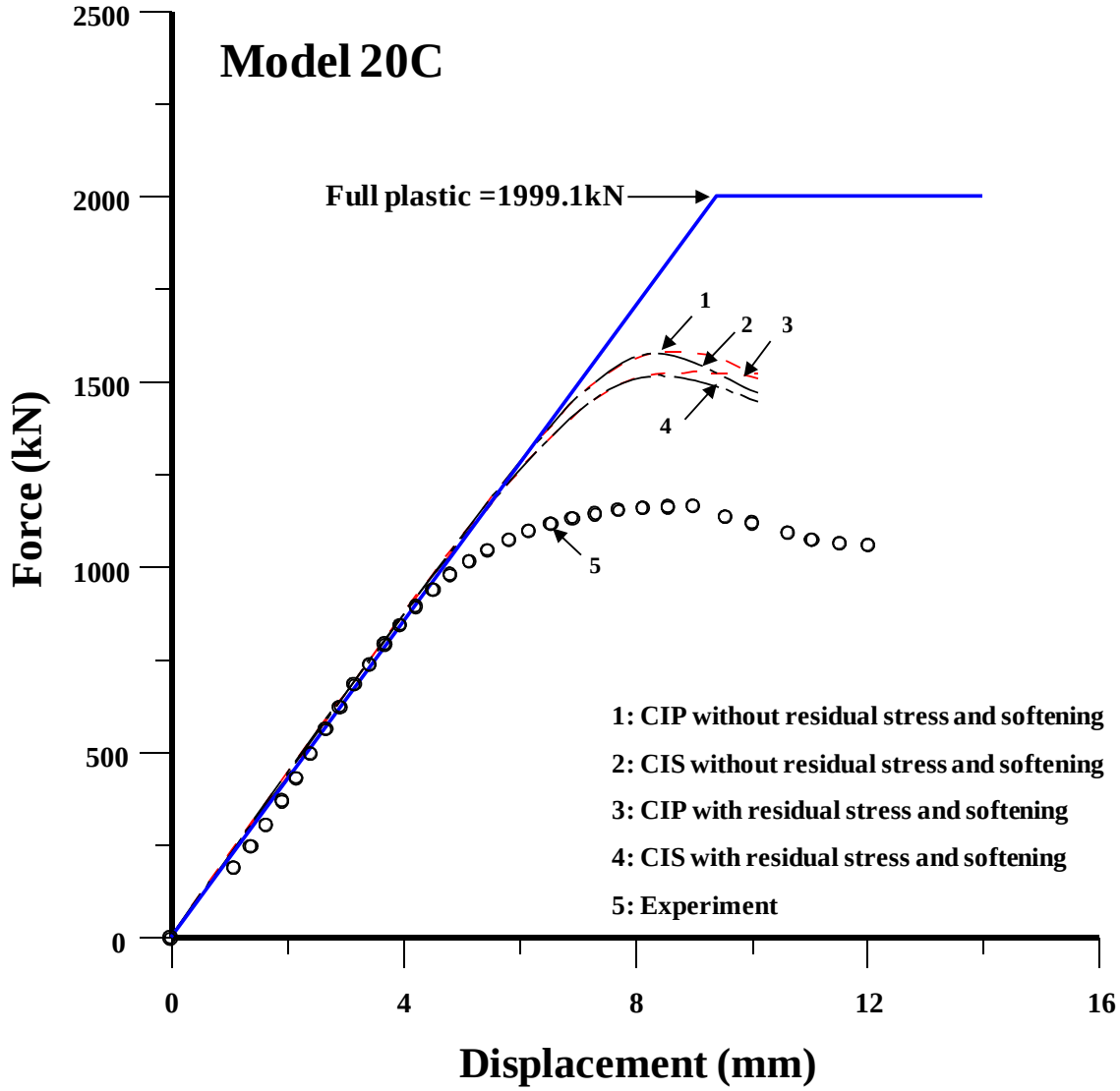

Figure 6.15 The axial compressive force versus the axial compressive displacement of test structure 20C

6.3 SSC-451 Database

Figures 6.15 to 6.26 show the relationships between the axial compressive force versus the axial compressive displacement of the test structures studied in SSC-451 via fusion welds. Tables 6.3 and 6.4 present a summary of the ultimate strength computations for these structures. It is found that the nonlinear finite element computations for all the test structures are comparable with the experimental results. This implies that the SSC-451 test structures collapsed intentionally via buckling collapse unlike the present test structures in which two structures collapsed unintentionally by delamination before the ultimate strength had been reached.

This database is utilized for a comparison of the ultimate strength performance of fusion welds versus that of friction stir welds, which is described in Chapter 7.

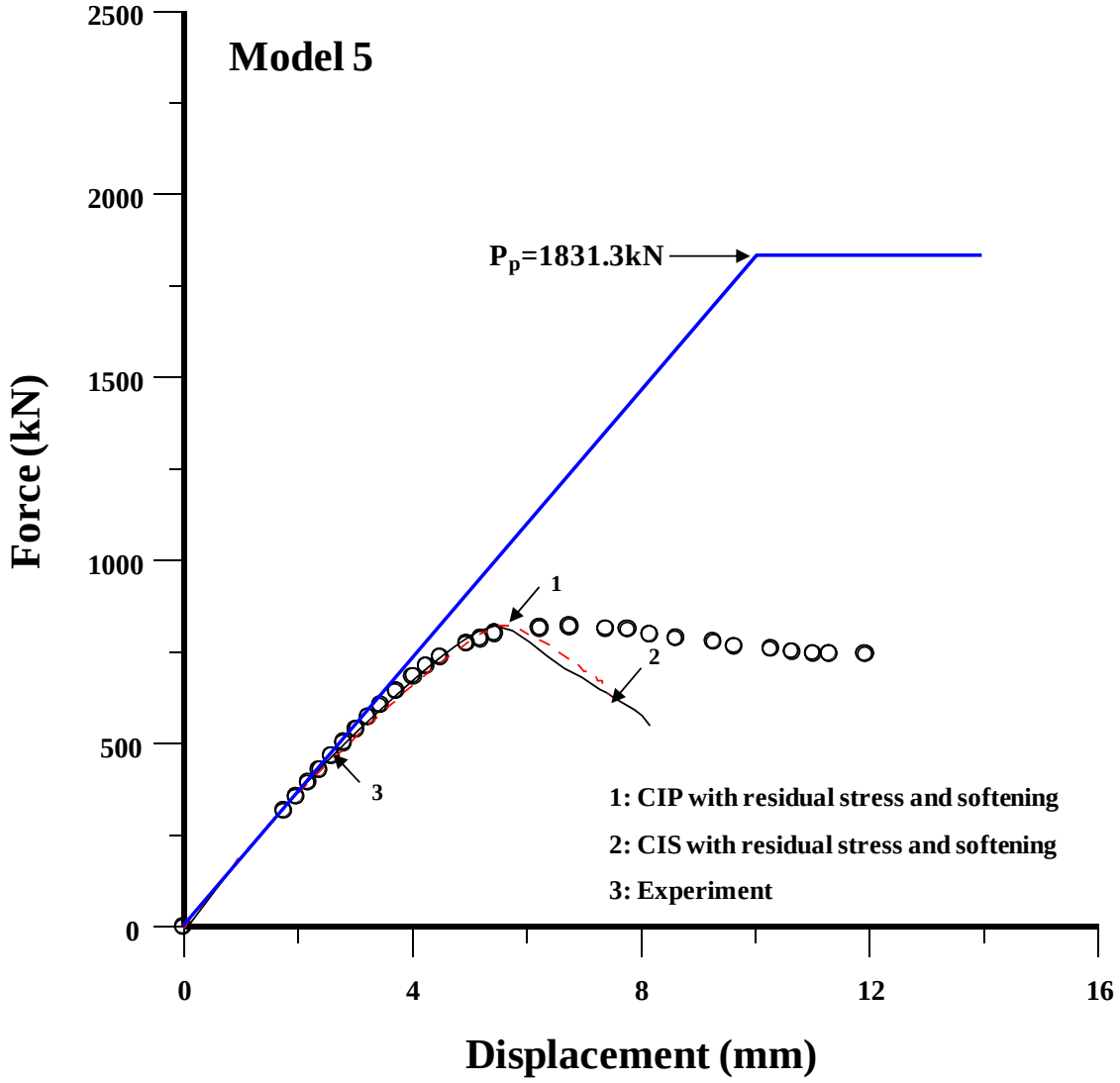

Figure 6.16 The axial compressive force versus the axial compressive displacement of test structure 5

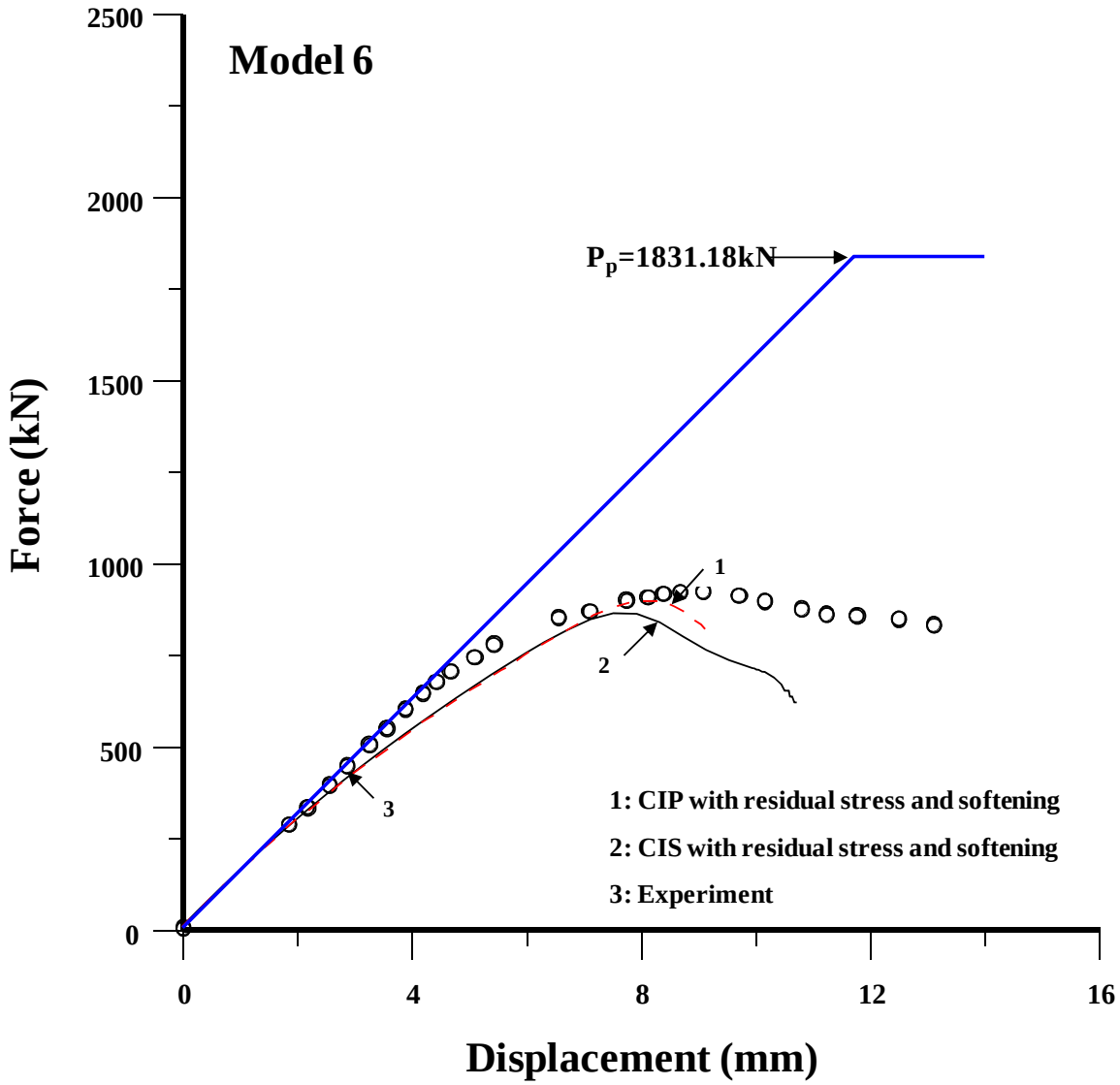

Figure 6.17 The axial compressive force versus the axial compressive displacement of test structure 6

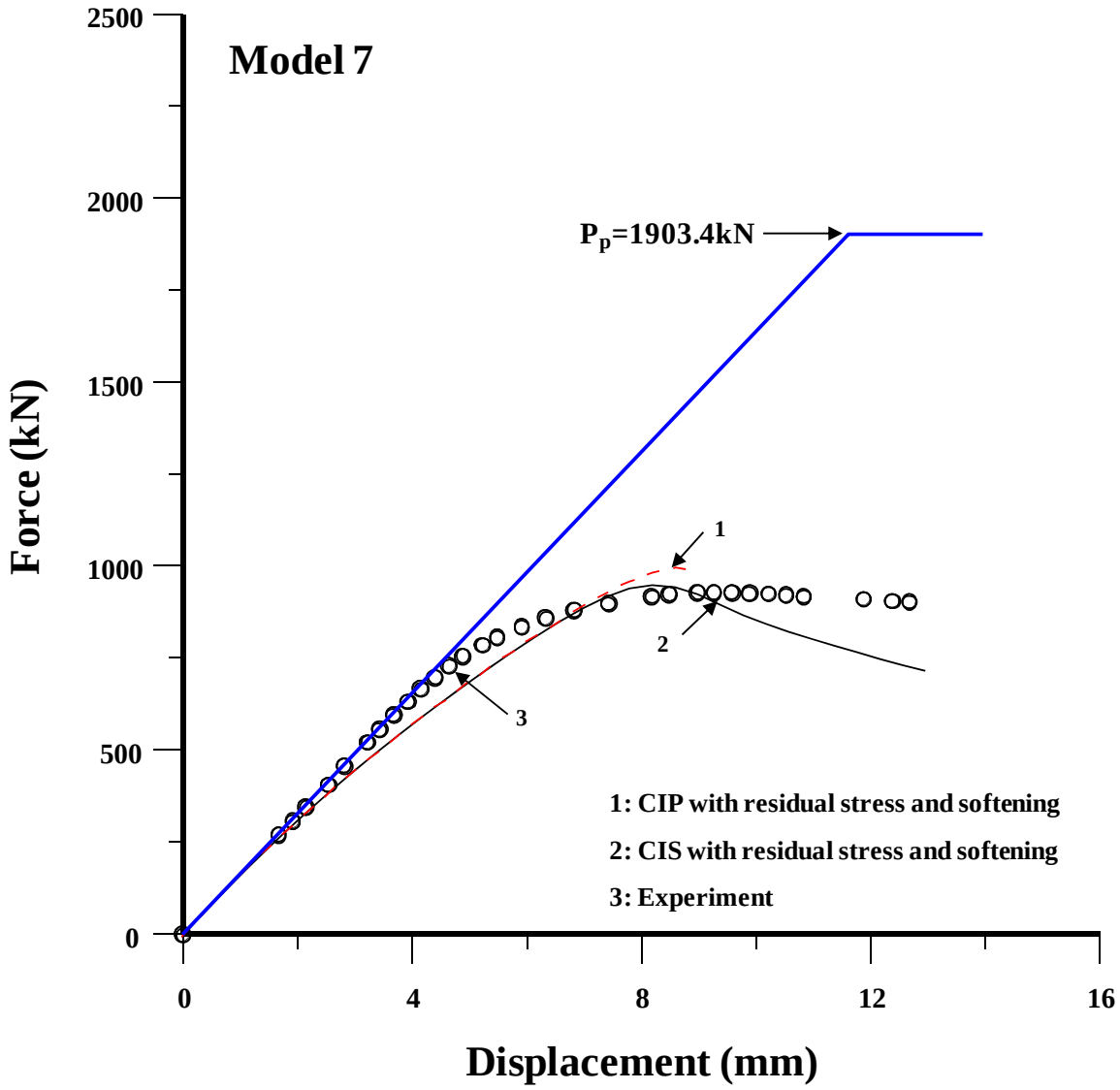

Figure 6.18 The axial compressive force versus the axial compressive displacement of test structure 7

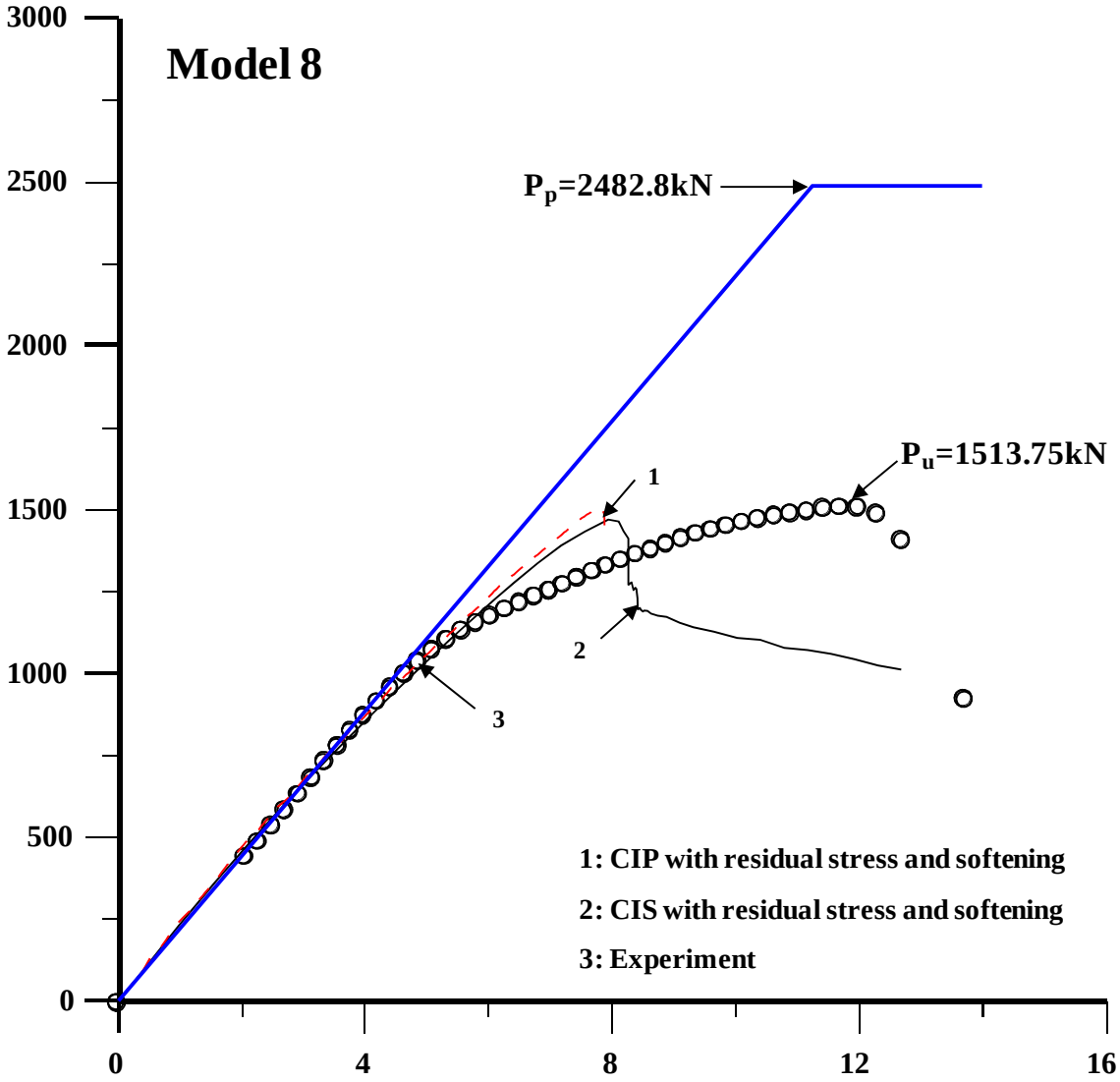

Figure 6.19 The axial compressive force versus the axial compressive displacement of test structure 8

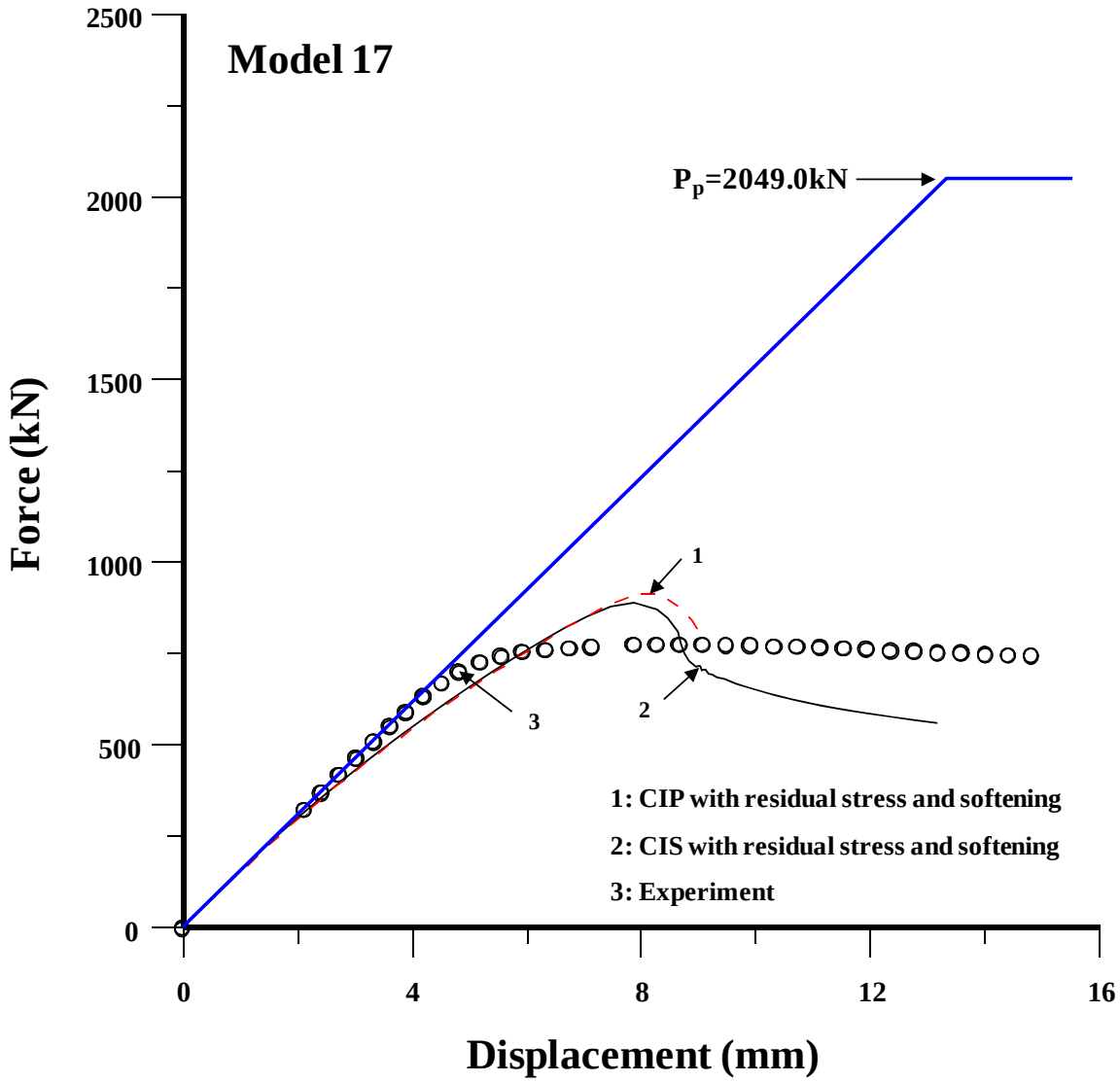

Figure 6.20 The axial compressive force versus the axial compressive displacement of test structure 17

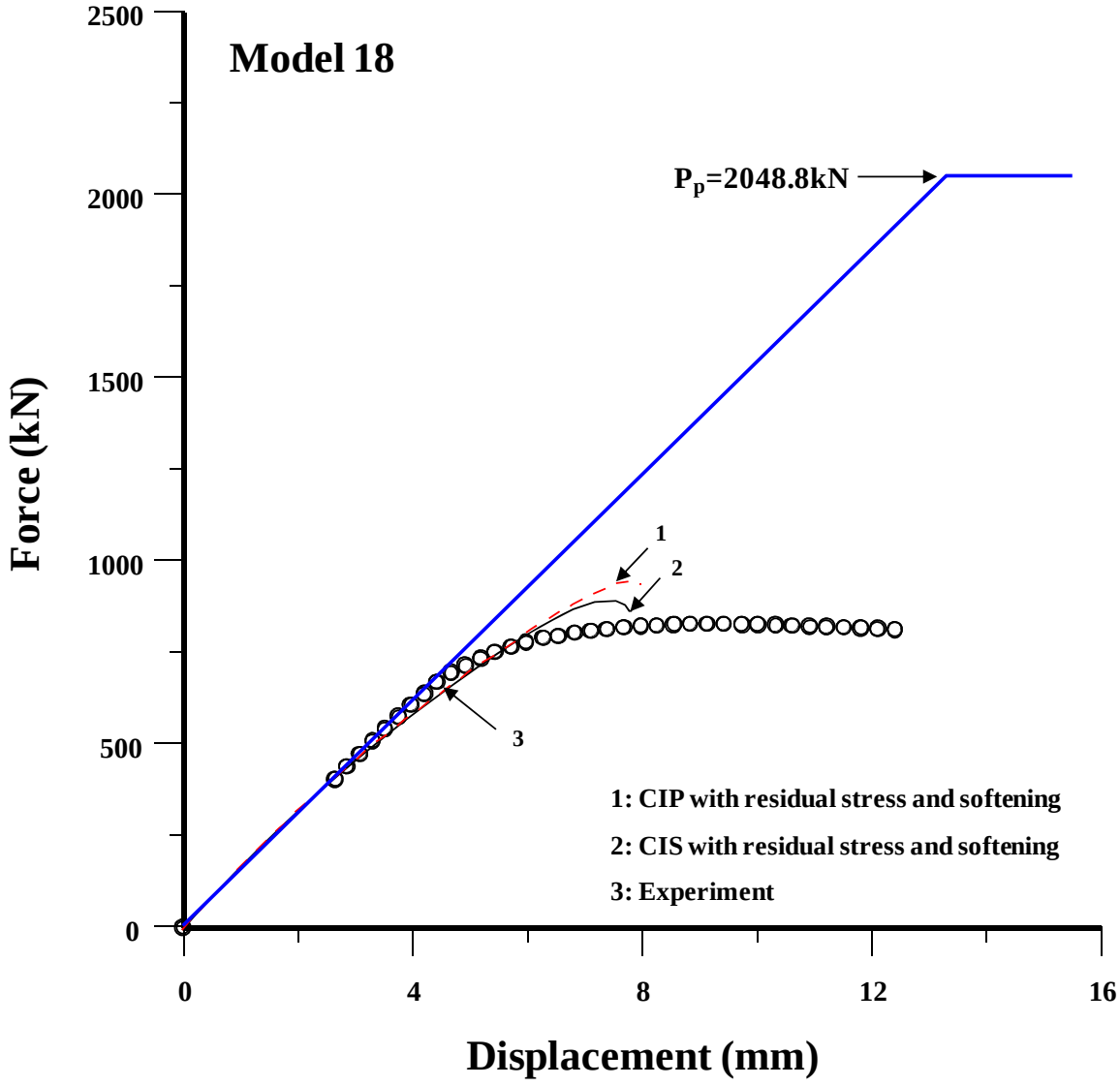

Figure 6.21 The axial compressive force versus the axial compressive displacement of test structure 18

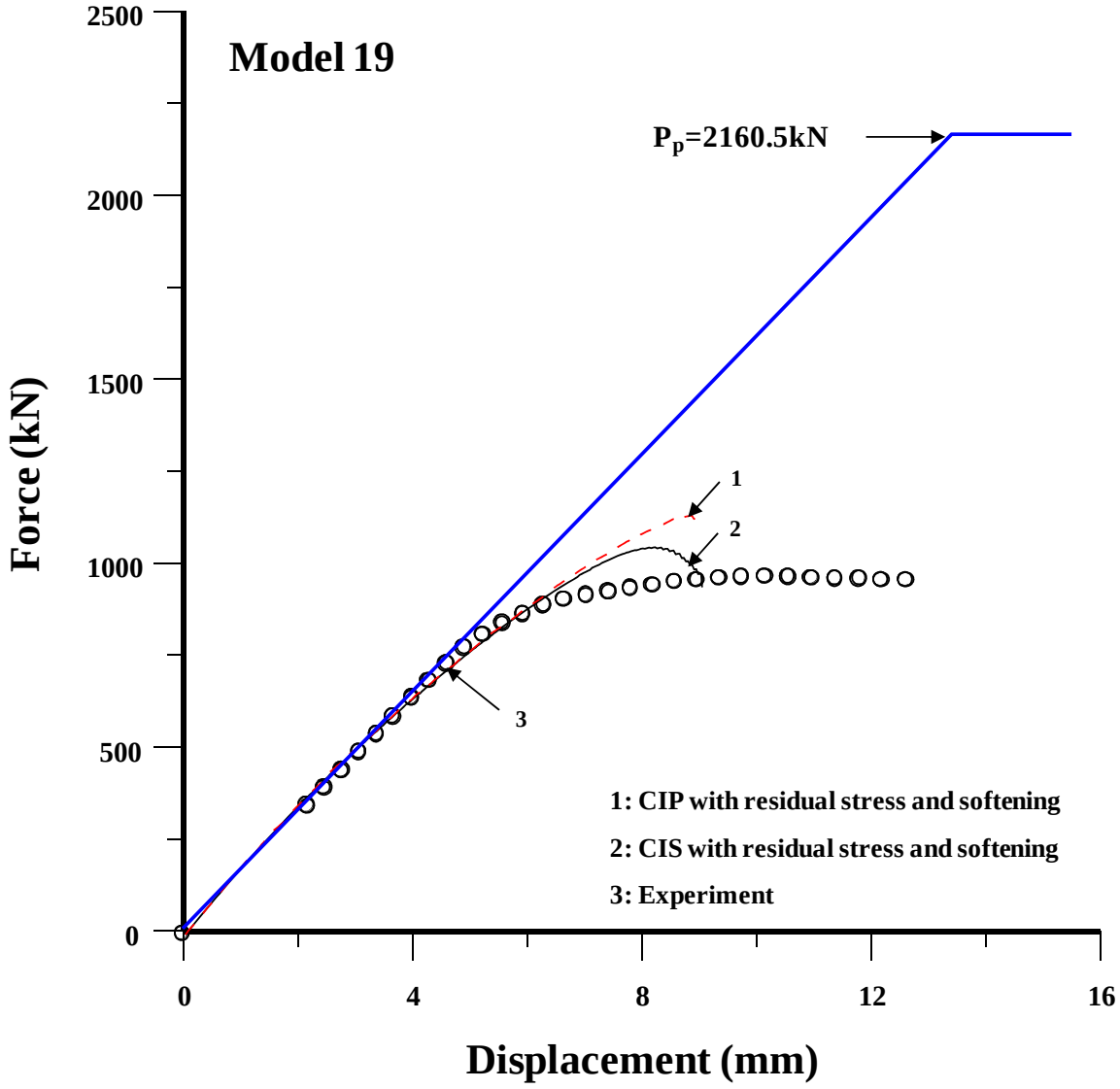

Figure 6.22 The axial compressive force versus the axial compressive displacement of test structure 19

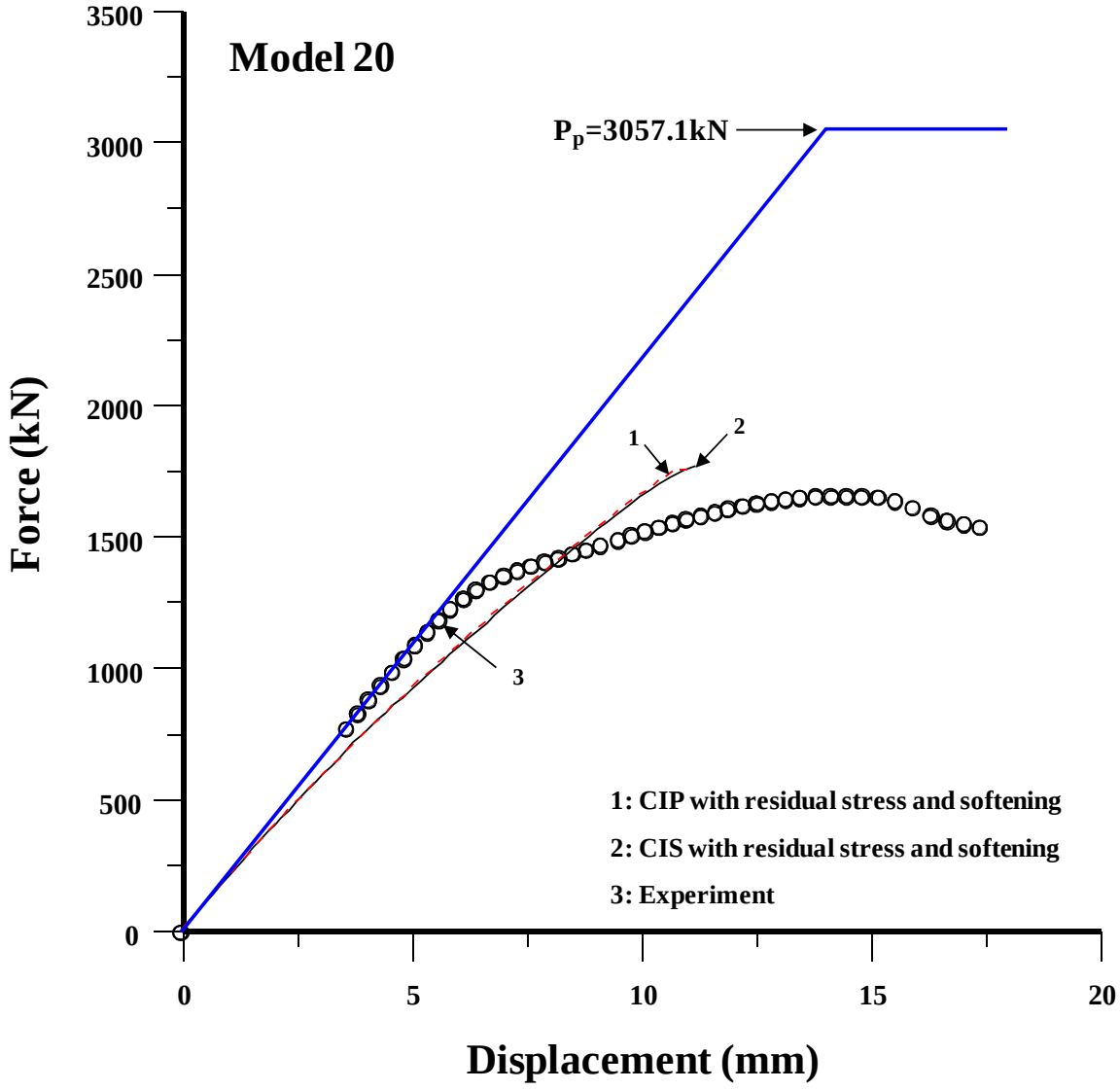

Figure 6.23 The axial compressive force versus the axial compressive displacement of test structure 20

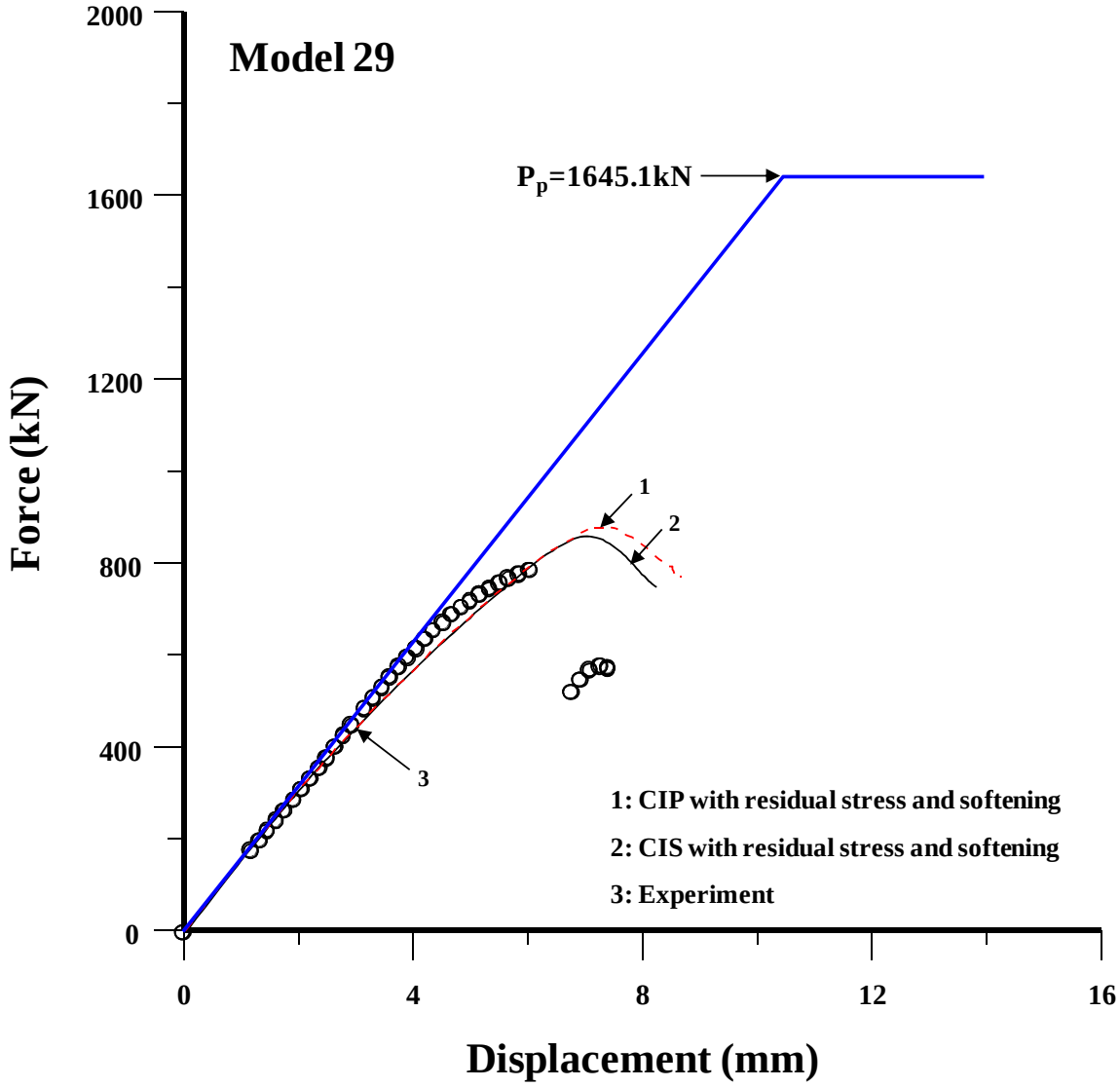

Figure 6.24 The axial compressive force versus the axial compressive displacement of test structure 29

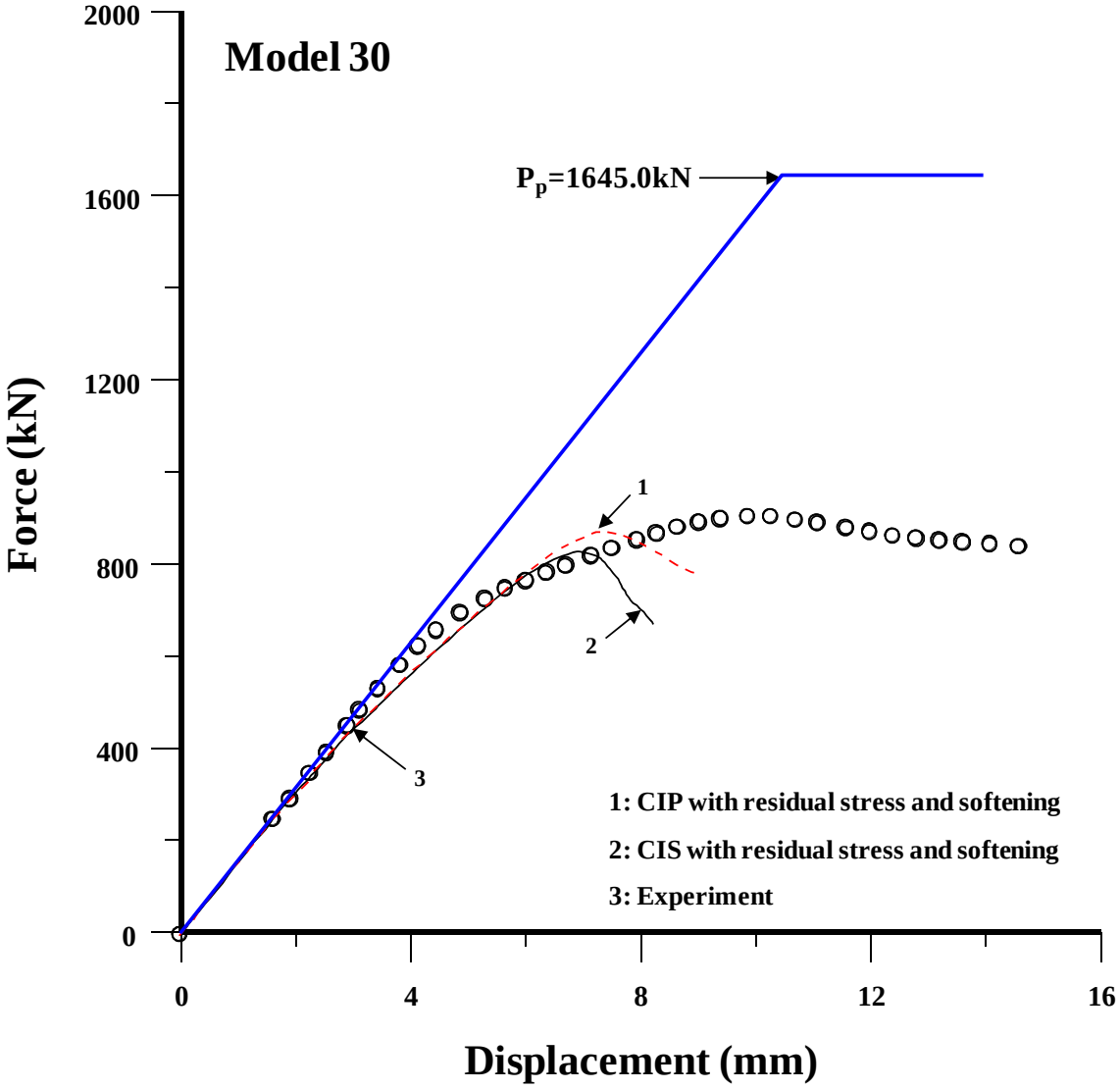

Figure 6.25 The axial compressive force versus the axial compressive displacement of test structure 30

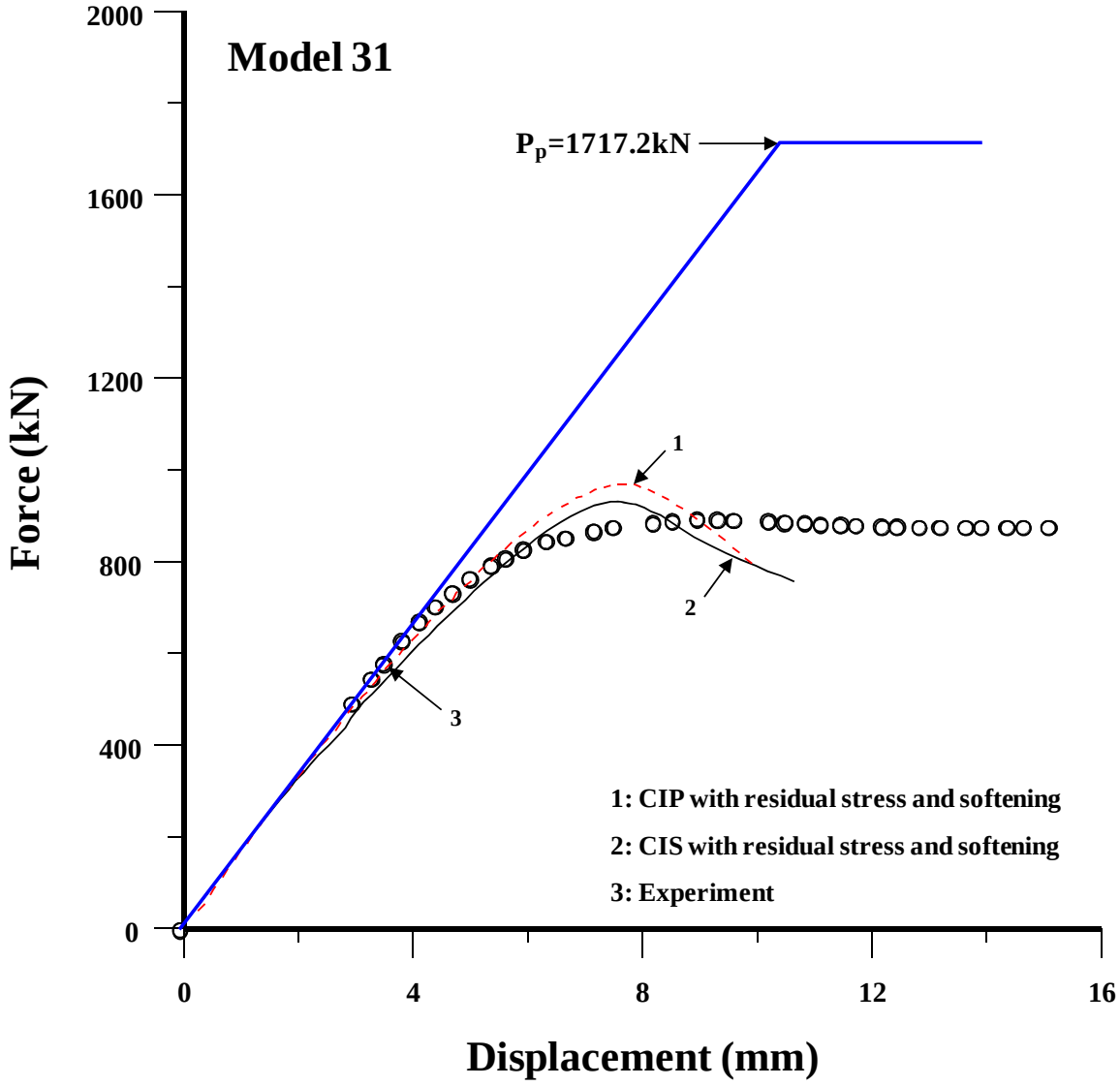

Figure 6.26 The axial compressive force versus the axial compressive displacement of test structure 31

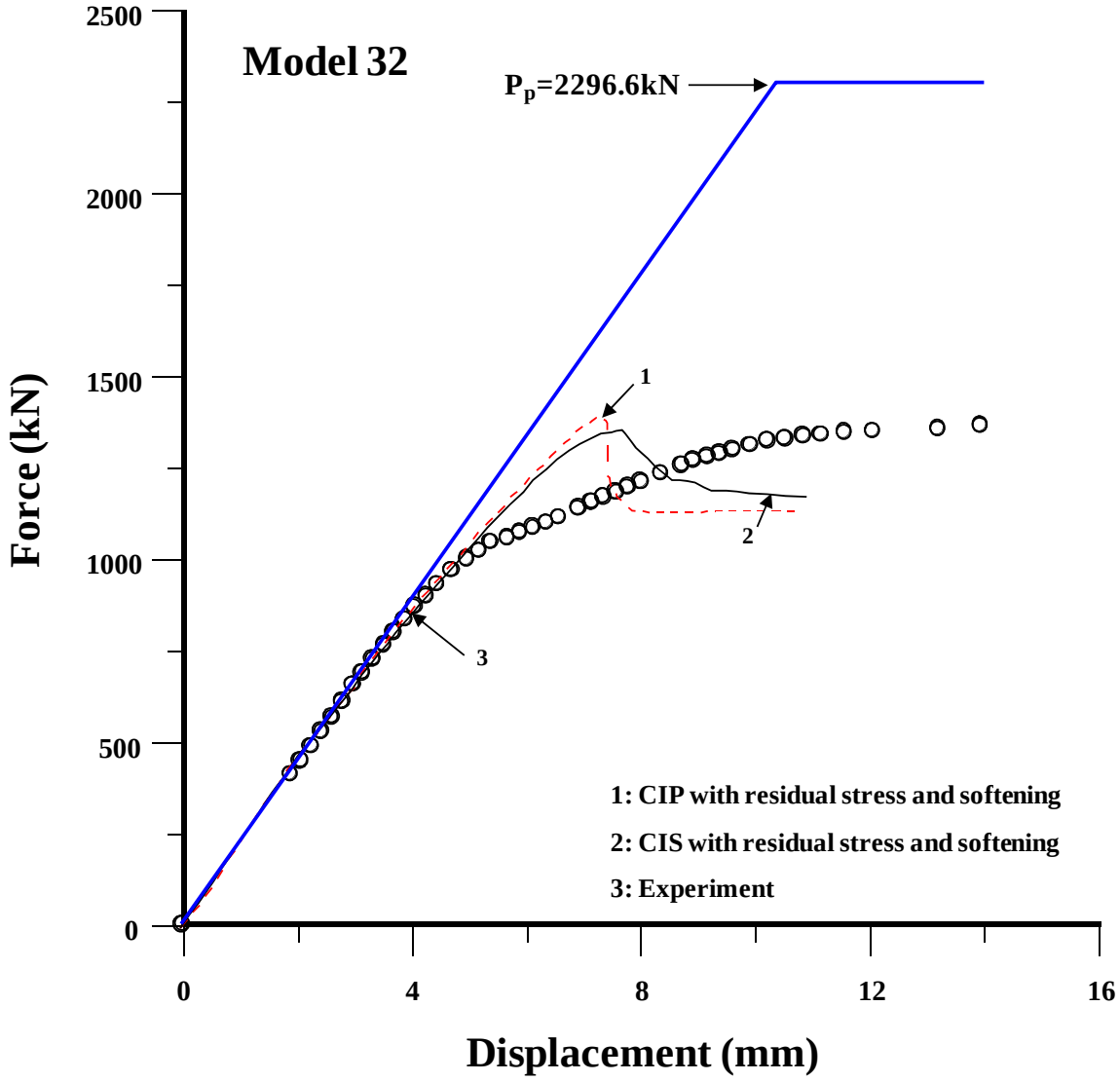

Figure 6.27 The axial compressive force versus the axial compressive displacement of test structure 32

Table 6.3 Summary of the ultimate compressive strength computations for the SSC-451 test structures in terms of the ultimate compressive stress normalized the equivalent yield stress

Model (Fig. No.)	Experiment		FEA	
			With residual stress and softening	
			CIP	CIS
	σ_{xu}/σ_{Yeq}	Collapse mode	σ_{xu}/σ_{Yeq}	σ_{xu}/σ_{Yeq}
5 (6.16)	0.448	III	0.478	0.471
6 (6.17)	0.530	III	0.516	0.495
7 (6.18)	0.516	III	0.554	0.526
8 (6.19)	0.615	V	0.604	0.590
17 (6.20)	0.431	III	0.506	0.491
18 (6.21)	0.460	III	0.532	0.500
19 (6.22)	0.513	III, IV	0.602	0.556
20 (6.23)	0.627	III, IV	0.575	0.582
29 (6.24)	0.447	V	0.486	0.475
30 (6.25)	0.515	V	0.532	0.508
31 (6.26)	0.494	III, IV	0.564	0.543
32 (6.27)	0.548	III, IV	0.608	0.594

Note: Collapse mode is as defined in Section 5.1; CIP = column-type initial distortion of the stiffeners in the x direction with compression on the plate side; CIS = column-type initial distortion of the stiffeners in the x direction with compression on the stiffener side; $\sigma_{xu} = P_u / A_t$ where A_t = total cross-sectional area of the entire stiffened panel.

Table 6.4 Summary of the ultimate strength computations for the SSC-451 test structures in terms of the ultimate force normalized by the fully plastic force

Model (Fig. No.)	P_p (kN)	Experiment		FEA	
		P_u (kN)	P_u/P_p	P_u (kN)	P_u/P_p
5 (6.16)	1831.3	777.8	0.425	816.6	0.446
6 (6.17)	1831.2	918.0	0.501	857.3	0.468
7 (6.18)	1903.4	931.8	0.490	954.6	0.502
8 (6.19)	2482.8	1513.8	0.610	1451.0	0.584
17 (6.20)	2049.0	778.0	0.380	884.4	0.432
18 (6.21)	2048.8	829.6	0.405	901.2	0.440
19 (6.22)	2160.5	970.5	0.449	1053.1	0.487
20 (6.23)	3057.1	1659.2	0.543	1757.6	0.575
29 (6.24)	1645.1	791.0	0.481	858.6	0.522
30 (6.25)	1645.0	908.7	0.552	835.2	0.508
31 (6.26)	1717.2	895.9	0.522	931.4	0.542
32 (6.27)	2296.6	1367.3	0.595	1363.0	0.593

Note: P_u = ultimate compressive force; P_p = fully plastic axial force.

Chapter 7 Comparison of Ultimate Compressive Strength Performance between Fusion Welds and Friction Stir Welds

7.1 Ultimate Compressive Strength Design Formulae for Fusion-welded Structures

When a continuous stiffened plate structure is modeled as an assembly of plate-stiffener combinations, it is recognized that the ultimate compressive strength of the representative plate-stiffener combination model can be given by the following equation (Paik & Thayamballi 2003).

$$\frac{\sigma_{xu}}{\sigma_{Yeq}} = \frac{1}{\sqrt{C_1 + C_2\lambda^2 + C_3\beta^2 + C_4\lambda^2\beta^2 + C_5\lambda^4}}, \tag{7.1}$$

where $C_1 \sim C_5$ = the coefficients to be determined from a database, σ_{Yeq} = equivalent yield strength calculated from the average yield strength as described in Section 3.2.2.

The ultimate strength, σ_{xu}, computed from Equation (7.1) should be smaller than the elastic buckling strength as a column, namely

$$\frac{\sigma_{xu}}{\sigma_{Yeq}} \le \frac{1}{\lambda^2}. \tag{7.2}$$

For welded steel stiffened plate structures, the following coefficients for Equation (7.1) have been suggested (Paik & Thayamballi 2003).

C_1 = 0.995, C_2 = 0.963, C_3 = 0.170, C_4 = 0.188, and C_5 = -0.067. (7.3)

The coefficients of Equation (7.1) for fusion fillet-welded aluminum stiffened plate structures were determined based on the SSC-451 database, depending on the type of stiffener, as follows (Paik 2007, Paik et al. 2008a).

- Tee or angle type (extruded or built-up):

C_1 = 1.318, C_2 = 2.759, C_3 = 0.185, C_4 = -0.177, and C_5 = 1.003. (7.4)

- Flat bar type:

C_1 = 2.50, C_2 = -0.588, C_3 = 0.084, C_4 = 0.069, and C_5 = 1.217. (7.5)

For fusion-welded aluminum stiffened plate structures with flat bar-type stiffeners, the ultimate compressive strength, σ_{xu}, computed from Equation (7.1), together with the coefficients of Equation (7.5), should be smaller than the following value and the elastic buckling stress defined in Equation (7.2), that is,

$$\frac{\sigma_{xu}}{\sigma_{Yeq}} \leq \frac{1}{\sqrt{-16.297 + 18.776\lambda + 17.716\beta - 22.507\lambda\beta}} . \qquad (7.6)$$

7.2 5083 Plates with β = 2.45~2.86

Figure 7.1 provides a comparison between the ultimate strength performance of fusion welds and friction stir welds for the test structures in which the plate part is made of 5083 alloys. Plate slenderness ratio β is in the range of 2.45 to 2.86, and the variation in the ultimate strength performance is represented as a function of column slenderness ratio λ which is computed as a representative plate-stiffener combination, i.e., for a single stiffener with attached plating.

The shaded region in Figure 7.1 indicates the ultimate strength of friction stir-welded test structures. The ultimate strength design formula solutions using Equation (7.1), together with the coefficients of Equation (7.4), are also compared.

It should be noted that test structure 20D-1, which was fabricated via friction stir-welded lap-joining, reached its ultimate strength unintentionally through delamination in the welded region rather than via buckling collapse.

It is evident from Figure 7.1 together with Tables 5.1, 5.2 and 6.1 to 6.4 that the ultimate strength performance of friction stir-welded aluminum structures is superior to that of fusion-welded aluminum structures. It is observed that the use of friction stir welds can increase the ultimate strength performance by 10~20% compared to fusion welds, as long as the quality of the friction stir-welded region is assured.

7.3 5383 Plates with β = 2.66~2.72

A similar comparison of the ultimate strength performance of fusion and friction stir welds for 5083 alloy plates is shown in Figure 7.2 for the test structures in which the plate part is made of 5383 alloys. Plate slenderness ratio β is in the range of 2.66 to 2.72, and the ultimate strength design formula solutions using Equation (7.1), together with the coefficients of Equation (7.4), are also compared. The shaded region in Figure 7.2 indicates the ultimate strength of friction stir-welded test structures.

It should be noted that test structure 20C, which was fabricated via friction stir-welded butt-joining, reached its ultimate strength unintentionally through delamination in the welded region rather than via buckling collapse. It is evident that a similar conclusion to that for the 5083 plates is reached for the friction stir-welded aluminum structures with 5383 alloy plates.

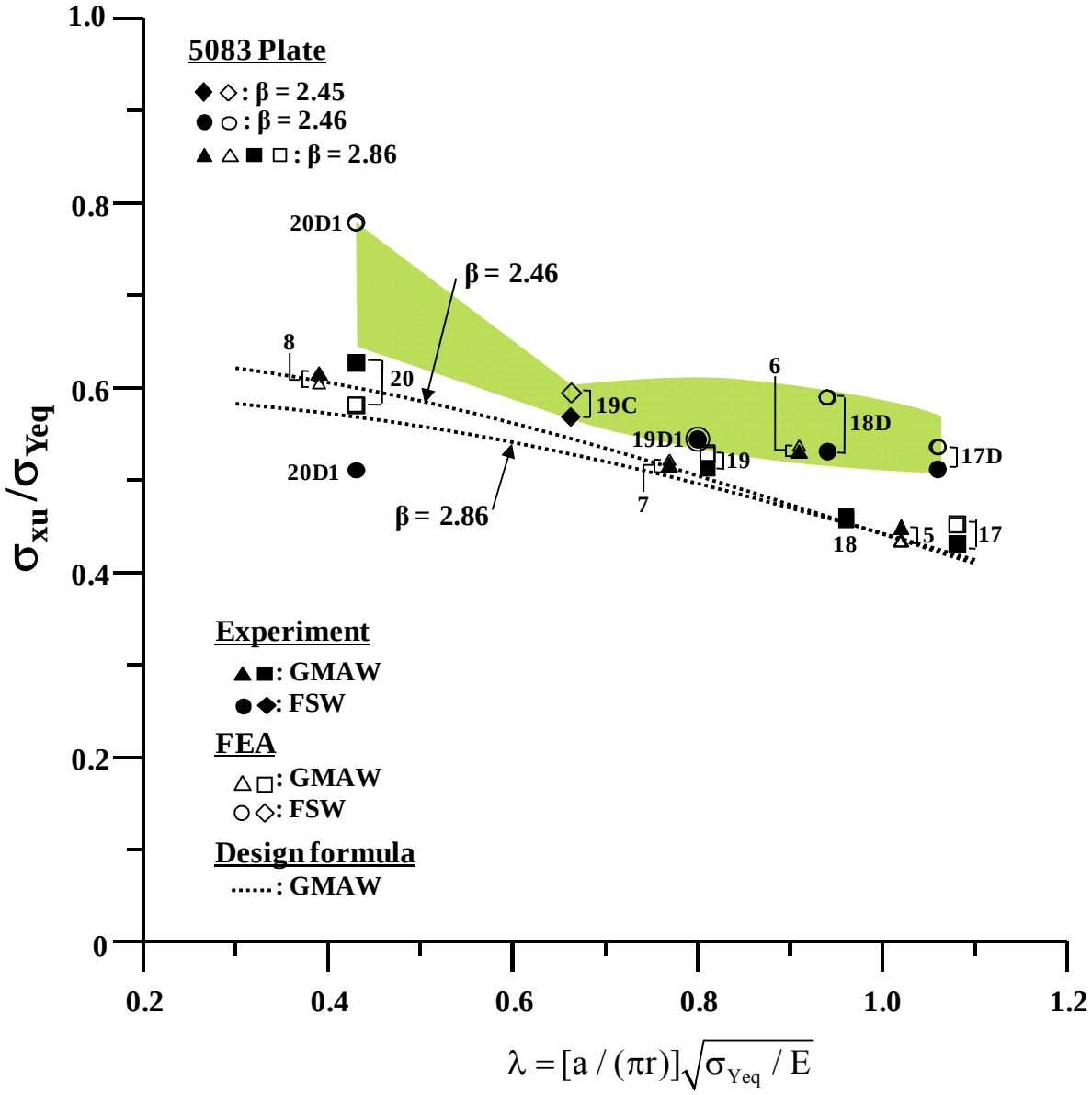

Figure 7.1 Variation in the ultimate compressive strength performance of fusion-welded and friction stir-welded aluminum stiffened plate structures with 5083 alloy plates

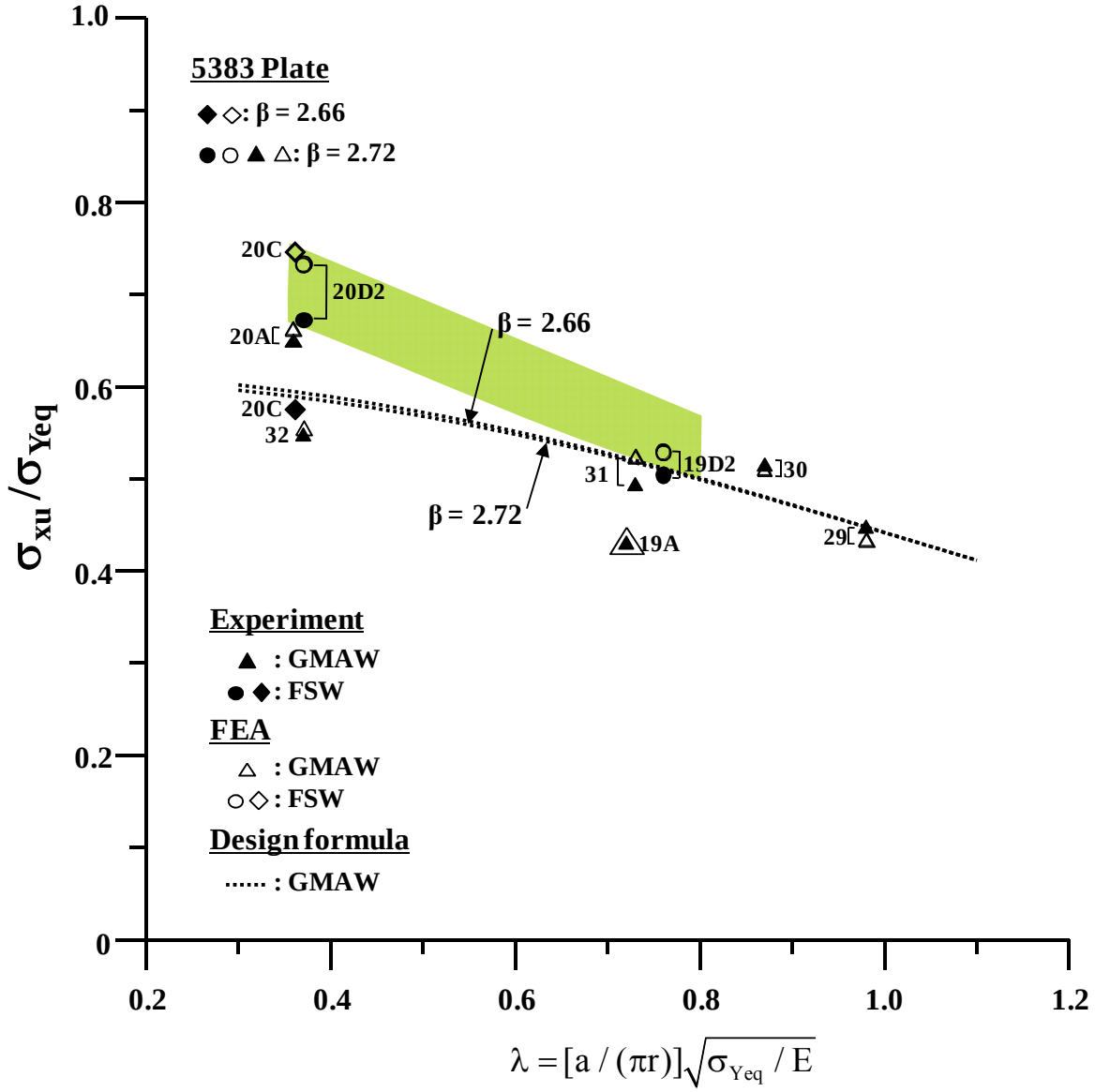

Figure 7.2 Variation in the ultimate compressive strength performance of fusion-welded and friction stir-welded aluminum stiffened plate structures with 5383 alloy plates

7.4 Ultimate Compressive Strength Design Formula for Friction Stir-welded Structures

The number of test data points valid for the anticipated buckling collapse mode of friction stir-welded structures is six, while the results of test structures 20D1 and 20C which had reached the ultimate limit state by an unintended collapse mode due to delamination in the friction stir-welded region are excluded.

Due to the limited amount of test data points, it is not straightforward to develop

ultimate strength design formula for friction stir-welded structures. Nevertheless, the present study attempts to determine the coefficients C_1 through C_5 of Equation (7.1) applying direct optimization and least square techniques as follows.

$$C_1 = 0.2870,\ C_2 = 0.0,\ C_3 = 0.2096,\ C_4 = 0.4937, \text{ and } C_5 = -0.6790. \qquad (7.7)$$

In terms of implementing the coefficients of Equation (7.7) into Equation (7.1), Equation (7.2) is applied. Also, the coefficients of Equation (7.7) are found to be valid for the column slenderness ratio smaller than 1.4. Figure 7.3 presents the accuracy of Equation (7.1) together with Equation (7.7) by a comparison with experimental results. It is seen from Figure 7.3 that the solutions of the ultimate strength design formula, i.e., Equation (7.1) with the coefficients of Equation (7.7), are in reasonably good agreement with the test data points of the friction stir-welded aluminum structures.

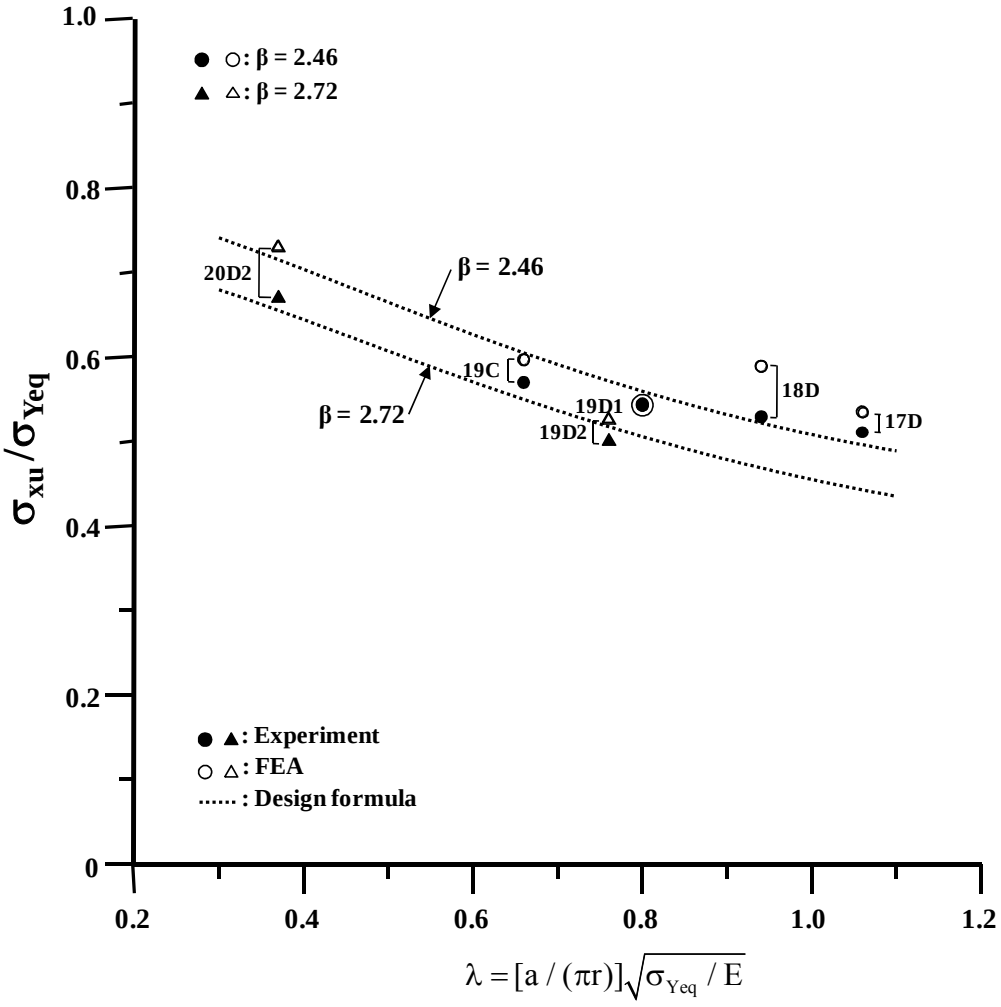

Figure 7.3 Accuracy of the ultimate compressive strength design formula for friction stir-welded aluminum structures

Chapter 8 Conclusions and Recommendations

The objectives of this study were to develop a mechanical buckling collapse test database for 5000's and 6000's series aluminum stiffened plate structures fabricated by friction stir welding and to compare these structures with similar aluminum plate panels fabricated by fusion welding in terms of weld-induced initial imperfections and ultimate compressive strength performance.

In SSC-451, the ultimate strength characteristics of 78 aluminum stiffened plate structures fabricated by fusion fillet welding were investigated through buckling collapse tests and the nonlinear finite element method. The statistics for the fusion weld-induced initial imperfections were analyzed in terms of the mean values and standard deviations at three levels, namely, the slight, average, and severe levels. Ultimate compressive strength design formulae were also developed for the fusion-welded aluminum stiffened plate structures based on the database of the buckling collapse tests and nonlinear finite element method computations. A total of 12 test structures in SSC-451 that had extruded stiffeners were selected and utilized for a comparison with a total of 10 test structures in the present study in which 8 test structures were fabricated by friction stir welding (6 lap-welds and 2 butt-welds) and 2 test structures were fabricated by fusion fillet welding.

The trends or benefits found to be associated with the fusion welding and friction stir welding procedures are discussed in Chapters 3 to 7. The following is a summary of these discussions.

Chapter 3 presents the mechanical properties of aluminum alloys in fusion- and friction-stir welded region of butt welds as well as in base (parent) material, which were obtained from tensile coupon tests. It is found that the tensile property in the butt-welded material of friction stir welding is equivalent or even better than that of fusion welding.

Chapter 4 presents the database of weld-induced initial imperfections for the aluminum stiffened plate structures obtained from SSC-451 and the present study, and also provides a comparison of the initial imperfections induced by fusion welds and those induced by friction stir welds. It is concluded that the initial imperfections induced by friction stir welding are smaller than those induced by fusion welding. Thus, the benefits of the friction stir welding procedure in this respect are clear.

Chapter 5 presents the database of the buckling collapse tests on the friction stir-welded aluminum stiffened plate structures. Most of the test structures fabricated by both friction stir and fusion welds (Models 19A and 20A) reached their ultimate strength through the anticipated collapse mode. However, all of the friction stir-welded test structures showed delamination in the welded region after or even before the ultimate strength had been reached. For example, delamination occurred in test structures 20D1 and 20C in the pre-collapse range. In contrast, no crack failure was observed in the fusion-welded region of test structures 19A and 20A as well as in the test structures studied in SSC-451 by fusion welds, before and after the ultimate strength had been reached. This indicates that the fusion-weld procedure is superior to the friction stir-weld procedure in terms of compressive strength performance in the welded region.

Since the pre-collapse delamination can significantly reduce the ultimate compressive strength of the structure, the quality assurance in the friction stir-welded region is highly required to prevent delamination failure. In friction stir lap-welded structures, i.e., joined between base plate and extruded stiffeners, delamination may not be of major concern in terms of the water tightness. However, delamination shall be of great concern in friction stir butt-welded structures, i.e., joined between flange free edges of extrusions because the water tightness is no longer assured after delamination. In this regard, the friction stir lap-welding may be more promising than the friction stir butt-welding to replace the fusion fillet-welding, as long as the delamination is concerned.

It is recognized that the mechanical property and delamination in the friction stir-welded region is significantly affected by the welding parameters such as width and depth of molten metal thin layer, molten temperature, rotating and forwarding speeds, and possible quick cooling, etc. It is thus important to establish optimum parameters of friction stir welding to assure the quality of the welded region and also to prevent any weld defects and delamination. Non-destructive test (NDT) methods can be used for the quality assurance in the friction stir welded region.

Chapter 6 presents a comparison of the nonlinear finite element method computations with the experimental results. It is found that this method is able to compute the ultimate strength behavior of welded aluminum structures with a reasonable degree of accuracy. However, it is important to realize that the computational results depend significantly on the structural modeling techniques applied. Through the comparison of the nonlinear finite element computations with experimental results, it turns out that test structures 20D1 and 20C must have collapsed unintentionally earlier.

Chapter 7 presents a comparison of the ultimate compressive strength performance of fusion fillet welds and friction stir butt- or lap-welds. It is found that this performance is 10-20% greater in the friction stir-welded aluminum structures than it is in the fusion-welded aluminum structures. This implies that the friction stir welding procedure is certainly superior to the fusion welding procedure in terms of ultimate compressive strength performance, as long as the delamination in the friction stir welded region is prevented.

It is considered that there are still a lot of challenging issues to be resolved to apply the friction stir welding technology for marine applications. Further studies are recommended as follows.

- Tensile coupon tests for friction stir lap-welds as well as friction stir butt-welds in terms of the mechanical property characterization,
- Microscopic examination of friction stir lap-welds as well as friction stir butt-welds,
- Additional buckling collapse tests for friction stir butt-welds by fabrication method C-2,
- Additional buckling collapse tests for friction stir lap-welds by fabrication method D with different parameters of friction stir welding process such as width and depth of molten thin layer to evaluate the pre- and post-collapse delamination phenomena and their causes.

References

AA (2005). Aluminum design manual, Table 3.3-2, The Aluminum Association, Arlington, Virginia, USA.

ABS (2006). Rules for material and welding, Part 2 Aluminum and fiber reinforced plastics, Chapter 5, Appendix 1, Table 2, American Bureau of Shipping, Houston, USA.

Alcan (2004). Aluminum and the sea, Paris, France.

ANSYS (2008). User's manual (version 11.0), ANSYS Inc., Canonsburg, PA, USA.

AWS (2004). Guide for aluminum hull welding, AWS D3.7, American Welding Society, USA.

Bang, H.S., Kim, H.J., Go, M.S., Chang, W.S. and Lee, C.W. (2002). A study on welding residual stress by numerical simulation on friction stir welding, International Journal of Korea Welding Society, Vol. 2, No. 1, pp. 62-66.

Biallas, G., Braun, R., Dalle Donne, C., Staniek, G. and Kaysser, W.A. (1999). Mechanical properties and corrosion behavior of friction stir welded 2024-T3, Proceedings of the 1st International Friction Stir Welding Symposium, Thousand Oaks, California.

Cavaliere, P., De Santis, A., Panella, F. and Squillace, A. (2009). Effect of welding parameters on mechanical and microstructural properties of dissimilar AA6082-AA2024 joints produced by friction stir welding, Materials and Design, Vol. 30, pp. 609-616.

Collette, M.D. (2005). Strength and reliability of aluminum stiffened panels, Ph.D. Thesis, University of Newcastle, Newcastle upon Tyne, UK.

Collette, M.D. (2007). The impact of fusion welds on the ultimate strength of aluminum structures, Proceedings of 10th International Symposium on Practical Design of Ships and Other Floating Structures (PRADS 2007), Houston, USA.

Colligan, K.J. (2004). Friction stir welding for ship construction, Concurrent Technologies Corporation, Harrisburg, PA.

Dawes, C.J. and Thomas, W.M. (1995). Friction stir joining of aluminum alloys, TWI Bulletin, The Welding Institute, November/December.

DNV (2008). Rules for classification of high speed, light craft and naval surface craft, Part 3, Chapter 3, Section 2, Table B4, Oslo, Norway.

Fratini, L. and Zuccarello, B. (2006). An analysis of though-thickness residual stresses in aluminum FSW butt joints, International Journal of Machine Tools & Manufacture, Vol. 46, pp. 611-619.

Hagstrom, J. and Sandstrom, R. (1998). Static and dynamic properties of joints in thin-walled aluminum extrusions, welded with different methods, Proceedings of 6th International Conference on Aluminum Alloys, Toyohashi, Japan, pp. 1447-1452.

Hashimoto, T., Nishikawa, N., Tazaki, S. and Enomoto, M. (1998). Mechanical properties of joints for aluminum alloys with friction stir welding process, Proceedings of 7th International Conference on Joints in Aluminum, Cambridge, UK, 15-17 April.

Inter Technology (2005). Measurement of residual stresses by the hole-drilling strain gauge method, Technical Note TN-503-6, Vishay Micro-Measurements, Don Mills, Ontario, Canada (www.intertechnology.com).

ISO (2007). International standard ISO 18072-1: Ships and marine technology – Ship structures – Part 1: General requirements for their limit state assessment, International Organization for Standardization, Geneva, Switzerland.
James, M.N., Hughes, D.J., Hattingh, D.G., Mills, G. and Webster, P.J. (2009). Residual stress and strain in MIG butt welds in 5083-H321 aluminum: As welded and fatigue cycled, International Journal of Fatigue, Vol. 31, pp. 28-40.
Kallee, S. (2000). Application of friction stir welding in the shipbuilding industry, Proceedings of International Conference on Lightweight Construction – Latest developments, RINA, 24-25 February, London.
Kamioka, M. and Okubo, K. (2005). Studies on fatigue properties of friction stir welded joints in structural thin aluminum alloys, Proceedings of the 5th International Forum on Aluminum Ships, Tokyo, Japan, 11-13 October, pp. 115-124.
Khandkar, M.H., Khan, J.A., Reynolds, A.P. and Sutton, M.A. (2006). Predicting residual thermal stresses in friction stir welded metals, Journal of Materials Processing Technology, Vol. 174, pp. 195-203.
Kramer, R. (2007). In-service performance of aluminum structural details, Ship Structure Committee Report, SSC-447, Washington DC.
Lombard, H., Hattingh, D.G., Steuwer, A. and James, M.N. (2009). Effect of process parameters on the residual stresses in AA5083-H321 friction stir welds, Materials Science and Engineering A, Vol. 501, pp. 119-124.
LR (2008). Lloyd's Register rules and regulations for the classification of special service craft, Vol.1, Part 2 Rules for the maintenance, testing and certification of materials, Chapter 8 – Aluminum alloys and Part 7 – Hull construction in aluminum, London, UK.
Mahoney, M.W., Rhodes, C.G., Flintoff, J.G., Spurling, R.A. and Bingel, W.H. (1998). Properties of friction stir welded 7075-T651 aluminum, Metallurgical and Materials Transactions A, Vol. 29A, pp. 1955-1964.
Masubuchi, K. (1980). Analysis of welded structures, Pergamon Press, Oxford, UK.
Midling, O.T., Oosterkamp, L.D. and Bersaas, J. (1998). Friction stir welding – Process and applications, Proceedings of 7th International Conference on Joints in Aluminum, Cambridge, UK, 15-17 April.
Mohlkert, L. (2005). New opportunities with friction stir welding, Proceedings of the 5th International Forum on Aluminum Ships, Tokyo, Japan, 11-13 October, pp. 111-113.
Murphy, A., McCune, W., Quinn, D. and Price, M. (2007). The characterization of friction stir welding process effects on stiffened panel buckling performance, Thin-Walled Structures, Vol. 5, pp. 339-351.
Nicholas, E.D. (1998). Developments in the friction stir welding of metals, Proceedings of 6th International Conference on Aluminum Alloys, Toyohashi, Japan, pp. 139-151.
Paik, J.K. (2007). Empirical formulations for predicting the ultimate compressive strength of welded aluminum stiffened panels, Thin-Walled Structures, Vol.45, pp.171-184.
Paik, J.K., Andrieu, C. and Cojeen, H.P. (2008a). Mechanical collapse testing on aluminum stiffened plate structures for marine applications, Marine Technology, Vol.45, No.4, pp. 228-240.
Paik, J.K., Hughes, O.F., Hess, P.E. and Renaud, C. (2005). Ultimate limit state design

technology for aluminum multi-hull ship structures, Trans. SNAME, Vol. 113, pp. 270-305.
Paik, J.K. and Sohn, J.M. (2009). Effects of welding residual stresses on high tensile steel plate ultimate strength: Nonlinear finite element method investigations, Proceedings of the 28th International Conference on Offshore Mechanics and Arctic Engineering (OMAE 2009), OMAE2009-79297, Honolulu, Hawaii, 31 May-5 June.
Paik, J.K. and Thayamballi, A.K. (2003). Ultimate limit state design of steel-plated structures, John Wiley & Sons, Chichester, UK.
Paik, J.K. and Thayamballi, A.K. (2007). Ship-shaped offshore installations: Design, building, and operation, Cambridge University Press, Cambridge, UK.
Paik, J.K., Thayamballi, A.K. Ryu, J.Y., Jang, J.H., Seo, J.K., Park, S.W., Seo, S.K., Renaud, C., Cojeen, H.P., and Kim, N.I. (2006). The statistics of weld induced initial imperfections in aluminum stiffened plate structures for marine applications, International Journal of Maritime Engineering, Vol.148, A4, pp.19-63.
Paik, J.K., Thayamballi, A.K., Ryu, J.Y., Jang, J.H., Seo, J.K., Park, S.W., Seo, S.K., Andrieu, C. and Kim, N.I. (2008b). Mechanical collapse testing on aluminum stiffened panels for marine applications, Ship Structure Committee Report, SSC-451, Washington DC.
Peel, M., Steuwer, A., Preuss, M. and Withers, P.J. (2003). Microstructure, mechanical properties and residual stresses as a function of welding speed in aluminum AA5083 friction stir welds, Acta Materialia, Vol. 51, pp. 4791-4801.
Prime, M.B., Gnaupel-Herold, T., Baumann, J.A., Lederich, R.J., Bowden, D.M. and Sebring, R.J. (2006). Residual stress measurements in a thick, dissimilar aluminum alloy friction stir weld, Acta Materialia, Vol. 54, pp. 4013-4021.
Przydatek, J. (2000). Friction stir welding with Lloyd's Register, Proceedings of International Conference on Lightweight Construction – Latest developments, RINA, 24-25 February, London.
Rhodes, C.G., Mahoney, M.W. and Bingel, W.H. (1997). Effects of friction stir welding on microstructure of 7075 aluminum, Scripta Materialia, Vol. 36, No. 1, pp. 69-75.
Sanderson, A., Punshon, C.S. and Russell, J.D. (2000). Advanced welding processes for fusion reactor fabrication, Fusion Engineering and Design, Vol. 49-50, pp. 77-87.
Sielski, R.A. (2007). Review of structural design of aluminum ships and crafts, Trans. SNAME, Vol. 115, pp. 1-30.
Sielski, R.A. (2008). Research needs in aluminum structure, Ships and Offshore Structures, Vol. 3, No. 1, pp. 57-65.
Staron, P., Kocak, M., Williams, S. and Wescott, A. (2004). Residual stress in friction stir-welded Al sheets, Physica B, Vol. 350, pp. e491-e493.
Thomas, W.M. (1998). Friction stir welding and related friction process characteristics, Proceedings of the 7th International Conference on Joints in Aluminum (INALCO'98), Cambridge, UK, April.
Thomas, W.M. and Nicholas, E.D. (1997). Friction stir welding for the transportation industry, Materials & Design, Vol. 18, Nos. 4/6, pp. 269-273.
Thomas, W.M., Nicholas, E.D., Needham, J.C., Murch, P., Temple-Smith, P. and Dawes, C.J. (1991). Friction stir welding, International Patent Application PCT/GB92/02203, GB Patent Application 9125978.8, December 6.
Thomas, W.M., Nicholas, E.D., Needham, J.C., Murch, P., Temple-Smith, P. and Dawes,

C.J. (1995). Friction stir welding, US Patent No. 5460317, October 25.
Thomas, W.M., Nicholas, E.D., Watts, E.R. and Staines, D.G. (2002). Friction based welding technology for aluminum, Proceedings of the 8th International Conference on Aluminum Alloys, Cambridge, UK, 2-5 July.
Thomas, W.M., Staines, D.G., Oakley, P.J. and Watts, E.R. (2005). Friction stir welding for aluminum applications – Process development, Proceedings of the 5th International Forum on Aluminum Ships, Tokyo, Japan, 11-13 October, pp. 137-144.
Zhang, Z. and Zhang, H.W. (2009a). Numerical studies on the effect of transverse speed in friction stir welding, Materials and Design, Vol. 30, pp. 900-907.
Zhang, Z. and Zhang, H.W. (2009b). Numerical studies on controlling of process parameters in friction stir welding, Journal of Materials Processing Technology, Vol. 209, pp. 241-270.

Appendix Mechanical Properties of the Materials after Buckling

Figures A.1 to A.10 show the stress-strain relationships of the materials that underwent buckling, as obtained from the tensile coupon tests. These materials were cut out of the test structures after the buckling collapse test, as shown in Figure A.11.

Table A.1 Comparison of the mechanical properties of virgin materials with those of the materials that experienced buckling

Material	Model	Elastic modulus (N/mm^2)	Yield stress (N/mm^2)	Ultimate tensile stress (N/mm^2)	Elongation (%)
5083-H112	Virgin	69856.8	167.2	307.67	33.09
	17D	69691.9	154.7	267.4	24.39
	18D	68326.1	140.1	266.5	22.35
	19D1	70202.7	138.3	264.6	23.35
	20D1	68675.5	138.7	267.5	22.94
	19C	69439.5	145.8	271.0	22.05
5383-H116	Virgin	70355.3	207.9	342.0	25.85
	19A	70254.6	194.6	307.1	12.67
	20A	70668.7	173.1	296.2	13.97
	19D2	70151.5	199.9	316.0	14.63
	20D2	69665.1	174.2	297.0	17.17
	20C	68044.7	173.5	297.1	15.20

Table A.1 presents a comparison of the mechanical properties of the materials that experienced buckling with those of virgin materials. All the tensile coupon test specimens of the materials after buckling were cut out in the plate longitudinal direction, although the mechanical properties of virgin materials are their average values in the longitudinal, transverse or diagonal directions as those indicated in Chapter 3.

As can be seen from Table A.1, the mechanical properties of the buckling-

experienced materials are inferior to those of the virgin materials. The yield stress, ultimate tensile stress and elongation of the materials that had undergone buckling are significantly reduced when compared to those of virgin materials, although the elastic modulus remains almost unchanged.

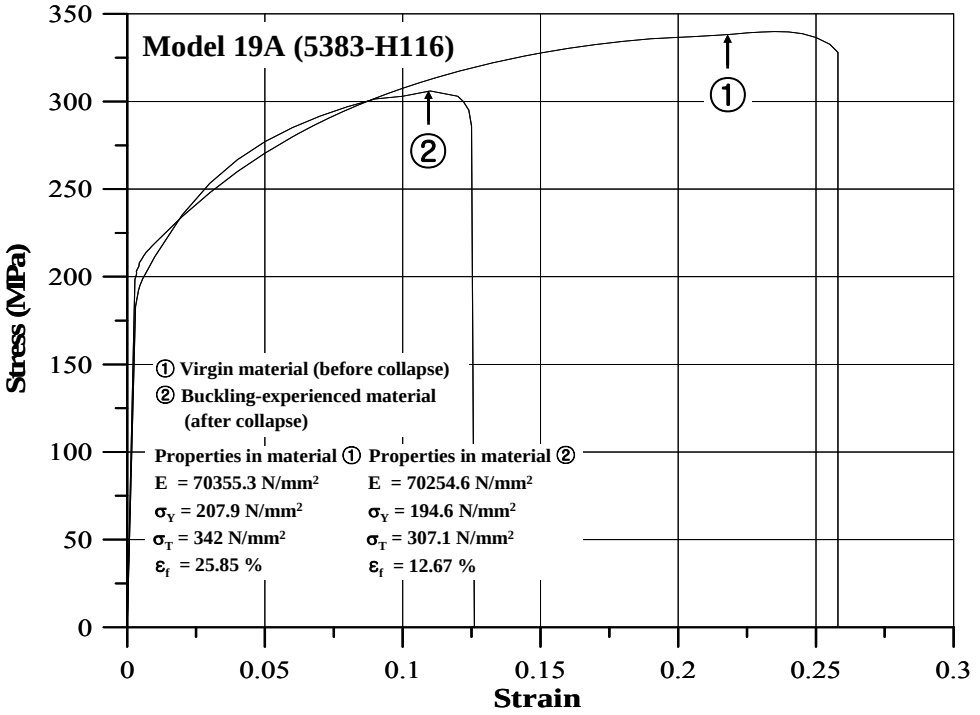

Figure A.1 The stress-strain relationship of material 5383-H116 after buckling in test structure 19A

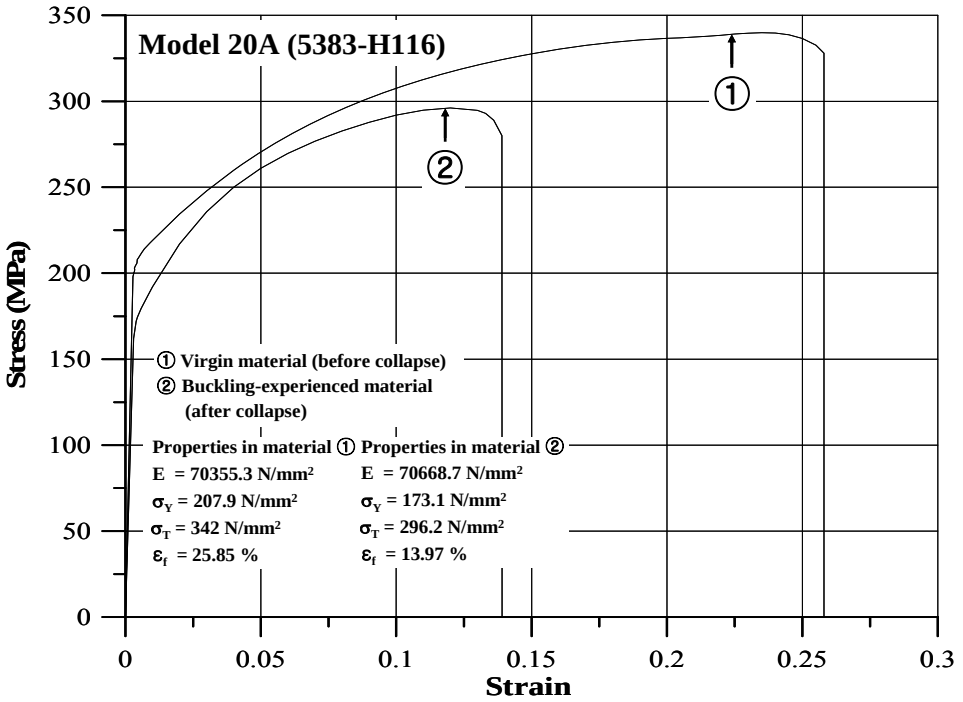

Figure A.2 The stress-strain relationship of material 5383-H116 after buckling in test structure 20A

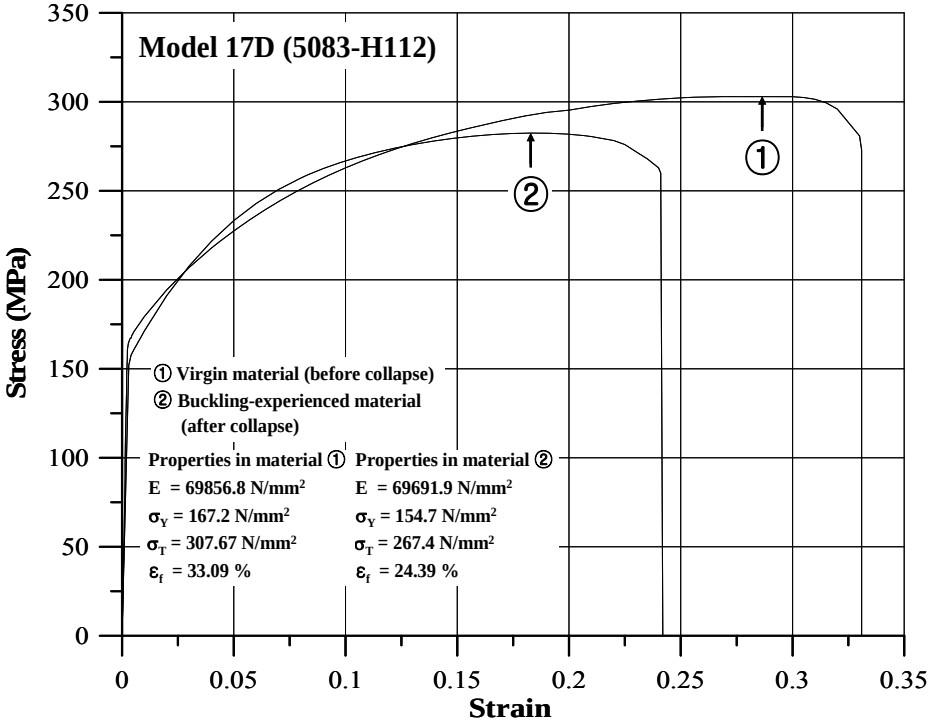

Figure A.3 The stress-strain relationship of material 5083-H112 after buckling in test structure 17D

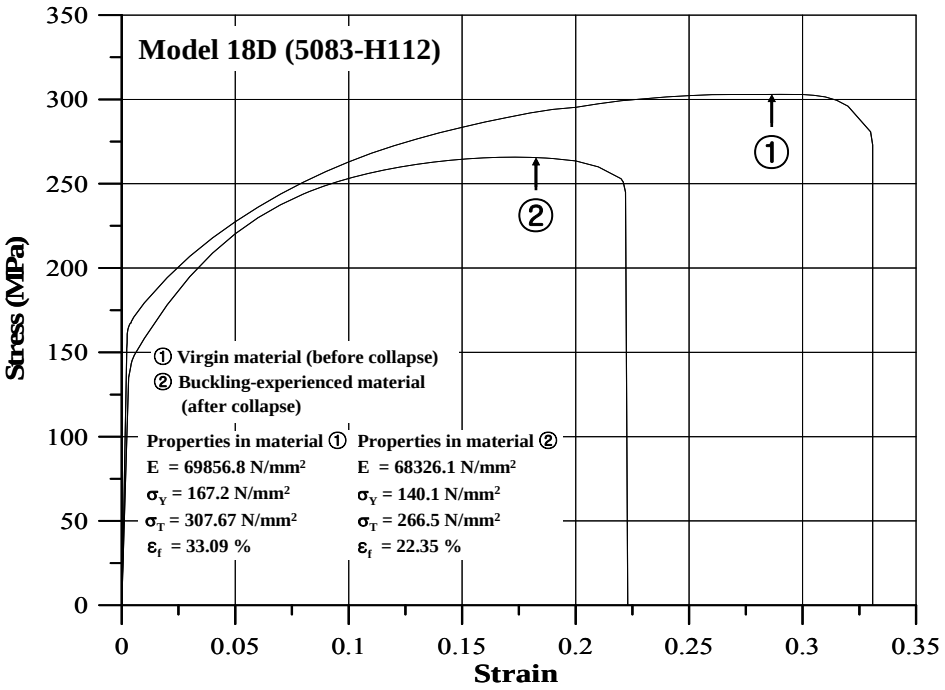

Figure A.4 The stress-strain relationship of material 5083-H112 after buckling in test structure 18D

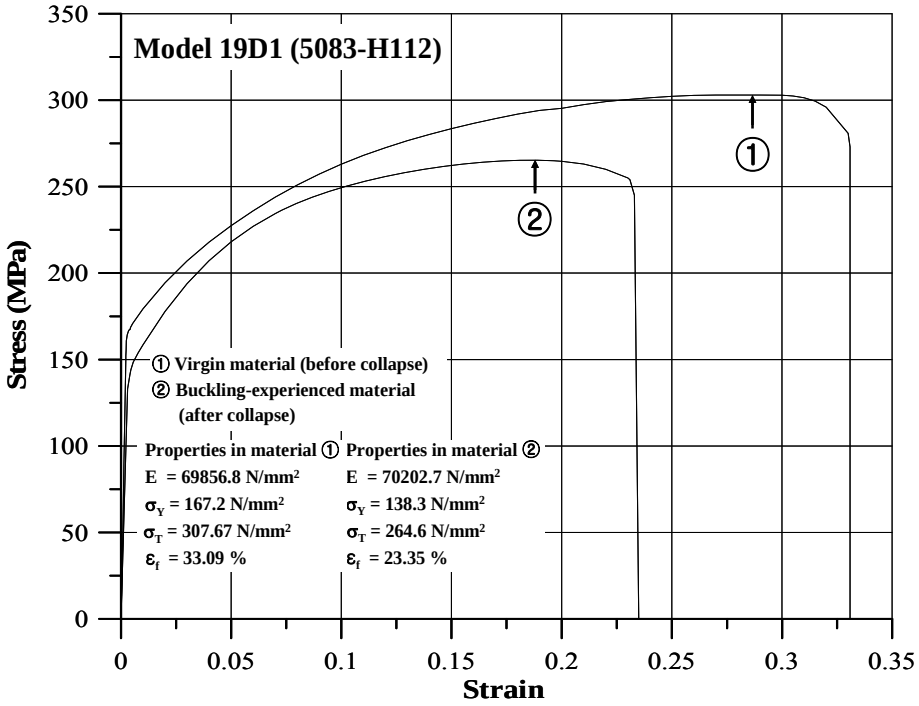

Figure A.5 The stress-strain relationship of material 5083-H112 after buckling in test structure 19D1

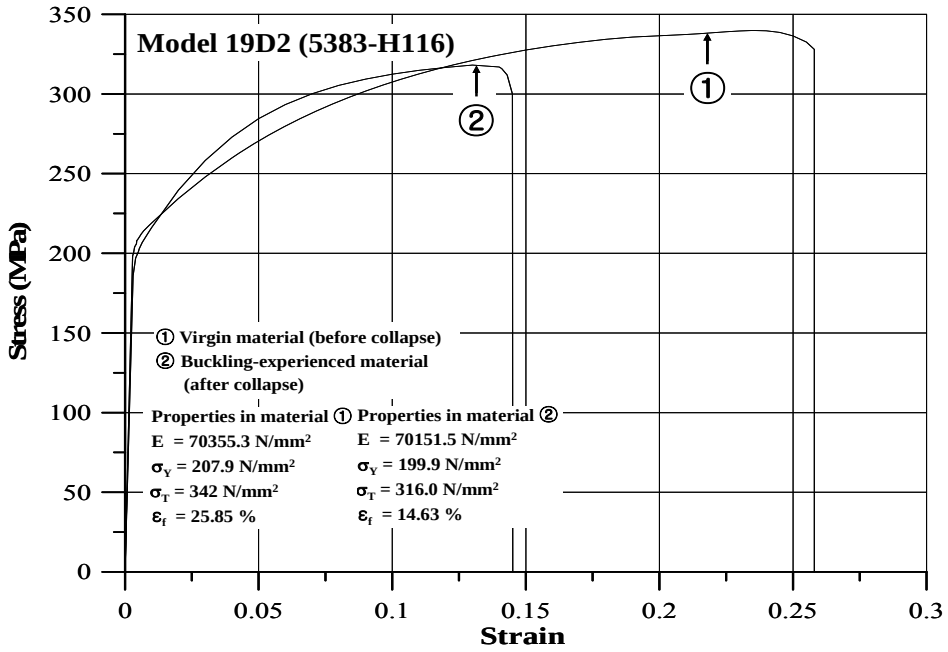

Figure A.6 The stress-strain relationship of material 5383-H116 after buckling in test structure 19D2

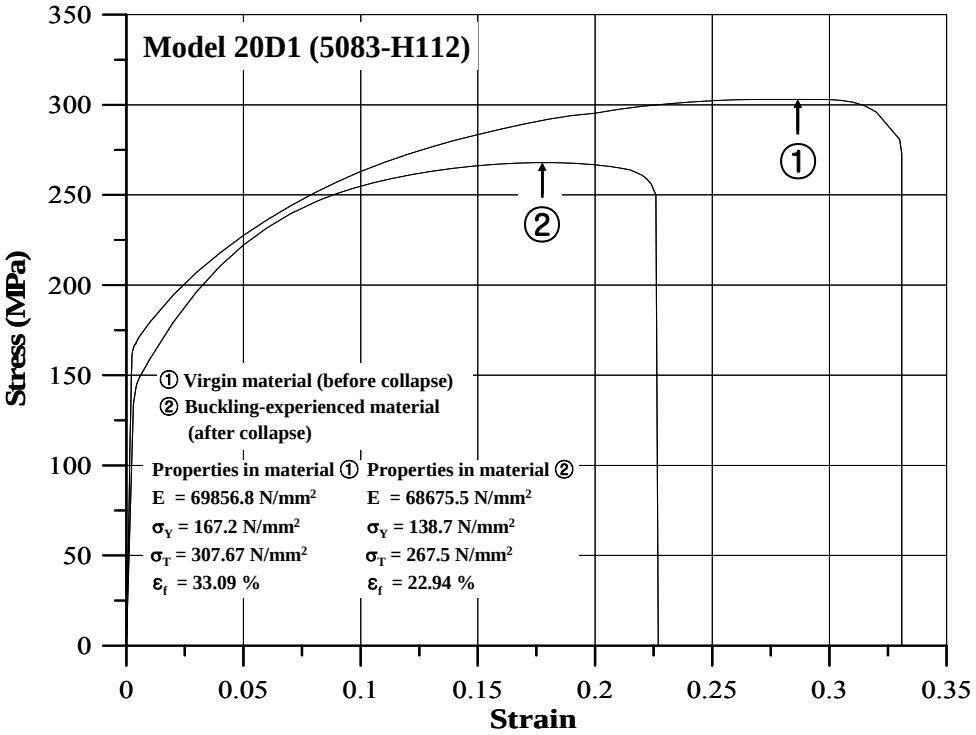

Figure A.7 The stress-strain relationship of material 5083-H112 after buckling in test structure 20D1

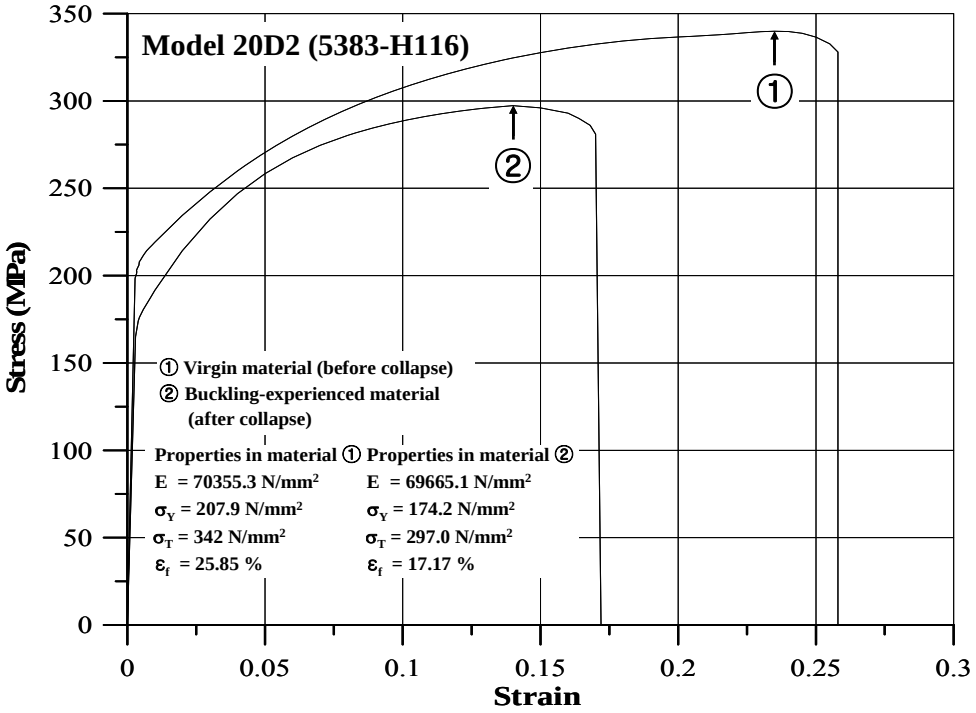

Figure A.8 The stress-strain relationship of material 5383-H116 after buckling in test structure 20D2

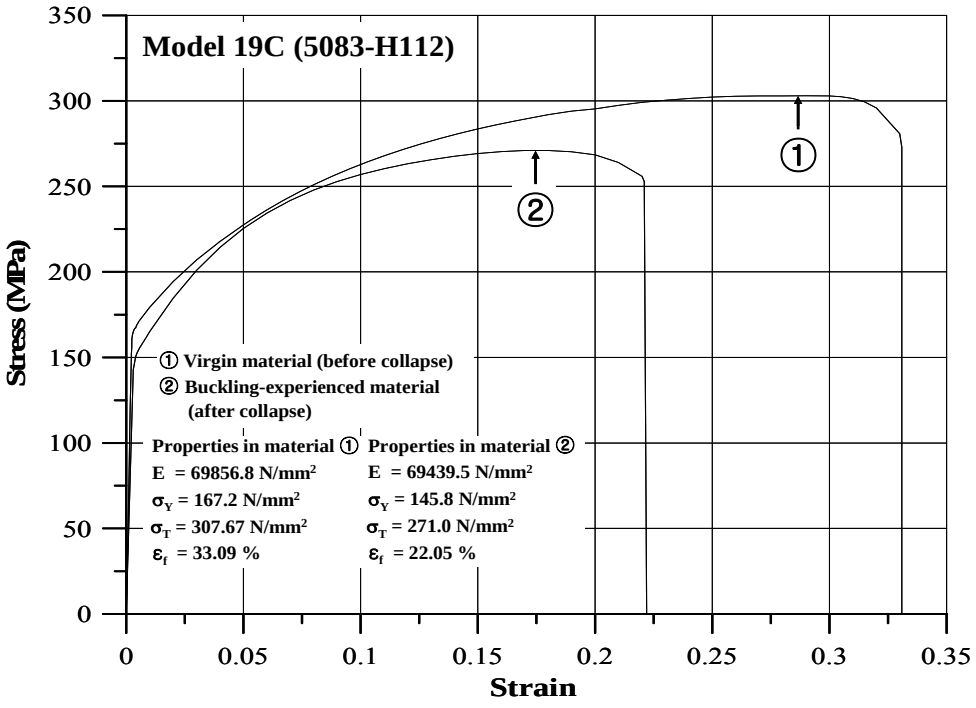

Figure A.9 The stress-strain relationship of material 5083-H112 after buckling in test structure 19C

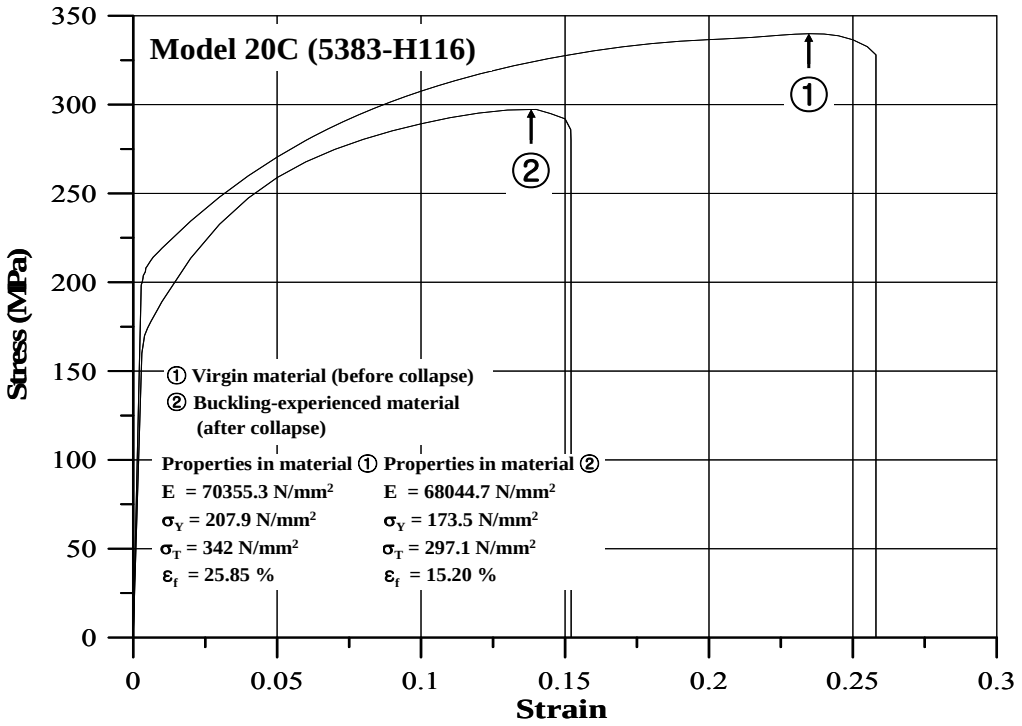

Figure A.10 The stress-strain relationship of material 5383-H116 after buckling in test structure 20C

Figure A.11 Photo of one of the test structures after the material test specimen had been cut out of the buckling collapsed structure

PROJECT TECHNICAL COMMITTEE MEMBERS

The following persons were members of the committee that represented the Ship Structure Committee to the Contractor as resident subject matter experts. As such they performed technical review of the initial proposals to select the contractor, advised the contractor in cognizant matters pertaining to the contract of which the agencies were aware, performed technical review of the work in progress and edited the final report.

Chairman

Members
Contracting Officer's Technical Representative:

Marine Board Liaison:

Executive Director Ship Structure Committee:

SHIP STRUCTURE COMMITTEE LIAISON MEMBERS

LIAISON MEMBERS

American Society of Naval Engineers	Captain Dennis K. Kruse (USN Ret.)
Bath Iron Works	Mr. Steve Tarpy
Colorado School of Mines	Dr. Stephen Liu
Edison Welding Institute	Mr. Rich Green
International Maritime Organization	Mr. Igor Ponomarev
Int'l Ship and Offshore Structure Congress	Dr. Alaa Mansour
INTERTANKO	Mr. Dragos Rauta
Massachusetts Institute of Technology	
Memorial University of Newfoundland	Dr. M. R. Haddara
National Cargo Bureau	Captain Jim McNamara
National Transportation Safety Board - OMS	Dr. Jack Spencer
Office of Naval Research	Dr. Yapa Rajapaksie
Oil Companies International Maritime Forum	Mr. Phillip Murphy
Samsung Heavy Industries, Inc.	Dr. Satish Kumar
United States Coast Guard Academy	Commander Kurt Colella
United States Merchant Marine Academy	William Caliendo / Peter Web
United States Naval Academy	Dr. Ramswar Bhattacharyya
University of British Columbia	Dr. S. Calisal
University of California Berkeley	Dr. Robert Bea
Univ. of Houston - Composites Eng & Appl.	
University of Maryland	Dr. Bilal Ayyub
University of Michigan	Dr. Michael Bernitsas
Virginia Polytechnic and State Institute	Dr. Alan Brown
Webb Institute	Prof. Roger Compton

RECENT SHIP STRUCTURE COMMITTEE PUBLICATIONS

Ship Structure Committee Publications on the Web - All reports from SSC 1 to current are available to be downloaded from the Ship Structure Committee Web Site at URL: http://www.shipstructure.org

SSC 445 – SSC 393 are available on the SSC CD-ROM Library. Visit the National Technical Information Service (NTIS) Web Site for ordering hard copies of all SSC research reports at URL: http://www.ntis.gov

SSC Report Number	Report Bibliography
SSC 455	Feasibility, Conceptual Design and Optimization of a Large Composite Hybrid Hull, Braun D., Pejcic M. 2008
SSC 454	Ultimate Strength and Optimization of Aluminum Extrusions, Collette M., Wang C. 2008
SSC 453	Welding Distortion Analysis Of Hull Blocks Using Equivalent Load Method Based On Inherent Strain, Jang C.D. 2008
SSC 452	Aluminum Structure Design and Fabrication Guide, Sielski R.A. 2007
SSC 451	Mechanical Collapse Testing on Aluminum Stiffened Panels for Marine Applications, Paik J.K. 2007
SSC 450	Ship Structure Committee: Effectiveness Survey, Phillips M.L., Buck R., Jones L.M. 2007
SSC 449	Hydrodynamic Pressures and Impact Loads for High Speed Catamaran / SES, Vorus W. 2007
SSC 448	Fracture Mechanics Characterization of Aluminum Alloys for Marine Structural Applications, Donald J.K., Blair A. 2007
SSC 447	Fatigue and Fracture Behavior of Fusion and Friction Stir Welded Aluminum Components, Kramer R. 2007
SSC 446	Comparative Study of Naval and Commercial Ship Structure Design Standards, Kendrick A., Daley C. 2007
SSC 445	Structural Survivability of Modern Liners, Iversen R. 2005
SSC 444	In-Service Non-Destructive Estimation of the Remaining Fatigue Life of Welded Joints, Dexter R.J., Swanson K.M., Shield C.K. 2005
SSC 443	Design Guidelines for Doubler Plate Repairs on Ship Structures Sensharma P.K., Dinovitzer A., Traynham Y. 2005